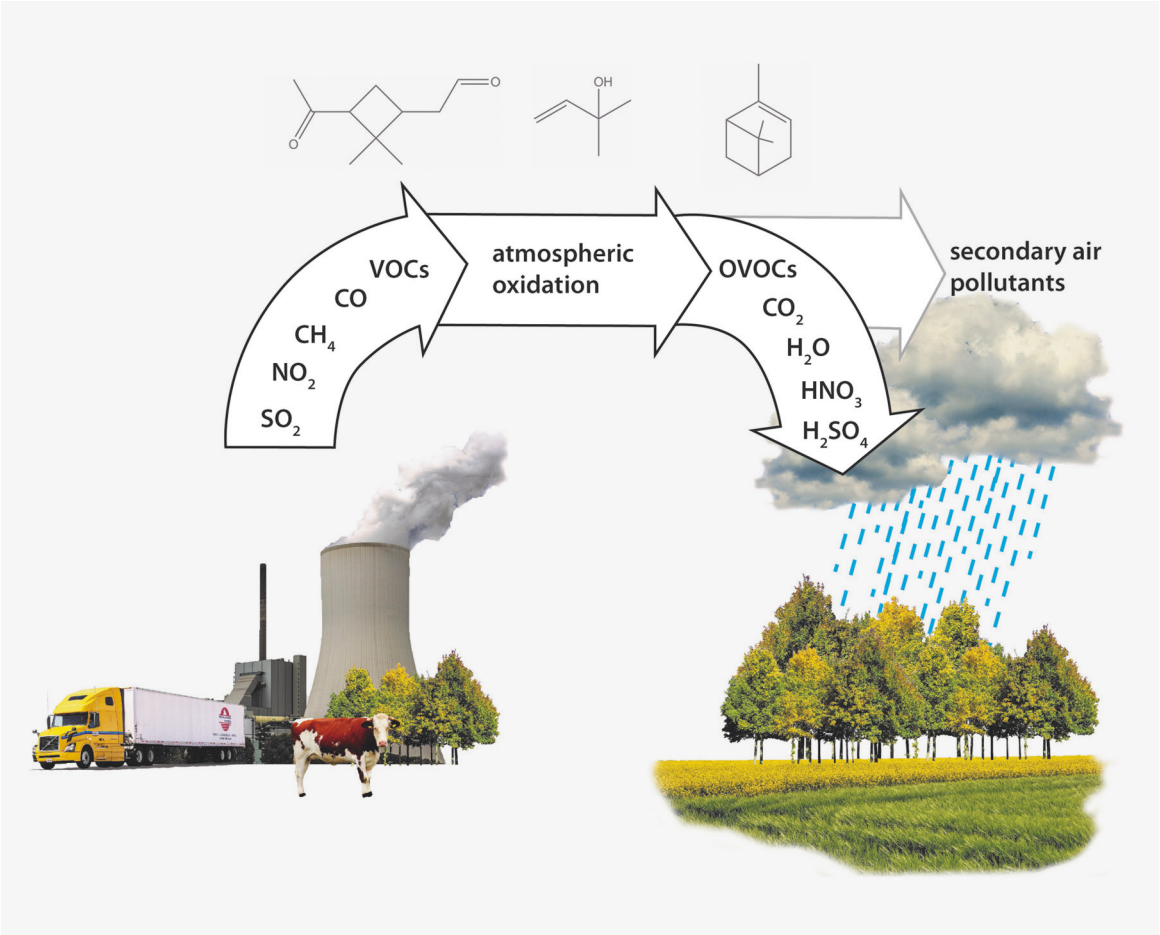

Experimental study of the chemical degradation of biogenic volatile organic compounds by atmospheric OH radicals

Michael Rolletter

Energie & Umwelt / Energy & Environment
Band / Volume 550
ISBN 978-3-95806-568-0

Mitglied der Helmholtz-Gemeinschaft

JÜLICH
Forschungszentrum

Schriften des Forschungszentrums Jülich
Reihe Energie & Umwelt / Energy & Environment Band / Volume 550

Forschungszentrum Jülich GmbH
Institut für Energie- und Klimaforschung
Troposphäre (IEK-8)

Experimental study of the chemical degradation of biogenic volatile organic compounds by atmospheric OH radicals

Michael Rolletter

Schriften des Forschungszentrums Jülich
Reihe Energie & Umwelt / Energy & Environment Band / Volume 550

ISSN 1866-1793 ISBN 978-3-95806-568-0

Bibliografische Information der Deutschen Nationalbibliothek.
Die Deutsche Nationalbibliothek verzeichnet diese Publikation in der
Deutschen Nationalbibliografie; detaillierte Bibliografische Daten
sind im Internet über http://dnb.d-nb.de abrufbar.

Herausgeber und Vertrieb:	Forschungszentrum Jülich GmbH Zentralbibliothek, Verlag 52425 Jülich Tel.: +49 2461 61-5368 Fax: +49 2461 61-6103 zb-publikation@fz-juelich.de www.fz-juelich.de/zb
Umschlaggestaltung:	Grafische Medien, Forschungszentrum Jülich GmbH
Druck:	Grafische Medien, Forschungszentrum Jülich GmbH
Copyright:	Forschungszentrum Jülich 2021

Schriften des Forschungszentrums Jülich
Reihe Energie & Umwelt / Energy & Environment, Band / Volume 550

D 38 (Diss. Köln, Univ., 2021)

ISSN 1866-1793
ISBN 978-3-95806-568-0

Vollständig frei verfügbar über das Publikationsportal des Forschungszentrums Jülich (JuSER)
unter www.fz-juelich.de/zb/openaccess.

Abstract

Approximately 1000 Tg of carbon is annually emitted by biogenic sources. In the atmosphere, these compounds are oxidized and thereby secondary air pollutants are formed such as secondary organic aerosol (SOA) and ozone, thus contribution to air quality and climate change. At daytime, biogenic volatile organic compounds (BVOCs) are mainly degraded by photolytically produced hydroxyl (OH) radicals. In the presence of nitric oxide (NO), OH initiated reactions proceed through radical chain reactions that involve organic peroxy radicals (RO_2). In field studies conducted in forested environments, which were characterized by large BVOC emissions and low NO concentrations, measured OH concentrations were largely underestimated by model calculations using state-of-the-art chemical models, thus underestimating the oxidative capacity of the atmosphere. In the degradation scheme of isoprene, the BVOC with the globally highest emission rate, new chemical pathways for OH regeneration that involve unimolecular reactions of RO_2 have been discovered. However, few studies exist, which investigate radical regeneration in the photooxidation of other abundant hydrocarbons and monoterpenes. This thesis aims for investigating potential new pathways for radical regeneration in the the photooxidation of three selected BVOCs that were abundant in previous field campaigns: 2-methyl-3-butene-2-ol (MBO), α-pinene, and the oxidation production of α-pinene, pinonaldehyde.

In total, five experiments, which were conducted in 2012 and 2014 in the atmospheric simulation chamber SAPHIR (Simulation of Atmospheric PHotochemistry In a large Reaction chamber), are analyzed. A comprehensive set of instruments provided concentration measurements of OH and hydroperoxy (HO_2) radicals, OH reactivity, injected BVOCs, formed oxidation products, NO_x (= NO + NO_2), and measurements of physical parameters (radiation, temperature, and pressure). In contrast to previous studies, all experiments were performed at ambient reactant concentrations and low NO mixing ratios (< 220 pptv, parts per trillion by volume) to simulate conditions that are typical in forested regions.

In the analysis of this work, measured concentration time series of radicals and organic compounds are compared to zero-dimensional box model calculations that are derived from the recent version of the Master Chemical Mechanism

(MCM). The MCM is a widely used state-of-the-art atmosperic chemical mechanism. In the MBO experiment, the model is capable to reproduce observed radical concentrations and measured product distributions. In contrast, the MCM significantly underestimates measured OH and HO_2 concentrations in the photooxidation of α-pinene and pinonaldehyde. However, the model can reproduce observed OH concentrations when modeled HO_2 concentrations are constrained to measurements. This shows that the current α-pinene and pinonaldehyde degradation mechanisms lack HO_2 sources. In addition, measurements of the oxidation product pinonaldehyde suggest that the yields of RO_2 radicals formed in the initial attack of OH on α-pinene are different than than previously assumed.

For each analyzed BVOC, sensitivity model studies were performed with modification of the MCM mechanism based on available theoretical studies that provide additional reaction pathways of RO_2 radicals, different branching ratios, and unimolecular reactions. Additional sensitivity runs were done to explain the missing HO_2 source.

In the pinonaldehyde experiments, the MCM strongly underestimates the pinonaldehyde degradation. This could be partly explained by the parameterization of the pinonladehyde photolysis rate in the MCM. In order to explain the observed pinonaldehyde consumption, the photolysis rate needs to be a factor of 3 higher than the values calculated with the parameterization in the MCM. This is consistent with calculations of the photolysis rate using the measured solar actinic flux spectrum, a published absorption spectrum, and adjusting the effective quantum yield to a value of 0.9.

At low NO concentrations, the reaction of RO_2 with HO_2 gains in importance in the competition with RO_2 reactions with NO. Recent studies showed that the reaction of acetylperoxy radicals ($CH_3C(O)O_2$) with HO_2 does not only terminate the radical reaction chain but can regenerate OH radicals and therefore can contribute to missing radical regenration in remote regions. The $CH_3C(O)O_2$ detection in previous laboratory studies was mainly done in the ultraviolet (UV). In this spectral area, the absorption spectra of different peroxy radicals overlap. This could lead to systematic errors in the determination of concentrations and reaction rate constants if not properly accounted for. In this thesis, the near infrared spectrum and absorption cross sections of $CH_3C(O)O_2$ were measured by cavity ring-down spectroscopy (CRDS). The newly measured absorption cross sections were used to convert $CH_3C(O)O_2$ absorbance into absolute concentrations. Mea-

sured $CH_3C(O)O_2$ concentration time series were used to validate the absorption cross section by redetermining the second-order reaction rate of the $CH_3C(O)O_2$ self-reaction. The newly measured absorption cross sections will help to achieve more accurate measurements of $CH_3C(O)O_2$ concentration in future laboratory experiments to better quantify the fraction of regenerated radicals.

The results presented in this thesis, help to discover new radical regeneration pathways and improve the understanding of model–measurement discrepancies, which have been observed in previous field experiments. However, future studies are needed that provide additional measurements of oxidation products and reaction intermediates to further resolve reaction pathways.

Zusammenfassung

Ungefähr 1000 Tg Kohlenstoff werden jedes Jahr aus biogenen Quellen emittiert. In der Atmosphäre werden diese Verbindungen oxidiert und bilden dabei sekundäre Luftschadstoffe, wie sekundäres organisches Aerosol (SOA) und Ozon, die Auswirkungen auf die Luftqualität und den Klimawandel haben. Tagsüber werden biogene volatile organische Verbindungen (BVOCs) hauptsächlich durch photolytisch gebildete Hydroxyl-Radikale (OH) abgebaut. In der Gegenwart von Stickstoffmonoxid (NO) verlaufen OH initiierte Reaktionen über Radikalketten ab, die organische Peroxy-Radikale (RO_2) beinhalten. In Feldstudien in bewaldeten Gebieten, die durch hohe BVOC Emissionen und geringe NO Konzentrationen charakterisiert waren, wurden gemessene OH Konzentrationen durch moderne chemische Modelle unterschätzt und damit die oxidative Kapazität der Atmosphäre zu niedrig vorausgesagt. Im Abbaumechanismus von Isopren, dem BVOC mit der höchsten globalen Emissionsrate, wurden neue chemische Pfade, die unimolekulare RO_2 Reaktionen beinhalten, zur OH Regeneration entdeckt. Allerdings existieren wenige Studien, die die Photooxidation anderer häufig vorkommender Kohlenwasserstoffe und Monoterpene untersuchen. Diese Dissertation hat das Ziel potentielle neue Pfade für die Radikalregeneration in der Photooxidation von drei ausgewählten BVOCs, die in zuvor publizierten Feldmesskampagnen relevant waren, zu untersuchen: 2-methyl-3- butene-2-ol (MBO), α-Pinen und das α-Pinen Oxidationsprodukt Pinonaldehyd.

Insgesamt wurden fünf Experimente analysiert, die 2012 und 2014 in der Atmosphärensimulationskammer SAPHIR (Simulation von Atmosphärischer PHotochemie In einer großen Reaktionskammer) durchgeführt wurden. Ein umfassender Satz Instrumente bot Konzentrationsmessungen von OH und Hydroperoxy-Radikalen (HO_2), injizierten BVOCs, gebildeten Oxidationsprodukten, NO_x (= NO + NO_2) sowie die Messung physikalischer Parameter (Strahlung, Temperatur und Druck). Im Gegensatz zu früheren Arbeiten wurden alle Experimente bei Umgebungskonzentration der Reaktanden und geringen NO Mischungsverhältnissen (< 220 pptv) durchgeführt, um Bedingungen zu simulieren, die typisch für bewaldete Gebiete sind.

In der Analyse dieser Arbeit werden gemessene Konzentrationszeitreihen von Radikalen und organischen Verbindungen mit Berechnungen eines nulldimensionalen Boxmodells verglichen, das die aktuellen Version des Master Chemical Mechanism (MCM) nutzt. Der MCM ist ein vielseitig verwendeter, hochmoderner, atmosphärenchemischer Mechanismus. Im MBO Experiment ist das Modell in der Lage beobachtete Radikalkonzentrationen und gemessene Produktverteilungen zu reproduzieren. Im Kontrast dazu unterschätzt der MCM signifikant die in der Photooxidation von α-Pinen und Pinonaldehyd gemessenen OH und HO_2 Konzentrationen. Allerdings kann das Modell die gemessenen OH Konzentrationen reproduzieren, wenn die HO_2 Konzentrationen im Modell durch die Messungen vorgegeben werden. Dies verdeutlicht, dass derzeitigen α-Pinen und Pinonaldehyd Abbaumechanismen eine HO_2 Quelle fehlt. Zusätzlich weisen Messungen des Oxidationsprodukts Pinonaldehyd darauf hin, dass die Ausbeuten der RO_2 Radikale, die beim initialen OH Angriff auf α-Pinen gebildet werden, anders als bisher angenommen sind.

Für jedes untersuchte BVOC wurden Sensitivitätsstudien mit Modifikationen des MCM Mechanismus durchgeführt, die auf verfügbaren theoretischen Studien basieren und zusätzliche Reaktionspfade von RO_2 Radikalen, andere Verzweigungsverhältnisse und unimolekulare Reaktionen bieten. Zusätzliche Sensitivitätsstudien wurden durchgeführt um die fehlende HO_2 Quelle zu erklären.

In den Pinonaldehyd Experimenten unterschätzt der MCM den Pinonaldehydabbau stark. Dies kann teilweise durch die Parametrisierung der Pinonaldehyd Photolyserate im MCM erklärt werden. Um den beobachteten Pinonaldehydverbrauch zu erklären, muss die Photolyserate um den Faktor 3 größer sein als die Werte, die mit der Parametrisierung im MCM berechnet werden. Das ist konsistent mit der Berechnung der Photolyserate mithilfe gemessener solar aktinischen Fluss Spektren, einem publizierten Absorptionsspektrum und einer auf den Wert 0.9 angepassten effektiven Quantenausbeute.

Bei geringen NO Konzentrationen gewinnt die Reaktion von RO_2 mit HO_2 an Bedeutung in der Konkurrenz mit der Reaktion von RO_2 mit NO. Neuere Studien zeigen, dass die Reaktion von Acetylperoxy-Radikalen ($CH_3C(O)O_2$) mit HO_2 nicht nur die Radikalkettenreaktion terminiert, sondern auch OH Radikale regenerieren kann und damit zur Erklärung der fehlenden Radikalregeneration in abgelegenen Regionen beitragen kann. Die Messungen von $CH_3C(O)O_2$ in früheren Laborstudien wurde hauptsächlich im Ultravioletten (UV) durchgeführt. In diesem

Spektralbereich überlappen die Absorptionsspektren von verschiedenen Peroxy-Radikalen. Dies kann, wenn nicht genügend berücksichtigt, zu systematischen Abweichungen bei der Bestimmung von Konzentrationen und Reaktionskonstanten führen. In dieser Arbeit wurden Spektrum und Absorptionsquerschnitte von $CH_3C(O)O_2$ im Nahinfrarot mithilfe der Cavity-ring-down-Spektroskopie (CRDS) gemessen. Der neu gemessene Absorptionsquerschnitt wurde benutzt, um $CH_3C(O)O_2$ Absorbanz in absolute Konzentrationen umzuwandeln. Gemessene $CH_3C(O)O_2$ Konzentrationszeitreihen wurden benutzt, um den Absorptionsquerschnitt durch die Neubestimmung der Reaktionskonstante zweiter Ordnung der $CH_3C(O)O_2$ Selbstreaktion zu validieren. Der neu gemessene Absorptionsquerschnitt wird helfen in zukünftigen Laborexperimenten genauere Messungen von $CH_3C(O)O_2$ Konzentrationen zu erhalten, um den Anteil der regenerierten Radikale besser zu quantifizieren.

Die hier präsentierten Ergebnisse helfen neue Radikalregenerationspfade aufzuklären und verbessern das Verständnis von Diskrepanzen zwischen Modell und Messung, die in früheren Feldexperimenten beobachtet wurden. Jedoch werden zukünftige Studien, die zusätzliche Messungen von Oxidationsprodukten und Reaktionszwischenprodukten bieten, benötigt, um Reaktionspfade weiter aufzuklären.

Contents

1 Introduction **1**
1.1 Biogenic VOCs in the troposphere 2
1.2 Tropospheric radical chemistry 6
1.2.1 Atmospheric OH radical sources 7
1.2.2 Chemical degradation of atmospheric trace gases 8
1.2.3 Radical termination reactions 10
1.2.4 Novel RO_2 chemistry 12
1.3 Objectives of this thesis 18

I Investigation of BVOC photooxidation in SAPHIR **22**

2 Methods **23**
2.1 Description of the experiments in SAPHIR 23
2.2 Instrumentation at the SAPHIR chamber 25
2.2.1 Radical detection 25
2.2.2 OH reactivity 27
2.2.3 VOC Measurements 28
2.2.4 Photolysis frequencies 29
2.3 Chamber specific properties 30
2.4 Experiment procedure 30
2.5 Model calculations 31

3 Photooxidation of MBO **34**
3.1 Introduction 35
3.2 Methods 37
3.2.1 Atmospheric simulation chamber SAPHIR 37
3.2.2 Experimental procedure 37

3.2.3 Instrumentation . . . 38
3.2.4 Model calculations . . . 39
3.3 Results and discussion . . . 40
3.3.1 Model comparison . . . 40
3.3.2 Model comparison including hydrogen shift reactions . . . 41
3.3.3 OH and HO_2 radicals budget analysis . . . 41
3.3.4 Comparison with previous studies . . . 43
3.4 Summary and conclusions . . . 43
3.5 References . . . 44

4 Photooxidation of α-pinene 49
4.1 Introduction . . . 50
4.1.1 Degradation mechanism for α-pinene . . . 51
4.2 Methods . . . 53
4.2.1 Experiments in the simulation chamber SAPHIR . . . 53
4.2.2 Instrumentation . . . 53
4.2.3 Model calculations . . . 54
4.3 Results and discussion . . . 54
4.3.1 Product yields . . . 54
4.3.2 Comparison of trace-gas measurements with MCM 3.3.1 model calculations . . . 56
4.3.3 Sensitivity model calculations . . . 57
4.3.4 Comparison with previous studies . . . 59
4.4 Summary and conclusions . . . 60
4.5 References . . . 61

5 Photooxidation of pinonaldehyde 65
5.1 Introduction . . . 67
5.2 Methods . . . 69
5.2.1 Atmospheric simulation chamber SAPHIR . . . 69
5.2.2 Instrumentation . . . 69
5.2.3 Experimental procedure . . . 71
5.2.4 Model calculations . . . 71
5.3 Results . . . 72
5.4 Discussion . . . 74

5.4.1 Pinonaldehyde photolysis 74
5.4.2 Photooxidation by OH 76
5.5 Summary and conclusions 79
5.6 References 81

6 Summary and discussion of BVOC studies 85
6.1 Overview of experiments 85
6.2 Product yields 87
6.3 Comparison of trace-gas measurements with model calculations . . . 89
6.3.1 MBO 90
6.3.2 α-pinene 92
6.3.3 Pinonaldehyde 93
6.4 Comparison with field studies 96
6.5 Implication for atmospheric chemistry 100

II Spectroscopic and kinetic measurements of acetylperoxy radicals 102

7 Introduction 103

8 Methods 106
8.1 Radical detection by cavity ring-down spectroscopy 106
8.2 Experimental setup 108
8.3 Radical generation 109
8.4 Experiment procedure 110
8.4.1 Kinetic measurements 110
8.4.2 Measurement of spectrum and absorption cross sections . . . 111

9 Absorption spectrum and absolute absorption cross sections of acetylperoxy radicals 113
9.1 Introduction 114
9.2 Experimental 115
9.2.1 Experimental setup 115
9.2.2 Absorption spectra measurements 116
9.3 Results and discussion 116
9.4 Conclusion 118

9.5 References 119

10 Kinetic study of acetylperoxy radical reactions **120**
10.1 The $CH_3C(O)O_2$ self-reaction 120
10.2 Outlook 123

III Conclusions **125**

References **129**

Acronyms **150**

Acknowledgements **152**

A Appendix **154**
A.1 Supplementary materials to Chapter 3 154
A.2 Supplementary materials to Chapter 4 157
A.3 Supplementary materials to Chapter 5 166
A.4 Supplementary materials to Chapter 9 177

B Anhänge gemäß Prüfungsordnung **195**
B.1 Own contribution 196
B.2 Erklärung zur Dissertation 198

1 Introduction

The dry atmosphere consists mainly of nitrogen (78.09 %), oxygen (20.95 %), and argon (0.93 %). In addition, the air in the lower troposphere contains a variable amount of water vapor between 0 and 4 %. The chemical composition of trace compounds in the the atmosphere is controlled by emissions, chemical reactions, transport, and deposition processes. Large amounts of volatile organic compounds (VOCs), nitrogen oxides, carbon monoxide (CO), sulfur containing compounds (sulfur dioxide (SO_2) and dimethyl sulfide), and halocarbons are emitted into the atmosphere every year. Emissions sources can be either of biogenic (e.g. vegetation, oceans, and vulcano eruptions) or anthropogenic origin (e.g. use of fossil fuels, industry, agriculture, and lifestock). Earth has entered the era of the Anthropocene (Crutzen, 2002), where human influence significantly interferes with ecosystems. In this context, prominent examples are the anthropogenic climate change and air pollution.

In the atmospheric degradation of VOCs, air pollutants such as ozone (O_3) and secondary organic aerosols (SOA) are formed, which directly affect human health (Lelieveld et al., 2020) and the environment (IPCC, 2018). In the late 1940s, high air pollution was reported on hot and sunny days in the Los Angeles area. This kind of air pollution was driven by the photochemical degradation of emitted VOCs in the presence of nitrogen oxides. Similarly, high ozone levels have been reported in industrialized countries all over the world (Finlayson-Pitts and Pitts, 2000). In the following decades, legal restrictions targeting emissions of anthropogenic VOCs and nitrogen oxides reduced air pollution. However, air pollution by ozone and particulate matter is still an issue especially in densely populated areas (e.g. India and China; Borck and Schrauth, 2019), areas with high occurrence of wildfires (e.g. Burke et al., 2021), and regions with intensive agriculture or livestock (e.g. Smit and Heederik, 2017).

In addition to their effect on air quality, many pollutants also affect the radiative balance of the atmosphere, thus contributing to climate change. For ex-

ample, ozone is a greenhouse gas contributing to global warming while aerosols influence the reflectivity of the atmosphere, cloud formation and characteristics, thus having a net cooling effect (Rosenfeld et al., 2014; IPCC, 2018). To improve local air quality and simultaneously mitigate climate change, a profound understanding of the Earth's chemical system is needed. However, the formation of gaseous and particulate products from biogenic volatile compounds (BVOCs) remains a large uncertainty in today's understanding of the atmosphere. The degradation of most VOCs is initiated by reaction with atmospheric hydroxyl (OH) radicals and proceeds through radical chain reactions involving organic peroxy radicals (RO_2). In general, the oxidation of VOCs decreases the atmospheric OH concentrations, thereby extending the lifetime of other trace gases that are also removed by OH radicals in the troposphere. An important example is methane which is exclusively removed by reaction with OH and represents one of the most effective greenhouse gases (Hantson et al., 2017). In the last 15 years, it has been discovered that previously unknown unimolecular RO_2 reactions moderate this effect by regenerating OH (Lelieveld et al., 2008; Hofzumahaus et al., 2009; Peeters et al., 2009; da Silva et al., 2010; Crounse et al., 2011; Fuchs et al., 2013).

In addition to field studies and laboratory kinetic experiments, simulation chamber and laboratory experiments help to resolve the exact nature of chemical reactions taking place in the atmosphere. Reaction rate constants as well as product yields from specific reactions or reaction systems can be measured. Under controlled conditions, findings from simulation chamber experiments can be used to test atmospheric models and propositions from theoretical chemistry. Therefore, simulation chamber and laboratory experiments are essential tools for the construction of comprehensive chemical models.

The aim of this thesis is to reinvestigate the mechanisms of the chemical degradation of important BVOCs under atmospheric conditions with state-of-the-art measurement techniques. As a result, the impact on atmospheric concentrations of OH, ozone, and oxidation products is analyzed.

1.1 Biogenic VOCs in the troposphere

The troposphere is the lowest layer of the atmosphere from the Earth's surface up to the tropopause. Its height varies with latitude and season and is typically

8–15 km. Warm air parcels are lifted up and undergo adiabatic expansion, which leads to a temperature decrease. The temperature decreases with a lapse rate of, on average, 6.5 $K\,km^{-1}$ (Finlayson-Pitts and Pitts, 2000) until the temperature starts to increase again in the stratosphere. The stratospheric temperature increase is mainly caused by absorption of ultraviolet radiation by ozone molecules converting electromagnetic radiation into heat. This temperature inversion uncouples the troposphere from the superincumbent stratosphere and limits the transport of trace gases between these two parts of the atmosphere. The exchange time is in the range of 5 years, meaning that only long-lived trace gases can be transported into higher atmospheric layers (Finlayson-Pitts and Pitts, 2000). This is a long time compared to the inter-hemispherical mixing of tropospheric air, which is in the order of 1 year. Intra-hemisperical mixing occurs within a few months (Seinfeld and Pandis, 2016).

Volatile organic compounds (VOCs) describe all gas-phase organic species. In this work, the discussion of organic compounds is limited to non-methane VOCs (NMVOCs) and therefore the term VOCs always refers to NMVOCs. Global VOC emissions are caused by anthropogenic ($\sim 10\,\%$) and biogenic ($\sim 90\,\%$) sources (Seinfeld and Pandis, 2016). Approximately 1000 Tg of carbon from biogenic volatile organic compounds (BVOCs) is emitted every year into the atmosphere (Guenther et al., 2012). The majority of these compounds is isoprene (53 %) followed by monoterpene species (16 %). The main source of BVOC emissions is leafage of terrestial vegetation, especially trees. Minor sources are oceanic and soil emissions. The main isoprene emitters are deciduous trees, while monoterpene emissions dominantly originate from coniferous trees (Steiner and Goldstein, 2007).

Monoterpene emissions are important in various regions of the Earth. Figure 1.1 shows an overview of annual monoterpene emissions around the globe (Hantson et al., 2017). Estimates were based on Lund-Potsdam-Jena General Ecosystem Simulator (LPJ-GUESS) that is a dynamic global vegetation model. Strong emissions can be seen in remote areas that are typically woodland.

The structures of isoprene and other BVOCs that are important in the scope of this thesis are shown in Figure 1.2. These compounds belong to the class of terpenes. Isoprene and 2-methyl-3-butene-2-ol (MBO) are hemiterpenes, which are the simplest group within all terpenoids. α-Pinene and β-pinene are examples of endocyclic and exocyclic monoterpenes, respectively. The presence of the

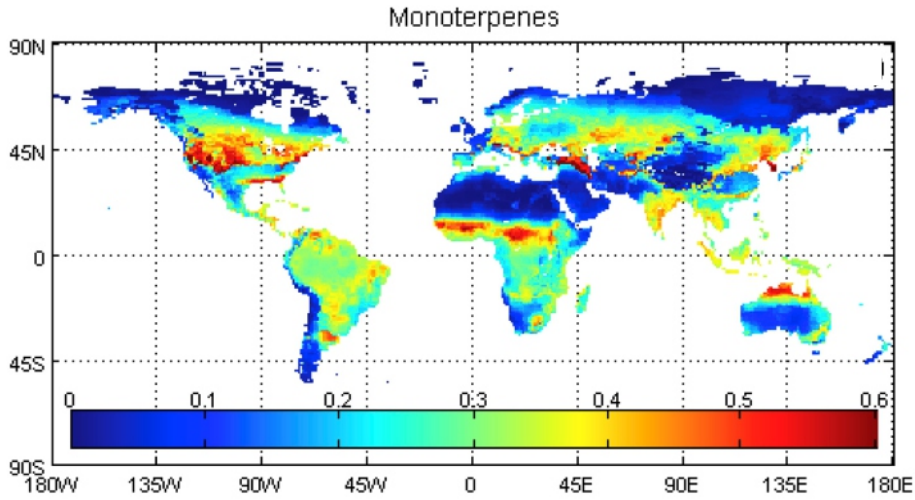

Figure 1.1: Simulated distribution of annual monoterpene emissions from 1971–2000 in gC yr^{-1} m^{-2}. Estimates are based on the dynamic global vegetation model LPJ-GUESS. Figure modified from Hantson et al. (2017) with permission from Elsevier.

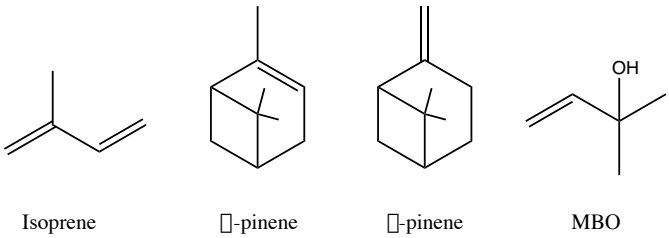

Figure 1.2: Chemical structures of isoprene, α-pinene, β-pinene, and 2-methyl-3-butene-2-ol (MBO).

C=C double bond enables rapid reactions with atmospheric oxidants like hydroxyl radicals, nitrate radicals (NO_3), and ozone. Annual BVOC emissions and average lifetimes in respect to the reaction with previously mentioned oxidants are shown in Table 1.1. The lifetime of most BVOCs is in the order of a few hours. Therefore, the chemical degradation takes place in the vicinity of emission sources. These emitted trace compounds significantly influence local chemical processes and air

Table 1.1: Global annual total emissions simulated for the year 2000 and calculated atmospheric lifetimes of most abundant BVOCs. Species that are investigated in this work are highlighted in bold.

BVOC	Emissions[a] / Tg year^{-1}	Lifetime[b] for reaction with		
		OH[c]	O_3[d]	NO_3[e]
Isoprene	535	1.4 h	1.3 days	1.6 h
α-pinene	66.1	2.6 h	4.6 h	11 min
trans-β-Ocimene	19.4	33 min	44 min	3 min
β-pinene	18.9	1.8 h	1.1 days	27 min
Limonene	11.4	49 min	2.0 h	5 min
Sabinene	9.0	1.2 h	4.8 h	7 min
Myrcene	8.7	39 min	50 min	6 min
3-carene	7.1	1.6 h	11 h	7 min
Camphene	4.0	2.6 h	18 days	1.7 h
MBO	2.2	2.4 h	1.7 days	7.7 days

[a] Values taken from Guenther et al. (2012)
[b] Values taken from Steiner and Goldstein (2007)
[c] Assumed OH radical concentration = 2.0×10^6 molecules cm^{-3}
[d] Assumed O_3 concentration = 7×10^{11} molecules cm^{-3}
[e] Assumed NO_3 radical concentration = 2.5×10^8 molecules cm^{-3}

quality.

During daytime, they are chemically transformed by ozonolysis reactions and the reaction with photochemically formed OH (Calogirou et al., 1999; Atkinson and Arey, 2003) producing RO_2. OH is partly regenerated in a radical reaction chain that involves reactions with NO, thereby producing NO_2. This radical reaction cycle impacts air quality because (1) the subsequent photolysis of NO_2 is the only chemical source for tropospheric O_3 and (2) oxygenated volatile organic compounds (OVOCs) are formed, which influence atmospheric OH concentrations and can be precursors for the formation of secondary organic aerosols (Glasius and Goldstein, 2016). For example, monoterpenes are the largest source of summertime organic aerosol in the southeastern United States (Zhang et al., 2018).

Removal of gaseous and particulate species in the atmosphere happens by dry and wet deposition. Dry deposition occurs at the Earth's surface and wet deposition describes processes that involve water (e.g. dissolution). Most trace gases

are emitted in a reduced or partially oxidized state and have a poor solubility in liquid water. Oxidation of these compounds improves their solubility and the substances can be washed out of the atmosphere by rain (Figure 1.3). For example, NO_2 has a low solubility and can be oxidized to HNO_3, which is very soluable in water and the principal source of nitrate in precipitation (Seinfeld and Pandis, 2016). In addition, oxidation reduces the volatility of products and thus leads to the formation of secondary organic aerosols, which are eventually removed from the atmosphere by deposition.

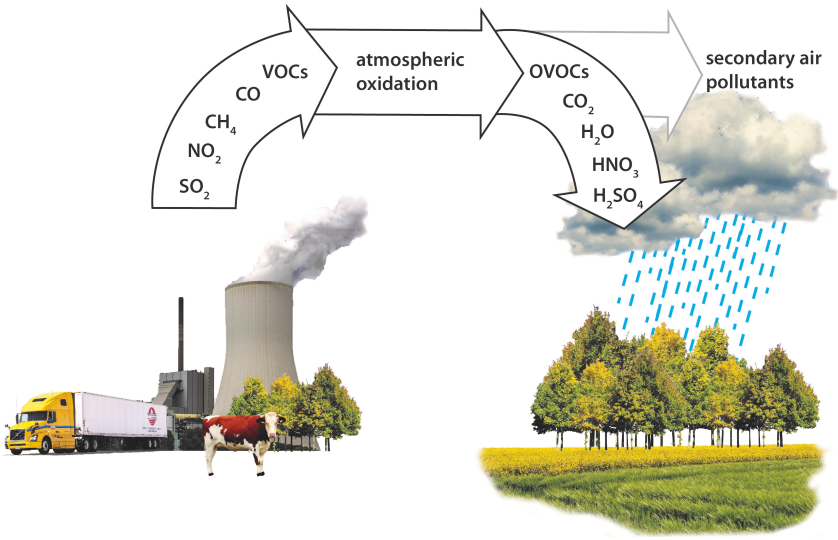

Figure 1.3: Atmospheric composition is controlled by emissions, atmospheric oxidation, and deposition processes. (Own figure, sources: pixabay)

1.2 Tropospheric radical chemistry

The following sections describe radical chemistry that is typical for conditions of the lower troposphere where highest VOC concentrations occur. Similar conditions are used for the experimental studies that are discussed in the later chapters. The theory listed here is based on Finlayson-Pitts and Pitts (2000) and Seinfeld and Pandis (2016).

1.2.1 Atmospheric OH radical sources

Hydroxyl radicals play a crucial role in tropospheric chemistry. They are the main oxidant during daytime and are often called the detergent of the atmosphere. OH reacts with most atmospheric trace gases, e.g. CO, H_2, CH_4, VOCs, oxygenated VOCs (aldehydes, ketones, and alcohols), SO_2, and nitrogen oxides. A selection of traces gases and the fraction of removal that is attributed to OH is shown in Table 1.2. Typically, the reaction with OH is the rate-determining step in the atmospheric degradation of trace gases. Therefore, OH concentrations directly control the atmospheric lifetime of these compounds.

Table 1.2: Trace gas emission rates and attributable removal by OH. Values are taken from Ehhalt (1999).

Trace gas	Global emission rates / Tg year^{-1}	removal by OH / %
CO	2800	85
CH_4	530	90
Isoprene	570	90
Terpenes[a]	140	90
NO_2	150	50
SO_2	300	30

[a] excluding isoprene

In the troposphere, OH radicals are mainly formed by the photolysis of ozone (O_3) by UV radiation with a wavelength below 340 nm (Moortgat and Ravishankara, 2015). In a first step, an electronically excited oxygen atom $O(^1D)$ is formed (R 1.1). Subsequently, the formed $O(^1D)$ molecule either reacts with water vapour to form two OH radicals (R 1.2) or is deactivated by collisions with a molecule M (R 1.3) that is typically molecular nitrogen or oxygen in the atmosphere.

$$O_3 + h\nu \longrightarrow O_2(^1\Delta) + O(^1D) \qquad (\lambda < 340\,\text{nm}) \qquad \text{(R 1.1)}$$

$$O(^1D) + H_2O \longrightarrow 2\,OH \qquad \text{(R 1.2)}$$

$$O(^1D) + M \longrightarrow O(^3P) + M \qquad \text{(R 1.3)}$$

Another OH source in polluted environments is the photolysis of nitrous acid

(HONO) by UV radiation ($\lambda \leq 390\,\text{nm}$).

$$\text{HONO} + h\nu \longrightarrow \text{OH} + \text{NO} \tag{R 1.4}$$

HONO is mainly formed by heterogenous processes at surfaces involving nitrogen oxides. This is especially relevant in urban environments at high NO_x concentrations. HONO photolysis is a main source of OH in urban areas in the morning (e.g. Alicke et al., 2003; Czader et al., 2012).

1.2.2 Chemical degradation of atmospheric trace gases

The chemical degradation of trace gases by OH is very efficient because OH radicals can be regenerated in a quasi-catalytical cycle. Therefore, one OH radical that is produced by ozone or HONO photolysis can oxidize several trace gas molecules before it is lost in radical termination reactions. A simple example is the oxidation of carbonmonoxide (CO) that proceeds through two reaction channels:

$$\text{OH} + \text{CO} + \text{M} \longrightarrow \text{CO}_2 + \text{H} + \text{M} \tag{R 1.5a}$$

$$\text{OH} + \text{CO} + \text{M} \longrightarrow \text{HOCO} + \text{M} \tag{R 1.5b}$$

In the first channel, CO is directly oxidized to CO_2. In the second channel, HOCO is formed and subsequently reacts with molecular oxygen to form CO_2 and a hydroperoxy radical (HO_2).

$$\text{HOCO} + \text{O}_2 \longrightarrow \text{CO}_2 + \text{HO}_2 \tag{R 1.6}$$

The hydrogen radical that is formed in Reaction R 1.5a is very reactive and quickly forms a HO_2 radical.

$$\text{H} + \text{O}_2 + \text{M} \longrightarrow \text{HO}_2 + \text{M} \tag{R 1.7}$$

As a net effect of Reactions R 1.5–R 1.7, the OH radical is converted to HO_2. In the polluted atmosphere where NO is present, OH is regenerated by Reaction R 1.8.

$$\text{HO}_2 + \text{NO} \longrightarrow \text{OH} + \text{NO}_2 \tag{R 1.8}$$

The formed nitrogen dioxide (NO_2) is photolysed at daytime forming O_3.

$$NO_2 + h\nu \longrightarrow NO + O(^3P) \quad \text{(R 1.9)}$$

$$O(^3P) + O_2 + M \longrightarrow O_3 + M \quad \text{(R 1.10)}$$

OH oxidation of saturated hydrocarbons proceeds by abstraction of a hydrogen atom and produces an alkyl radical (R) and H_2O. The VOC degradation in the presence of NO follows the scheme:

$$RH + OH \longrightarrow R + HO_2 \quad \text{(R 1.11)}$$

$$R + O_2 + M \longrightarrow RO_2 + M \quad \text{(R 1.12)}$$

$$RO_2 + NO \longrightarrow RO + NO_2 \quad \text{(R 1.13)}$$

$$RO + O_2 \longrightarrow R'CHO + HO_2 \quad \text{(R 1.14)}$$

The formed alkyl radical subsequently adds molecular oxygen to form an organic peroxy radical (RO_2). Then, RO_2 reacts with NO to form alkoxy radicals (RO). Subsequently, RO reacts with molecular oxygen to form HO_2 and carbonyl compounds, e.g. aldehydes, as first stable products. These partly oxidized compounds are called oxygenated volatile organic compounds (OVOCs). OVOCs themselves mainly react with OH but some compounds undergo photolysis. For example, the simplest aldehyde, formaldehyde, can photolyze and subsequently form HO_2 according to Reaction R 1.7.

$$HCHO + h\nu \longrightarrow H + CHO \quad \text{(R 1.15)}$$

$$HCHO + h\nu \longrightarrow H_2 + CO \quad \text{(R 1.16)}$$

Analogous to the oxidation of CO, NO_2 is produced in Reaction R 1.13 and subsequently photolyzed (R 1.9), thereby contributing to the formation of ozone.

The conversion from OH to HO_2 and vice versa is fast (< 1 s) in the presence of NO (> 4 ppbv), and steady state conditions apply. Therefore, both radicals are summarized as HO_x (= OH + HO_2) radical family. A schematic of the atmospheric radical cycle is shown in Figure 1.4.

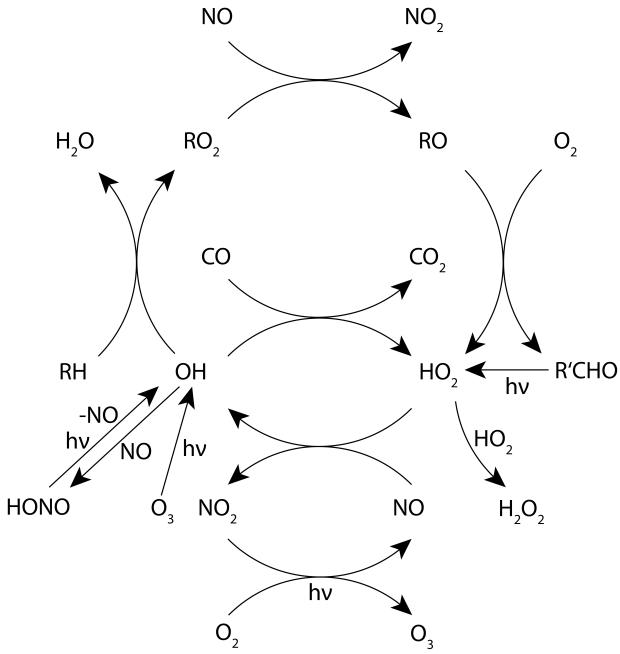

Figure 1.4: Simplified schematic of the daytime radical chemistry in the lower troposphere. See text for details.

1.2.3 Radical termination reactions

Radical-radical reactions terminate the reaction chain of HO_x. In a pristine environment, in the absence of NO emissions, the Reactions R 1.17 and R 1.18 play a role.

$$OH + HO_2 \longrightarrow H_2O + O_2 \quad \text{(R 1.17)}$$

$$HO_2 + HO_2 \longrightarrow H_2O_2 + O_2 \quad \text{(R 1.18)}$$

In polluted air, mainly reactions forming nitric acid (HNO_3) and peroxynitric acid (HO_2NO_2) take place.

$$OH + NO_2 + M \longrightarrow HNO_3 + M \quad \text{(R 1.19)}$$

$$HO_2 + NO_2 + M \rightleftharpoons HO_2NO_2 + M \quad \text{(R 1.20)}$$

HO_2NO_2 is thermally unstable and at temperatures of the lower troposphere, decomposes within 20 seconds. Thus, competing HO_2NO_2 losses by reaction with OH, photolysis or deposition are not significant. Reaction R 1.19 is the dominant loss of HO_x radicals in the polluted atmosphere. In addition, it is a main loss pathway for NO_x. Due to the wet deposition, HNO_3 contributes to acidic rain.

Organic peroxy radicals can undergo chain terminating reactions that form stable products, for example in the self- or cross-reaction of RO_2.

$$RO_2 + RO_2 \longrightarrow RO + RO + O_2 \quad \text{(R 1.21a)}$$
$$\longrightarrow R'CHO + ROH + O_2 \quad \text{(R 1.21b)}$$
$$\longrightarrow ROOR + O_2 \quad \text{(R 1.21c)}$$

The RO_2 self- and cross-reactions can form two alkoxy radicals (R 1.21a), thus propagating the radical reaction chain. In contrast, Reaction R 1.21b terminates the radical reaction chain forming alcohols in combination with carbonyl compounds. The formation of dialkyl epoxides (R 1.21c) is negligible (Seinfeld and Pandis, 2016).

Similarly, stable hydroperoxides (ROOH) are formed in the reaction of RO_2 with HO_2.

$$RO_2 + HO_2 \longrightarrow ROOH + O_2 \quad \text{(R 1.22a)}$$

Hydroperoxides can be removed by wet and dry deposition, be photolysed and regenerate OH or react with OH itself. Depending on the RO_2 structure, other reaction pathways can also be of importance in the reaction with HO_2:

$$RO_2 + HO_2 \longrightarrow ROH + O_3 \quad \text{(R 1.22b)}$$
$$\longrightarrow RO + OH + O_2 \quad \text{(R 1.22c)}$$

Reaction channels R 1.22a and R 1.22b are chain terminating reactions that lead to the formation of stable oxidation products. In contrast, reaction channel R 1.22c propagates the radical reaction chain and regenerates new RO and OH radicals.

In a polluted environment with high NO_x conditions, RO_2 can form thermally instable peroxy nitrates ($ROONO_2$) that can act as a reservoir species for NO_x and

RO_2.

$$RO_2 + NO_2 + M \rightleftharpoons ROONO_2 + M \quad \text{(R 1.23)}$$

An important example is the peroxyacetyl nitrate (PAN) that is formed from the acetylperoxy radical ($CH_3C(O)O_2$). It is a toxic secondary air pollutant. Its lifetime at 298 K is around 3 h. However, at low temperatures, it has a relative long lifetime (57 h at 273 K) and can be transported over long distances in the lower troposphere. It can reactivate NO and RO_2 when the air warms up again (Finlayson-Pitts and Pitts, 2000).

In addition to forming an alkoxy radical (R 1.13), the reaction of RO_2 with NO can result in radical loss, if stable alkyl nitrates ($RONO_2$) are formed:

$$RO_2 + NO + M \longrightarrow RONO_2 + M \quad \text{(R 1.24)}$$

$RONO_2$ hydrolyzes to form nitric acid, thus contributing to an increase in aerosol mass. Furthermore, formation of $RONO_2$ can be an important NO_x sink at sufficiently high VOC levels (Browne et al., 2013; Romer Present et al., 2020).

Organic nitrate yields strongly depend on the chemical structure of RO_2. Typical yields in the photooxidation of simple linear alkanes are increasing with the length of the carbon chain from 1 % in ethane to 23 % in n-octane (Atkinson, 1997; Arey et al., 2001). Organic nitrate yields in the oxidation of isoprene, a major emitted BVOC, have been reported in the range of 4-15 % (Fisher et al., 2016, and references therein). Other terpene species show even higher yields, for example α-pinene has a nitrate yield of 18-25 % (Noziere et al., 1999; Rindelaub et al., 2015).

1.2.4 Novel RO_2 chemistry

Emitted BVOCs are unsaturated hydrocarbons that have one or multiple C=C bonds. In the atmosphere, BVOCs are oxidized by OH, NO_3, and O_3. The daytime oxidation by OH is initialized by a) addition of OH to the double bond (see Figure 1.5) or b) H-abstraction from the hydrogen-carbon bond by OH. The prevalent fate for most BVOCs is the OH addition forming β-hydroxy substituted alkyl radicals. However, for aldehydes containing a C=O bond, the H-abstraction is important (Atkinson and Arey, 2003). Hydroxy alkyl radicals subsequently add

molecular oxygen (see Reaction R 1.12) to form hydroxy substituted peroxy radicals.

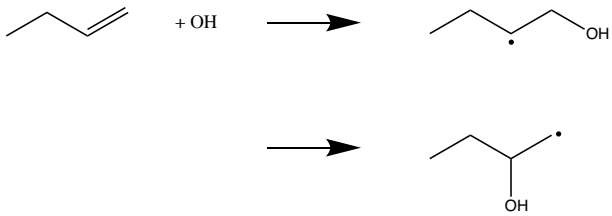

Figure 1.5: Example for an OH addition to the double bond of 1-butene.

Addition of O_3 to the carbon-carbon double bond forms a primary ozonoide, which rapidly decomposes via two pathways to a carbonyl compound and a Criegee intermediate (CI) each. The general mechanism is shown in Figure 1.6. CI are zwitterionic with a low contribution of biradicalic character (Vereecken et al., 2014). Due to the exothermic reaction, CI have a large excess energy and are instable. In the atmosphere, the fate of CI is stabilization by collisions and removal by bimolecular or unimolecular reactions (Taatjes et al., 2014).

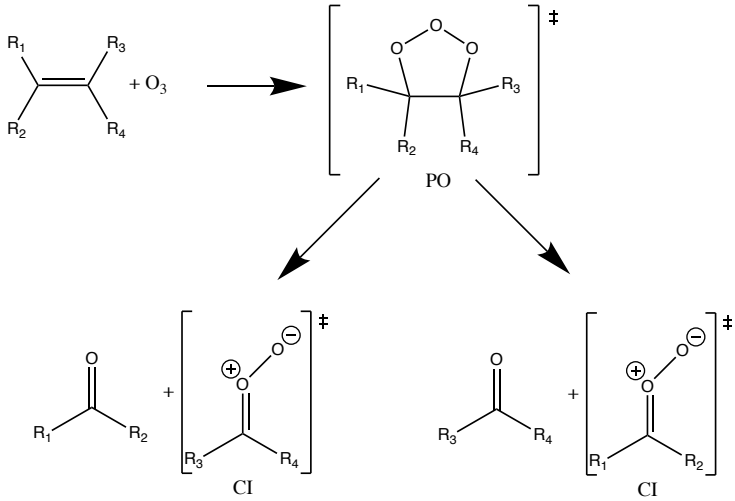

Figure 1.6: General ozonolysis mechanism: after the O_3 addition, a primary ozonoide (PO) is formed which subsequently decomposes to stable carbonyl compound and Criegee intermediate (CI; Seinfeld and Pandis, 2016).

Field studies conducted in forested environments, which were characterized by large BVOC emissions and low NO concentrations, showed large underestimation of OH radical concentrations by state-of-the-art chemical models (e.g., Lelieveld et al., 2008; Hofzumahaus et al., 2009; Whalley et al., 2011). Under these atmospheric conditions, it is expected that radical regeneration by the reaction sequence R 1.13, R 1.14, and R 1.8 (NO-type recycling; Figure 1.7) is suppressed due to the dominance of radical termination reactions such as the reaction of RO_2 with HO_2. A conceptual dependence of OH on NO_2 is shown in Figure 1.7. OH concentrations are normalized to the maximum achievable in model calculations with variable nitrogen oxide concentrations. The figure shows normalized NO_2 concentrations on the x-axis. At daytime, NO and NO_2 concentrations are in a photochemical equilibrium that consists of Reactions R 1.9, R 1.10, and the back reaction of NO with O_3 that forms NO_2.

The trend of modeled OH (blue line, Figure 1.7) can be explained in dependence

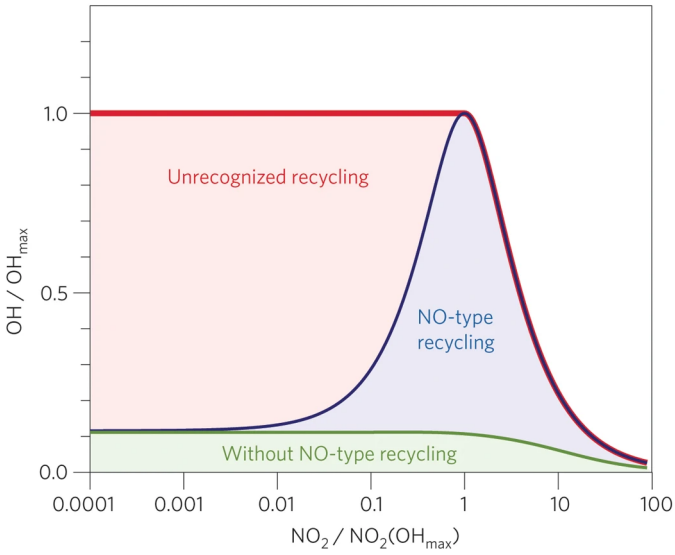

Figure 1.7: Conceptual dependence of OH on NO_2. NO_2 and OH concentrations are normalized as explained in Rohrer et al. (2014). The blue curved depicts the OH concentration that is described by existing chemical models. The red curve shows measured OH concentrations. Figure by Rohrer et al. (2014). Reprinted by permission from Springer Nature.

of NO_x concentrations. When moving from a pristine environment towards an environment with typical anthropogene activity, NO concentrations are increased, thus enhancing the NO-type regeneration. Then, OH concentrations can be explained from the radical reaction chain, regenerating OH via peroxy radical reactions with NO. This OH regeneration type is associated with the formation of O_3. When NO_x concentrations further increase, normalized OH concentrations are reduced by reaction with NO_2 (R 1.19). In the range of maximum NO-type regeneration and high NO_x concentrations, modeled and observed OH concentrations agree. At $NO_2/NO_2(OH_{max}) < 1$, models predict a decrease of OH concentrations with decreasing NO_x. For pristine environments that are characterized by low NO_x concentrations, additional OH regeneration reactions were postulated as a general explanation for the relative high OH concentrations measured in the presence of high BVOC concentrations (Rohrer et al., 2014, and references therein). As one possible explanation for atmospheric air with large isoprene concentrations, experimental and theoretical studies have indeed discovered new chemical pathways for OH regeneration that involve unimolecular reactions of isoprene peroxy radicals. It was recognized that this class of RO_2 reactions can be generally important for the regeneration of OH and HO_2 in an atmosphere with little NO.

Unimolecular reactions like isomerisation and decomposition can be relevant when their reaction rates are fast enough to compete with the RO_2 + NO reaction. This chemistry has been known in the field of combustion since the 1980s as autoxidation (e.g., Cox and Cole, 1985; Jorand et al., 1996) but its relevance for atmospheric chemistry has only recently been recognized (e.g., Peeters et al., 2009; da Silva, 2010; Praske et al., 2018; Bianchi et al., 2019). A simple autoxidation example is shown in Figure 1.8. Characteristic for autoxidation are intramolecular H-shift reactions in the RO_2 molecules. These sigmatropic rearrangements lead to the formation of hydroperoxyalkyl radicals (QOOH). In the next step, QOOH can add an additional O_2 molecule to form a new RO_2 (O_2QOOH) that subsequently reacts with NO, HO_2, and RO_2, or undergoes another internal H-abstraction. The presence of an -OOH group can enhance reaction rates of H-migration by H-bonding and inductive effects (Vereecken and Nozière, 2020). In sufficiently large molecules, multiple H-shift reactions can be chained and numerous O_2 units are added to a molecules. This leads to the formation of multifunctional, highly oxygenated organic molecules (HOMs) (Kalafut-Pettibone et al.,

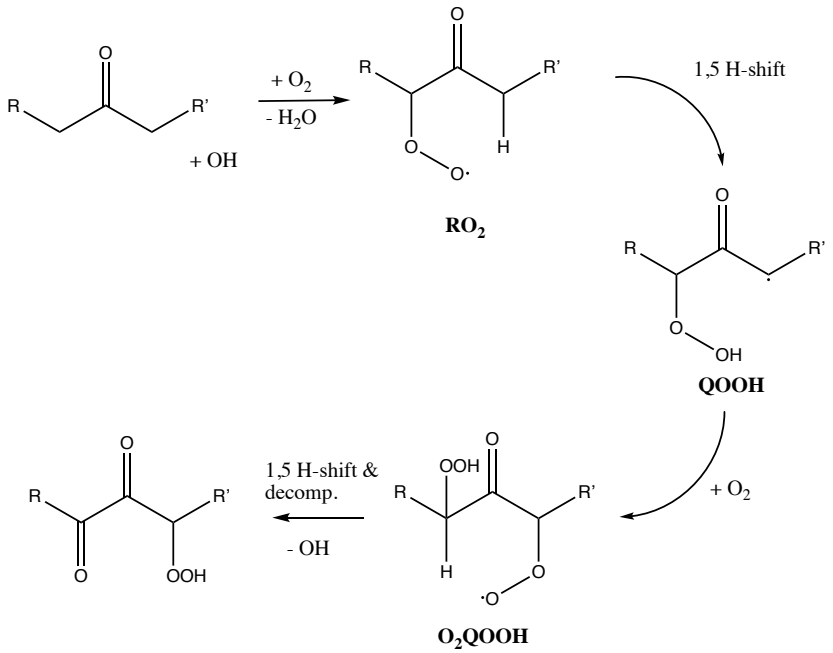

Figure 1.8: Simplified autoxidation scheme (Crounse et al., 2013).

2013; Ehn et al., 2014; Bianchi et al., 2019). HOMs are low-volatile precursors that are important in the formation of SOA.

HO_x formation by isomerization and decomposition of RO_2 has been reported in the oxidation of isoprene (Peeters et al., 2009, 2014; Crounse et al., 2011; Fuchs et al., 2013; Møller et al., 2019; Novelli et al., 2020) and methacrolein (Crounse et al., 2012; Fuchs et al., 2014). Based on the Leuven Isoprene Mechanisms (LIM; Peeters et al., 2009, 2014), currently available atmospheric models were extended by an extensive isoprene chemistry including unimolecular reactions. However, H-migration reactions of RO_2 species with a different origin than isoprene are not well represented in current atmospheric models.

In addition to radical regeneration by unimolecular reactions, laboratory studies reported OH radical regeneration in the bimolecular reaction of acylperoxy radicals with HO_2, which was previously considered to be a radical termination reaction only (e.g. Hasson et al., 2004; Dillon and Crowley, 2008). Reaction rate coefficients at 298 K of simple alkylperoxy species with HO_2 increase with the

number of carbon atoms (Boyd et al., 2003). Usually the HO_2 + RO_2 reaction terminates the radical reaction chain and forms a stable hydroperoxide compound (see reaction R 1.22a). However, for acylperoxy radicals a general scheme of the reaction with HO_2 can be written as:

$$RC(O)O_2 + HO_2 \longrightarrow RC(O)OOH + O_2 \quad \text{(R 1.25a)}$$
$$\longrightarrow RC(O)OH + O_3 \quad \text{(R 1.25b)}$$
$$\longrightarrow RC(O)O + OH + O_2 \quad \text{(R 1.25c)}$$

The OH yield of Reaction R 1.25c depends on the chemical structue of the acylperoxy radical. Reported OH yields for acylperoxy radicals with R = CH_3, C_2H_5, and C_3H_7 are in the range of 0.4 to 0.5 (Hasson et al., 2004, 2012).

In a theoretical study, Archibald et al. (2009) proposed a reaction pathway for RO_2 with OH that could play a role at low NO conditions. In 2014, the reaction rate constant for a peroxy radical reaction with OH was measured for the first time by Bossolasco et al. (2014). The reaction of RO_2 with OH proceeds through four reaction channels, which are shown here for the simplest peroxy radical, methylperoxy (CH_3O_2):

$$CH_3O_2 + OH \longrightarrow CH_2O_2 + H_2O \quad \text{(R 1.26a)}$$
$$\longrightarrow CH_3O + HO_2 \quad \text{(R 1.26b)}$$
$$\longrightarrow CH_3OH + O_2 \quad \text{(R 1.26c)}$$
$$\longrightarrow CH_3OOOH \quad \text{(R 1.26d)}$$

Here, reaction pathways R 1.26a, R 1.26c, and R 1.26d terminate the radical reaction chain. However, Reaction R 1.26b regenerates an alkoxy radical and HO_2, thus propagating the radical reaction chain. The reaction rate constant and the HO_2 yield depends on the RO_2 structure. An overview for C_1 to C_4 RO_2 is given in Table 1.3. The HO_2 yield decreases with increasing number of carbon atoms. Reactions of larger RO_2 with OH have not been studied yet. However, Fittschen (2019) proposed that the dominant atmospheric fate of RO_2 radicals that contain more than 3 carbon atoms is the formation of a trioxide (ROOOH) following Reaction R 1.26d.

Table 1.3: Summary of reaction rate constants and HO_2 yields for the reaction of different RO_2 with OH.

Reaction	k / $\times 10^{-10}$ cm^3 s^{-1}	HO_2 yield / %	Reference
CH_3O_2 + OH	(1.0 ± 0.3)	90 ± 10	Fittschen (2019)
$CH_2H_5O_2$ + OH	(1.2 ± 0.3)	75 ± 15	Faragó et al. (2015)
$CH_3H_7O_2$ + OH	(1.4 ± 0.3)	41 ± 8	Assaf et al. (2018)
$CH_4H_9O_2$ + OH	(1.5 ± 0.3)	15 ± 3	Assaf et al. (2018)

1.3 Objectives of this thesis

Similar to isoprene-rich environments, measured OH and HO_2 concentrations were found to be underestimated by atmospheric chemical models in forest environments where chemical loss of OH is dominated by reactions with MBO and monoterpenes. For example, the Bio-hydro-atmosphere interactions of Energy, Aerosols, Carbon, H_2O, Organics and Nitrogen – Rocky Mountain Organic Carbon Study (BEACHON-ROCS, Ortega et al., 2014) was conducted in 2010 in the Manitou Experimental Forest (Colorado, USA). The forest consists mainly of ponderosa pine, Douglas fir, mixed conifer, and aspen. BVOC emissions were dominated by MBO (daily average $\sim$ 1600 pptv) followed by monoterpenes (daily average $\sim$ 500 pptv) (Kim et al., 2013; Wolfe et al., 2014). Here, model calculations were performed using the University of Washington Chemical Model (UWCM), which is based on the widely used Master Chemical Mechanism (MCM). From all available atmospheric chemical mechanism, the MCM is the most extensive one (see Section 2.5 for more details). Model results underestimated HO_2 radical concentrations by up to a factor of 3, and OH concentrations could only be reproduced by the model, if HO_2 was constrained to measurements. When HO_2 concentrations are underestimated, OH regeneration via reaction R 1.8 is also underestimated and atmospheric OH concentrations are predicted too low. Kim et al. (2013) suggested an unidentified HO_2 source that may be due to photolysis of OVOCs or reactions of RO_2.

Another example is the Hyytiälä United Measurements of Photochemistry and Particles in Air – Comprehensive Organic Precursor Emission and Concentration study (HUMPPA-COPEC) field campaign that took place in a boreal forest in Finland in 2010. The forest consists mainly of Pinus sylvestris L., and measured α-pinene mixing ratios peaked around 1 ppbv. The study showed similar results

as reported by Kim et al. (2013) for the site in the Rocky Mountains. Model calculations underestimated HO_2 concentrations by up to 70 % compared to observations. Analysis of the HO_x production and loss terms indicates that at high VOC concentrations 70 % of the OH production is not explained by model results. Hens et al. (2014) attributed this to a missing HO_2 source. A second model run (MIM3) using an extended mechanism that includes new additions that are based on radical regeneration mechanisms found for isoprene (Taraborrelli et al., 2012) improved the model-measurement agreement. However, for most of the modeled data, HO_2 concentrations were 40 % lower than observations.

The OH regeneration in the photooxidation of isoprene is well known based on numerous experimental and theoretical studies. In contrast to isoprene, radical regeneration in the chemistry of other abundant hydrocarbons and monoterpenes is less well investigated. Theoretical studies investigated the possible role of unimolecular reactions in the degradation of BVOCs (Fantechi et al., 2002; Vereecken et al., 2007; Knap et al., 2016; Iyer et al., 2018). However, there is a general lack of experimental data under low NO conditions for validation of theoretical calculations. In contrast to previous laboratory studies, experiments in the atmospheric simulation chamber SAPHIR (Simulation of Atmospheric PHotochemistry In a large Reaction chamber) in Jülich allow the use of atmospheric reactant concentrations under natural sunlight and a direct measurement of HO_x. The large (270 m^3) chamber has been used to investigate, for example, the photochemical degradation of isoprene (Fuchs et al., 2013), aromatics (Nehr et al., 2014), and β-pinene (Kaminski et al., 2017). In this thesis, studies on monoterpenes that have been started by Kaminski (2014) are continued. This thesis analyzes the photooxidation of three selected BVOCs that could have played an important role in the reported field campaigns: a) 2-methyl-3-butene-2-ol (MBO), which is typically emitted by lodgepole and ponderosa pines mainly in Northern America; b) α-pinene, which is emitted by many conifers, especially pines; c) pinonaldehyde, which is a first generation product from the α-pinene degradation. The following questions are addressed in this work:

- Can state-of-the-art atmospheric models correctly predict OH and HO_2 concentrations and the formation of primary oxidation products in the photooxidation of MBO, α-pinene, and pinonaldehyde?
- Which role has the novel RO_2 chemistry in the photooxidation of the studied

VOCs?

- How can existing theoretical studies and newly determined experimental data improve mechanisms?

The experiments were conducted in SAPHIR under conditions that are typical for forested environments. Measured radical and VOC concentration time series are compared to zero dimensional boxmodel calculations which use the recent version of the Master Chemical Mechanism (MCM 3.3.1) as a state-of-the-art chemical mechanism. Product yields are determined for each experiment and compared to literature data. In addition, the impact of model modifications based on theoretical studies from literature is tested. The main focus of this thesis is to find explanations for radical regeneration in the degradation schemes of the three investigated VOCs.

Acylperoxy radicals are formed from biogenic precursors and could contribute to explain discrepancies between modeled and measured radical concentrations in field experiments due to radical regeneration in the reaction with HO_2. Significant OH yields of up to 0.6 have been reported in the reaction of acetylperoxy radicals ($CH_3C(O)O_2$) with HO_2 (Groß et al., 2014). The detection of $CH_3C(O)O_2$ in previous kinetic laboratory studies was mainly done in the UV region. In this region, the absorption spectra of different peroxy radicals overlap, which could lead to systematic errors if not properly accounted for.

In the second part of this thesis, the near infrared spectrum and absolute cross sections of $CH_3C(O)O_2$ are measured. This will help to achieve more accurate measurements of their concentration in laboratory experiments to better quantify the fraction of radicals that are regenerated. The newly determined absorption cross sections are used to convert measured $CH_3C(O)O_2$ absorbance into absolute concentrations. Measured $CH_3C(O)O_2$ concentration time profiles allow to reinvestigate second-order kinetics of the $CH_3C(O)O_2$ self-reaction to validate the measured absorption cross section. In the future, this can be used to reinvestigate second-order kinetics of the reaction system $CH_3C(O)O_2$ with HO_2.

The content of this thesis is divided into three parts. The first part deals with the studies on the photooxidation of MBO, α-pinene, and pinonaldehyde in the SAPHIR chamber, which are included as three peer-reviewed articles. The second part includes one publication about the measured spectroscopic infrared data of acetylperoxy radicals and non-published results of kinetic experiments with

these radicals. The third part concludes this thesis and gives an outlook to future work.

Part I

- Novelli et al. (2018): Photooxidation of MBO (Chapter 3)
- Rolletter et al. (2019): Photooxidation of α-pinene (Chapter 4)
- Rolletter et al. (2020b): Photooxidation of pinonaldehyde (Chapter 5)

Part II

- Rolletter et al. (2020a): Absorption spectrum and absorption cross sections of acetylperoxy radicals (Chapter 9)
- Kinetic study of acetylperoxy radicals (Chapter 10)

Part III

- Conclusions

The experiments in the atmosphere simulation chamber SAPHIR have required a team of people who operated the chamber and the analytical instruments that are connected to the chamber. This thesis uses the measurement data provided by the SAPHIR team for analysis, modeling, and interpretation of the VOC photooxidation experiments. Similarly, the experiments conducted at the Université Lille were supported by the group of Dr. C. Fittschen, who provided the experimental facilities to conduct the spectroscopic and kinetic measurements presented in this work. An overview of individual contributions to published articles can be found in Appendix B.1 or directly in the author contribution section of each article.

Part I

Investigation of BVOC photooxidation in SAPHIR

2 Methods

The studies on the photooxidation of MBO, α-pinene, and pinonaldehyde were performed in the Simulation of Atmospheric PHotochemistry In a large Reaction chamber located at the Forschungszentrum Jülich. A general description of the simulation chamber, instrumentation, and experiment procedure is given in the following chapter. Specific details for reported experiments can be found in the publications listed in Chapters 3–5.

2.1 Description of the experiments in SAPHIR

The SAPHIR chamber is a facility built to study reactions of the troposphere under controlled, realistic conditions and is located at Forschungszentrum Jülich. As the chamber itself has been described elsewhere (Rohrer et al., 2005; Poppe et al., 2007; Schlosser et al., 2007), only a short overview is given here. A picture of the chamber can be seen in Fig. 2.1. The chamber has a double wall and is made out of an inert Fluorinated Ethylene Propylene (FEP) foil (DuPont). It is of cylindrical shape (length: 18 m, diameter: 8 m) and has a volume of 270 m^3. It has a volume to surface ratio of 1.08 m^{-1}. The higher the ratio is, the smaller is the probability of collisions of molecules with the chamber wall compared to gas-phase collisions. Collisions with the wall potentially result in heterogeneous reactions that complicate the interpretation of observations with respect to gas-phase reactions, which are subject of the work. The large volume allows simultaneous sampling by numerous measuring instruments. Sampled air is replaced by a flow of synthetic air that leads to a dilution of trace gases by approximately 4 % per hour. Experiments are usually performed at reactant concentrations that are similar to natural concentrations in the atmosphere. This avoids that impurities could interfere with measurements. Therefore, the synthetic air used for experiments is mixed from evaporated ultra-pure liquid nitrogen and oxygen (Linde,

Figure 2.1: Picture of the SAPHIR chamber. Copyright "Forschungszentrum Jülich / Sascha Kreklau"

purity $\geq$ 99.99990 %). The volume between the inner and outer wall is constantly flushed with pure synthetic air. This measure and a slight overpressure ($\sim$ 35 hPa) avoid diffusion of atmospheric trace gases through the chamber walls into the inner chamber. The chamber foil has a transmittance of $\sim$ 85 % for solar radiation (Bohn and Zilken, 2005). Therefore, natural sunlight can be used as light source, initiating the photooxidation of trace gases. The chamber is equipped with a shutter system that allows to operate the chamber under light and dark conditions. At both ends of the chamber, fans ensure a rapid mixing of air. Measurement devices are typically mounted outside of the chamber to avoid additional surfaces inside the chamber. Sampling is done with short inlet lines to avoid a change in the chemical composition of the sampled air while is is transported to the instruments.

2.2 Instrumentation at the SAPHIR chamber

The chemical experiments were performed in the concentration range of atmospheric trace gases. Therefore, highly sensitive analytical techniques were needed for the measurement of chemical compounds (Table 2.1).

2.2.1 Radical detection

Two different optical instruments were used for radical measurements in SAPHIR. Differential optical absorption spectroscopy (DOAS) was used to measure OH, and laser-induced fluorescence (LIF) was used to measure both OH and HO_2.

DOAS (Dorn et al., 1995; Hausmann et al., 1997) is a direct OH detection method that measures the absorption of UV light by OH radicals at 308 nm. The OH concentration is calculated from the measured optical density after the Beer-Lambert law using differential absorption cross sections. Broad- and narrow-band spectral structures are separated in an absorption spectrum in order to isolate narrow trace gas absorption structures (Platt and Stutz, 2008). "Slow" changes, such as caused by Rayleigh and Mie scattering, are separated from "rapid" variations, for example caused by absorption features of a molecule. By removing the broadband structures with a mathematical fit procedure, a differential spectrum is derived. Measured differential spectra are fitted with reference spectra to derive concentrations. In the experiments discussed here, reference spectra of OH, HCHO, and an unidentified absorber X are used. This is an absolute measurement that does not need calibration.

The second instrument, the LIF instrument (Holland et al., 1995; Fuchs et al., 2011), uses the fluorescence assay by gas expansion (FAGE) technique developed by Hard et al. (1984). Ambient air is sampled through a pinhole nozzle with 0.3–0.4 mm diameter into a measurement cell at reduced pressure (4.0 hPa). A pulsed detection laser (8.5 kHz) with a wavelength of 308 nm passes through the measurement cell via baffle arms and overlaps perpendicularly with the gas beam. OH radicals are excited by the laser at the $Q_1(3)$ absorption line, and subsequently the emitted fluorescence is measured by a photomultiplier tube (PMT). The reduced pressure in the measurement cell allowed minimizing collision quenching and extending the lifetime of the excited state, so that the discrimination between the laser pulse and OH fluorescence was possible. To convert the measured flu-

Table 2.1: Instrumentation for radical and trace gas measurements.

Species	Technique	Time resolution	1σ precision	1σ accuracy	Instrument
OH	DOAS[a]	205 s	0.6×10^6 cm^{-3}	6.5 %	Jülich DOAS
OH	LIF[b]	47 s	0.6×10^6 cm^{-3}	13 %	Jülich LIF
HO_2	LIF[b]	47 s	1.5×10^7 cm^{-3}	16 %	Jülich LIF
k_{OH}	Laser photolysis + LIF[b]	180 s	0.3 s^{-1}	0.5 s^{-1}	Jülich LIF
NO	Chemiluminescence	180 s	4 pptv	5 %	Eco Physics TR 780
NO_2	Chemiluminescence	180 s	2 pptv	5 %	Eco Physics TR 780
O_3	UV-absorption	10 s	1 pptv	5 %	Eco Physics TR 780
VOCs	PTR–TOF–MS[c]	40 s	15 pptv	14 %	Ionicon Analytik
VOCs	GC–FID[d]	30 min	(4-8) %	5 %	Agilent 7890N
HONO	LOPAP[e]	300 s	1.3 pptv	10 %	QUMA Elektronik & Analytik
HCHO	DOAS[a]	100 s	20 %	10 %	Jülich DOAS
HCHO	Hantzsch monitor[a]	120 s	20 pptv	5 %	AERO Laser AL4001
photolysis freq.	spectroradiometer	60 s	10 %	10 %	Bentham 300

[a] DOAS = Differential Optical Absorption Spectroscopy
[b] LIF = Laser-Induced Fluorescence
[c] PTR–TOF–MS = Proton Transfer Reaction Time-Of-Flight Mass Spectrometer
[d] GC–FID = Gas Chromatography – Flame Ionisation Detector
[e] LOPAP = Long-Path-Absorption-Photometer

orescence intensity into concentrations, the instrument is calibrated by a radical source that generates OH radicals by water photolysis at 185 nm with a mercury vapour lamp.

Previous studies reported possible interferences in the OH detection by LIF for some instruments (Mao et al., 2012; Novelli et al., 2014) that depend on chemical composition and on the geometry of the different instruments. A study with the instrument used in our experiments (Fuchs et al., 2016) showed no significant interference at atmospherically relevant conditions. Interferences could only be observed for exceptionally high, non-atmospheric reactant concentrations of ozone (300–900 ppbv) and some alkenes (1–450 ppbv). Therefore, no interferences are expected for conditions used in the experiments reported in this work. This was confirmed by the good agreement of both OH measurement techniques within 15 % and is consistent with previous measurement campaigns (Schlosser et al., 2007, 2009; Fuchs et al., 2012).

The LIF instrument also measures HO_2 concentrations in a second measurement cell. For this purpose, HO_2 is chemically converted to OH by adding NO directly after the inlet nozzle (see reaction R 1.8). The measured fluorescence is the sum of OH and HO_2 radicals. The HO_2 concentration is derived by subtracting the measured OH concentration. Fuchs et al. (2011) reported a possible interference from RO_2 radicals that can react with NO and rapidly form additional HO_2. In the experiments here, NO concentrations were low enough that the RO_2 conversion to HO_2 is suppressed and interferences can be assumed to be negligible.

2.2.2 OH reactivity

OH radicals have a large reactivity towards various atmospheric trace compounds. The total OH reactivity k_{OH} is defined as the pseudo first-order rate constant and is equivalent to the inverse of the OH lifetime τ_{OH}:

$$k_{\mathrm{OH}} = \tau_{\mathrm{OH}}^{-1} = \sum_i k_{\mathrm{OH+X}_i}[\mathrm{X}_i] \tag{2.1}$$

where $[\mathrm{X}_i]$ is the concentration of species X_i and $k_{\mathrm{OH+X}_i}$ the corresponding second-order rate constant.

The OH reactivity is measured by a laser photolysis – laser-induced fluorescence (LP–LIF) instrument (Lou et al., 2010; Fuchs et al., 2017). An initial homo-

geneously distributed OH radical concentration is produced by ozone photolysis in a flow tube. Radiation is provided by a pulsed low repetition laser (1 Hz) at 266 nm. After the photolysis shot, produced OH radicals subsequently react with sampled reaction partners. The reaction volume is continuously probed and the temporal change in OH concentration is measured with a high time resolution of 1 ms in a LIF measurement cell. The change of concentration over time is described as:

$$-\frac{\mathrm{d}[\mathrm{OH}]}{\mathrm{d}t} = \sum_i k_{\mathrm{OH+X}_i}[\mathrm{OH}]_\mathrm{t} \tag{2.2}$$

The reaction partners X_i are present in an excess compared to OH ($[\mathrm{X}_i] \gg [\mathrm{OH}]$). In consequence, $[\mathrm{X}_i]$ does not change during the time of the measurement of one decay curve (1 s). Therefore, the reaction rate only depends on the OH concentration.

$$[\mathrm{OH}]_\mathrm{t} = [\mathrm{OH}]_0 \exp\left(-\sum_i k_{\mathrm{OH+X}_i}[\mathrm{X}_i]t\right) \tag{2.3}$$

The OH reactivity is derived by applying an exponential fit to the measured OH decay.

2.2.3 VOC Measurements

VOCs are measured by different techniques in the chamber experiments. Most organic compounds are detected by proton transfer reaction – time-of-flight mass spectrometry (PTR–TOF–MS, Lindinger et al., 1998; Jordan et al., 2009). A hollow cathode discharge source produces H_3O^+ reagent ions that are injected into the drift tube where the proton transfer to the sampled VOCs takes place. A transfer lense system assures a high transmittance into the TOF–mass spectrometer. The PTR–TOF–MS was calibrated for selected compounds using a diffusion source (Gautrois and Koppmann, 1999) in these experiments. Substances were evaporated from thermostated (30 °C) glass vials and transported with a small flow of ultrapure nitrogen to a mixing chamber where an additional dilution can be applied. Concentrations were determined by the mass loss of the individual compound and the dilution flow.

In addition to the PTR–TOF–MS, some compounds are also detected by gas chromatography with a flame ionisation detector (GC–FID, Wegener et al., 2007; Kaminski, 2014). Samples are taken from a heated inlet line (79 °C) and concentrated with a thermal desorption system (TDS, Gerstel). An internal standard (tetrachloroethylene) was added to the sample flow to to monitor changes in the sensitivity of the calibration with a calibration standard (Apel 8). Depending on polarity and boiling point, the analytes are separated by the GC column and subsequently detected by the FID or a masspectrometer (Agilent 5875C). In the FID, the analyte is burned with hydrogen and the formed ions are detected and recorded in the chromatogram.

In addition to the detection by DOAS, formaldehyde (HCHO) is measured by a Hantzsch Monitor (AeroLaser; Glowania et al., 2021). In a stripping coil, gaseous HCHO is brought into aqueous solution. Then, dissolved HCHO samples are mixed with 2,4-pentadione and ammonia. In the Hantzsch reaction 3,5-diacetly-1,4-dihydrolutidine (DDL) is formed. DDL absorbs light at 410 nm and subsequently emits fluorescence light around 510 nm that is detected by a PMT. The Hantzsch intrument was calibrated for the experiments with a liquid HCHO standard.

2.2.4 Photolysis frequencies

Photolysis frequencies (j) of NO_2, HONO, O_3, and pinonaldehyde were calculated from actinic flux density spectra that are derived from measurements of total and diffuse spectral actinic flux densities outside the chamber:

$$j = \int \sigma(\lambda)\phi(\lambda)F_\lambda(\lambda)\mathrm{d}\lambda \tag{2.4}$$

with σ the absorption cross section, ϕ the quantum yield, and F the actinic flux. From these measurements direct sun contributions are calculated. The direct and diffuse actinic flux densities are then used as input for a model which calculates mean chamber spectra by taking into account the time-dependent effects of shadings of the chamber steel frame and the weakly wavelength-dependent transmittance of the Teflon films (Bohn and Zilken, 2005). This method is regularly evaluated by dedicated experiments using the chamber as a chemical actinometer (Bohn et al., 2005). The absorption spectra and quantum yields used for the calculations of NO_2, HONO, and O_3 to calculate photolysis frequencies are

taken from literature (Mérienne et al., 1995; Troe, 2000; Stutz et al., 2000; Daumont et al., 1992; Matsumi et al., 2002). The pinonaldehyde photolysis frequency is discussed in more detail in Chapter 5.

2.3 Chamber specific properties

Nitrious acid (HONO), formaldehyde (HCHO), and acetone are formed in the illuminated chamber by unknown chemical processes on the surface of the chamber foil. The source strengths S_i of these chamber sources can be determined in reference experiments when only humidified synthetic air is present in the chamber. From such experiments, an empirical parameterisation has been derived (Rohrer et al., 2005):

$$S_{\mathrm{HONO}} = \alpha_{\mathrm{HONO}} \times j_{\mathrm{NO_2}} \times \left(1 + \frac{RH}{11.6\%}\right) \times \exp\left(-\frac{3950\mathrm{K}}{T}\right) \tag{2.5}$$

$$S_{\mathrm{HCHO}} = \alpha_{\mathrm{HCHO}} \times j_{\mathrm{NO_2}} \times \left(0.21 + 2.6 \times 10^{-2} \times \frac{RH}{\%}\right) \times \exp\left(-\frac{2880\mathrm{K}}{T}\right) \tag{2.6}$$

$$S_{\mathrm{Acetone}} = \alpha_{\mathrm{Acetone}} \times j_{\mathrm{NO_2}} \times \left(0.21 + 2.6 \times 10^{-2} \times \frac{RH}{\%}\right) \times \exp\left(-\frac{2880\mathrm{K}}{T}\right) \tag{2.7}$$

where α_i are scaling factors which are adjusted for each experiment and compound. For the experiments here, this was achieved by observing the increase of the concentration of these species before the injection of VOCs. It is assumed that the scaling factor stays constant within an individual experiment. This is verified by day-long reference experiments without added VOCs.

2.4 Experiment procedure

Before an experiment was started, the chamber was flushed in the dark with pure synthetic air until residual trace gases from previous experiments were diluted

below the detection limits of instruments. This was typically done over night with a flow rate of synthetic air of 150 $m^3 h^{-1}$. At the beginning of an experiment, CO_2 was added as an inert tracer to verify the dilution rate of trace gases measured by the massflow controllers that controlled the replenish flow of synthetic air into the chamber. Next, the chamber air was humidified by boiling Milli-Q® water and adding it into the chamber with a carrier gas flow of synthetic air until water vapour mixing ratios of around 2 % were reached. The chamber was only humidified in the beginning and water concentrations decreased over the course of the experiments due to dilution with dry synthetic air. For most experiments, 40–70 ppbv ozone was injected. Ozone was produced by a silent discharge ozonizer and flushed into the chamber. The ozone concentrations were in the normal atmospheric range and assured that NO concentrations were kept within a few hundreds pptv by suppressing NO in the reaction with ozone. Usually, the shutter system was opened before adding the VOC. As soon as the chamber was illuminated, nitrous acid, formaldehyde, and acetone were formed heterogeneously from small chamber sources and emitted from the chamber walls (see Section 2.3). The HONO photolysis subsequently formed OH and NO. After a "zero-air phase" where no VOCs were added, α-pinene and MBO were injected three times from high-concentrated gas mixtures prepared in Silcosteel canisters (Restek) in intervals of approximately 2 hours. The time between the injections allowed studying the VOC oxidation. Pinonaldehyde has a very low vapour pressure and making it impossible to prepare gas-mixtures. Instead, pinonaldehyde was heated in a glass vial, and the vapour was flushed into the chamber with a carrier gas flow of nitrogen. In the pinonaldehyde experiments, the roof was not opened before a stable pinonaldehde concentration was observed by the PTR–TOF–MS.

2.5 Model calculations

For the analysis of SAPHIR experiments, measured concentration time series of injected VOCs, formed products such as acetone and formaldehyde, OH and HO_2 radicals, NO_x, and O_3 are compared to simulations by a zero-dimensional chemical box model. FACSIMILE (MCPA Software) in combination with the EASY Interface (Easy AtmoSpheric chemistrY; Brauers and Rohrer, 1999) was used to numer-

ically integrate sets of differential equations which describe the time dependent reaction rates of chemical compounds that are involved in the VOC photooxidation. The solver simulates the time dependent development of concentrations for given boundary conditions (e.g. temperature, pressure, and radiation). Model output data were processed in Interactive Data Language (IDL, Harris Geospatial Solutions).

In order to model trace gas and radical concentrations observed in the chamber experiments, the chemistry from the Master Chemical Mechanism (MCM) in the recent version 3.3.1 was used (Jenkin et al., 1997; Saunders et al., 2003; MCM, 2017). The MCM is a widely used near explicit atmospheric chemical mechanism. It consists of about 17,000 elementary reactions and of 6,700 individual species. The MCM is regularly updated. It uses reaction rate constants and photochemical data that come from the IUPAC recommendations (Atkinson et al., 2006) and/or new publications of experimental and theoretical studies of reactions. In addition, structure activity relationships (SAR) are used when no data is available. SARs provide rate coefficients related to structural properties of chemical species. SARs are developed based on experimental datasets and are available for many different reactions and substance classes, e. g. OH reaction with organic compounds (Kwok and Atkinson, 1995), decomposition of substituted alkoxy radicals (Vereecken and Peeters, 2009), and H-migration in peroxy radicals (Vereecken and Nozière, 2020). SAR was also used in this thesis to develop a mechanism for the subsequent oxidation of 4-hydroxynorpinonaldehyde (see Appendix A.3). For our analysis, the MCM was extended by implementing chamber-specific processes like dilution and sources for HONO, formaldehyde, and acetone in the sunlit chamber. The dilution rate was calculated from the monitored replenishment flow rate.

NO, NO_2, HONO, water vapor mixing ratio, temperature, and pressure were constrained to measurements. While photolysis frequencies (j) for NO_2, HONO, O_3, and pinonaldehyde were calculated from actinic flux measurement, all other photolysis frequencies were calculated for clear-sky conditions as parameterized in MCM 3.3.1 but scaled by the ratio of measured to calculated j_{NO2} to account for shading of the sunlight by clouds and construction elements of the chamber.

Trace gas and radical concentrations were calculated on a 1 min time base. VOC and O_3 injections were introduced as sources only present at the injection time. The O_3 source strengths were adjusted to match observed O_3 concentrations at

the time of the injection. Correspondingly, VOC sources were adjusted to match the observed increase in the OH reactivity. For the experiment in which no k_{OH} measurements were available, the observed increase of the VOC concentration as measured by a PTR–TOF–MS were used instead. In contrast to PTR–TOF–MS measurements, the measured k_{OH} values are independent of a concentration calibration.

3 Photooxidation of MBO

The content of this chapter was published as "Evaluation of OH and HO_2 concentrations and their budgets during photooxidation of 2-methyl-3-butene-2-ol (MBO) in the atmospheric simulation chamber SAPHIR" by A. Novelli, M. Kaminski, M. Rolletter, I. H. Acir, B. Bohn, H. P. Dorn, X. Li, A. Lutz, S. Nehr, F. Rohrer, R. Tillmann, R. Wegener, F. Holland, A. Hofzumahaus, A. Kiendler-Scharr, A. Wahner, and H. Fuchs in Atmospheric Chemistry and Physics, 18, 11409-11422, DOI: 10.5194/acp-18-11409-2018, 2018, under the Creative Commons Attribution 3.0 License. The supplementary material is provided in Appendix A.1.

Atmos. Chem. Phys., 18, 11409–11422, 2018
https://doi.org/10.5194/acp-18-11409-2018

Atmospheric Chemistry and Physics
Open Access
EGU

Evaluation of OH and HO_2 concentrations and their budgets during photooxidation of 2-methyl-3-butene-2-ol (MBO) in the atmospheric simulation chamber SAPHIR

Anna Novelli[1], Martin Kaminski[1,a], Michael Rolletter[1], Ismail-Hakki Acir[1,b], Birger Bohn[1], Hans-Peter Dorn[1], Xin Li[1,c], Anna Lutz[2], Sascha Nehr[1,d], Franz Rohrer[1], Ralf Tillmann[1], Robert Wegener[1], Frank Holland[1], Andreas Hofzumahaus[1], Astrid Kiendler-Scharr[1], Andreas Wahner[1], and Hendrik Fuchs[1]

[1]Institute of Energy and Climate Research, IEK-8: Troposphere, Forschungszentrum Jülich GmbH, Jülich, Germany
[2]Department of Chemistry and Molecular Biology, University of Gothenburg, Gothenburg, Sweden
[a]now at: Bundesamt für Verbraucherschutz, Abteilung 5 – Methodenstandardisierung, Referenzlaboratorien und Antibiotikaresistenz, Berlin, Germany
[b]now at: Institute of Nutrition and Food Sciences, Food Chemistry, University of Bonn, Bonn, Germany
[c]now at: State Key Joint Laboratory of Environmental Simulation and Pollution Control, College of Environmental Sciences and Engineering, Peking University, Beijing, China
[d]now at: INBUREX Consulting GmbH, Process Safety, Hamm, Germany

Correspondence: Anna Novelli (a.novelli@fz-juelich.de) and Hendrik Fuchs (h.fuchs@fz-juelich.de)

Received: 5 February 2018 – Discussion started: 14 March 2018
Revised: 18 July 2018 – Accepted: 31 July 2018 – Published: 15 August 2018

Abstract. Several previous field studies have reported unexpectedly large concentrations of hydroxyl and hydroperoxyl radicals (OH and HO_2, respectively) in forested environments that could not be explained by the traditional oxidation mechanisms that largely underestimated the observations. These environments were characterized by large concentrations of biogenic volatile organic compounds (BVOC) and low nitrogen oxide concentration. In isoprene-dominated environments, models developed to simulate atmospheric photochemistry generally underestimated the observed OH radical concentrations. In contrast, HO_2 radical concentration showed large discrepancies with model simulations mainly in non-isoprene-dominated forested environments. An abundant BVOC emitted by lodgepole and ponderosa pines is 2-methyl-3-butene-2-ol (MBO), observed in large concentrations for studies where the HO_2 concentration was poorly described by model simulations. In this work, the photooxidation of MBO by OH was investigated for NO concentrations lower than 200 pptv in the atmospheric simulation chamber SAPHIR at Forschungszentrum Jülich. Measurements of OH and HO_2 radicals, OH reactivity (k_{OH}), MBO, OH precursors, and organic products (acetone and formaldehyde) were used to test our current understanding of the OH-oxidation mechanisms for MBO by comparing measurements with model calculations. All the measured trace gases agreed well with the model results (within 15 %) indicating a well understood mechanism for the MBO oxidation by OH. Therefore, the oxidation of MBO cannot contribute to reconciling the unexplained high OH and HO_2 radical concentrations found in previous field studies.

1 Introduction

The hydroxyl radical (OH) is the most important daytime oxidant in the troposphere and its concentration affects the fate of many pollutants thus having a direct impact on the formation of ozone (O_3) and oxygenated volatile organic compounds (OVOCs), and as such influencing particle formation and climate. Understanding the OH radical formation and destruction paths is therefore critical.

Measurements of OH radicals in environments characterized by low nitrogen oxide (NO) concentrations, pristine conditions, and isoprene being the most abundantly measured biogenic volatile organic compound (BVOC; Carslaw et al.,

2001; Tan et al., 2001; Lelieveld et al., 2008; Whalley et al., 2011; Wolfe et al., 2011a), as well as in environments characterized by mixed emissions from biogenic and anthropogenic sources (Hofzumahaus et al., 2009; Lu et al., 2012, 2013; Tan et al., 2017), have shown a significant underestimation of observed OH concentrations by state-of-the-art models. In addition, the analysis of the OH budget using only measured species obtained by comparing all known OH radical sources together with the OH radical loss rate has demonstrated that the discrepancy with model simulations is due to a large missing OH radical source (Rohrer et al., 2014). Theoretical studies have proposed new OH recycling paths which, contrary to traditional mechanisms, do not require NO for the regeneration of HO_x from RO_2 radicals. The proposed mechanism involves unimolecular reactions of specific isoprene peroxy radicals (RO_2; Dibble, 2004; Peeters et al., 2009, 2014; Nguyen et al., 2010; Peeters and Müller, 2010; Silva et al., 2010; Peeters and Nguyen, 2012). Laboratory (Crounse et al., 2011) and chamber studies (Fuchs et al., 2013) have confirmed this mechanism and have helped with constraining its atmospheric impact. At the same time, other trace gases have been investigated as the results from the isoprene studies show that OH recycling through isoprene-RO_2, alone, is not sufficient to explain the OH concentrations observed in the field. Chamber and laboratory studies on methacrolein (Crounse et al., 2012; Fuchs et al., 2014), methyl vinyl ketone (MVK; Praske et al., 2015), isoprene hydroxy hydroperoxide (D'Ambro et al., 2017), and glyoxal (Feierabend et al., 2008; Lockhart et al., 2013) – important products from the oxidation of isoprene by OH – have also shown new OH recycling paths as predicted by theory (Peeters et al., 2009; da Silva, 2010, 2012; Setokuchi, 2011). Further laboratory studies also have discovered OH radical recycling in the bimolecular reaction of HO_2 with acyl peroxy radicals which was previously considered to be a radical termination reaction only (Dillon and Crowley, 2008; Groß et al., 2014; Praske et al., 2015). These results underline the need to carefully investigate the OH radical budget, at least for the most abundant volatile organic compounds (VOCs), to test our current knowledge.

In a similar way, the HO_2 radical concentrations measured in several field campaigns performed in forested areas have shown measurement discrepancies with model calculations, highlighting an incomplete understanding of the chemistry involving formation and loss paths of HO_2 radicals. In some environments, the model tends to overestimate the measured HO_2 concentration (Stone et al., 2011), while in others there is the tendency to underestimate the measurements (Kubistin et al., 2010; Wolfe et al., 2011b, 2014; Hens et al., 2014). It has been recently shown that HO_2 radical measurements performed by laser-induced fluorescence (LIF) via conversion of HO_2 into OH after reaction with NO are likely affected by an interference that originates from organic peroxy radicals (Fuchs et al., 2011; Nehr et al., 2011; Whalley et al., 2013; Lew et al., 2018). Therefore some of the discrepancies observed in previous studies may be partly caused by inaccurate HO_2 radical measurements. Nevertheless, recent studies where this peroxy radical interference is accounted for still showed discrepancies with model calculations (Griffith et al., 2013; Hens et al., 2014; Wolfe et al., 2014). These recent studies, performed in environments where isoprene was not the dominantly measured BVOC, were all characterized by poor agreement between modelled and measured results for both OH and HO_2 concentrations, with the measurements being up to a factor of 3 higher than the model results. Good agreement was observed between modelled and measured OH radicals when the model is constrained to the HO_2 radical measurements. These studies have concluded that there is a missing HO_2 source for environments where the dominantly measured BVOCs are monoterpenes and 2-methyl-3-butene-2-ol (MBO; Hens et al., 2014; Wolfe et al., 2014). Corresponding photooxidation studies have been performed for β-pinene in the SAPHIR chamber at the Forschungszentrum Jülich. Consistent with field studies, a significant (up to a factor of 2) model underprediction of both OH and HO_2 concentrations was observed when β-pinene was oxidized by OH under low-NO conditions (< 300 pptv; Kaminski et al., 2017). The observed discrepancies in the chamber could be explained by additional HO_2 production, for which Kaminski et al. (2017) proposed a mechanism involving unimolecular radical reactions and photolysis of oxygenated products.

MBO is the dominant emission from lodgepole (*Pinus Contorta*) and ponderosa (*Pinus Ponderosa*) pines (Goldan et al., 1993; Harley et al., 1998). Its global emission is lower than that of isoprene (Guenther et al., 2012) but in forested areas within the western US, MBO is the most abundant BVOC measured contributing to most of the measured OH reactivity (Nakashima et al., 2014; Ortega et al., 2014). In the atmosphere, MBO reacts primarily with OH forming two peroxy radicals that yield acetone, glycolaldehyde, 2-hydroxy-2-methylpropanal (HMPR), and formaldehyde after reaction with NO (Fantechi et al., 1998; Ferronato et al., 1998; Carrasco et al., 2006; Fig. 1). The reaction of the peroxy radicals with HO_2 yields two different dihydroxy hydroperoxides (MBOAOOH and MBOBOOH, Fig. 1). Recent theoretical studies have described a mechanism that involves additional hydrogen shift reactions for the RO_2 that reforms OH and produces HO_2 (Knap et al., 2015, 2016). As the predicted unimolecular reaction rate following the hydrogen shift is, at most, 1.1×10^{-3} s^{-1} (at 298 K and 1013 hPa) the study by Knap et al. (2016) concludes that in environments where the NO concentration is high (> 1 ppbv), the reaction between RO_2 and NO will be the dominant loss path for RO_2 radicals, and in forested areas, where the NO concentration is lower than 0.2 ppbv, reactions with HO_2 and RO_2 will dominate the RO_2 fate.

In this study, the photooxidation of MBO initiated by OH radicals is investigated in the atmospheric simulation chamber SAPHIR in the presence of approximately 200 pptv of NO. The OH and HO_2 budgets are analysed and a compari-

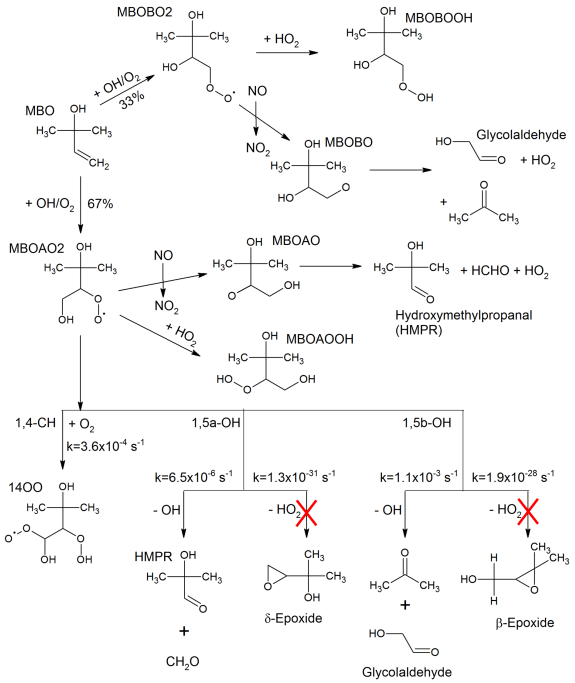

Figure 1. Simplified MBO OH-oxidation reaction scheme as described in the MCM version 3.3.1, including 1,4 and 1,5 H-shift reactions and their rate coefficients at 1013 hPa and 298 K as suggested by Knap et al. (2016). These H-shift reactions were added to the MCM version 3.3.1 kinetic model for a sensitivity test excluding the ones forming the epoxides (marked with the red crosses).

son with an up-to-date model is performed to test the current understanding of the oxidation processes of this important BVOC.

2 Methods

2.1 Atmospheric simulation chamber SAPHIR

The experiment performed in this study was conducted in the atmospheric simulation chamber SAPHIR at the Forschungszentrum Jülich, Germany. The chamber allows for the investigation of oxidation processes and mechanisms of organic compounds at atmospheric conditions in a controlled environment. The SAPHIR chamber has a cylindrical shape with a volume of 270 m^3 and is made of a double-walled Teflon (FEP) film that is inert and has a high transmittance for solar radiation (Bohn and Zilken, 2005). It is equipped with a shutter system that is opened during photolysis experiments allowing the natural solar radiation to penetrate the chamber. The air provided to the chamber is mixed from ultra-pure nitrogen and oxygen (Linde, > 99.99990 %). A fan in the chamber ensures a complete mixing of trace gases within 2 minutes. The pressure in the chamber is slightly higher than ambient pressure ($\sim$ 30 Pa higher) to avoid external air penetrating the chamber. Due to small leakages and air consumption by instruments, a dilution rate of $\sim 4\,\%\,h^{-1}$ was required during this study. More details regarding the chamber can be found elsewhere (Rohrer et al., 2005; Poppe et al., 2007; Schlosser et al., 2007).

2.2 Experimental procedure

At the beginning of the experiment, only synthetic air was present after flushing during the night. Evaporated Milli-Q® water was first introduced into the dark chamber by a carrier flow of synthetic air until a concentration of $\sim 5 \times 10^{17}$ cm^{-3}

Table 1. Instrumentation for radical and trace-gas quantification during the MBO oxidation experiment.

	Technique	Time resolution	1σ precision	1σ accuracy
OH	LIF	47 s	0.3×10^6 cm^{-3}	13 %
OH	DOAS	200 s	0.8×10^6 cm^{-3}	6.5 %
HO_2	LIF	47 s	1.5×10^7 cm^{-3}	16 %
k_{OH}	Laser-photolysis + LIF	180 s	0.3 s^{-1}	10 %
NO	Chemiluminescence	180 s	4 pptv	5 %
NO_2	Chemiluminescence	180 s	2 pptv	5 %
HONO	LOPAP	300 s	1.3 pptv	12 %
O_3	UV-absorption	10 s	1 ppbv	5 %
MBO and Acetone	PTR-TOF-MS	30 s	> 15 pptv	< 14 %
MBO	GC	30 min	4–8 %	5 %
HCHO	Hantzsch monitor	120 s	20 pptv	5 %

of water vapour was reached. Ozone produced by a silent discharge ozonizer (O3onia) was subsequently added to reach 40 pbbv in the chamber and was used to keep the concentration of NO within a few hundreds of pptv. This initial phase is defined as the dark phase. After opening the shutter system of the chamber, nitrous acid (HONO) was photochemically formed on the Teflon surface and released into the chamber. Its subsequent photolysis produced OH radicals and NO (Rohrer et al., 2005) during this so-called "zero-air" phase. Afterwards, the MBO was injected three times at intervals of about 2 hours using a high-concentration gas mixture of MBO ($\sim$ 600 ppm, 98 %, from Merck) premixed in a Silcosteel canister (Restek) to reach $\sim$ 4 ppbv of MBO in the chamber after each injection. Two additional experiments where performed at very similar conditions but due to instrumental failures, they could not be included in this study. The experiment shown is composed of three independent injections of MBO and the range of NO and O_3 in the chamber is analogous to what was observed in the field studies where large concentrations of MBO were measured ($\sim$ 50 ppb of O_3 and 150 pptv of NO) giving confidence that what was observed in this study can be compared to ambient data.

2.3 Instrumentation

Table 1 summarizes the instruments available during the experiment, quoting time resolution, 1σ accuracy, and precision for each instrument. The concentrations of OH and HO_2 radicals were measured with the LIF instrument permanently in use at the SAPHIR chamber and described previously (Holland et al., 2003; Fuchs et al., 2011). Recent studies have shown the possibility of interferences on the OH signal measured by LIF instruments that depend both on the chemical conditions of the sampled air and on the geometry of the different instruments (Mao et al., 2012; Novelli et al., 2014; Rickly and Stevens, 2018). A laboratory study performed with this LIF instrument (Fuchs et al., 2016) showed only interferences for high ozone concentrations (300–900 ppbv) together with BVOC concentrations ranging from 1 to 450 ppbv, which are far beyond any condition encountered in this study. Therefore, the OH radical concentration measured by the LIF instrument in this study is considered free from interferences. In addition, OH was measured by differential optical absorption spectroscopy (DOAS; Dorn et al., 1995). Numerous intercomparisons between the LIF and the DOAS instrument in the SAPHIR chamber (Schlosser et al., 2007, 2009; Fuchs et al., 2012) showed very good agreement between these two instruments giving high reliability to the OH radical measurements performed in the chamber. OH concentration measurements by DOAS in this study were on average 14 % lower than those by LIF. This difference was well within the combined accuracies of measurements and was taken into account as additional uncertainty in OH concentration measurements in the analysis of this study, for which mainly OH data from the LIF instrument was used.

Several studies have proven that RO_2 radicals can cause an interference signal in the HO_2 radicals measured by conversion to OH after reaction with an excess of NO (Fuchs et al., 2011; Hornbrook et al., 2011; Whalley et al., 2013; Lew et al., 2018). It was shown that a reasonable approach for avoiding the interference is to lower the concentration of NO reacting with the sampled air inside the instrument. During this study, the NO concentration ($\sim 2.5 \times 10^{13}$ cm^{-3}) was thus adjusted to lower the interference to a minimum as described in Fuchs et al. (2011). As during the investigation of the interference from RO_2 originating from the oxidation of different VOCs, MBO was not tested; the amount of interference that arises from its oxidation products is not known (Fuchs et al., 2011; Whalley et al., 2013; Lew et al., 2018). An upper limit could be estimated from experiments with isoprene peroxy radicals at similar operational conditions of the instrument. The relative detection sensitivity for RO_2 radicals originated from isoprene, compared to the HO_2 signal, was among the largest of the studied peroxy radical species, with a value of 20 % under the conditions of the present work (Fuchs et al., 2011). This value is considered to be a reasonable estimate

bias in the HO_2 radical measurements and will be considered later in the discussion. The OH reactivity (k_{OH}), the inverse lifetime of OH, was measured by a pump and probe technique coupled with a time-resolved detection of OH by LIF (Lou et al., 2010; Fuchs et al., 2017). MBO was measured by a proton-transfer-reaction time-of-flight mass spectrometer (PTR-TOF-MS; Lindinger et al., 1998; Jordan et al., 2009) and a gas chromatography system (GC; Wegener et al., 2007) with a PTR-TOF-MS to GC ratio of 1.1 ± 0.1, and acetone by PTR-TOF-MS. As the PTR-TOF-MS was calibrated only for the species listed above, concentrations for other species were not available. Formaldehyde (HCHO) was detected with a Hantzsch monitor (Kelly and Fortune, 1994); HONO with a long-path absorption photometry (LOPAP; Li et al., 2014); carbon monoxide (CO) with a reduction gas analysis instrument (RGA; Wegener et al., 2007); carbon dioxide (CO_2), methane (CH_4), and water vapour by an instrument applying cavity ring-down spectroscopy (CRDS; Picarro); NO and nitrogen dioxide (NO_2) with chemiluminescence (CL; Ridley et al., 1992); and O_3 by UV absorption (Ansyco). Photolysis frequencies were calculated from measurements of solar actinic radiation by a spectroradiometer (Bohn et al., 2005; Bohn and Zilken, 2005).

2.4 Model calculations

A zero-dimensional box model using chemical mechanistic information from the Master Chemical Mechanism, MCM version 3.3.1 (Jenkin et al., 1997; Saunders et al., 2003) downloaded via website: http://mcm.leeds.ac.uk/MCM (last access: February 2018) was used to calculate radical and trace gas concentrations. The model was implemented with specific chamber-related properties. First, a dilution rate was applied to all the trace gases present in the model to account for the dilution from the replenishing flow. The background production of HONO, HCHO, and acetone, known to occur in the sunlit chamber (Rohrer et al., 2005; Karl et al., 2006), was parameterized by an empirical function that depends on temperature, relative humidity, and solar radiation. Source strengths were adjusted to match the time series of HCHO and acetone during the zero-air phase, when the chamber was the only source for these species (~ 0.3 ppbv h^{-1}). These chamber sources also impacted the OH reactivity measured during the zero-air phase. Ideally, after accurately accounting for the chamber sources, the OH reactivity should be well represented by the model, but it is commonly the case that there is still the need for an OH reactant equivalent to $\sim 1.0\,s^{-1}$ of OH reactivity. This unexplained reactivity is parameterized with a co-reactant Y added to the model, which converts OH to HO_2 in the same way as CO does (Fuchs et al., 2012, 2014; Kaminski et al., 2017). The concentration of Y was adjusted to match the observed OH reactivity during the zero-air phase of the experiment and was kept constant throughout the experiment. The uncertainty in the OH reactivity in this experiment was $\pm 0.6\,s^{-1}$ determined by the uncertainty in the instrumental zero ($1.5\,s^{-1}$) of the OH reactivity instrument. This uncertainty was applied in sensitivity runs of the model, but had a minor effect on the results discussed here.

The unknown chemical nature of the background reactivity that dominates the loss of OH radicals for the zero-air phase of the experiment strongly limits the ability of the simple model used during this phase in reproducing the measured radical concentrations. Additional parameters such as, for example, a loss path for HO_2 radicals could improve the agreement with the model results but would hinder the concept of using a simple model. A test run of the model using CH_4 as species Y instead of CO was performed and the results are shown in Fig. S1 of the Supplement. It can be clearly seen that using CH_4 as species Y instead of CO does increase the agreement between measured and modelled HO_2 radicals during the zero-air phase, but has a negligible impact on the agreement observed once the MBO is injected. This underlines how the radical concentrations are insensitive to the nature of the Y species once the MBO is present in the chamber. As the zero-air phase serves to check the status of the chamber to identify, for example, unexpected contamination and has no impact on the chemistry once MBO dominates the OH reactivity, no model calculation is shown for this part of the experiment in the following.

Because of the unknown chemical nature of the background reactivity that dominates the loss of OH radicals for the zero-air phase of the experiment, agreement between measured and modelled radical concentrations cannot be expected during this initial phase. Therefore, no model calculation is shown for this part of the experiment.

Photolysis frequencies (j values) for O_3, NO_2, HONO, hydrogen peroxide (H_2O_2), and formaldehyde were constrained to the measurements. All the other photolysis frequencies present in the model were first calculated for clear sky conditions according to the MCM 3.3.1 and then scaled by the ratio of measured to calculated $j(NO_2)$ to account for clouds and transmission of the chamber film. The model was constrained to measured water vapour, chamber pressure (ambient pressure), and temperature, as well as NO, NO_2, and HONO. Values were reinitiated every minute. MBO and O_3 injections were implemented in the model by applying a source just active for the time of the injection. The O_3 source was adjusted to match the concentration measured at the injection and the MBO source to match the change in OH reactivity at the injection time. For completeness, the model included the reaction of MBO with O_3 although this reaction contributed on average 3 % to the reactivity of MBO which was dominated by the reaction with OH radicals.

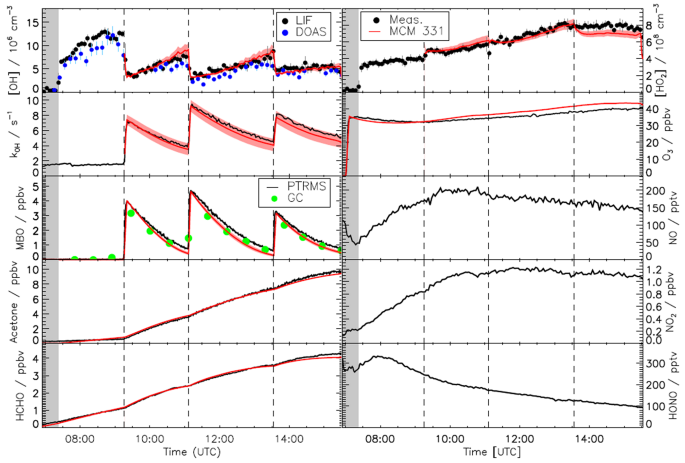

Figure 2. Measured time series of OH, HO_2, MBO, acetone, formaldehyde, O_3, trace gases, and OH reactivity compared to results obtained from modelling using the MCM version 3.3.1. There are no model results for NO, NO_2, or HONO as the model was constrained to the measurements. The red shaded areas represent the uncertainty in the model due to the uncertainties of the zero of the OH reactivity measurements (see text for details). Grey shaded areas indicate the times before opening the chamber roof and vertical dashed lines indicate the times when MBO was injected.

3 Results and discussion

3.1 Model comparison

Figure 2 shows the time series for the trace gases measured during the MBO experiment compared to the model including the sensitivity runs for the uncertainty introduced by the zero OH-reactivity value. At the beginning of the experiment, during the dark phase, formation of radicals was not expected as the roof was closed and only water vapour and ozone were added. The reactivity of $1.7\,s^{-1}$ observed during this phase was due to desorption of trace gases from the walls of the chamber that could be observed during the humidification process. Some of these trace gases are HONO, HCHO, and acetone as seen from their slow but steady increase. Immediately after opening of the roof, there was production of OH and HO_2 radicals and NO_x from the photolysis of HONO and HCHO. After the injection of MBO, the OH reactivity was dominated by the reaction with MBO ($\sim 70\,\%$ for all three MBO injections) and its oxidation products contributed significantly to the OH reactivity, up to 40 %, once most of the MBO had reacted away. Good agreement between modelled and measured concentrations, well within the accuracy of the different instruments, could be observed for the majority of the species when MBO was oxidized by OH in this experiment. Formation of both measured major products from the oxidation of MBO, formaldehyde, and acetone was well reproduced by the model (averaged measurement to model ratio of 1.00 ± 0.02 for both). The modelled OH fitted the observation with an average measurement to model ratio of 1.0 ± 0.2 and the agreement between modelled and measured HO_2, although less good compared to the OH, was still satisfying (0.9 ± 0.1). The MBO decays due to its reaction with OH radicals were slightly overpredicted by the model (average observed to model ratio of 1.3 ± 0.2) in accordance with the measured decline of OH reactivity. This is in agreement with the PTR-TOF-MS measurement. However, results did not change significantly if the model was constrained to measured MBO concentrations.

The major uncertainties in this measurement–model comparison are introduced by the uncertainty of the zero measurement of the OH reactivity data and by the possible interference of RO_2 radicals in the measured HO_2 signal. The first mostly affects the agreement between measured and modelled results for the OH reactivity itself. Modelled OH and HO_2 radicals are also partially affected but the uncertainty introduced is lower than the accuracy of radical measurements while the remaining modelled species are not influenced. As mentioned in the instrumental description section, 20 % is the upper limit for the interference from RO_2 radicals that could be expected from MBO on the HO_2 signal, based on the experiments performed with isoprene (Fuchs et al., 2011) for the conditions the instrument was run with. The

HO_2 concentration obtained from the model when accounting for this RO_2 interference would be, on average, only 8 % larger ($\sim 5.5 \times 10^7$ cm^{-3}) than the HO_2 concentration without any RO_2 interference for the periods in the experiment where the MBO was present in the chamber. This value is lower than the accuracy of the HO_2 measurement itself and has an insignificant impact on the other trace gases.

3.2 Model comparison including hydrogen shift reactions

In a recent theoretical work from Knap et al. (2016), hydrogen shift reactions (H-shift) in the peroxy radicals originated after photooxidation of four different methyl-buten-ol isomers were investigated. The 1,4, 1,5 and 1,6 H-shift reactions were studied and the rate coefficients at ambient temperature and pressure were given. For the photooxidation of the MBO isomer under investigation in this study, predicted products are OH and HO_2 radicals, 2-hydroxy-2-methylpropanal (HMPR), acetone, and glycolaldehyde (Fig. 1). Also β- and δ-epoxides are proposed as possible products although, due to their extremely slow unimolecular rate coefficients (Fig. 1), they are insignificant. As a sensitivity study, the three H-shift reactions, excluding the branching towards the epoxides, were included in the MCM 3.3.1 model as shown in Fig. 1, using the upper limit rate coefficients at 1013 hPa and 298 K as calculated by Knap et al. (2016). In the model, the H-shift reactions proceed directly to the final stable products without formation of intermediates. As expected from the low reaction rates for these reactions, their addition to the MBO degradation scheme has a very small impact with a change of less than 1 % on any of the trace gases modelled in our chamber study bringing no improvement in the already good agreement between measurements and model calculations. This is consistent with the study by Knap et al. (2016) where they concluded that H-shift reactions are not relevant for the oxidation scheme of MBO even for low NO conditions (< 50 pptv), where the reaction with HO_2 remains the dominant loss process for the MBO-RO_2 radicals. This is also expected as MBO contains only one double bond and the fast H-shift reactions observed for isoprene and methacrolein are favoured by the formation of conjugated double bonds in the stable radical co-products (Peeters and Nguyen, 2012).

3.3 OH and HO_2 radicals budget analysis

The calculation of the experimental OH budget helps with identifying possible missing OH sources, assuming the correctness of the measured OH concentration and OH reactivity. The total experimental OH loss rate, L_{OH}, is given by the product of the OH concentration and the OH reactivity and, as the OH radical is assumed to be in steady-state, it should be equal to the total OH production rate (P_{OH}; Eq. 1); P_{OH} includes the OH production rate from known sources, P_{OH}Meas (Eq. 2), plus other possible sources; L_{OH} can be compared with P_{OH}Meas, which can be calculated from the measured data.

$$L_{OH} = k_{OH} \times [OH] \approx P_{OH} = P_{OH}\text{Meas} + \text{other sources} \quad (1)$$

$$P_{OH}\text{Meas} = \left([HO_2] \times [NO] \times k_{HO_2+NO}\right) + ([HONO] \times j(HONO)) + ([O_3] \times j(O^1D) \times y) + ([HO_2] \times [O_3] \times k_{HO_2+O_3}) \quad (2)$$

Here [OH], [HO_2], [NO], [HONO], and [O_3] represent the measured concentrations of the trace gases; k_{HO_2+NO} and $k_{HO_2+O_3}$ the rate coefficients of HO_2 with NO and ozone, respectively; j(HONO) and $j(O^1D)$ the photolysis rates of HONO and O_3, respectively; and y is the fraction of $O(^1D)$ reacting with water vapour multiplied with the OH yield of the $O(^1D) + H_2O$ reaction. If all the sources contributing to the OH production are included in the calculation, then $P_{OH}\text{Meas} \approx P_{OH}$. In this study, the known OH sources considered are the following: reaction of NO and HO_2, reaction of O_3 and HO_2, photolysis of HONO, and photolysis of O_3. The formation of OH from ozonolysis of MBO is not included as it does not contribute noticeably.

Figure 3 shows the comparison between P_{OH}Meas and the total experimental OH loss, L_{OH}. The averaged ratio between P_{OH}Meas and L_{OH} is 0.9 ± 0.1 (1σ). A small deviation from unity, which would indicate a missing OH source contributing at most 20 % to the total OH production, is obtained. Nevertheless, if the errors of the different measurements are taken into account, this deviation becomes insignificant. For example, the total error of the total experimental OH loss is ~ 17 % to which the errors of the measured traces gases, mainly of the HO_2 radicals (16 %) and of the rate coefficients (~ 10 %) used to calculate the P_{OH}Meas, should be added. From these considerations, the experimental OH budget can be considered closed and no additional OH sources aside from the ones considered in Eq. (2) are needed to explain the OH radicals loss.

Figure 3 also depicts the total modelled OH production P_{OH}Mod. This is included in the analysis of the experimental OH radical budget to understand how well the OH-formation paths in the model can describe the measurements. The averaged ratio between P_{OH}Mod and L_{OH} provides a value of 1.0 ± 0.1 (1σ). The good agreement observed between P_{OH}Mod and L_{OH} indicates that the model is able to correctly represent the OH radical sources. The averaged difference between P_{OH}Mod and P_{OH}Meas is $(2.3 \pm 1.9) \times 10^6$ cm^{-3} s^{-1}. A large part of the difference, $\sim 1.5 \times 10^6$ cm^{-3} s^{-1}, is due to additional OH radical sources included in the model and not considered in the experimental OH production, e.g. RO_2 (CH_3CO_3 and $HOCH_2CO_3$) reacting with HO_2 forming OH. The additional small discrepancy ($\sim 0.8 \times 10^6$ cm^{-3} s^{-1}) is due to the differences observed for HO_2 and ozone between measurements and model calculations.

The analysis of the HO_2 budget is shown in Fig. 4. Here, different from the OH budget, the measured HO_2 loss rate,

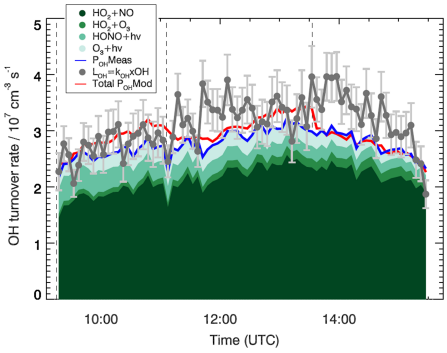

Figure 3. OH budget for the MBO experiment. The experimentally determined total OH loss rate, L_{OH}, and individual production terms are shown. For comparison, the red line indicates the total modelled OH production, P_{OH}Mod, which equals the modelled loss rate. Vertical dashed lines indicate the times when MBO was injected. Error bars (1σ) for L_{OH} include the accuracy of measurements.

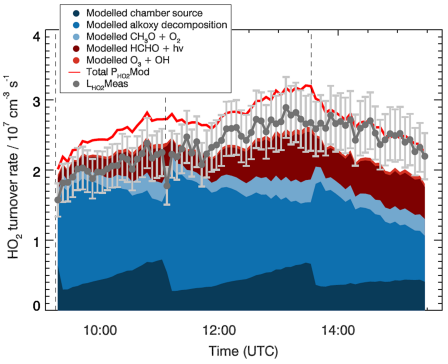

Figure 4. HO_2 budget for the MBO experiment. The loss rate of HO_2 calculated from measured NO, ozone, and HO_2 concentrations, L_{HO_2}Meas, and individual modelled production terms are shown. For comparison, the red line indicates the total modelled HO_2 production, P_{HO_2}Mod, which equals the total modelled loss rate. Vertical dashed lines indicate the times when MBO was injected. Error bars (1σ) for L_{HO_2}Meas include the accuracy of HO_2 measurements.

L_{HO_2}, is compared to the total modelled HO_2 production rate, P_{HO_2}Mod. This comparison provides information on the completeness in the understanding of the HO_2 production and loss processes for the MBO photooxidation mechanism. Within the model, the 15 most important HO_2 production paths are explicitly considered and depicted in Fig. 4. The largest contribution to the HO_2 production comes from decomposition of alkoxy radicals with a subsequent reaction with oxygen (51 %, see, as an example, reaction of MBOAO from Fig. 1), followed by the conversion of OH by species Y (20 %) which is specific to the SAPHIR chamber and therefore not atmospherically relevant. Smaller contributions originate from formaldehyde photolysis (18 %), and H-abstraction reaction by oxygen from the methoxy radical (CH_3O, 8 %). As most of the relevant species contributing to the HO_2 production rate such as the alkoxy radicals were not measured and the background reactivity Y cannot be specified, it is not possible to calculate the production rate of HO_2 only from measured species as it was done for the OH radical budget.

The HO_2 radical is expected to be lost mainly via its reaction with NO accounting for ~ 90 % of the total loss rate calculated from the model. Additional losses are $HO_2 + HO_2$ self-reaction, reaction with ozone, and reaction with the first generation RO_2 produced from the MBO oxidation (MBOAO2 and MBOBO2, Fig. 1). Therefore, the majority of the HO_2 loss rate can be obtained from measured NO, HO_2, and ozone concentrations (Eq. 3).

$$L_{HO_2}\text{Meas} = ([HO_2] \times [NO] \times k_{HO_2+NO}) + ([HO_2] \times [HO_2] \times k_{HO_2+HO_2}) + ([HO_2] \times [O_3] \times k_{HO_2+O_3}) \quad (3)$$

Here $[HO_2]$, $[NO]$, and $[O_3]$ represent the measured concentrations of the trace gases, k_{HO_2+NO}, $k_{HO_2+HO_2}$, and $k_{HO_2+O_3}$ the rate coefficients of HO_2 with NO, itself, and O_3, respectively. The measured HO_2 loss rate, L_{HO_2}Meas, is in good agreement with the total modelled HO_2 production rate with an average ratio of measured to modelled rates of 0.8 ± 0.1. The agreement with the total modelled HO_2 production increases (average ratio of measured to modelled rates of 0.9 ± 0.1) when including in the L_{HO_2}Meas the modelled loss rate by the reaction of HO_2 with modelled RO_2 radicals. The largest discrepancies are observed during the first injection of MBO, because the calculated HO_2 production rate is smaller than what is obtained from the model. The main reason is the lower measured HO_2 concentration (13 %) compared to the model during this period. With the increasing agreement between modelled and measured HO_2 radical also the agreement in the HO_2 budget increases.

The good agreement observed in the HO_2 budget, although partly relying on modelled species concentrations, indicates that the HO_2 production, within this chamber experiment, can be explained by alkoxy radical decomposition, photolysis of formaldehyde, and the chamber-specific Y source.

3.4 Comparison with previous studies

MBO was the major BVOC measured in two field campaigns which included measurements of OH and HO_2 radicals and a comparison with model calculations. The Biosphere Effects on Aerosols and Photochemisty Experiment II (BEARPEX09) campaign was performed near the Blodgett Forest Research Station in the Californian Sierra Nevada mountains (Mao et al., 2012). This campaign was characterized by large MBO concentrations (daily average ~ 3000 pptv), followed by isoprene (daily average ~ 1700 pptv) and monoterpenes (α-pinene, daily average 100 pptv and β-pinene, daily average 70 pptv). Both measured OH and HO_2 radicals compared reasonably well with modelled calculations, in agreement with the results observed in this chamber study.

The 2010 Bio-hydro-atmosphere interactions of Energy, Aerosols, Carbon, H_2O, Organics and Nitrogen – Rocky Mountain Organic Carbon Study (BEACHON-ROCS) was performed in the Manitou Experimental Forest in the Front Range of the Rocky Mountains in Colorado (Ortega et al., 2014). Here the dominantly measured BVOC was MBO (daily average ~ 1600 pptv) followed by monoterpenes (daily average ~ 500 pptv) (Kim et al., 2013). As observed for the OH radical budget within this study, during the BEACHON-ROCS campaign the calculated OH concentration from ozone photolysis and from the recycling via HO_2 plus NO reaction, divided by the measured OH reactivity, agreed with the measured OH concentration (Kim et al., 2013). No additional OH recycling paths were necessary to close the OH budget. Nevertheless, during the BEACHON-ROCS campaign, the model was able to reproduce the OH radical concentration only when constrained to the HO_2 radical measurements as the model underestimated the measured HO_2 radicals up to a factor of 3 (Kim et al., 2013; Wolfe et al., 2014). This is different from what was observed in the chamber experiment discussed in this study where a good agreement was found between modelled and measured HO_2 concentration. The base models used during both campaigns contained the same MBO oxidation scheme as tested in this study and as described in the MCM 3.3.1.

One difference between the two field studies is the BVOC compositions. During the BEARPEX09 campaign, the concentration of the measured monoterpenes relative to the concentration of MBO during daytime was smaller (6 %) compared to what was observed during the BEACHON-ROCS campaign (31 %). Two recent studies in environments with large concentrations of monoterpenes (Hens et al., 2014; Kaminski et al., 2017) also showed model calculations largely underestimating HO_2 radical measurements. Both studies concluded that the unaccounted HO_2 source seems to originate from monoterpene-oxidation products. The results collected by Hens et al. (2014) and by Kaminski et al. (2017) together with what is observed in this chamber study support that model–measurement discrepancies for HO_2 radicals in the BEACHON-ROCS campaign are not related to the MBO and its oxidation products but rather to the presence of monoterpenes and, as they were present in smaller concentrations, they would need to constitute a very efficient source of HO_2 radicals.

4 Summary and conclusions

A photooxidation experiment on 2-methyl-3-butene-2-ol (MBO), an important BVOC emitted by lodgepole and ponderosa pines, was performed in the atmospheric simulation chamber SAPHIR. Measurements of OH and HO_2 radicals and OH reactivity together with other important trace gases were compared to results from a state-of-the-art chemical mechanistic model (MCM v3.3.1). The overall agreement is very good: firstly, an average observed to modelled ratio of 1.0 ± 0.2 and 0.9 ± 0.1 is found for OH and HO_2 radicals, respectively. Also the MBO decay caused by reaction with OH radicals fits the expected decay from the model (average observed to modelled ratio of MBO concentration of 1.3 ± 0.2) and is consistent with the measured OH reactivity. Moreover, the major measured products, acetone, and formaldehyde, both match the model calculation with an average ratio of 1.00 ± 0.02. Addition of H-shift reactions from RO_2 radicals to the kinetic model as suggested in the literature (Knap et al., 2016) does not have a significant impact on the model results as expected from the small reaction rates ($< 1.1 \times 10^{-3}$ s^{-1}). The observed closure for both OH and HO_2 radical budgets indicates that their chemistry is well described by our current understanding of the MBO OH-initiated degradation processes.

The good agreement within the experimental OH budget is consistent with what was observed in previous field campaigns where MBO was the dominant BVOC measured (Mao et al., 2012; Kim et al., 2013). However, there was no closure for the HO_2 budget or agreement between measurements and model results when a larger concentration of monoterpenes was also observed (Wolfe et al., 2014). This discrepancy cannot be explained by MBO photooxidation as a good agreement between measured and calculated concentration of HO_2 is found in this chamber study. As large discrepancies were also observed for chamber studies with β-pinene (Kaminski et al., 2017) and in environments with large monoterpene concentrations (Hens et al., 2014), it is reasonable to assume that field observation for HO_2 radicals could be explained by an additional HO_2 radical source from monoterpene oxidation products, as proposed by Kaminski et al. (2017).

Data availability. The data from the experiment in the SAPHIR chamber used in this work are available on the EUROCHAMP data homepage (https://data.eurochamp.org/, last access: August 2018).

The Supplement related to this article is available online at https://doi.org/10.5194/acp-18-11409-2018-supplement.

Author contributions. HF and AH designed the experiments. HF conducted the HO_x radical measurements and SN was responsible for the OH reactivity measurements. BB conducted the radiation measurements. MK and RW were responsible for the GC measurements. RT, AL, and IHA were responsible for the PTR-MS measurements. XL was responsible for the HONO measurements and HPD for the DOAS OH data. FR was responsible for the NO_x and O_3 data. MR helped with the model. AN analysed the data and wrote the paper with the help of HF, FH, BB, AH, AKS, and AW.

Competing interests. The authors declare that they have no conflict of interest.

Acknowledgements. This work was supported by the EU FP-7 program EUROCHAMP-2 (grant agreement no. 228335). This project has received funding from the European Research Council (ERC) under the European Union's Horizon 2020 research and innovation program (SARLEP grant agreement no. 681529).

The article processing charges for this open-access publication were covered by a Research Centre of the Helmholtz Association.

Edited by: Dwayne Heard
Reviewed by: two anonymous referees

References

Bohn, B. and Zilken, H.: Model-aided radiometric determination of photolysis frequencies in a sunlit atmosphere simulation chamber, Atmos. Chem. Phys., 5, 191–206, https://doi.org/10.5194/acp-5-191-2005, 2005.

Bohn, B., Rohrer, F., Brauers, T., and Wahner, A.: Actinometric measurements of NO_2 photolysis frequencies in the atmosphere simulation chamber SAPHIR, Atmos. Chem. Phys., 5, 493–503, https://doi.org/10.5194/acp-5-493-2005, 2005.

Carrasco, N., Doussin, J. F., Picquet-Varrault, B., and Carlier, P.: Tropospheric degradation of 2-hydroxy-2-methylpropanal, a photo-oxidation product of 2-methyl-3-buten-2-ol: Kinetic and mechanistic study of its photolysis and its reaction with OH radicals, Atmos. Environ., 40, 2011–2019, https://doi.org/10.1016/j.atmosenv.2005.11.042, 2006.

Carslaw, N., Creasey, D. J., Harrison, D., Heard, D. E., Hunter, M. C., Jacobs, P. J., Jenkin, M. E., Lee, J. D., Lewis, A. C., Pilling, M. J., Saunders, S. M., and Seakins, P. W.: OH and HO_2 radical chemistry in a forested region of north-western Greece, Atmos. Environ. , 35, 4725–4737, https://doi.org/10.1016/S1352-2310(01)00089-9, 2001.

Crounse, J. D., Paulot, F., Kjaergaard, H. G., and Wennberg, P. O.: Peroxy radical isomerization in the oxidation of isoprene, Phys. Chem. Chem. Phys., 13, 13607–13613, https://doi.org/10.1039/c1cp21330j, 2011.

Crounse, J. D., Knap, H. C., Ørnsø, K. B., Jørgensen, S., Paulot, F., Kjaergaard, H. G., and Wennberg, P. O.: Atmospheric Fate of Methacrolein. 1. Peroxy Radical Isomerization Following Addition of OH and O_2, J. Phys. Chem. A, 116, 5756–5762, https://doi.org/10.1021/jp211560u, 2012.

D'Ambro, E. L., Møller, K. H., Lopez-Hilfiker, F. D., Schobesberger, S., Liu, J., Shilling, J. E., Lee, B. H., Kjaergaard, H. G., and Thornton, J. A.: Isomerization of Second-Generation Isoprene Peroxy Radicals: Epoxide Formation and Implications for Secondary Organic Aerosol Yields, Environ. Sci. Technol., 51, 4978–4987, https://doi.org/10.1021/acs.est.7b00460, 2017.

da Silva, G.: Hydroxyl radical regeneration in the photochemical oxidation of glyoxal: kinetics and mechanism of the $HC(O)CO + O_2$ reaction, Phys. Chem. Chem. Phys., 12, 6698–6705, https://doi.org/10.1039/b927176g, 2010.

da Silva, G.: Reaction of Methacrolein with the Hydroxyl Radical in Air: Incorporation of Secondary O_2 Addition into the MACR + OH Master Equation, J. Phys. Chem. A, 116, 5317–5324, https://doi.org/10.1021/jp303806w, 2012.

Dibble, T. S.: Intramolecular Hydrogen Bonding and Double H-Atom Transfer in Peroxy and Alkoxy Radicals from Isoprene, J. Phys. Chem. A, 108, 2199–2207, https://doi.org/10.1021/jp0306702, 2004.

Dillon, T. J. and Crowley, J. N.: Direct detection of OH formation in the reactions of HO_2 with $CH_3C(O)O_2$ and other substituted peroxy radicals, Atmos. Chem. Phys., 8, 4877–4889, https://doi.org/10.5194/acp-8-4877-2008, 2008.

Dorn, H.-P., Brandenburger, U., Brauers, T., and Hausmann, M.: A New In Situ Laser Long-Path Absorption Instrument for the Measurement of Tropospheric OH Radicals, J. Atmos. Sci., 52, 3373–3380, https://doi.org/10.1175/1520-0469(1995)052<3373:anisll>2.0.co;2, 1995.

Fantechi, G., Jensen, N. R., Hjorth, J., and Peeters, J.: Mechanistic studies of the atmospheric oxidation of methyl butenol by OH radicals, ozone and NO_3 radicals, Atmos. Environ., 32, 3547–3556, https://doi.org/10.1016/S1352-2310(98)00061-2, 1998.

Feierabend, K. J., Zhu, L., Talukdar, R. K., and Burkholder, J. B.: Rate Coefficients for the OH + HC(O)C(O)H (Glyoxal) Reaction between 210 and 390 K, J. Phys. Chem. A, 112, 73–82, https://doi.org/10.1021/jp0768571, 2008.

Ferronato, C., Orlando, J. J., and Tyndall, G. S.: Rate and mechanism of the reactions of OH and Cl with 2-methyl-3-buten-2-ol, Nat. Geosci., 103, 25579–25586, https://doi.org/10.1029/98JD00528, 1998.

Fuchs, H., Bohn, B., Hofzumahaus, A., Holland, F., Lu, K. D., Nehr, S., Rohrer, F., and Wahner, A.: Detection of HO_2 by laser-induced fluorescence: calibration and interferences from RO_2 radicals, Atmos. Meas. Tech., 4, 1209–1225, https://doi.org/10.5194/amt-4-1209-2011, 2011.

Fuchs, H., Dorn, H.-P., Bachner, M., Bohn, B., Brauers, T., Gomm, S., Hofzumahaus, A., Holland, F., Nehr, S., Rohrer, F., Tillmann, R., and Wahner, A.: Comparison of OH concentration measurements by DOAS and LIF during SAPHIR chamber experiments at high OH reactivity and low NO concentration, Atmos. Meas.

Tech., 5, 1611–1626, https://doi.org/10.5194/amt-5-1611-2012, 2012.

Fuchs, H., Hofzumahaus, A., Rohrer, F., Bohn, B., Brauers, T., Dorn, H. P., Haseler, R., Holland, F., Kaminski, M., Li, X., Lu, K., Nehr, S., Tillmann, R., Wegener, R., and Wahner, A.: Experimental evidence for efficient hydroxyl radical regeneration in isoprene oxidation, Nat. Geosci., 6, 1023–1026, https://doi.org/10.1038/Ngeo1964, 2013.

Fuchs, H., Acir, I.-H., Bohn, B., Brauers, T., Dorn, H.-P., Häseler, R., Hofzumahaus, A., Holland, F., Kaminski, M., Li, X., Lu, K., Lutz, A., Nehr, S., Rohrer, F., Tillmann, R., Wegener, R., and Wahner, A.: OH regeneration from methacrolein oxidation investigated in the atmosphere simulation chamber SAPHIR, Atmos. Chem. Phys., 14, 7895–7908, https://doi.org/10.5194/acp-14-7895-2014, 2014.

Fuchs, H., Tan, Z., Hofzumahaus, A., Broch, S., Dorn, H.-P., Holland, F., Künstler, C., Gomm, S., Rohrer, F., Schrade, S., Tillmann, R., and Wahner, A.: Investigation of potential interferences in the detection of atmospheric RO_x radicals by laser-induced fluorescence under dark conditions, Atmos. Meas. Tech., 9, 1431–1447, https://doi.org/10.5194/amt-9-1431-2016, 2016.

Fuchs, H., Novelli, A., Rolletter, M., Hofzumahaus, A., Pfannerstill, E. Y., Kessel, S., Edtbauer, A., Williams, J., Michoud, V., Dusanter, S., Locoge, N., Zannoni, N., Gros, V., Truong, F., Sarda-Esteve, R., Cryer, D. R., Brumby, C. A., Whalley, L. K., Stone, D., Seakins, P. W., Heard, D. E., Schoemaecker, C., Blocquet, M., Coudert, S., Batut, S., Fittschen, C., Thames, A. B., Brune, W. H., Ernest, C., Harder, H., Muller, J. B. A., Elste, T., Kubistin, D., Andres, S., Bohn, B., Hohaus, T., Holland, F., Li, X., Rohrer, F., Kiendler-Scharr, A., Tillmann, R., Wegener, R., Yu, Z., Zou, Q., and Wahner, A.: Comparison of OH reactivity measurements in the atmospheric simulation chamber SAPHIR, Atmos. Meas. Tech., 10, 4023–4053, https://doi.org/10.5194/amt-10-4023-2017, 2017.

Goldan, P. D., Kuster, W. C., Fehsenfeld, F. C., and Montzka, S. A.: The observation of a C_5 alcohol emission in a North American pine forest, Geophys. Res. Lett., 20, 1039–1042, https://doi.org/10.1029/93GL00247, 1993.

Griffith, S. M., Hansen, R. F., Dusanter, S., Stevens, P. S., Alaghmand, M., Bertman, S. B., Carroll, M. A., Erickson, M., Galloway, M., Grossberg, N., Hottle, J., Hou, J., Jobson, B. T., Kammrath, A., Keutsch, F. N., Lefer, B. L., Mielke, L. H., O'Brien, A., Shepson, P. B., Thurlow, M., Wallace, W., Zhang, N., and Zhou, X. L.: OH and HO_2 radical chemistry during PROPHET 2008 and CABINEX 2009 – Part 1: Measurements and model comparison, Atmos. Chem. Phys., 13, 5403–5423, https://doi.org/10.5194/acp-13-5403-2013, 2013.

Groß, C. B. M., Dillon, T. J., Schuster, G., Lelieveld, J., and Crowley, J. N.: Direct Kinetic Study of OH and O_3 Formation in the Reaction of $CH_3C(O)O_2$ with HO_2, J. Phys. Chem. A, 118, 974–985, https://doi.org/10.1021/jp412380z, 2014.

Guenther, A. B., Jiang, X., Heald, C. L., Sakulyanontvittaya, T., Duhl, T., Emmons, L. K., and Wang, X.: The Model of Emissions of Gases and Aerosols from Nature version 2.1 (MEGAN2.1): an extended and updated framework for modeling biogenic emissions, Geosci. Model Dev., 5, 1471–1492, https://doi.org/10.5194/gmd-5-1471-2012, 2012.

Harley, P., Fridd-Stroud, V., Greenberg, J., Guenther, A., and Vasconcellos, P.: Emission of 2-methyl-3-buten-2-ol by pines: A potentially large natural source of reactive carbon to the atmosphere, J. Geophys. Res.-Atmos., 103, 25479–25486, https://doi.org/10.1029/98JD00820, 1998.

Hens, K., Novelli, A., Martinez, M., Auld, J., Axinte, R., Bohn, B., Fischer, H., Keronen, P., Kubistin, D., Nölscher, A. C., Oswald, R., Paasonen, P., Petäjä, T., Regelin, E., Sander, R., Sinha, V., Sipilä, M., Taraborrelli, D., Tatum Ernest, C., Williams, J., Lelieveld, J., and Harder, H.: Observation and modelling of HO_x radicals in a boreal forest, Atmos. Chem. Phys., 14, 8723–8747, https://doi.org/10.5194/acp-14-8723-2014, 2014.

Hofzumahaus, A., Rohrer, F., Lu, K., Bohn, B., Brauers, T., Chang, C.-C., Fuchs, H., Holland, F., Kita, K., Kondo, Y., Li, X., Lou, S., Shao, M., Zeng, L., Wahner, A., and Zhang, Y.: Amplified Trace Gas Removal in the Troposphere, Science, 324, 1702–1704, https://doi.org/10.1126/science.1164566, 2009.

Holland, F., Hofzumahaus, A., Schafer, R., Kraus, A., and Patz, H. W.: Measurements of OH and HO(2) radical concentrations and photolysis frequencies during BERLIOZ, J. Geophys. Res.-Atmos., 108, PHO 2-1–PHO 2-23, https://doi.org/10.1029/2001jd001393, 2003.

Hornbrook, R. S., Crawford, J. H., Edwards, G. D., Goyea, O., Mauldin III, R. L., Olson, J. S., and Cantrell, C. A.: Measurements of tropospheric HO_2 and RO_2 by oxygen dilution modulation and chemical ionization mass spectrometry, Atmos. Meas. Tech., 4, 735–756, https://doi.org/10.5194/amt-4-735-2011, 2011.

Jenkin, M. E., Saunders, S. M., and Pilling, M. J.: The tropospheric degradation of volatile organic compounds: A protocol for mechanism development, Atmos. Environ., 31, 81–104, https://doi.org/10.1016/S1352-2310(96)00105-7, 1997.

Jordan, A., Haidacher, S., Hanel, G., Hartungen, E., Mark, L., Seehauser, H., Schottkowsky, R., Sulzer, P., and Mark, T. D.: A high resolution and high sensitivity proton-transfer-reaction time-of-flight mass spectrometer (PTR-TOF-MS), Int. J. Mass. Spectrom., 286, 122–128, https://doi.org/10.1016/j.ijms.2009.07.005, 2009.

Kaminski, M., Fuchs, H., Acir, I.-H., Bohn, B., Brauers, T., Dorn, H.-P., Häseler, R., Hofzumahaus, A., Li, X., Lutz, A., Nehr, S., Rohrer, F., Tillmann, R., Vereecken, L., Wegener, R., and Wahner, A.: Investigation of the β-pinene photooxidation by OH in the atmosphere simulation chamber SAPHIR, Atmos. Chem. Phys., 17, 6631–6650, https://doi.org/10.5194/acp-17-6631-2017, 2017.

Karl, M., Dorn, H.-P., Holland, F., Koppmann, R., Poppe, D., Rupp, L., Schaub, A., and Wahner, A.: Product study of the reaction of OH radicals with isoprene in the atmosphere simulation chamber SAPHIR, J. Atmos. Chem., 55, 167–187, https://doi.org/10.1007/s10874-006-9034-x, 2006.

Kelly, T. J. and Fortune, C. R.: Continuous Monitoring of Gaseous Formaldehyde Using an Improved Fluorescence Approach, Int. J. Environ. An. Ch., 54, 249–263, https://doi.org/10.1080/03067319408034093, 1994.

Kim, S., Wolfe, G. M., Mauldin, L., Cantrell, C., Guenther, A., Karl, T., Turnipseed, A., Greenberg, J., Hall, S. R., Ullmann, K., Apel, E., Hornbrook, R., Kajii, Y., Nakashima, Y., Keutsch, F. N., DiGangi, J. P., Henry, S. B., Kaser, L., Schnitzhofer, R., Graus, M., Hansel, A., Zheng, W., and Flocke, F. F.: Evaluation of HO_x

sources and cycling using measurement-constrained model calculations in a 2-methyl-3-butene-2-ol (MBO) and monoterpene (MT) dominated ecosystem, Atmos. Chem. Phys., 13, 2031–2044, https://doi.org/10.5194/acp-13-2031-2013, 2013.

Knap, H. C., Jorgensen, S., and Kjaergaard, H. G.: Theoretical investigation of the hydrogen shift reactions in peroxy radicals derived from the atmospheric decomposition of 3-methyl-3-buten-1-ol (MBO331), Chem. Phys. Lett., 619, 236–240, https://doi.org/10.1016/j.cplett.2014.11.056, 2015.

Knap, H. C., Schmidt, J. A., and Jorgensen, S.: Hydrogen shift reactions in four methyl-buten-ol (MBO) peroxy radicals and their impact on the atmosphere, Atmos. Environ., 147, 79–87, https://doi.org/10.1016/j.atmosenv.2016.09.064, 2016.

Kubistin, D., Harder, H., Martinez, M., Rudolf, M., Sander, R., Bozem, H., Eerdekens, G., Fischer, H., Gurk, C., Klüpfel, T., Königstedt, R., Parchatka, U., Schiller, C. L., Stickler, A., Taraborrelli, D., Williams, J., and Lelieveld, J.: Hydroxyl radicals in the tropical troposphere over the Suriname rainforest: comparison of measurements with the box model MECCA, Atmos. Chem. Phys., 10, 9705–9728, https://doi.org/10.5194/acp-10-9705-2010, 2010.

Lelieveld, J., Butler, T. M., Crowley, J. N., Dillon, T. J., Fischer, H., Ganzeveld, L., Harder, H., Lawrence, M. G., Martinez, M., Taraborrelli, D., and Williams, J.: Atmospheric oxidation capacity sustained by a tropical forest, Nature, 452, 737–740, https://doi.org/10.1038/nature06870, 2008.

Lew, M. M., Dusanter, S., and Stevens, P. S.: Measurement of interferences associated with the detection of the hydroperoxy radical in the atmosphere using laser-induced fluorescence, Atmos. Meas. Tech., 11, 95–109, https://doi.org/10.5194/amt-11-95-2018, 2018.

Li, X., Rohrer, F., Hofzumahaus, A., Brauers, T., Häseler, R., Bohn, B., Broch, S., Fuchs, H., Gomm, S., Holland, F., Jäger, J., Kaiser, J., Keutsch, F. N., Lohse, I., Lu, K., Tillmann, R., Wegener, R., Wolfe, G. M., Mentel, T. F., Kiendler-Scharr, A., and Wahner, A.: Missing Gas-Phase Source of HONO Inferred from Zeppelin Measurements in the Troposphere, Science, 344, 292–296, https://doi.org/10.1126/science.1248999, 2014.

Lindinger, W., Hansel, A., and Jordan, A.: On-line monitoring of volatile organic compounds at pptv levels by means of proton-transfer-reaction mass spectrometry (PTR-MS) – Medical applications, food control and environmental research, Int. J. Mass Spectrom., 173, 191–241, https://doi.org/10.1016/S0168-1176(97)00281-4, 1998.

Lockhart, J., Blitz, M., Heard, D., Seakins, P., and Shannon, R.: Kinetic Study of the OH + Glyoxal Reaction: Experimental Evidence and Quantification of Direct OH Recycling, J. Phys. Chem. A, 117, 11027–11037, https://doi.org/10.1021/jp4076806, 2013.

Lou, S., Holland, F., Rohrer, F., Lu, K., Bohn, B., Brauers, T., Chang, C. C., Fuchs, H., Häseler, R., Kita, K., Kondo, Y., Li, X., Shao, M., Zeng, L., Wahner, A., Zhang, Y., Wang, W., and Hofzumahaus, A.: Atmospheric OH reactivities in the Pearl River Delta – China in summer 2006: measurement and model results, Atmos. Chem. Phys., 10, 11243–11260, https://doi.org/10.5194/acp-10-11243-2010, 2010.

Lu, K. D., Rohrer, F., Holland, F., Fuchs, H., Bohn, B., Brauers, T., Chang, C. C., Häseler, R., Hu, M., Kita, K., Kondo, Y., Li, X., Lou, S. R., Nehr, S., Shao, M., Zeng, L. M., Wahner, A., Zhang, Y. H., and Hofzumahaus, A.: Observation and modelling of OH and HO_2 concentrations in the Pearl River Delta 2006: a missing OH source in a VOC rich atmosphere, Atmos. Chem. Phys., 12, 1541–1569, https://doi.org/10.5194/acp-12-1541-2012, 2012.

Lu, K. D., Hofzumahaus, A., Holland, F., Bohn, B., Brauers, T., Fuchs, H., Hu, M., Häseler, R., Kita, K., Kondo, Y., Li, X., Lou, S. R., Oebel, A., Shao, M., Zeng, L. M., Wahner, A., Zhu, T., Zhang, Y. H., and Rohrer, F.: Missing OH source in a suburban environment near Beijing: observed and modelled OH and HO_2 concentrations in summer 2006, Atmos. Chem. Phys., 13, 1057–1080, https://doi.org/10.5194/acp-13-1057-2013, 2013.

Mao, J., Ren, X., Zhang, L., Van Duin, D. M., Cohen, R. C., Park, J.-H., Goldstein, A. H., Paulot, F., Beaver, M. R., Crounse, J. D., Wennberg, P. O., DiGangi, J. P., Henry, S. B., Keutsch, F. N., Park, C., Schade, G. W., Wolfe, G. M., Thornton, J. A., and Brune, W. H.: Insights into hydroxyl measurements and atmospheric oxidation in a California forest, Atmos. Chem. Phys., 12, 8009–8020, https://doi.org/10.5194/acp-12-8009-2012, 2012.

Nakashima, Y., Kato, S., Greenberg, J., Harley, P., Karl, T., Turnipseed, A., Apel, E., Guenther, A., Smith, J., and Kajii, Y.: Total OH reactivity measurements in ambient air in a southern Rocky mountain ponderosa pine forest during BEACHON-SRM08 summer campaign, Atmos. Environ., 85, 1–8, https://doi.org/10.1016/j.atmosenv.2013.11.042, 2014.

Nehr, S., Bohn, B., and Wahner, A.: Prompt HO_2 Formation Following the Reaction of OH with Aromatic Compounds under Atmospheric Conditions, J. Phys. Chem. A, 116, 6015–6026, https://doi.org/10.1021/jp210946y, 2011.

Nguyen, T. L., Vereecken, L., and Peeters, J.: HO_x Regeneration in the Oxidation of Isoprene III: Theoretical Study of the key Isomerisation of the Z-δ-hydroxyperoxy Isoprene Radicals, Chem.Phys.Chem., 11, 3996–4001, https://doi.org/10.1002/cphc.201000480, 2010.

Novelli, A., Hens, K., Tatum Ernest, C., Kubistin, D., Regelin, E., Elste, T., Plass-Dülmer, C., Martinez, M., Lelieveld, J., and Harder, H.: Characterisation of an inlet pre-injector laser-induced fluorescence instrument for the measurement of atmospheric hydroxyl radicals, Atmos. Meas. Tech., 7, 3413–3430, https://doi.org/10.5194/amt-7-3413-2014, 2014.

Ortega, J., Turnipseed, A., Guenther, A. B., Karl, T. G., Day, D. A., Gochis, D., Huffman, J. A., Prenni, A. J., Levin, E. J. T., Kreidenweis, S. M., DeMott, P. J., Tobo, Y., Patton, E. G., Hodzic, A., Cui, Y. Y., Harley, P. C., Hornbrook, R. S., Apel, E. C., Monson, R. K., Eller, A. S. D., Greenberg, J. P., Barth, M. C., Campuzano-Jost, P., Palm, B. B., Jimenez, J. L., Aiken, A. C., Dubey, M. K., Geron, C., Offenberg, J., Ryan, M. G., Fornwalt, P. J., Pryor, S. C., Keutsch, F. N., DiGangi, J. P., Chan, A. W. H., Goldstein, A. H., Wolfe, G. M., Kim, S., Kaser, L., Schnitzhofer, R., Hansel, A., Cantrell, C. A., Mauldin, R. L., and Smith, J. N.: Overview of the Manitou Experimental Forest Observatory: site description and selected science results from 2008 to 2013, Atmos. Chem. Phys., 14, 6345–6367, https://doi.org/10.5194/acp-14-6345-2014, 2014.

Peeters, J. and Müller, J.-F.: HO_x radical regeneration in isoprene oxidation via peroxy radical isomerisations. II: experimental evidence and global impact, Phys. Chem. Chem. Phys, 12, 14227–14235, https://doi.org/10.1039/c0cp00811g, 2010.

Peeters, J. and Nguyen, T. L.: Unusually Fast 1,6-H Shifts of Enolic Hydrogens in Peroxy Radicals: Formation of the First-Generation C2 and C3 Carbonyls in the Oxi-

dation of Isoprene, J. Phys. Chem. A, 116, 6134–6141, https://doi.org/10.1021/jp211447q, 2012.

Peeters, J., Nguyen, T. L., and Vereecken, L.: HO_x radical regeneration in the oxidation of isoprene, Phys. Chem. Chem. Phys, 11, 5935–5939, https://doi.org/10.1039/b908511d, 2009.

Peeters, J., Müller, J.-F., Stavrakou, T., and Nguyen, V. S.: Hydroxyl Radical Recycling in Isoprene Oxidation Driven by Hydrogen Bonding and Hydrogen Tunneling: The Upgraded LIM1 Mechanism, J. Phys. Chem. A, 118, 8625–8643, https://doi.org/10.1021/jp5033146, 2014.

Poppe, D., Brauers, T., Dorn, H.-P., Karl, M., Mentel, T., Schlosser, E., Tillmann, R., Wegener, R., and Wahner, A.: OH-initiated degradation of several hydrocarbons in the atmosphere simulation chamber SAPHIR, J. Atmos. Chem., 57, 203–214, https://doi.org/10.1007/s10874-007-9065-y, 2007.

Praske, E., Crounse, J. D., Bates, K. H., Kurtén, T., Kjaergaard, H. G., and Wennberg, P. O.: Atmospheric Fate of Methyl Vinyl Ketone: Peroxy Radical Reactions with NO and HO_2, J. Phys. Chem. A, 119, 4562–4572, https://doi.org/10.1021/jp5107058, 2015.

Rickly, P. and Stevens, P. S.: Measurements of a potential interference with laser-induced fluorescence measurements of ambient OH from the ozonolysis of biogenic alkenes, Atmos. Meas. Tech., 11, 1–16, https://doi.org/10.5194/amt-11-1-2018, 2018.

Ridley, B. A., Grahek, F. E., and Walega, J. G.: A Small, High-Sensitivity, Medium-Response Ozone Detector Suitable for Measurements from Light Aircraft, J. Atmos. Ocean. Tech., 9, 142–148, https://doi.org/10.1175/1520-0426(1992)009<0142:ASHSMR>2.0.CO;2, 1992.

Rohrer, F., Bohn, B., Brauers, T., Brüning, D., Johnen, F.-J., Wahner, A., and Kleffmann, J.: Characterisation of the photolytic HONO-source in the atmosphere simulation chamber SAPHIR, Atmos. Chem. Phys., 5, 2189–2201, https://doi.org/10.5194/acp-5-2189-2005, 2005.

Rohrer, F., Lu, K., Hofzumahaus, A., Bohn, B., Brauers, T., Chang, C.-C., Fuchs, H., Häseler, R., Holland, F., Hu, M., Kita, K., Kondo, Y., Li, X., Lou, S., Oebel, A., Shao, M., Zeng, L., Zhu, T., Zhang, Y., and Wahner, A.: Maximum efficiency in the hydroxyl-radical-based self-cleansing of the troposphere, Nat. Geosci., 7, 559–563, https://doi.org/10.1038/ngeo2199, 2014.

Saunders, S. M., Jenkin, M. E., Derwent, R. G., and Pilling, M. J.: Protocol for the development of the Master Chemical Mechanism, MCM v3 (Part A): tropospheric degradation of non-aromatic volatile organic compounds, Atmos. Chem. Phys., 3, 161–180, https://doi.org/10.5194/acp-3-161-2003, 2003.

Schlosser, E., Bohn, B., Brauers, T., Dorn, H.-P., Fuchs, H., Häseler, R., Hofzumahaus, A., Holland, F., Rohrer, F., Rupp, L., Siese, M., Tillmann, R., and Wahner, A.: Intercomparison of Two Hydroxyl Radical Measurement Techniques at the Atmosphere Simulation Chamber SAPHIR, J. Atmos. Chem., 56, 187–205, https://doi.org/10.1007/s10874-006-9049-3, 2007.

Schlosser, E., Brauers, T., Dorn, H.-P., Fuchs, H., Häseler, R., Hofzumahaus, A., Holland, F., Wahner, A., Kanaya, Y., Kajii, Y., Miyamoto, K., Nishida, S., Watanabe, K., Yoshino, A., Kubistin, D., Martinez, M., Rudolf, M., Harder, H., Berresheim, H., Elste, T., Plass-Dülmer, C., Stange, G., and Schurath, U.: Technical Note: Formal blind intercomparison of OH measurements: results from the international campaign HOxComp, Atmos. Chem. Phys., 9, 7923–7948, https://doi.org/10.5194/acp-9-7923-2009, 2009.

Setokuchi, O.: Trajectory calculations of OH radical- and Cl atom-initiated reaction of glyoxal: atmospheric chemistry of the HC(O)CO radical, Phys. Chem. Chem. Phys., 13, 6296–6304, https://doi.org/10.1039/C0CP01942A, 2011.

Silva, G. D., Graham, C., and Wang, Z.-F.: Unimolecular β-Hydroxyperoxy Radical Decomposition with OH Recycling in the Photochemical Oxidation of Isoprene, Environ. Sci. Technol., 44, 250–256, https://doi.org/10.1021/es900924d, 2010.

Stone, D., Evans, M. J., Edwards, P. M., Commane, R., Ingham, T., Rickard, A. R., Brookes, D. M., Hopkins, J., Leigh, R. J., Lewis, A. C., Monks, P. S., Oram, D., Reeves, C. E., Stewart, D., and Heard, D. E.: Isoprene oxidation mechanisms: measurements and modelling of OH and HO_2 over a South-East Asian tropical rainforest during the OP3 field campaign, Atmos. Chem. Phys., 11, 6749–6771, https://doi.org/10.5194/acp-11-6749-2011, 2011.

Tan, D., Faloona, I., Simpas, J. B., Brune, W., Shepson, P. B., Couch, T. L., Sumner, A. L., Carroll, M. A., Thornberry, T., Apel, E., Riemer, D., and Stockwell, W.: HO_x budgets in a deciduous forest: Results from the PROPHET summer 1998 campaign, J. Geophys. Res., 106, 24407–24427, https://doi.org/10.1029/2001jd900016, 2001.

Tan, Z., Fuchs, H., Lu, K., Hofzumahaus, A., Bohn, B., Broch, S., Dong, H., Gomm, S., Häseler, R., He, L., Holland, F., Li, X., Liu, Y., Lu, S., Rohrer, F., Shao, M., Wang, B., Wang, M., Wu, Y., Zeng, L., Zhang, Y., Wahner, A., and Zhang, Y.: Radical chemistry at a rural site (Wangdu) in the North China Plain: observation and model calculations of OH, HO_2 and RO_2 radicals, Atmos. Chem. Phys., 17, 663–690, https://doi.org/10.5194/acp-17-663-2017, 2017.

Wegener, R., Brauers, T., Koppmann, R., Rodríguez Bares, S., Rohrer, F., Tillmann, R., Wahner, A., Hansel, A., and Wisthaler, A.: Simulation chamber investigation of the reactions of ozone with short-chained alkenes, J. Geophys. Res.-Atmos., 112, D13301, https://doi.org/10.1029/2006JD007531, 2007.

Whalley, L. K., Edwards, P. M., Furneaux, K. L., Goddard, A., Ingham, T., Evans, M. J., Stone, D., Hopkins, J. R., Jones, C. E., Karunaharan, A., Lee, J. D., Lewis, A. C., Monks, P. S., Moller, S. J., and Heard, D. E.: Quantifying the magnitude of a missing hydroxyl radical source in a tropical rainforest, Atmos. Chem. Phys., 11, 7223–7233, https://doi.org/10.5194/acp-11-7223-2011, 2011.

Whalley, L. K., Blitz, M. A., Desservettaz, M., Seakins, P. W., and Heard, D. E.: Reporting the sensitivity of laser-induced fluorescence instruments used for HO_2 detection to an interference from RO_2 radicals and introducing a novel approach that enables HO_2 and certain RO_2 types to be selectively measured, Atmos. Meas. Tech., 6, 3425–3440, https://doi.org/10.5194/amt-6-3425-2013, 2013.

Wolfe, G. M., Thornton, J. A., Bouvier-Brown, N. C., Goldstein, A. H., Park, J.-H., McKay, M., Matross, D. M., Mao, J., Brune, W. H., LaFranchi, B. W., Browne, E. C., Min, K.-E., Wooldridge, P. J., Cohen, R. C., Crounse, J. D., Faloona, I. C., Gilman, J. B., Kuster, W. C., de Gouw, J. A., Huisman, A., and Keutsch, F. N.: The Chemistry of Atmosphere-Forest Exchange (CAFE) Model – Part 2: Application to BEARPEX-2007 observations, Atmos. Chem. Phys., 11, 1269–1294, https://doi.org/10.5194/acp-11-1269-2011, 2011a.

Wolfe, G. M., Thornton, J. A., McKay, M., and Goldstein, A. H.: Forest-atmosphere exchange of ozone: sensitivity to very reactive biogenic VOC emissions and implications for in-canopy photochemistry, Atmos. Chem. Phys., 11, 7875–7891, https://doi.org/10.5194/acp-11-7875-2011, 2011b.

Wolfe, G. M., Cantrell, C., Kim, S., Mauldin III, R. L., Karl, T., Harley, P., Turnipseed, A., Zheng, W., Flocke, F., Apel, E. C., Hornbrook, R. S., Hall, S. R., Ullmann, K., Henry, S. B., DiGangi, J. P., Boyle, E. S., Kaser, L., Schnitzhofer, R., Hansel, A., Graus, M., Nakashima, Y., Kajii, Y., Guenther, A., and Keutsch, F. N.: Missing peroxy radical sources within a summertime ponderosa pine forest, Atmos. Chem. Phys., 14, 4715–4732, https://doi.org/10.5194/acp-14-4715-2014, 2014.

4 Photooxidation of α-pinene

The content of this chapter was published as “Investigation of the α-pinene photooxidation by OH in the atmospheric simulation chamber SAPHIR” by M. Rolletter, M. Kaminski, I. H. Acir, B. Bohn, H. P. Dorn, X. Li, A. Lutz, S. Nehr, F. Rohrer, R. Tillmann, R. Wegener, A. Hofzumahaus, A. Kiendler-Scharr, A. Wahner, and H. Fuchs, in Atmospheric Chemistry and Physics, 19, 11635-11649, DOI: 10.5194/acp-19-11635-2019, 2019, under Creative Commons Attribution 4.0 License. The supplementary material is provided in Appendix A.2.

Atmos. Chem. Phys., 19, 11635–11649, 2019
https://doi.org/10.5194/acp-19-11635-2019

Atmospheric Chemistry and Physics
Open Access
EGU

Investigation of the α-pinene photooxidation by OH in the atmospheric simulation chamber SAPHIR

Michael Rolletter[1], Martin Kaminski[1,a], Ismail-Hakki Acir[1,b], Birger Bohn[1], Hans-Peter Dorn[1], Xin Li[1,c], Anna Lutz[2], Sascha Nehr[1,d], Franz Rohrer[1], Ralf Tillmann[1], Robert Wegener[1], Andreas Hofzumahaus[1], Astrid Kiendler-Scharr[1], Andreas Wahner[1], and Hendrik Fuchs[1]

[1]Institute of Energy and Climate Research, IEK-8: Troposphere, Forschungszentrum Jülich GmbH, Jülich, Germany
[2]Department of Chemistry and Molecular Biology, University of Gothenburg, Gothenburg, Sweden
[a]now at: Federal Office of Consumer Protection and Food Safety, Department 5: Method Standardisation, Reference Laboratories, Resistance to Antibiotics, Berlin, Germany
[b]now at: Institute of Nutrition and Food Sciences, Food Chemistry, University of Bonn, Bonn, Germany
[c]now at: State Key Joint Laboratory of Environmental Simulation and Pollution Control, College of Environmental Sciences and Engineering, Peking University, Beijing, China
[d]now at: European University of Applied Sciences, Brühl, Germany

Correspondence: Hendrik Fuchs (h.fuchs@fz-juelich.de)

Received: 24 May 2019 – Discussion started: 4 June 2019
Revised: 13 August 2019 – Accepted: 19 August 2019 – Published: 17 September 2019

Abstract. The photooxidation of the most abundant monoterpene, α-pinene, by the hydroxyl radical (OH) was investigated at atmospheric concentrations in the atmospheric simulation chamber SAPHIR. Concentrations of nitric oxide (NO) were below 120 pptv. Yields of organic oxidation products are determined from measured time series giving values of 0.11 ± 0.05, 0.19 ± 0.06, and 0.05 ± 0.03 for formaldehyde, acetone, and pinonaldehyde, respectively. The pinonaldehyde yield is at the low side of yields measured in previous laboratory studies, ranging from 0.06 to 0.87. These studies were mostly performed at reactant concentrations much higher than observed in the atmosphere. Time series of measured radical and trace-gas concentrations are compared to results from model calculations applying the Master Chemical Mechanism (MCM) 3.3.1. The model predicts pinonaldehyde mixing ratios that are at least a factor of 4 higher than measured values. At the same time, modeled hydroxyl and hydroperoxy (HO_2) radical concentrations are approximately 25 % lower than measured values. Vereecken et al. (2007) suggested a shift of the initial organic peroxy radical (RO_2) distribution towards RO_2 species that do not yield pinonaldehyde but produce other organic products. Implementing these modifications reduces the model–measurement gap of pinonaldehyde by 20 % and also improves the agreement in modeled and measured radical concentrations by 10 %. However, the chemical oxidation mechanism needs further adjustment to explain observed radical and pinonaldehyde concentrations. This could be achieved by adjusting the initial RO_2 distribution, but could also be done by implementing alternative reaction channels of RO_2 species that currently lead to the formation of pinonaldehyde in the model.

1 Introduction

Approximately 1000 Tg of carbon from biogenic volatile organic compounds (BVOCs) is emitted every year into the atmosphere (Guenther et al., 2012). The majority of these compounds is isoprene (53 %) followed by monoterpene species (16 %). Within the group of monoterpenes α-pinene is the most abundant species with a contribution of 6.6 % to the global emission of BVOCs. During daytime, the prevalent sinks of these compounds are ozonolysis reactions and the reaction with photochemically formed hydroxyl radicals (OH) (Calogirou et al., 1999; Atkinson and Arey, 2003) producing organic peroxy radicals (RO_2). OH is reformed in a radical reaction chain that involves reactions with nitric oxide (NO), thereby producing NO_2. This radical reaction cycle

Published by Copernicus Publications on behalf of the European Geosciences Union.

impacts air quality because (1) the subsequent photolysis of NO_2 is the only chemical source for tropospheric ozone (O_3) and (2) oxygenated volatile organic compounds (OVOCs) are formed, which can be precursors for the formation of secondary organic aerosols (SOAs) (Glasius and Goldstein, 2016).

Field studies conducted in forested environments, which were characterized by large BVOC emissions and low NO concentrations, showed large discrepancies between measured OH radical concentrations and predictions of model calculations (e.g., Lelieveld et al., 2008; Hofzumahaus et al., 2009; Whalley et al., 2011). Under these conditions, it is expected that radical recycling is suppressed due to the dominance of radical termination reactions such as the reaction of RO_2 with hydroperoxy radicals (HO_2). Recent theoretical and laboratory studies of the chemistry of isoprene, which was often an important OH reactant in these field experiments, however, revealed that unimolecular RO_2 reactions that efficiently reform OH can compete with the reaction of RO_2 and NO for these conditions (Peeters et al., 2009, 2014; Crounse et al., 2011, 2012; Fuchs et al., 2013, 2014).

In contrast to isoprene, radical recycling in the chemistry of monoterpenes is less well investigated for conditions where field measurements indicate missing OH productions. Compared to isoprene, the degradation chemistry of monoterpene species is more complicated due to their more complex structure leading to a higher number of possible reactions and products. Laboratory and theoretical studies of the OH oxidation of α- and β-pinene focused on product yields and experiments were often performed at high reactant concentrations (see for example Vereecken et al., 2007; Vereecken and Peeters, 2012; Eddingsaas et al., 2012). The main products of the α-pinene + OH photooxidation are pinonaldehyde, acetone, and formaldehyde (HCHO). Product yields determined in previous laboratory studies were highly variable. For example, pinonaldehyde yields ranged from 6 % to 87 % (Larsen et al., 2001; Noziére et al., 1999).

In two field studies in environments in which monoterpenes and 2-methyl-3-buten-2-ol (MBO) were the most important biogenic organic compounds (Kim et al., 2013; Hens et al., 2014) missing OH production in model calculations was found. In addition, HO_2 concentrations were underestimated. If the model was constrained to measured HO_2, model–measurement discrepancies in OH became small due to the enhanced OH production in the reaction of HO_2 with NO. This indicated that the chemical system of monoterpenes as currently implemented in models lacks an HO_2 source. A chamber study investigating the OH oxidation of β-pinene gave similar results (Kaminski et al., 2017). Another chamber study looking at the OH oxidation of MBO showed that OH recycling in the MBO chemistry is well understood, indicating that monoterpenes are responsible for the missing HO_2 in the field campaigns (Novelli et al., 2018).

In this study, the photooxidation of α-pinene by OH was investigated in experiments in the atmospheric simulation chamber SAPHIR (Simulation of Atmospheric PHotochemistry In a large Reaction chamber) at Forschungszentrum Jülich. Experiments were performed under controlled and atmospherically relevant conditions found in forested environments with NO mixing ratios less than 120 pptv. Aerosol formation did not play a role in these experiments because no significant nucleation was observed. Measured time series were compared to model results from the Master Chemical Mechanism in the recent version 3.3.1 (MCM, 2019; Jenkin et al., 1997; Saunders et al., 2003). The impact of modifications in the chemical degradation mechanism suggested in a theoretical work by Vereecken et al. (2007) was tested. This includes the formation of new products and the change of branching ratios compared to the MCM.

1.1 Degradation mechanism for α-pinene

A simplified scheme giving the reactions most relevant in the experiments here is shown in Fig. 1. The α-pinene oxidation is initiated by the OH attack. As implemented in the MCM, OH adds to the carbon–carbon double bond of α-pinene, forming three different RO_2 radicals, APINAO2, APINBO2, and APINCO2 (names and yields taken from the MCM).

$$\alpha\text{-pinene} + \text{OH} \rightarrow \text{APINAO2} \quad \text{(yield: 0.57)} \tag{R1}$$

$$\alpha\text{-pinene} + \text{OH} \rightarrow \text{APINBO2} \quad \text{(yield: 0.35)} \tag{R2}$$

$$\alpha\text{-pinene} + \text{OH} \rightarrow \text{APINCO2} \quad \text{(yield: 0.08)} \tag{R3}$$

According to the MCM, APINAO2 and APINBO2 are the mainly produced radicals of the reaction of α-pinene with OH with a contribution of 92 %, while APINCO2 makes only a minor contribution of 8 %. Hydrogen abstraction by OH is not considered in the MCM. Consecutive reactions of the organic peroxy radicals with NO form alkoxy radicals, mostly APINAO and APINBO, which undergo a fast ring-opening and subsequent O_2 reaction yielding pinonaldehyde and HO_2. This gives an overall pinonaldehyde yield of 84 % for these reaction pathways in the MCM under conditions of high NO. In contrast, the subsequent reaction of APINCO does not form pinonaldehyde, but product species include acetone and HCHO. Acetone and HCHO are also formed in the subsequent oxidation of pinonaldehyde, which is significant on the timescale of our experiments. Additional reactions of peroxy radicals forming nitrates and reactions with HO_2 are not shown.

Vereecken et al. (2007) investigated the reaction of α-pinene with OH using quantum-chemical calculations proposing modifications of branching ratios and additional reaction pathways. Firstly, three additional minor reaction channels of the attack of OH on α-pinene leading to an H abstraction are included. The total yield was calculated to be 12 %. These new pathways lead mainly to an increase in formaldehyde and also in acetone compared to the MCM. In contrast, less pinonaldehyde is formed. Secondly, the branching ratios of the other RO_2 species were revised. The addition of OH to the double bond was calculated to result in the

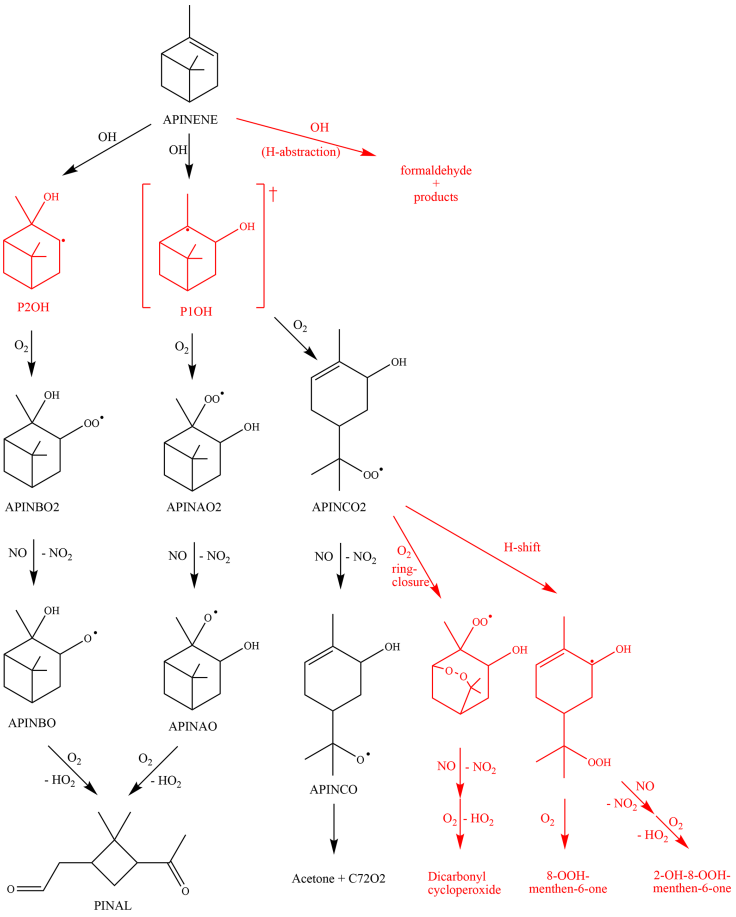

Figure 1. Simplified reaction of α-pinene as described in the MCM and modifications suggested by Vereecken et al. (2007) (shown in red). The hydrogen abstraction consists of three different pathways with a total contribution of 12 %. The ring-closure and H-shift reactions in the Vereecken mechanism outrun the formation of APINCO and therefore no acetone is directly formed in contrast to the MCM. RO_2 reactions with NO forming nitrate species are not shown. See text for details. The names are taken from the MCM (black) and according to Vereecken et al. (2007) (red).

OH attachment on both sites of attack, forming the adducts P1OH and P2OH with similar probability. P2OH further reacts with oxygen and forms the RO_2 radical APINBO2. Consequently, the APINBO2 yield is increased to 44 % compared to 35 % in the MCM. The tertiary radical P1OH is chemically activated. It is either thermally stabilized forming the RO_2 radical APINAO2 after the O_2 addition or it undergoes a prompt ring-opening of the four member rings resulting in the RO_2 species APINCO2. The overall yield of APINAO2 and APINCO2 is 22 % each, suggested by Vereecken et al. (2007), compared to 57 % for APINAO2 and 7.5 % for APINCO2 assumed in the MCM. In addition,

Vereecken et al. (2007) calculated that a 1,6-H-shift reaction and a ring-closure reaction of APINCO2 leading to 8-OOH-menthen-6-one, 2-OH-8-ooh-menthen-6-one, and a dicarbonyl cycloperoxide can compete with its reaction with NO. For conditions of the experiments of this work the dominant pathways are both unimolecular reactions, which are faster than the reaction with NO by a factor of at least 100. As a consequence, no acetone is directly formed in this pathway in contrast to the MCM.

Because the formation of APINCO2 does not produce pinonaldehyde in the subsequent chemistry in contrast to APINAO2 and APINBO2, the shift in the RO_2 distribution in the mechanism by Vereecken et al. (2007) leads to an overall pinonaldehyde yield of 60 % compared to 84 % in the MCM.

2 Methods

2.1 Experiments in the simulation chamber SAPHIR

The experiments in this study were performed in the outdoor atmospheric simulation chamber SAPHIR at Forschungszentrum Jülich, Germany. The chamber has been described in detail before (e.g., Rohrer et al., 2005). The cylindrically shaped chamber (length 18 m, diameter 5 m, volume 270 m^3) is made of a double-wall Teflon (FEP) film, which provides a high transmittance for the entire spectrum of solar radiation. A slight overpressure (30 Pa) in the chamber ensures that no air from the outside penetrates the chamber. A small flow of synthetic air that replaces the air sampled by the instruments and maintains the overpressure leads to a dilution of trace gases of approximately 4 % per hour. The synthetic air used for experiments is mixed from evaporated ultrapure liquid nitrogen and oxygen (Linde, purity $\geq$ 99.99990 %). Two fans inside the chamber are operated to ensure a rapid mixing of trace gases. A shutter system can keep the chamber dark, for example at the beginning of an experiment, and is opened to expose the chamber air to natural sunlight to perform photooxidation experiments. Small amounts of nitric acid (HONO), formaldehyde, and acetone are photolytically formed on the Teflon surface with source strengths of 100 to 200 pptv per hour when the chamber is illuminated by solar radiation (Rohrer et al., 2005). The primary source for OH radicals is the photolysis of HONO emitted by the chamber, also leading to a continuous increase in NO_x ($= NO_2 + NO$) in the experiment.

Two experiments were performed at similar conditions for this work: on 30 August 2012 at NO mixing ratios of less than 100 pptv and on 2 July 2014 at NO mixing ratios of less than 120 pptv. Before the experiments, the chamber was flushed with synthetic air until the concentrations of trace gases from previous experiments were below the detection limits of the instruments. The chamber air was humidified by flushing water vapor from boiling Milli-Q® water into the chamber together with a high flow of synthetic air. The relative humidity was approximately 70 % at the beginning of the experiments and decreased mainly due to the increase in the temperature during the day to approximately 20 % in the end of an experiment. A total of 40 ppbv ozone produced by a discharge ozonizer (O3Onia) was injected to simulate conditions typical for forested areas before the chamber roof was opened. In the first 2 h, the zero-air phase, no other reactive species were added, in order to quantify the small chamber sources for HONO, HCHO, acetone, and the background OH reactivity. Afterwards, α-pinene was injected from a high-concentration gas mixture of α-pinene in O_2 prepared in a SilcoNert-coated stainless steel canister (Restek) three times with time intervals of approximately 2 h. The time between the injections allowed us to study the photochemical degradation. The maximum α-pinene concentrations were 3.8 ppbv. After the initial phase, the OH reactivity was dominated by the injected α-pinene and its oxidation products, so that the background reactivity becomes secondary.

The additional loss of trace gases on the chamber surface is assumed to be negligible on the timescale of the experiment. The loss of α-pinene and pinonaldehyde, one of the oxidation products of α-pinene, was experimentally tested by injecting α-pinene and pinonaldehyde, respectively, into the clean chamber in the dark. The observed loss of these VOCs was consistent with the dilution due to the replenishment flow, demonstrating that there was no significant loss of α-pinene and pinonaldehyde on the Teflon film of the chamber.

2.2 Instrumentation

The set of instruments used in this work is listed in Table 1 giving the 1σ accuracies and precisions.

OH was measured by laser-induced fluorescence (LIF) exciting OH at 308 nm (Holland et al., 1995; Fuchs et al., 2011). Previous studies reported interferences in the OH detection by LIF for some instruments (Mao et al., 2012; Novelli et al., 2014). A laboratory study investigating potential interferences from alkene ozonolysis reactions with the LIF instrument at SAPHIR (Fuchs et al., 2016) gave no hint for significant interferences for atmospherically relevant conditions. Only for exceptionally high, non-atmospheric reactant concentrations of ozone (300–900 ppbv) and some alkenes (1–450 ppbv) could interferences be observed. Hence, no interferences are expected for conditions of the experiments in this work. In addition, OH was detected by differential optical absorption spectroscopy (DOAS; Dorn et al., 1995). OH concentration measurements of both instruments agreed on average within 15 %. A similarly good agreement between both instruments has been found in previous studies (e.g., Schlosser et al., 2009; Fuchs et al., 2012).

The LIF instrument also measured the HO_2 concentrations in a second fluorescence cell, in which HO_2 is chemically converted to OH in a reaction with added NO. Fuchs et al. (2011) reported that this detection scheme can be affected by

interferences from organic peroxy radicals (RO_2) that also react with NO and rapidly form HO_2. Consequently, in the experiments of this work, the NO concentrations were reduced to suppress the conversion of RO_2 as described in Fuchs et al. (2011) so that interferences become unimportant.

OH reactivity (k_{OH}), the inverse lifetime of OH, was measured with a pump-probe instrument (Lou et al., 2010; Fuchs et al., 2017). High OH concentrations are generated in a flow tube by laser flash photolysis of ozone in the presence of water and the decay of OH caused by ambient OH reactants is measured by LIF at the end of the flow-tube. The pseudo-first-order decay rate constant fitted to the time-resolved OH measurements gives the total OH reactivity. Unfortunately, OH reactivity could only be measured in the experiment conducted in 2012 because the instrument failed in the experiment in 2014.

α-pinene and oxygenated organic compounds expected to be formed in the α-pinene oxidation, acetone and pinonaldehyde, were detected by a proton-transfer-reaction time-of-flight mass spectrometer (PTR-TOF-MS; Lindinger et al., 1998; Jordan et al., 2009). However, only for one of the experiments (2 July, 2014) was the PTR-TOF-MS calibrated to quantify pinonaldehyde. In addition, a gas chromatograph with a flame ionization detector (GC–FID) was used for the measurements of α-pinene and acetone. VOC concentrations measured by a GC–FID were on average 25 % lower than those measured by a PTR-TOF-MS for the experiment conducted in 2012 and 15 % lower for the experiment in 2014. This discrepancy needs to be taken into account as additional uncertainty. Formaldehyde that is also expected to be produced in the oxidation of α-pinene was measured by a Hantzsch monitor and by differential optical absorption spectroscopy. The measured concentrations agreed on average within 6 %.

CO and water vapor mixing ratios were monitored with a cavity ring-down instrument (Picarro), NO and NO_2 using a chemiluminescence instrument (Eco Physics), and O_3 with an UV absorption instrument (Ansyco). Photolysis frequencies were calculated from solar actinic flux densities measured by a spectroradiometer (Bohn et al., 2005; Bohn and Zilken, 2005).

2.3 Model calculations

The time series of trace-gas compounds and radicals were calculated by a zero-dimensional box model applying the chemistry of the Master Chemical Mechanism in the recent version 3.3.1.

The MCM was extended by chamber-specific processes like dilution and small sources of HONO, formaldehyde, acetaldehyde, and acetone that are present in the sunlit chamber (Rohrer et al., 2005). The chamber sources were implemented as continuous sources that are parameterized by temperature, relative humidity, and radiation as described by Rohrer et al. (2005). This function was scaled for each experiment, such that the observed acetone and HCHO time series were matched during the zero air phase when no chemical production was expected. It was assumed that the scaling factors remained constant over the course of one experiment.

The dilution rate was calculated from the monitored replenishment flow rate. NO, NO_2, HONO, water vapor mixing ratio, temperature, and pressure were constrained to measurements. While photolysis frequencies for NO_2, HONO, O_3, and pinonaldehyde were calculated from actinic flux measurement, all other photolysis frequencies were calculated for clear-sky conditions as parameterized in MCM 3.3.1 but scaled by the ratio of measured to calculated $j(NO_2)$ to account for cloud coverage and chamber effects. The pinonaldehyde photolysis frequency was calculated, based on the measured absorption cross sections of pinonaldehyde by Hallquist et al. (1997) and a quantum yield of 1. These photolysis frequencies are greater by a factor of 3.5 compared to the parameterization in the MCM.

Modeled parameters were calculated on a 1 min time base. α-pinene and O_3 injections were introduced as sources only present at the time of injection. The O_3 source strengths were adjusted to match measurements at the time of the injection. Similarly, the α-pinene source was adjusted to the increase in the OH reactivity. For the experiment where no k_{OH} measurements were available, the increased α-pinene concentrations measured by a PTR-TOF-MS were used instead.

Sensitivity studies (M1) were performed applying modifications of the MCM based on a theoretical study by Vereecken et al. (2007). An overview of the model modifications applied to the MCM is given in Tables S2 and S3 in the Supplement. The mechanism based on Vereecken et al. (2007) differs from the MCM in new pathways, branching ratios, and product yields. RO_2 radicals formed from the reactions of this modified mechanism are assumed to react similar to other RO_2 species with NO, HO_2, and other RO_2 species. Additional first-generation oxygenated organic compounds are formed that are not part of the MCM. In the model run denoted M1, no further reactions of these products were implemented.

Branching ratios of the initial OH + α-pinene reaction were further adjusted in model run M2 to better match observations. An overview of the simplified reaction scheme indicating the differences between the model runs is shown in Table 3.

3 Results and discussion

3.1 Product yields

The fate of the RO_2 and therefore also product yields depends on the NO concentration. At low NO levels, the reaction of RO_2 with HO_2 and RO_2 recombination reactions can compete with the reaction of RO_2 with NO. For NO mixing ratios of up to 120 ppt in the experiment on 2 July 2014,

approximately 70 % of the RO_2 radicals reacted with NO and 30 % with HO_2, while RO_2 self-reactions were not significant. Product species quantified in the experiments were mainly formed in the reaction of RO_2 with NO. In contrast, the reaction of RO_2 with HO_2 terminated the radical chain reactions and forms hydroperoxide species (ROOH) that were not detected.

Product yields were calculated from measured product concentrations in relation to the α-pinene that reacted with OH. The α-pinene and pinonaldehyde concentrations were determined by a PTR-TOF-MS. Acetone concentrations were derived from interpolated GC–FID data to exclude possible interferences on the quantifier ion of acetone in the PTR-TOF-MS. Because products were further oxidized in the experiment or partly had sources not related to the α-pinene chemistry, a correction was applied. The correction procedure used here follows the description in Galloway et al. (2011) and Kaminski et al. (2017). The α-pinene reacted away was corrected for dilution and its reaction with O_3. Ozonolysis accounted for approximately 25 % of the loss of α-pinene. Product concentrations were corrected for their loss from photolysis, from their reaction with OH, and from dilution. In addition, their production from the chamber sources and from the α-pinene ozonolysis was subtracted from the measured concentrations. Acetone and HCHO chamber source strengths were determined in the initial phase of each experiment when the chamber air was already exposed to sunlight, but before the injection of α-pinene. The production rates were 0.04 and between 0.11 and 0.27 ppbv h^{-1} for acetone and formaldehyde, respectively. For acetone the chamber source contributed only 10 % to the overall formed acetone. In contrast, up to 60 % of the total measured HCHO was formed on the chamber walls, which could lead to an additional bias of the determined yield. A detailed description of the corrections is given in the Supplement. Yields and reaction rate constants used for the correction were taken from recommendations in Atkinson et al. (2006) also used in the MCM.

Figure 2 shows the relation between the consumed α-pinene and product concentrations. The product yields were determined from the slopes of the relation resulting in yields for pinonaldehyde of (5 ± 3) %, for acetone of (19 ± 6) %, and for formaldehyde of (11 ± 5) %. The uncertainty for the pinonaldehyde yield is 1σ derived from measurements and errors of the applied correction in one experiment in 2014, when pinonaldehyde was quantified. The stated acetone and HCHO yields are the combined result from both experiments in 2012 and 2014 and the error gives the range of values derived in the two experiments. The relationships between consumed α-pinene and acetone and formaldehyde are not exactly linear because both are not only directly formed in the reaction of α-pinene with OH, but also from the subsequent oxidation of products such as pinonaldehyde. Therefore, acetone and formaldehyde yields increase over the course of the experiment. The slope at the early stage of the experiment, when only a little α-pinene reacted away, best reflects their formation yield directly from the α-pinene + OH reaction, whereas the slope at later times gives the overall yield of the α-pinene degradation. The nonlinear behavior is most strongly pronounced for formaldehyde, for which the yield increased from 5 % to 20 % over the course of the experiment.

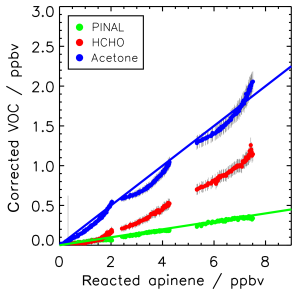

Figure 2. Yield of pinonaldehyde, acetone, and formaldehyde determined from the slope of the relation between consumed α-pinene and measured oxidation product concentrations for the experiment on 2 July 2014. Organic oxidation product concentrations are corrected for losses and production not related to the α-pinene + OH reaction (see text for details). Colored lines give the results of a linear regression. The HCHO yield is determined from the initial slope but increases at later times of the experiments as indicated by the increasing slope of the relationship.

Results of this work are compared to results from previous studies in Table 2. Yields of pinonaldehyde that were detected by various instruments in previous studies were highly variable ranging from 6 % to 87 %. High yields of 37 %–87 % are reported in the studies by Hatakeyama et al. (1991) and Noziére et al. (1999), in which Fourier-transform infrared spectroscopy (FT-IR) was applied. Larsen et al. (2001) found a pinonaldehyde yield of 6 % also measured using FT-IR. FT-IR measurements may suffer from interferences from other carbonyl compounds, which could have led to overestimated yields (Eddingsaas et al., 2012). Studies measuring pinonaldehyde with a GC–FID (Arey et al., 1990; Hakola et al., 1994; Jaoui and Kamens, 2001; Aschmann et al., 2002; Lee et al., 2006) and PTR-MS (Lee et al., 2006; Wisthaler et al., 2001) gave similar yields that are in the range of 28 % to 34 %.

Except for some experiments performed in the absence of NO, experiments in previous studies were carried out under conditions when RO_2 reacted mainly with NO.

In a recent study by Isaacman-VanWertz et al. (2018), the carbon budget was analyzed during the photooxidation of α-pinene by OH making use of various mass spectrometry instruments. While the carbon budget was found to be closed

Table 1. Instrumentation for radical and trace-gas measurements.

Species	Technique	Time resolution	1σ precision	1σ accuracy
OH	DOAS[a]	205 s	0.6×10^6 cm^{-3}	6.5 %
OH	LIF[b]	47 s	0.6×10^6 cm^{-3}	13 %
HO_2	LIF[b]	47 s	1.5×10^7 cm^{-3}	16 %
k_{OH}	Laser photolysis + LIF[b]	180 s	0.3 s^{-1}	0.5 s^{-1}
NO	Chemiluminescence	180 s	4 pptv	5 %
NO_2	Chemiluminescence	180 s	2 pptv	5 %
O_3	UV absorption	10 s	1 pptv	5 %
α-pinene, pinonaldehyde, and acetone	PTR-TOF-MS[c]	40 s	15 pptv	14 %
α-pinene and acetone	GC–FID[d]	30 min	(4–8) %	5 %
HONO	LOPAP[e]	300 s	1.3 pptv	10 %
HCHO	DOAS[a]	100 s	20 %	10 %
Photolysis freq.	Spectroradiometer	60 s	10 %	10 %

[a] DOAS: differential optical absorption spectroscopy. [b] LIFL: laser-induced fluorescence. [c] PTR-TOF-MS: proton-transfer-reaction time-of-flight mass spectrometer. [d] GC–FID: gas chromatograph–flame ionization detector. [e] LOPAP: long-path-absorption photometer.

at the end of their experiment, the initial phase showed a discrepancy of up to 30 % between measured species including pinonaldehyde and α-pinene that reacted away. This indicates that a substantial fraction of products was not detected, consistent with low pinonaldehyde yields found in this and previous studies. Although no pinonaldehyde yield was reported, the yield can be estimated to be less than 20 % from figures shown in Isaacman-VanWertz et al. (2018).

The pinonaldehyde yield in the study here agrees within the stated errors with the yields reported by Larsen et al. (2001), but is lower than in all other previous studies, which used significantly higher α-pinene mixing ratios of hundreds of parts per billion by volume or even several parts per million by volume. Concentrations of this work were close to those typically found in ambient air. This appears to be the major difference between the experiments here and previous experiments.

The acetone yield in this study of 19 ± 6 % is higher by nearly a factor of 2 compared to previously reported values. The higher acetone yield corresponds to the lower pinonaldehyde yield and could therefore be a result of reaction pathways that do not lead to the formation of pinonaldehyde but forming acetone instead.

Only a few of the previous studies reported formaldehyde yields. The yield determined in this study agrees within the stated uncertainty with values in Noziére et al. (1999) (zero NO), Larsen et al. (2001), Wisthaler et al. (2001), and Lee et al. (2006), but is significantly lower than the yield in the studies by Hatakeyama et al. (1991) and Noziére et al. (1999) (high NO). Like for acetone, additional pathways not included in the mechanism could lead to HCHO formation instead of pinonaldehyde. It is also not clear if HCHO yields of the different studies are comparable because the yield increases, whether organic products are further oxidized during the experiment (Fig. 2). The studies by Hatakeyama et al. (1991) and Noziére et al. (1999) (high NO) were performed at high reactant concentrations and high NO concentrations, which accelerate the oxidation rate.

Few studies were performed in the presence of water, which can have an impact on product yields as shown for the product yields in the ozonolysis of α-pinene (Tillmann et al., 2010). A water dependence in the OH degradation mechanism of α-pinene has not been reported yet. In general, yields of products strongly depend on the fate of RO_2. Most of the studies were performed at high reactant concentrations and also in the presence of high NO concentrations. Therefore RO_2 recombination reactions might have played a larger role compared to the chamber experiment here. In addition, the fast oxidation of α-pinene led to particle formation in some of the studies, and therefore additional heterogeneous chemistry affected the results (e.g., Noziére et al., 1999). The chamber study here was performed at atmospheric reactant concentrations such that the RO_2 lifetime was approximately 0.5 min with respect to reactions with both HO_2 and NO, but was long enough that potential isomerization reactions could compete. The differences in the RO_2 fate likely explain the large variety of yields in the different studies. This demonstrates the importance of performing experiments at atmospheric levels of reactants as done in this study.

3.2 Comparison of trace-gas measurements with MCM 3.3.1 model calculations

Time series of measured species are compared to model calculations using the MCM for the experiment conducted on 2 July 2014 (Figs. 3 and 4). This experiment is discussed here in more detail because measurements of pinonaldehyde were available in contrast to the experiment in 2012. Time series for the experiment in 2012 are shown in Fig. 5.

After the first α-pinene injection, OH chemistry is dominated by reactions with α-pinene. Thereby formed pinonaldehyde is overestimated in the MCM by a factor of 4.

Table 2. Yields of pinonaldehyde, formaldehyde, and acetone for the reaction of α-pinene + OH compared to literature values. Experimental conditions and applied measurement technique for the detection of organic compounds are additionally listed.

	Yield (%)			Exp. conditions			
Reference	Pinonaldehyde	Acetone	HCHO	α-pinene (ppbv)	NO (ppbv)	Water (rH %)	Technique
Arey et al. (1990)	29	–	–	400–900	10 000	0	GC–FID
Hatakeyama et al. (1991)	56 ± 4	–	54 ± 5	950–1300	390–2300	9	FT-IR
Hakola et al. (1994)	28 ± 5	–	–	350–1000	10 000	0	GC–FID
Noziére et al. (1999)	87 ± 20	9 ± 6	23 ± 9	200–2700	4000	0	FT-IR
Jaoui and Kamens (2001)	28	–	–	940–980	430–490	18–40	Denuder, GC–MS
Larsen et al. (2001)	6 ± 2	11 ± 3	8 ± 1	1400–1600	1000	2–5	FT-IR
Aschmann et al. (2002)	28 ± 5	–	–	400–900	7000–9000	0	GC–FID
Lee et al. (2006)	30 ± 0.3	6	16	109	9	0	PTR-MS
Noziére et al. (1999)	37 ± 7	7 ± 2	8 ± 1	200–2700	NO free	0	FT-IR
Wisthaler et al. (2001)	34 ± 9	11 ± 2	8 ± 1	1000–1300	NO free	0	PTR-MS
this work	5 ± 3 [a]	19 ± 6 [b]	11 ± 5 [b]	3.8	< 0.1	30–60	PTR-TOF-MS

[a] Yield determined in the 2014 experiment. [b] Combined yield from experiments in 2012 and 2014.

Table 3. RO_2 yields for the different model runs and the resulting pinonaldehyde yields for the chamber experiments.

	Yield (%)				
Model run	APINAO2	APINBO2	APINCO2	Pinonaldehyde	
MCM	57.2	35.3	7.5	84	MCM 3.1.1
M1	22	44	22	60	Vereecken et al. (2007)
M2	0	5	83	5	adjusted to the measured pinonaldehyde yield

The pinonaldehyde concentrations increase directly after the VOC injections but start to decrease 1 h later due to its consumption by photolysis and reaction with OH. The model underestimates OH and HO_2 concentrations by approximately 25 %. Because too much pinonaldehyde is formed in the model, the OH consumption is overestimated, which can partly be the reason for the smaller OH concentrations than observed.

Three α-pinene injections with concentrations of 2–3 ppbv each were performed. The modeled α-pinene consumption is slightly slower by approximately 10 % than measured, consistent with the lower modeled OH compared to measured OH. This is also seen in a slower decrease in the modeled OH reactivity compared to measurements carried out in the experiment in 2012 (Fig. 5). The fact that OH reactivity is dominated by α-pinene specifically shortly after its injection supports that α-pinene decays are slower in the model compared to observations.

The production of acetone in the model matches the observations within the stated errors. In contrast, the formation of formaldehyde is slightly overestimated by around 10 %.

Modeled and measured O_3 concentrations start to slightly deviate in the second half of the experiment but agree over the whole experiment within the measurement uncertainty.

3.3 Sensitivity model calculations

Sensitivity model runs were performed to test if shortcomings of the MCM model results can be explained by either recent studies reported in literature or further adjustments.

Figure 3 shows in orange a sensitivity run with HO_2 and pinonaldehyde concentrations constrained to measurements. Modeled and measured OH concentrations agree within the stated uncertainty and the time behavior is reproduced in contrast to the MCM model run. This indicates that the radical budget is closed. As a result of the higher OH concentration the α-pinene is consumed faster compared to the MCM and the resulting decay reproduces the observations within the measurement uncertainty. Constraining only the HO_2 data is not sufficient because the OH loss by pinonaldehyde would be overestimated.

The application of the mechanism by Vereecken et al. (2007) reduces the pinonaldehyde yield by 24 % compared to the MCM, reducing the model–measurement discrepancy by a factor of 2 (Fig. 4). The lower pinonaldehyde yield also results in an increased OH concentration because decomposition products like acetone, which reacts more slowly with OH, are produced instead. Therefore, the OH loss rate constant is reduced compared to the results obtained with the MCM. This reduces the model–measurement discrepancy to 10 %. As discussed above, higher OH concentrations also

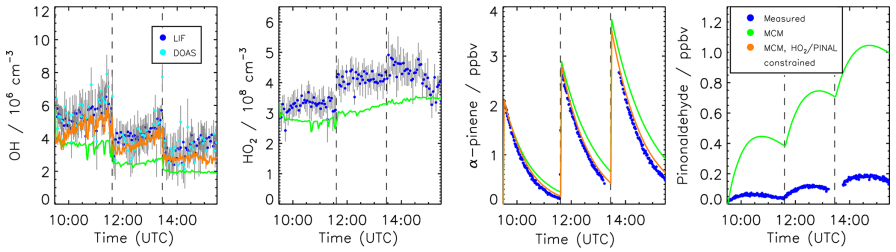

Figure 3. Time series of measured and modeled concentrations of radicals, α-pinene, and pinonaldehyde for an MCM model run with and without having HO_2 and pinonaldehyde constrained to measurements (experiment on 2 July 2014).

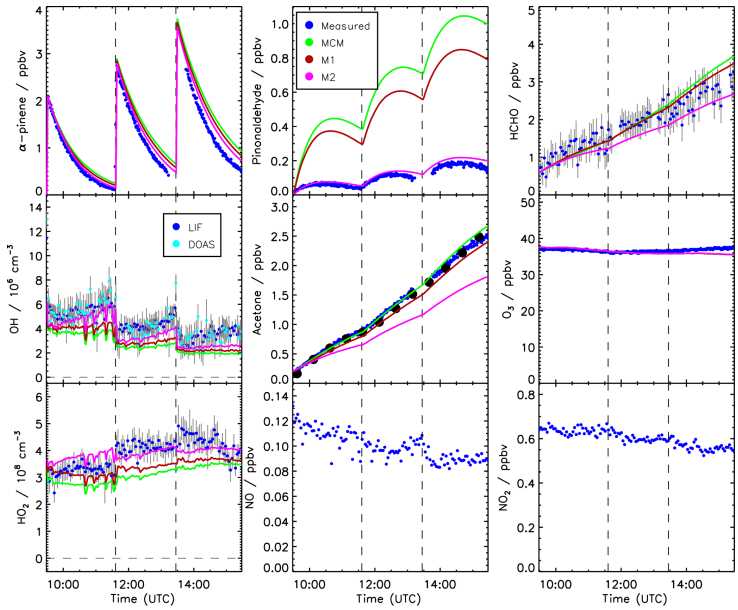

Figure 4. Time series of measured and modeled concentrations of radicals and inorganic and organic compounds during the α-pinene photooxidation at low NO (experiment on 2 July 2014).

lead to a faster consumption of the α-pinene, so that the model–measurement agreement of α-pinene is also improved to within 5 %. This is also consistent with results obtained in the experiment performed in 2012, when OH reactivity was measured. OH reactivity is approximately 20 % higher than predicted by the MCM at the end of the experiment, whereas agreement within 8 % is achieved when modifications by Vereecken et al. (2007) are applied. However, there is more uncertainty in the total OH reactivity determined from the model because reaction rate constants of the products dicarbonyl cycloperoxide, 8-OOH-menthen-6-one, and 2-OH-8-OOH-menthen-6-one that are formed instead of pinonaldehyde from the subsequent reaction of APINCO2 can only be

estimated. Here, a similar reaction rate constant like the one for pinonaldehyde is assumed.

The modifications suggested by Vereecken et al. (2007) reduce the model–measurement discrepancies for radicals, OH reactivity, α-pinene, and pinonaldehyde without changing the reasonable agreement for formaldehyde and acetone, but measured pinonaldehyde concentrations are still significantly lower than predicted by the model. Because APINCO2 is the only RO_2 species that does not form pinonaldehyde, another sensitivity study (M2) was performed for which the RO_2 distribution is adjusted, such that modeled pinonaldehyde concentrations match observations. This requires a yield of APINCO2 of 86 % making the prompt ring-opening reaction subsequent to the OH attachment to α-pinene the most important pathway. The yields for the other two RO_2 species are consequently reduced to 0 % and 5 % for APINAO2 and APINBO2, respectively. The minor reaction pathways suggested by Vereecken et al. (2007) (H abstractions) remained unchanged in this model run. A similar shift in the RO_2 distribution towards APINCO2 was proposed by Xu et al. (2019). The authors reported a branching ratio of 69 % for the initial OH addition forming P1OH and a branching ratio of 97 % for the subsequent ring-opening reaction. The resulting overall APINCO2 yield was 60 % (see Supplement).

If this model modification is applied, HO_2 radical concentrations are increased by up to 30 % giving reasonable agreement within the stated uncertainties between modeled values and measurements (Fig. 4). The increased HO_2 together with a reduced OH loss rate due to the decreased pinonaldehyde concentration result in up to 30 % higher modeled OH radical concentrations compared to M1, which agree with measurements within the measurement uncertainty. In M2, acetone and formaldehyde are now underestimated by approximately 20 % and 10 %, respectively, because the production by the photooxidation of pinonaldehyde is decreased. The underestimation of acetone and formaldehyde may be caused by the missing unknown degradation chemistry of products which are postulated in the mechanism by Vereecken et al. (2007). Vereecken et al. (2007) suggest that, for example, dicarbonyl cycloperoxide formed in the revised oxidation scheme likely produces acetone.

The change of the RO_2 yields is only one possibility to match the measured pinonaldehyde mixing ratios and does not imply that this is the correct oxidation scheme. If the initial RO_2 branching ratio suggested by Vereecken et al. (2007) is correct, then unknown reactions of APINAO2 and APINBO2 or APINAO and APINBO, which suppress the pinonaldehyde formation, could also explain the discrepancies. These unknown reactions need to be significantly faster than the currently known reactions to compete with the other reactants NO, HO_2, and RO_2.

3.4 Comparison with previous studies

The oxidation scheme of β-pinene that has a similar structure as α-pinene has previously been investigated in the SAPHIR chamber for comparable conditions (Kaminski et al., 2017) giving similar results obtained for α-pinene here. α- and β-pinene are isomers, which differ from each other by the position of the double bond. The double bond is endocylic in α-pinene and exocyclic in β-pinene. Like the assumed major oxidation product, pinonaldehyde, for α-pinene, the main oxidation product of β-pinene, nopinone, was found to be overestimated by up to a factor of 3 using the MCM model calculations in Kaminski et al. (2017). Similar to α-pinene, Vereecken and Peeters (2012) suggested a dominant ring-opening reaction after the addition of OH to the double bond of β-pinene that leads to products other than nopinone. The chamber study by Kaminski et al. (2017) confirms that the measured nopinone concentration is consistent with this mechanism. In addition, these reaction pathways can lead to a faster production of HO_2 and improve the model–measurement agreement of OH and HO_2 concentrations.

Two field campaigns in environments in which monoterpene species were the dominant reactive organic compounds showed large discrepancies between modeled and observed OH and HO_2 radical concentrations. During the Bio-hydro-atmosphere interactions of Energy, Aerosols, Carbon, H_2O, Organics, and Nitrogen-Rocky Mountain Organic Carbon Study (BEACHON-ROCS) campaign in 2010 in a forested area, the main biogenic organic compounds were 2-methyl-3-butene-2-ol (MBO) and monoterpenes with average mixing ratios of 1.6 ppbv and 0.5 ppbv, respectively. Model calculations conducted with the University of Washington Chemical Model (UWCM) underestimated HO_2 radical concentrations by up to a factor of 3 and OH concentrations could only be reproduced by the model, if HO_2 was constrained to measurements (Kim et al., 2013).

During the HUMPPA-COPEC (Hyytiälä United Measurements of Photochemistry and Particles in Air – Comprehensive Organic Precursor Emission and Concentration study) field campaign in 2010 in a boreal forest in Finland, α-pinene mixing ratios peaked around 1 ppbv. Again, the model calculations with CAABA/MECCA (Chemistry As A Boxmodel Application/Module Efficiently Calculating the Chemistry of the Atmosphere) gave similar results as reported by Kim et al. (2013) for the site in the Rocky Mountains. Modeled k_{OH} and HO_2 concentrations were both underestimated by model calculations. Hens et al. (2014) attributed this to a missing HO_2 source.

Results from both field campaigns are consistent with findings in the chamber experiments for α-pinene here and β-pinene reported by Kaminski et al. (2017). MBO was also an important OH reactant during the BEACHON-ROCS campaign, but is likely not responsible for the observed model–measurement discrepancies. A chamber experiment reported

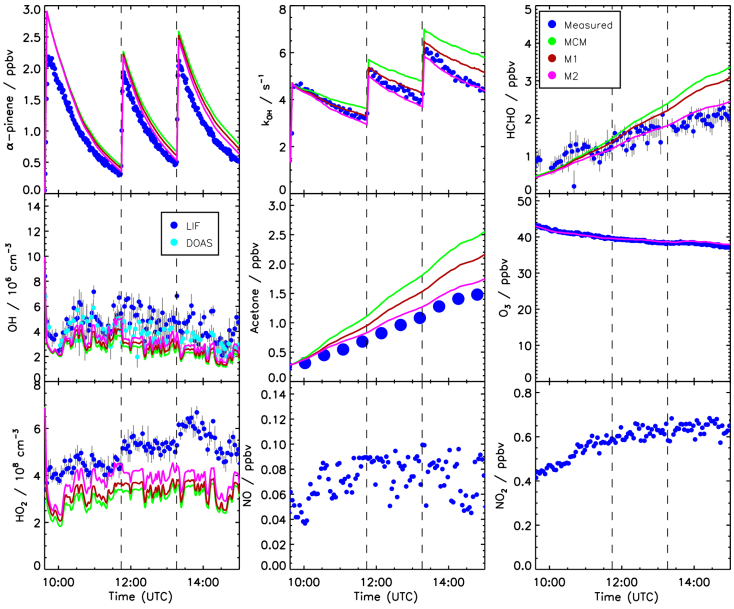

Figure 5. Time series of measured and modeled concentrations of radicals and inorganic and organic compounds during the α-pinene photooxidation at low NO (experiment on 30 August 2012).

by Novelli et al. (2018) demonstrated that the radical budget in the oxidation of MBO is well understood by current chemical models. In addition, quantum-chemical calculations by Knap et al. (2016) showed that H-shift isomerization reactions are negligible for RO_2 radicals formed in the reaction of OH with MBO.

In a recent laboratory study, Eddingsaas et al. (2012) investigated the α-pinene oxidation by OH at low NO_x conditions, when the fate of RO_2 radicals was dominated by $RO_2 + HO_2$ reactions. The authors suggest that pinonaldehyde is formed from $RO_2 + HO_2$ through an alkoxy radical channel that regenerates OH (Eddingsaas et al., 2012) and from the photooxidation and photolysis of α-pinene hydroxy hydroperoxides formed in this reaction. Pinonaldehyde yields were not measured but estimated to be around 33 % for low NO_x. These results do not contradict results here because only approximately 30 % of the RO_2 reacted with HO_2 in the chamber experiment and less hydroxy hydroperoxides are formed.

Recently Xu et al. (2019) evaluated unimolecular reaction pathways in the photooxidation of α-pinene by OH. The authors described that the hydroxy group and carbon–carbon double bond found in APINCO2 enhances the rates of unimolecular reactions. This is consistent with the faster HO_2 production observed in this work that was reproduced by the model after increasing the branching ratio of the APINCO2 formation. Xu et al. (2019) further reported that unimolecular reactions in the α-pinene degradation do not convert NO to NO_2 and therefore impact the O_3 formation. For our experiment conditions no discrepancies in the O_3 concentrations are observed.

4 Summary and conclusions

The photooxidation of α-pinene was investigated in the atmospheric simulation chamber SAPHIR. Two experiments were performed under atmospheric α-pinene concentrations ($\leq$ 3.8 ppbv) and medium NO conditions ($\leq$ 120 pptv). Measured time series were compared to model results applying the recent version of the Master Chemical Mechanism version 3.3.1.

Model calculations lead to approximately 25 % lower OH and HO_2 radical concentrations than measured. In addition, pinonaldehyde is the major organic oxidation product in the MCM (84 %), whereas the measured pinonaldehyde

yield is only (5 ± 3) % in the chamber experiment. This is in the lower range of previous pinonaldehyde yields determined in laboratory experiments which range between 6 % and 87 %. This large range might reflect the variety of conditions in the experiments. In addition, laboratory studies were often performed at high NO and α-pinene concentrations. The chamber study in this work is the first one using atmospheric conditions of reactant concentrations. Yields of acetone (0.19 ± 0.06) and formaldehyde (0.11 ± 0.05) in this study are reproduced by model calculations applying the MCM.

Reaction pathways from quantum-chemical calculations by Vereecken et al. (2007) were implemented in sensitivity model runs leading to a reduction in the model–measurement discrepancies for the radical and pinonaldehyde concentrations by approximately 10 % and 25 %, respectively. The major change is due to a shift in the branching ratio of the RO_2 distribution after the OH addition to α-pinene, favoring reaction pathways that do not lead to the production of pinonaldehyde. Further adjustments of this distribution can bring model predictions into agreement with observations, but other unknown reaction pathways that reduce the pinonaldehyde yield could also explain the observations.

A chamber study on β-pinene by Kaminski et al. (2017), supported by quantum-chemical calculations by Vereecken and Peeters (2012), reported that a similar shift in the initial RO_2 branching ratio towards a ring-opening reaction was needed to explain product distribution and radical concentrations. Results are consistent with findings in field studies (Kim et al., 2013; Hens et al., 2014) where monoterpene emissions were high. Similar to the chamber studies for α- and β-pinene, models gave significantly less OH and HO_2 compared to measured values.

Further experiments with a more detailed analysis of the organic oxidation products could help to clarify the exact reaction mechanism and further support results from quantum-chemical calculations.

Data availability. Data of the experiments in the SAPHIR chamber used in this work are available on the EUROCHAMP data home page (https://data.eurochamp.org/, last access: 28 April 2019, Eurochamp, 2019).

Supplement. The supplement related to this article is available online at: https://doi.org/10.5194/acp-19-11635-2019-supplement.

Author contributions. MR analyzed the data and wrote the paper. HF and MK designed the experiments. HF conducted the HO_x radical measurements and SN was responsible for the OH reactivity measurements. BB conducted the radiation measurements. MK and RW were responsible for the GC measurements. RT, AL, and IHA were responsible for the PTR-TOF-MS measurements. XL was responsible for the HONO measurements and HPD for the DOAS OH data. FR was responsible for the NO_x and O_3 data. All co-authors commented on the paper.

Competing interests. The authors declare that they have no conflict of interest.

Financial support. This research has been supported by the European Commission, H2020 European Research Council (grant no. SARLEP (681529)), the European Commission, H2020 Research Infrastructures (grant no. EUROCHAMP-2020 (730997)), and the Deutsche Forschungsgemeinschaft (grant no. BO 1580/3-1).

The article processing charges for this open-access publication were covered by a Research Centre of the Helmholtz Association.

Review statement. This paper was edited by Harald Saathoff and reviewed by two anonymous referees.

References

Arey, J., Atkinson, R., and Aschmann, S. M.: Product study of the gas-phase reactions of monoterpenes with the OH radical in the presence of NO_x, J. Geophys. Res., 95, 18539–18546, https://doi.org/10.1029/JD095iD11p18539, 1990.

Aschmann, S. M., Atkinson, R., and Arey, J.: Products of reaction of OH radicals with α-pinene, J. Geophys. Res., 107, ACH 6–1–ACH 6–7, https://doi.org/10.1029/2001JD001098, 2002.

Atkinson, R. and Arey, J.: Atmospheric degradation of volatile organic compounds, Chem. Rev., 103, 4605–4638, https://doi.org/10.1021/cr0206420, 2003.

Atkinson, R., Baulch, D. L., Cox, R. A., Crowley, J. N., Hampson, R. F., Hynes, R. G., Jenkin, M. E., Rossi, M. J., Troe, J., and IUPAC Subcommittee: Evaluated kinetic and photochemical data for atmospheric chemistry: Volume II – gas phase reactions of organic species, Atmos. Chem. Phys., 6, 3625–4055, https://doi.org/10.5194/acp-6-3625-2006, 2006.

Bohn, B. and Zilken, H.: Model-aided radiometric determination of photolysis frequencies in a sunlit atmosphere simulation chamber, Atmos. Chem. Phys., 5, 191–206, https://doi.org/10.5194/acp-5-191-2005, 2005.

Bohn, B., Rohrer, F., Brauers, T., and Wahner, A.: Actinometric measurements of NO_2 photolysis frequencies in the atmosphere simulation chamber SAPHIR, Atmos. Chem. Phys., 5, 493–503, https://doi.org/10.5194/acp-5-493-2005, 2005.

Calogirou, A., Jensen, N. R., Nielsen, C. J., Kotzias, D., and Hjorth, J.: Gas-phase reactions of nopinone, 3-isopropenyl-6-oxo-heptanal, and 5-methyl-5-vinyltetrahydrofuran-2-ol with OH, NO_3, and ozone, Environ Sci. Technol., 33, 453–460, https://doi.org/10.1021/es980530j, 1999.

Crounse, J. D., Paulot, F., Kjaergaard, H. G., and Wennberg, P. O.: Peroxy radical isomerization in the oxidation of isoprene, Phys. Chem. Chem. Phys., 13, 13607–13613, https://doi.org/10.1039/C1CP21330J, 2011.

Crounse, J. D., Knap, H. C., Ornso, K. B., Jorgensen, S., Paulot, F., Kjaergaard, H. G., and Wennberg, P. O.: On the atmospheric fate of methacrolein: 1. Peroxy radical isomerization following addition of OH and O_2, J. Phys. Chem. A, 116, 5756–5762, https://doi.org/10.1021/jp211560u, 2012.

Dorn, H. P., Neuroth, R., and Hofzumahaus, A.: Investigation of OH absorption cross sections of rotational transitions in the $A^2\Sigma^+$, $\nu' = 0 \leftarrow X^2\Pi$, $\nu-0$ band under atmospheric conditions: Implications for tropospheric long-path absorption measurements, J. Geophys. Res., 100, 7397–7409, https://doi.org/10.1029/94jd03323, 1995.

Eddingsaas, N. C., Loza, C. L., Yee, L. D., Seinfeld, J. H., and Wennberg, P. O.: α-pinene photooxidation under controlled chemical conditions – Part 1: Gas-phase composition in low- and high-NO_x environments, Atmos. Chem. Phys., 12, 6489–6504, https://doi.org/10.5194/acp-12-6489-2012, 2012.

Eurochamp: Database of Atmospheric Simulation Chamber Studies, https://data.eurochamp.org/, last access: 28 April, 2019.

Fuchs, H., Bohn, B., Hofzumahaus, A., Holland, F., Lu, K. D., Nehr, S., Rohrer, F., and Wahner, A.: Detection of HO_2 by laser-induced fluorescence: calibration and interferences from RO_2 radicals, Atmos. Meas. Tech., 4, 1209–1225, https://doi.org/10.5194/amt-4-1209-2011, 2011.

Fuchs, H., Dorn, H.-P., Bachner, M., Bohn, B., Brauers, T., Gomm, S., Hofzumahaus, A., Holland, F., Nehr, S., Rohrer, F., Tillmann, R., and Wahner, A.: Comparison of OH concentration measurements by DOAS and LIF during SAPHIR chamber experiments at high OH reactivity and low NO concentration, Atmos. Meas. Tech., 5, 1611–1626, https://doi.org/10.5194/amt-5-1611-2012, 2012.

Fuchs, H., Hofzumahaus, A., Rohrer, F., Bohn, B., Brauers, T., Dorn, H.-P., Häseler, R., Holland, F., Kaminski, M., Li, X., Lu, K., Nehr, S., Tillmann, R., Wegener, R., and Wahner, A.: Experimental evidence for efficient hydroxyl radical regeneration in isoprene oxidation, Nat. Geosci., 6, 1023–1026, https://doi.org/10.1038/NGEO1964, 2013.

Fuchs, H., Acir, I.-H., Bohn, B., Brauers, T., Dorn, H.-P., Häseler, R., Hofzumahaus, A., Holland, F., Kaminski, M., Li, X., Lu, K., Lutz, A., Nehr, S., Rohrer, F., Tillmann, R., Wegener, R., and Wahner, A.: OH regeneration from methacrolein oxidation investigated in the atmosphere simulation chamber SAPHIR, Atmos. Chem. Phys., 14, 7895–7908, https://doi.org/10.5194/acp-14-7895-2014, 2014.

Fuchs, H., Tan, Z., Hofzumahaus, A., Broch, S., Dorn, H.-P., Holland, F., Künstler, C., Gomm, S., Rohrer, F., Schrade, S., Tillmann, R., and Wahner, A.: Investigation of potential interferences in the detection of atmospheric RO_x radicals by laser-induced fluorescence under dark conditions, Atmos. Meas. Tech., 9, 1431–1447, https://doi.org/10.5194/amt-9-1431-2016, 2016.

Fuchs, H., Tan, Z., Lu, K., Bohn, B., Broch, S., Brown, S. S., Dong, H., Gomm, S., Häseler, R., He, L., Hofzumahaus, A., Holland, F., Li, X., Liu, Y., Lu, S., Min, K.-E., Rohrer, F., Shao, M., Wang, B., Wang, M., Wu, Y., Zeng, L., Zhang, Y., Wahner, A., and Zhang, Y.: OH reactivity at a rural site (Wangdu) in the North China Plain: contributions from OH reactants and experimental OH budget, Atmos. Chem. Phys., 17, 645–661, https://doi.org/10.5194/acp-17-645-2017, 2017.

Galloway, M. M., Huisman, A. J., Yee, L. D., Chan, A. W. H., Loza, C. L., Seinfeld, J. H., and Keutsch, F. N.: Yields of oxidized volatile organic compounds during the OH radical initiated oxidation of isoprene, methyl vinyl ketone, and methacrolein under high-NO_x conditions, Atmos. Chem. Phys., 11, 10779–10790, https://doi.org/10.5194/acp-11-10779-2011, 2011.

Glasius, M. and Goldstein, A. H.: Recent Discoveries and Future Challenges in Atmospheric Organic Chemistry, Environ. Sci. Technol., 50, 2754–2764, https://doi.org/10.1021/acs.est.5b05105, 2016.

Guenther, A. B., Jiang, X., Heald, C. L., Sakulyanontvittaya, T., Duhl, T., Emmons, L. K., and Wang, X.: The Model of Emissions of Gases and Aerosols from Nature version 2.1 (MEGAN2.1): an extended and updated framework for modeling biogenic emissions, Geosci. Model Dev., 5, 1471–1492, https://doi.org/10.5194/gmd-5-1471-2012, 2012.

Hakola, H., Arey, J., Aschmann, S. M., and Atkinson, R.: Product formation from the gas-phase reactions of OH radicals and O_3 with a series of monoterpenes, J. Atmos. Chem., 18, 75–102, https://doi.org/10.1007/BF00694375, 1994.

Hallquist, M., Wängberg, I., and Ljungström, E.: Atmospheric fate of carbonyl oxidation products originating from α-pinene and Δ3-carene: determination of rate of reaction with OH and NO_3 radicals, UV absorption cross sections, and vapor pressures, Environ. Sci. Technol., 31, 3166–3172, https://doi.org/10.1021/es970151a, 1997.

Hatakeyama, S., Izumi, K., Fukuyama, T., Akimoto, H., and Washida, N.: Reactions of OH with α-pinene and β-pinene in air: Estimate of global CO production from the atmospheric oxidation of terpenes, J. Geophys. Res., 96, 947–958, https://doi.org/10.1029/90JD02341, 1991.

Hens, K., Novelli, A., Martinez, M., Auld, J., Axinte, R., Bohn, B., Fischer, H., Keronen, P., Kubistin, D., Nölscher, A. C., Oswald, R., Paasonen, P., Petäjä, T., Regelin, E., Sander, R., Sinha, V., Sipilä, M., Taraborrelli, D., Tatum Ernest, C., Williams, J., Lelieveld, J., and Harder, H.: Observation and modelling of HO_x radicals in a boreal forest, Atmos. Chem. Phys., 14, 8723–8747, https://doi.org/10.5194/acp-14-8723-2014, 2014.

Hofzumahaus, A., Rohrer, F., Lu, K., Bohn, B., Brauers, T., Chang, C.-C., Fuchs, H., Holland, F., Kita, K., Kondo, Y., Li, X., Lou, S., Shao, M., Zeng, L., Wahner, A., and Zhang, Y.: Amplified trace gas removal in the troposphere, Science, 324, 1702–1704, https://doi.org/10.1126/science.1164566, 2009.

Holland, F., Heßling, M., and Hofzumahaus, A.: In situ measurement of tropospheric OH radicals by laser-induced fluorescence – a description of the KFA instrument, J. Atmos. Sci., 52, 3393–3401, https://doi.org/10.1175/1520-0469(1995)052<3393:ISMOTO>2.0.CO;2, 1995.

Isaacman-VanWertz, G., Massoli, P., O'Brien, R., Lim, C., Franklin, J. P., Moss, J. A., Hunter, J. F., Nowak, J. B., Canagaratna, M. R., Misztal, P. K., Arata, C., Roscioli, J. R., Herndon, S. T., Onasch, T. B., Lambe, A. T., Jayne, J. T., Su, L., Knopf, D. A., Goldstein, A. H., Worsnop, D. R., and Kroll, J. H.: Chemical evolution of atmospheric organic carbon over multiple generations of oxidation, Nat. Chem., 10, 462–468, https://doi.org/10.1038/s41557-018-0002-2, 2018.

Jaoui, M. and Kamens, R. M.: Mass balance of gaseous and particulate products analysis from α-pinene/NO_x/air in the presence of natural sunlight, J. Geophys. Res., 106, 12541–12558, https://doi.org/10.1029/2001JD900005, 2001.

Jenkin, M. E., Saunders, S. M., and Pilling, M. J.: The tropospheric degradation of volatile organic compounds: A protocol for mechanism development, Atmos. Environ., 31, 81–104, 1997.

Jordan, A., Haidacher, S., Hanel, G., Hartungen, E., Märk, L., Seehauser, H., Schottkowsky, R., Sulzer, P., and Märk, T. D.: A high resolution and high sensitivity proton-transfer-reaction time-of-flight mass spectrometer (PTR-TOF-MS), Int. J. Mass Spectrom., 286, 122–128, https://doi.org/10.1016/j.ijms.2009.07.005, 2009.

Kaminski, M., Fuchs, H., Acir, I.-H., Bohn, B., Brauers, T., Dorn, H.-P., Häseler, R., Hofzumahaus, A., Li, X., Lutz, A., Nehr, S., Rohrer, F., Tillmann, R., Vereecken, L., Wegener, R., and Wahner, A.: Investigation of the β-pinene photooxidation by OH in the atmosphere simulation chamber SAPHIR, Atmos. Chem. Phys., 17, 6631–6650, https://doi.org/10.5194/acp-17-6631-2017, 2017.

Kim, S., Wolfe, G. M., Mauldin, L., Cantrell, C., Guenther, A., Karl, T., Turnipseed, A., Greenberg, J., Hall, S. R., Ullmann, K., Apel, E., Hornbrook, R., Kajii, Y., Nakashima, Y., Keutsch, F. N., DiGangi, J. P., Henry, S. B., Kaser, L., Schnitzhofer, R., Graus, M., Hansel, A., Zheng, W., and Flocke, F. F.: Evaluation of HO_x sources and cycling using measurement-constrained model calculations in a 2-methyl-3-butene-2-ol (MBO) and monoterpene (MT) dominated ecosystem, Atmos. Chem. Phys., 13, 2031–2044, https://doi.org/10.5194/acp-13-2031-2013, 2013.

Knap, H. C., Schmidt, J. A., and Jørgensen, S.: Hydrogen shift reactions in four methyl-buten-ol (MBO) peroxy radicals and their impact on the atmosphere, Atmos. Environ., 147, 79–87, https://doi.org/10.1016/j.atmosenv.2016.09.064, 2016.

Larsen, B. R., Di Bella, D., Glasius, M., Winterhalter, R., Jensen, N. R., and Hjorth, J.: Gas-phase OH oxidation of monoterpenes: Gaseous and particulate products, J. Atmos. Chem., 38, 231–276, https://doi.org/10.1023/A:1006487530903, 2001.

Lee, A., Goldstein, A. H., Kroll, J. H., Ng, N. L., Varutbangkul, V., Flagan, R. C., and Seinfeld, J. H.: Gas-phase products and secondary aerosol yields from the photooxidation of 16 different terpenes, J. Geophys. Res., 111, D17305, https://doi.org/10.1029/2006JD007050, 2006.

Lelieveld, J., Butler, T. M., Crowley, J. N., Dillon, T. J., Fischer, H., Ganzeveld, L., Harder, H., Lawrence, M. G., Martinez, M., Taraborrelli, D., and Williams, J.: Atmospheric oxidation capacity sustained by a tropical forest, Nature, 452, 737–740, https://doi.org/10.1038/nature06870, 2008.

Lindinger, W., Hansel, A., and Jordan, A.: On-line monitoring of volatile organic compounds at pptv levels by means of proton-transfer-reaction mass spectrometry (PTR-MS) – Medical applications, food control and environmental research, Int. J. Mass Spectrom., 173, 191–241, https://doi.org/10.1016/s0168-1176(97)00281-4, 1998.

Lou, S., Holland, F., Rohrer, F., Lu, K., Bohn, B., Brauers, T., Chang, C. C., Fuchs, H., Häseler, R., Kita, K., Kondo, Y., Li, X., Shao, M., Zeng, L., Wahner, A., Zhang, Y., Wang, W., and Hofzumahaus, A.: Atmospheric OH reactivities in the Pearl River Delta – China in summer 2006: measurement and model results, Atmos. Chem. Phys., 10, 11243–11260, https://doi.org/10.5194/acp-10-11243-2010, 2010.

Mao, J., Ren, X., Zhang, L., Van Duin, D. M., Cohen, R. C., Park, J.-H., Goldstein, A. H., Paulot, F., Beaver, M. R., Crounse, J. D., Wennberg, P. O., DiGangi, J. P., Henry, S. B., Keutsch, F. N., Park, C., Schade, G. W., Wolfe, G. M., Thornton, J. A., and Brune, W. H.: Insights into hydroxyl measurements and atmospheric oxidation in a California forest, Atmos. Chem. Phys., 12, 8009–8020, https://doi.org/10.5194/acp-12-8009-2012, 2012.

MCM: The Master Chemical Mechanism, v3.3.1, http://mcm.leeds.ac.uk/MCM, last access: 28 April, 2019.

Novelli, A., Hens, K., Tatum Ernest, C., Kubistin, D., Regelin, E., Elste, T., Plass-Dülmer, C., Martinez, M., Lelieveld, J., and Harder, H.: Characterisation of an inlet pre-injector laser-induced fluorescence instrument for the measurement of atmospheric hydroxyl radicals, Atmos. Meas. Tech., 7, 3413–3430, https://doi.org/10.5194/amt-7-3413-2014, 2014.

Novelli, A., Kaminski, M., Rolletter, M., Acir, I.-H., Bohn, B., Dorn, H.-P., Li, X., Lutz, A., Nehr, S., Rohrer, F., Tillmann, R., Wegener, R., Holland, F., Hofzumahaus, A., Kiendler-Scharr, A., Wahner, A., and Fuchs, H.: Evaluation of OH and HO_2 concentrations and their budgets during photooxidation of 2-methyl-3-butene-2-ol (MBO) in the atmospheric simulation chamber SAPHIR, Atmos. Chem. Phys., 18, 11409–11422, https://doi.org/10.5194/acp-18-11409-2018, 2018.

Noziére, B., Barnes, I., and Becker, K.-H.: Product study and mechanisms of the reactions of α-pinene and of pinonaldehyde with OH radicals, J. Geophys. Res., 104, 23645–23656, https://doi.org/10.1029/1999JD900778, 1999.

Peeters, J., Nguyen, T. L., and Vereecken, L.: HO_x radical regeneration in the oxidation of isoprene, Phys. Chem. Chem. Phys., 11, 5935–5939, https://doi.org/10.1039/b908511d, 2009.

Peeters, J., Müller, J.-F., Stavrakou, T., and Nguyen, V. S.: Hydroxyl radical recycling in isoprene oxidation driven by hydrogen bonding and hydrogen tunneling: The upgraded LIM1 mechanism, J. Phys. Chem. A, 118, 8625–8643, https://doi.org/10.1021/jp5033146, 2014.

Rohrer, F., Bohn, B., Brauers, T., Brüning, D., Johnen, F.-J., Wahner, A., and Kleffmann, J.: Characterisation of the photolytic HONO-source in the atmosphere simulation chamber SAPHIR, Atmos. Chem. Phys., 5, 2189–2201, https://doi.org/10.5194/acp-5-2189-2005, 2005.

Saunders, S. M., Jenkin, M. E., Derwent, R. G., and Pilling, M. J.: Protocol for the development of the Master Chemical Mechanism, MCM v3 (Part A): tropospheric degradation of non-aromatic volatile organic compounds, Atmos. Chem. Phys., 3, 161–180, https://doi.org/10.5194/acp-3-161-2003, 2003.

Schlosser, E., Brauers, T., Dorn, H.-P., Fuchs, H., Häseler, R., Hofzumahaus, A., Holland, F., Wahner, A., Kanaya, Y., Kajii, Y., Miyamoto, K., Nishida, S., Watanabe, K., Yoshino, A., Kubistin, D., Martinez, M., Rudolf, M., Harder, H., Berresheim, H., Elste, T., Plass-Dülmer, C., Stange, G., and Schurath, U.: Technical Note: Formal blind intercomparison of OH measurements: results from the international campaign HO_xComp, Atmos. Chem. Phys., 9, 7923–7948, https://doi.org/10.5194/acp-9-7923-2009, 2009.

Tillmann, R., Hallquist, M., Jonsson, Å. M., Kiendler-Scharr, A., Saathoff, H., Iinuma, Y., and Mentel, Th. F.: Influence of relative humidity and temperature on the production of pinonaldehyde and OH radicals from the ozonolysis of α-pinene, Atmos. Chem. Phys., 10, 7057–7072, https://doi.org/10.5194/acp-10-7057-2010, 2010.

Vereecken, L. and Peeters, J.: A theoretical study of the OH-initiated gas-phase oxidation mechanism of β-pinene ($C_{10}H_{16}$):

first generation products, Phys. Chem. Chem. Phys., 14, 3802–3815, https://doi.org/10.1039/C2CP23711C, 2012.

Vereecken, L., Müller, J. F., and Peeters, J.: Low-volatility poly-oxygenates in the OH-initiated atmospheric oxidation of α-pinene: impact of non-traditional peroxyl radical chemistry, Phys. Chem. Chem. Phys., 9, 5241–5248, https://doi.org/10.1039/B708023A, 2007.

Whalley, L. K., Edwards, P. M., Furneaux, K. L., Goddard, A., Ingham, T., Evans, M. J., Stone, D., Hopkins, J. R., Jones, C. E., Karunaharan, A., Lee, J. D., Lewis, A. C., Monks, P. S., Moller, S. J., and Heard, D. E.: Quantifying the magnitude of a missing hydroxyl radical source in a tropical rainforest, Atmos. Chem. Phys., 11, 7223–7233, https://doi.org/10.5194/acp-11-7223-2011, 2011.

Wisthaler, A., Jensen, N. R., Winterhalter, R., Lindinger, W., and Hjorth, J.: Measurements of acetone and other gas phase product yields from the OH-initiated oxidation of terpenes by proton-transfer-reaction mass spectrometry (PTR-MS), Atmos. Environ., 35, 6181–6191, https://doi.org/10.1016/S1352-2310(01)00385-5, 2001.

Xu, L., Møller, K. H., Crounse, J. D., Otkjær, R. V., Kjaergaard, H. G., and Wennberg, P. O.: Unimolecular Reactions of Peroxy Radicals Formed in the Oxidation of α-Pinene and β-Pinene by Hydroxyl Radicals, J. Phys. Chem. A, 123, 1661–1674, https://doi.org/10.1021/acs.jpca.8b11726, 2019.

5 Photooxidation of pinonaldehyde

The content of this chapter was published as “Photooxidation of pinonaldehyde at ambient conditions investigated in the atmospheric simulation chamber SAPHIR” by M. Rolletter, M. Blocquet, M. Kaminski, B. Bohn, H. P. Dorn, A. Hofzumahaus, F. Holland, X. Li, F. Rohrer, R. Tillmann, R. Wegener, A. Kiendler-Scharr, A. Wahner, and H. Fuchs, in Atmospheric Chemistry and Physics, 20, 13701-13719, DOI: 10.5194/acp-20-13701-2020, 2020, under Creative Commons Attribution 4.0 License. The supplementary material is provided in Appendix A.3.

Atmos. Chem. Phys., 20, 13701–13719, 2020
https://doi.org/10.5194/acp-20-13701-2020

Atmospheric Chemistry and Physics
Open Access
EGU

Photooxidation of pinonaldehyde at ambient conditions investigated in the atmospheric simulation chamber SAPHIR

Michael Rolletter[1], Marion Blocquet[1,a], Martin Kaminski[1,b], Birger Bohn[1], Hans-Peter Dorn[1], Andreas Hofzumahaus[1], Frank Holland[1], Xin Li[1,c], Franz Rohrer[1], Ralf Tillmann[1], Robert Wegener[1], Astrid Kiendler-Scharr[1], Andreas Wahner[1], and Hendrik Fuchs[1]

[1]Institute of Energy and Climate Research, IEK-8: Troposphere, Forschungszentrum Jülich GmbH, Jülich, Germany
[a]now at: Ministère de l'Education Nationale et de la Jeunesse, 110 rue de Grenelle, 75357 Paris SP 07, France
[b]now at: Federal Office of Consumer Protection and Food Safety, Department 5: Method Standardization, Reference Laboratories, Resistance to Antibiotics, Berlin, Germany
[c]now at: College of Environmental Sciences and Engineering, Peking University, Beijing, China

Correspondence: Hendrik Fuchs (h.fuchs@fz-juelich.de)

Received: 31 March 2020 – Discussion started: 14 April 2020
Revised: 22 July 2020 – Accepted: 24 September 2020 – Published: 14 November 2020

Abstract. The photooxidation of pinonaldehyde, one product of the α-pinene degradation, was investigated in the atmospheric simulation chamber SAPHIR under natural sunlight at low NO concentrations (< 0.2 ppbv) with and without an added hydroxyl radical (OH) scavenger. With a scavenger, pinonaldehyde was exclusively removed by photolysis, whereas without a scavenger, the degradation was dominated by reaction with OH. In both cases, the observed rate of pinonaldehyde consumption was faster than predicted by an explicit chemical model, the Master Chemical Mechanism (MCM, version 3.3.1). In the case with an OH scavenger, the observed photolytic decay can be reproduced by the model if an experimentally determined photolysis frequency is used instead of the parameterization in the MCM. A good fit is obtained when the photolysis frequency is calculated from the measured solar actinic flux spectrum, absorption cross sections published by Hallquist et al. (1997), and an effective quantum yield of 0.9. The resulting photolysis frequency is 3.5 times faster than the parameterization in the MCM. When pinonaldehyde is mainly removed by reaction with OH, the observed OH and hydroperoxy radical (HO_2) concentrations are underestimated in the model by a factor of 2. Using measured HO_2 as a model constraint brings modeled and measured OH concentrations into agreement. This suggests that the chemical mechanism includes all relevant OH-producing reactions but is missing a source for HO_2. The missing HO_2 source strength of (0.8 to 1.5) ppbv h^{-1} is similar to the rate of the pinonaldehyde consumption of up to 2.5 ppbv h^{-1}. When the model is constrained by HO_2 concentrations and the experimentally derived photolysis frequency, the pinonaldehyde decay is well represented. The photolysis of pinonaldehyde yields 0.18 ± 0.20 formaldehyde molecules at NO concentrations of less than 200 pptv, but no significant acetone formation is observed. When pinonaldehyde is also oxidized by OH under low NO conditions (maximum 80 pptv), yields of acetone and formaldehyde increase over the course of the experiment from 0.2 to 0.3 and from 0.15 to 0.45, respectively. Fantechi et al. (2002) proposed a degradation mechanism based on quantum-chemical calculations, which is considerably more complex than the MCM scheme and contains additional reaction pathways and products. Implementing these modifications results in a closure of the model–measurement discrepancy for the products acetone and formaldehyde, when pinonaldehyde is degraded only by photolysis. In contrast, the underprediction of formed acetone and formaldehyde is worsened compared to model results by the MCM, when pinonaldehyde is mainly degraded in the reaction with OH. This shows that the current mechanisms lack acetone and formaldehyde sources for low NO conditions like in these experiments. Implementing the modifications suggested by Fantechi et al. (2002) does not improve the model–measurement agreement of OH and HO_2.

Published by Copernicus Publications on behalf of the European Geosciences Union.

1 Introduction

Globally, emissions of biogenic non-methane volatile organic compounds (NMVOCs) in the atmosphere are 10 times higher than emissions of anthropogenic NMVOCs (Guenther et al., 2012). Of these emissions, monoterpenes (C10 compounds) represent approximately 15 % (Guenther et al., 2012) of the total emissions. Monoterpenes are mainly oxidized in the atmosphere by ozonolysis or their reaction with the hydroxyl radical (OH) during daytime. However, oxidation by the nitrate radical (NO_3) during nighttime can also be of importance enhanced by nocturnal monoterpene emissions (Calogirou et al., 1999; Atkinson and Arey, 2003). Oxidation products significantly contribute to the global production of, for example, acetone (Jacob et al., 2002). In addition, low-volatility organic oxidation products play an important role for the formation of secondary organic aerosol (SOA) (Kanakidou et al., 2000). The oxidation of monoterpenes and their oxidation products is also of importance for the tropospheric ozone production (Schwantes et al., 2020).

Field measurements indicate that there is a lack of understanding of the radical chemistry connected to the photooxidation of monoterpenes (e.g., Peeters et al., 2001; Capouet et al., 2004, and references therein). Hydroperoxy radical (HO_2) concentrations measured in environments dominated by monoterpenes are not well understood by model calculations, for example, in a campaign performed in the foothills of the Rocky Mountains (Kim et al., 2013) and in a boreal forest in Finland (Hens et al., 2014). In these campaigns, modeled HO_2 concentrations were lower by a factor of 2 and 2.5, respectively, compared to measurements. Chamber studies investigating the oxidation of α- and β-pinene also gave higher HO_2 concentrations than model calculations suggest (Kaminski et al., 2017; Rolletter et al., 2019).

Among the monoterpenes, α-pinene is the most abundant (Guenther et al., 2012). Pinonaldehyde is one of the first-generation oxidation products. In the α-pinene photooxidation, initially three different peroxy radicals (RO_2) are formed, and two of them eventually form pinonaldehyde. Several field campaigns reported pinonaldehyde concentrations measured on filter samples (Kavouras et al., 1999; Alves et al., 2002; Boy et al., 2004; Cahill et al., 2006; Rissanen et al., 2006; Herckes et al., 2006; Plewka et al., 2006) or in the analysis of rain and snow samples (Satsumabayashi et al., 2001). Only a few studies reported ambient gas-phase concentrations of pinonaldehyde. Field studies in the San Bernardino National Forest, California (Yu et al., 1999), and the German Fichtelgebirge (Müller et al., 2006) reported pinonaldehyde concentrations in the gas phase of approximately 0.15 ppbv. Another study by Cahill et al. (2006) conducted in the Sierra Nevada Mountains of California measured 0.05 to 0.30 ppbv gaseous pinonaldehyde. Pinonaldehyde yields from the photochemical degradation of α-pinene with OH were measured in laboratory experiments ranging from 6 % to 87 % (Larsen et al., 2001; Noziére et al., 1999). The high variability could be due to different chemical conditions with partially high reactant concentrations used in these experiments. A recent study in the atmospheric simulation chamber SAPHIR used ambient reactant concentrations ([α-pinene] ≤ 3.8 ppbv, [NO] < 120 pptv, (310 ± 5) K) and reported a low yield of 5 % (Rolletter et al., 2019). As currently implemented in the Master Chemical Mechanism (MCM, 2017; Jenkin et al., 1997; Saunders et al., 2003), pinonaldehyde is formed with a total yield of 84 %. In contrast, a theory-based study by Vereecken et al. (2007) suggested a different branching ratio of initial RO_2 and additional reaction channels which lead to pinonaldehyde yields of 60 % in total for low atmospheric NO conditions (≤ 1 ppbv NO). Our previous study (Rolletter et al., 2019) showed that further adjustment of the initial RO_2 branching ratio in a mechanism based on Vereecken et al. (2007) was necessary to explain the low measured pinonaldehyde yield of 5 % for conditions similar to the experiments discussed here. A similar change in RO_2 branching ratios was found in an experimental study by Xu et al. (2019).

The photochemistry of pinonaldehyde has been investigated in only a few experimental studies (Noziére et al., 1999; Jaoui and Kamens, 2003; Capouet et al., 2004) in addition to a few theoretical studies (Glasius et al., 1997; Vereecken and Peeters, 2002; Fantechi et al., 2002; Dash and Rajakumar, 2012). The pinonaldehyde degradation during daytime is controlled by photolysis and the reaction with OH radicals, resulting in an atmospheric lifetime on the order of a few hours due to its fast reaction with OH (Atkinson et al., 2004). The lifetime of pinonaldehyde with respect to photodissociation strongly depends on the season and the latitude but can be comparable to the reaction with OH (Hallquist et al., 1997). The main oxidation products (Fig. 1) of the photolysis and OH reactions are norpinonaldehyde (NORPINAL; names are taken from the MCM), pinonic acid (PINONIC), perpinonic acid (PERPINONIC), formaldehyde (HCHO), and acetone. So far there has been only one study by Noziére et al. (1999) reporting yields for the reaction with OH for HCHO and acetone of (152 ± 56) % and (15 ± 7) %, respectively.

A simplified oxidation scheme of pinonaldehyde is shown in Fig. 1. As implemented in the MCM, the photolysis of pinonaldehyde (PINAL) leads to dissociation in HCO and an organic radical, both of which react with O_2 to form CO, HO_2, and the peroxy radical C96O2.

$$\mathrm{PINAL} + h\nu + \mathrm{O_2} \rightarrow \mathrm{C96O2} + \mathrm{CO} + \mathrm{HO_2} \quad \text{(R1)}$$

The oxidation of pinonaldehyde by OH is initiated by H abstraction mainly at the aldehyde group forming primary RO_2. In the MCM, an acyl peroxy radical (C96CO3) and

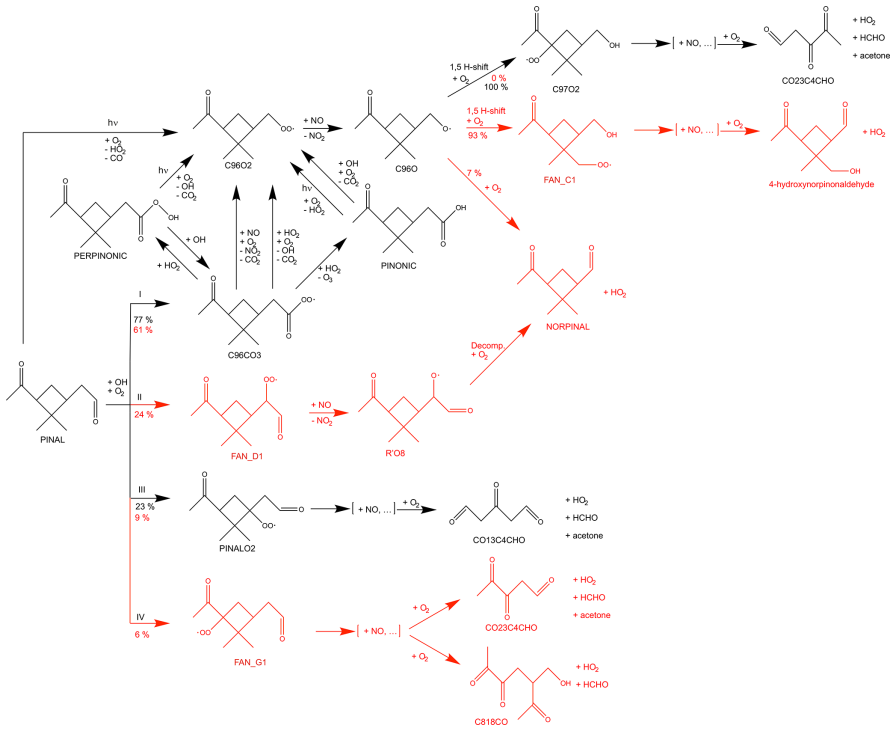

Figure 1. Simplified oxidation scheme of pinonaldehyde as described in the MCM (black) and modifications in the model derived by Fantechi et al. (2002) (red). [+NO, ...] represents reaction sequences that are initiated by peroxy radical reactions with NO and eventually form carbonyl compounds plus HO_2. Possible reactions of RO_2 with other RO_2 are not shown. $RO_2 + HO_2$ reactions are only shown for the major peroxy radical C96CO3. See text for details.

PINALO2 are formed.

$$\mathrm{PINAL + OH + O_2 \rightarrow C96CO3 \quad (yield : 0.77)} \qquad \text{(R2)}$$

$$\mathrm{PINAL + OH + O_2 \rightarrow PINALO2 \quad (yield : 0.23)} \qquad \text{(R3)}$$

In the presence of high nitric oxide (NO) concentrations, RO_2 reacts with NO and forms either alkoxy radicals (RO) or organic nitrate compounds ($RONO_2$). In the reaction forming an alkoxy radical, NO is converted to NO_2 and HO_2 to OH, respectively. The alkoxy radical subsequently reacts with O_2 to form a carbonyl compound and HO_2, decomposes, or isomerizes. At low NO concentrations, RO_2 reactions with HO_2 terminating the radical chain reactions and forming stable hydroxyperoxides (ROOH) increase in importance. Formed stable organic products of $RO_2 + NO$ and $RO_2 + HO_2$ reactions can further react with OH or photolyze.

The reaction of the most important RO_2 radical, C96CO3, with HO_2 can either directly form the same product (C96O2) as its reaction with NO or can form the stable products, i.e., pinonic and perpinonic acid. Subsequently, pinonic and perpinonic acid are photolyzed or react with OH, and thereby produce the peroxy radical C96O2 again. Similarly, other $RO_2 + HO_2$ reactions not shown in Fig. 1 produce the same species that are produced by $RO_2 + NO$ reactions.

In the atmosphere, the peroxy radical C96O2 can react with nitric oxide (NO) to form the corresponding alkoxy radical C96O.

$$\mathrm{C96O2 + NO \rightarrow C96O + NO_2} \qquad \text{(R4)}$$

C96O undergoes isomerization or decomposition reactions producing formaldehyde, acetone, or 3,4-dioxopentanal (CO23C4CHO).

The main products of the subsequent chemistry of the other peroxy radical PINALO2, including multiple reactions with NO and decomposition reactions, are HO_2, a tricarbonyl compound, acetone, and formaldehyde.

In contrast to the MCM, the theoretical study by Fantechi et al. (2002) predicts other decomposition reactions of products of the $RO_2 + NO$ reaction (Fig. 1). Whereas other theory-based studies investigated the reaction rate of pinonaldehyde + OH (Glasius et al., 1997) and the probability of H-abstraction by OH at various sites of pinonaldehyde (Vereecken and Peeters, 2002; Dash and Rajakumar, 2012), Fantechi et al. (2002) also analyzed the subsequent chemistry of the initially formed organic peroxy radicals. Instead of forming acetone and formaldehyde in the further degradation of C96O, Fantechi et al. (2002) suggest that the main fraction of C96O undergoes a series of isomerization reactions and reactions with NO forming 4-hydroxynorpinonaldehyde. In contrast to the MCM, the four-membered ring structure is retained in the formed products. A small fraction ($\sim 7\%$) directly forms norpinonaldehyde (NORPINAL) after H-abstraction by O_2. The modifications by Fantechi et al. (2002) are limited to $RO_2 + NO$ chemistry, and no detailed analysis of $RO_2 + HO_2$ reactions was done in their work. Nevertheless, modifications suggested by Fantechi et al. (2002) also affect $RO_2 + HO_2$ chemistry if products from these reactions are the same as from the reaction of $RO_2 + NO$ as implemented in the MCM. In the model by Fantechi et al. (2002) some $RO_2 + NO$ reactions also led to the formation of organic nitrates with yields between 14 % and 28 %, which lower the yield of formed HO_2 and carbonyl compounds.

Fantechi et al. (2002) proposed two additional relevant (yields > 5 %) peroxy radicals formed by the initial OH attack. Accordingly, the yields of C96CO3 and PINALO2 are changed from 77 % to 61 % and 23 % to 9 % compared to the MCM, respectively. The first additional reaction channel with a branching ratio of 24 % leads to a formation of norpinonaldehyde. The second additional reaction channel with only a minor contribution of 6 % forms in the subsequent chemistry acetone, formaldehyde, and a tri-carbonyl-hydroxy compound.

In this work, the photochemistry of pinonaldehyde was investigated under controlled atmospheric conditions, including atmospherically reactant concentrations and natural sunlight in the outdoor chamber SAPHIR (Simulation of Atmospheric PHotochemistry In a large Reaction Chamber), at Forschungszentrum Jülich. This study focuses on (a) the determination of the pinonaldehyde photolysis frequency, (b) quantification of HO_x ($= OH + HO_2$) radicals in the OH–oxidation of pinonaldehyde, and (c) the determination of acetone and formaldehyde yields of both photolysis and OH oxidation. Measurements of pinonaldehyde, degradation products, and HO_X radicals are compared to model calculations applying the Master Chemical Mechanism v3.3.1. Sensitivity model runs are performed including reaction pathways and yields suggested by the theoretical study of Fantechi et al. (2002), and the impact of the proposed mechanism on concentrations of organic compounds and HO_x radicals is analyzed.

2 Methods

2.1 Atmospheric simulation chamber SAPHIR

Details of the SAPHIR chamber can be found elsewhere (e.g., Rohrer et al., 2005; Bohn et al., 2005) and the chamber is only briefly described here. It is of cylindrical shape (18 m length, 5 m diameter and 270 m^3 volume) and is made of a double-wall Teflon (FEP) film. The FEP ensures inertness of the surfaces and minimizes wall effects. This outdoor chamber allows for studying the photochemical reactions under natural sunlight because the FEP film is transmissive for the entire solar spectrum. The chamber is equipped with a shutter system that can shield the chamber from sunlight.

Ultra-pure synthetic air used in the experiments is mixed from liquid nitrogen and oxygen (Linde, purity >99.9999 %). The pressure inside the chamber is slightly (30 Pa) above ambient pressure to prevent impurities from ambient air leaking into the chamber. Air that is consumed by instruments or is lost due to small leakages is replenished to keep a constant pressure. The replenishment flow is in the range of 9 to 12 $m^3 h^{-1}$, leading to a dilution of trace gases of 3 % h^{-1} to 4 % h^{-1}. Rapid mixing of air is ensured by the operation of two fans inside the chamber.

In the sunlit chamber, there are small sources for nitrous acid (HONO), formaldehyde (HCHO), and acetone. Their formation rates depend on the intensity of solar radiation, relative humidity, and temperature (Rohrer et al., 2005). The photolysis of HONO is the major primary source for nitrogen oxides and OH. Approximately 250 pptv h^{-1} NO_x, 200 pptv h^{-1} HCHO, and 100 pptv h^{-1} acetone were formed in the experiments in this study.

2.2 Instrumentation

An overview of used instruments and their 1 σ accuracies and precision is given in Table 1.

OH radicals were measured by laser-induced fluorescence (LIF). The instrument operated at the SAPHIR chamber has been described elsewhere (e.g., Holland et al., 2003; Fuchs et al., 2012). Chamber air is sampled through an inlet nozzle into a low-pressure measurement cell, where OH is excited by pulsed laser radiation at 308 nm. Its fluorescence is subsequently detected by gated photon counting. In addition, HO_2 radicals are indirectly detected after chemical conversion to OH by NO in another measurement cell (Fuchs et al., 2011). The instrument is calibrated by a radical source, in which OH

Table 1. Instrumentation for radical and trace gas detection during the pinonaldehyde oxidation experiments.

	Technique	Time resolution	1σ precision	1σ accuracy
OH	DOAS[a] (Dorn et al., 1995a; Hausmann et al., 1997; Schlosser et al., 2007)	205 s	0.8×10^6 cm^{-3}	6.5 %
OH	LIF[b] (Holland et al., 2003; Fuchs et al., 2012)	47 s	0.3×10^6 cm^{-3}	13 %
HO_2	LIF[b] (Fuchs et al., 2011)	47 s	1.5×10^7 cm^{-3}	16 %
NO	Chemiluminescence (Rohrer and Brüning, 1992)	180 s	4 pptv	5 %
NO_2	Chemiluminescence (Rohrer and Brüning, 1992)	180 s	2 pptv	5 %
O_3	UV absorption (Ansyco)	10 s	5 ppbv	5 %
Pinonaldehyde, acetone	PTR-TOF-MS[c] (Lindinger et al., 1998)	30 s	15 pptv	6 %
Acetone	GC-FID[d] (Kaminski et al., 2017)	30 min	20 pptv	5 %
HCHO	Hantzsch monitor (AeroLaser)	120 s	20 pptv	5 %
HCHO	DOAS[a]	100 s	20 %	10 %
HONO	LOPAP[e] (Li et al., 2014)	300 s	1.3 pptv	13 %
Photolysis frequencies	Spectroradiometer (Bohn et al., 2005)	60 s	10 %	10 %

[a] Differential Optical Absorption Spectroscopy. [b] Laser-Induced Fluorescence. [c] Proton Transfer Reaction Time-Of-Flight Mass Spectrometry. [d] Gas Chromatography Flame Ionization Detector. [e] Long-Path Absorption Photometer.

and HO_2 are produced by water vapor photolysis at 185 nm (Fuchs et al., 2011).

Interferences can occur in the HO_2 measurements because of concurrent conversion of specific RO_2 radicals that produce OH in the reaction with NO on a similar timescale to HO_2 (Fuchs et al., 2011; Whalley et al., 2013; Lew et al., 2018). Because the conversion of RO_2 requires at least two reaction steps with NO, in contrast to HO_2 for which only one reaction step leads to the formation of OH, this interference can be minimized if the conversion efficiency of HO_2 is below 10 %. This can be achieved by adjusting the NO concentration in the HO_2 cell. This was done in this study so that it can be assumed that potential interferences in the HO_2 detection were negligible.

In addition, OH was measured by differential optical absorption spectrometry (DOAS; Dorn et al., 1995b), which is an absolute measurement technique. Measured OH concentrations of both instruments agreed on average within 15 %, similar to results in previous experiments (Fuchs et al., 2012).

Organic compounds were measured by proton transfer reaction time-of-flight mass spectrometry (PTR-TOF-MS; Lindinger et al., 1998; Jordan et al., 2009) and by gas chromatography that was coupled to a flame ionization detector (GC-FID). The PTR-TOF-MS was calibrated for pinonaldehyde using a diffusion source (Gautrois and Koppmann, 1999) and for acetone using a gas standard. An internal standard (tetrachloro-ethylene) was added to the GC-FID sample flow to monitor changes in the sensitivity of the calibration with a calibration standard (Apel 8). Formaldehyde was measured by a Hantzsch instrument and by DOAS. The Hantzsch instrument was calibrated using liquid HCHO standards.

Photolysis frequencies (j) of NO_2, HONO, O_3, and pinonaldehyde were calculated from actinic flux density spectra that are derived from measurements of total and diffuse spectral actinic flux densities outside the chamber. From these measurements, direct sun contributions are calculated. The direct and diffuse actinic flux densities are used as input for a model that calculates mean chamber spectra by taking into account the time-dependent effects of shadings of the chamber steel frame and the transmittance of the Teflon film which is > 0.8 in the complete solar spectral range (Bohn and Zilken, 2005). Mean photolysis frequencies are then calculated by the following equation:

$$j = \int \sigma(\lambda)\phi(\lambda)F_\lambda(\lambda)\mathrm{d}\lambda, \quad (1)$$

where σ is the absorption cross section, ϕ is the quantum yield, and F is the actinic flux. The absorption cross sections and quantum yields of NO_2, HONO, and O_3 used for the cal-

culations of photolysis frequencies are taken from the literature (Mérienne et al., 1995; Troe, 2000; Stutz et al., 2000; Daumont et al., 1992; Matsumi et al., 2002). The method is regularly evaluated by dedicated experiments using the chamber as a chemical actinometer (Bohn et al., 2005). The pinonaldehyde photolysis frequency is discussed in more detail in Sect. 4.1.

NO and NO_2 were measured by chemiluminescence (Eco Physics), water vapor mixing ratios were measured by a cavity ring-down instrument (Picarro), and ozone (O_3) was measured by an UV absorption instrument (Ansyco).

2.3 Experimental procedure

Before the experiment, the chamber was flushed with dry, synthetic air to dilute trace gases from previous experiments below the detection limits of the instruments. A total of 20 ppmv of CO_2 was injected as a dilution tracer in the beginning of each experiment. Water from a Milli-Q device was boiled and flushed into the chamber together with a high flow of synthetic air ($150\,m^3\,h^{-1}$). The chamber was only humidified in the beginning of an experiment reaching initial water vapor concentrations of about 2 %, which decreased over the course of an experiment due to the dilution with dry synthetic air.

Pinonaldehyde (Orgentis chemicals, 98.2 %) was heated in a glass vial, and the vapor was flushed together with a small flow of dry nitrogen into the chamber using a short Teflon tube. After the injection had been stopped, the sample line was removed to avoid further evaporation of pinonaldehyde from the injection system into the chamber. The initial pinonaldehyde concentrations were 6.5 and 16.5 ppbv in the experiments on 17 and 18 July 2014, respectively. The chamber roof was opened after a stable pinonaldehyde concentration was observed by the PTR-TOF-MS instrument.

In one experiment (18 July 2014), 2500 ppbv of cyclohexane was additionally injected after the humidification. Cyclohexane served as scavenger for OH in this experiment in order to study the pinonaldehyde photolysis independently from its reaction with OH.

In the other experiment (17 July 2014), 70 ppbv of ozone produced from a silent discharge ozonizer (O3Onia) was injected after humidification so that a low NO concentration (maximum 80 pptv) was obtained during the experiment. In this experiment, approximately 20 % of reacted pinonaldehyde was photolyzed, and the remaining 80 % reacted with OH. The reaction of pinonaldehyde with ozone is very slow ($k = (8.9 \pm 1.4) \times 10^{-20}\,cm^3\,s^{-1}$, Glasius et al., 1997), and therefore ozonolysis reactions did not play a role in the experiments here.

2.4 Model calculations

The Master Chemical Mechanism (MCM) in its latest version 3.3.1 was applied as base model for box model calculations (MCM, 2017; Jenkin et al., 1997; Saunders et al., 2003). FACSIMILE was used as solver for differential equations in the model calculations.

In order to account for chamber effects, the following modifications were added to the MCM model. Dilution to all trace gases was applied. The dilution rate was calculated from the monitored replenishment flow rate that was consistent with the dilution of the CO_2 tracer. Small chamber sources of formaldehyde and acetone were parameterized based on reference experiments as described in Rohrer et al. (2005), Karl et al. (2006), and Kaminski et al. (2017).

Temperature, pressure, H_2O, NO, NO_2, HONO, and O_3 concentrations were constrained to measured values. These constraints were used because chamber NO sources cannot be modeled accurately and could therefore lead to wrong conclusions in the analysis of turnover rates of radicals.

Photolysis frequencies, which were not measured, were calculated for clear sky conditions by the parameterization included in the MCM. They were scaled to take cloud cover and the transmission of the Teflon film into account by the ratio of measured to modeled photolysis frequency of NO_2. This also applies for the photolysis frequency of pinonaldehyde in the base model case (MCM). All other model runs used the experimentally derived pinonaldehyde photolysis frequency (see Sect. 4.1).

The injection of pinonaldehyde was modeled as a source only present during the time period of injection to match the pinonaldehyde increase as measured by PTR-TOF-MS.

In a sensitivity study, the pinonaldehyde oxidation scheme developed by Fantechi et al. (2002) was implemented. In this mechanism, additional reaction pathways of the pinonaldehyde reaction with OH that are not included in the MCM are suggested. Only the four reaction pathways with significant yields (> 5 %) were implemented for the sensitivity model run (Fig. 1). In addition, the fate of the most abundant RO_2 formed from the reaction of pinonaldehyde with OH or photolysis is different in this model compared to the MCM mechanism (see above). Reaction rate constants and branching ratios were used as described in Fantechi et al. (2002). Simple rate coefficients such as KDEC ($= 1 \times 10^6$) and KRO2NO ($= 2.7 \times 10^{-12}\,\exp(360/T)$) from the MCM were used, when no specific reaction rate constants were mentioned. To account for possible $RO_2 + HO_2$ reactions, a reaction scheme based on the reaction C97O2 + HO_2 was added for all newly introduced RO_2 species not included in the MCM. $RO_2 + HO_2$ reactions form a corresponding hydroxyperoxide (ROOH) that can either react with OH to regenerate the RO_2 or photolyze to form the corresponding alkoxy radical (RO). Modifications by Fantechi et al. (2002) describe the chemistry from the OH attack on pinonaldehyde until the formation of stable products 4-hydroxynorpinonaldehyde, norpinonaldehyde, CO23C4CHO, and C818CO. The chemistry of the products norpinonaldehyde, CO23C4CHO, and C818CO was treated as described in the MCM. For 4-

Table 2. Overview of different model calculations.

Model run	Model	$j_{\text{pinonaldehyde}}$	HO_2
MCM	MCM[a]	MCM[b]	calculated
MCM_a	MCM[a]	exp.[c]	calculated
MCM_b	MCM[a]	exp.[c]	constrained
FAN_a	Fantechi et al.[d]	exp.[c]	calculated
FAN_b	Fantechi et al.[d]	exp.[c]	constrained
S1	like FAN_a, with additional $RO_2 \rightarrow HO_2$ ($0.1\,s^{-1}$) for RO_2 = C96CO3, FAN_D1, PINALO2, and FAN_G1		
S1_mod	like FAN_a, with additional $RO_2 \rightarrow HO_2$ ($0.1\,s^{-1}$) for RO_2 = FAN_D1, PINALO2, and FAN_G1		
S1_mod_hv	like FAN_a, with additional $RO_2 \rightarrow RO_2$isom ($0.1\,s^{-1}$) for RO_2 = FAN_D1, PINALO2, and FAN_G1 followed by $RO_2\text{isom} + h\nu \rightarrow HO_2$ (j_{glyoxal}) and $RO_2\text{isom} + NO \rightarrow HO_2 + NO_2$ (KRO2NO[a])		
S2	like FAN_a, with additional photolysis ($0.2 \times j_{NO2}$) of first-generation pinonaldehyde products (4-hydroxynorpinonaldehyde, NORPINAL, CO13C4CHO, CO23C4CHO, C818CO)		
S3	like FAN_a, with subsequent degradation of 4-hydroxynorpinonaldehyde		
$2 \times$ KRO2NO	like FAN_a, with an enhanced reaction rate of $2 \times$ KRO2NO[a] for all $RO_2 + NO$ reactions		

[a] Master Chemical Mechanism v3.3.1. [b] Parametrization used by MCM v3.3.1. [c] Calculated from the measured solar actinic spectrum, using the absorption spectrum by Hallquist et al. (1997) and an estimated effective quantum yield of 0.9. [d] Mechanism by Fantechi et al. (2002) replaces pinonaldehyde chemistry in MCM (see the Supplement).

hydroxynorpinonaldehyde, no follow-up chemistry was considered.

Both the MCM and Fantechi et al. (2002) mechanism were tested under different conditions. An overview of used model calculations is given in Table 2.

3 Results

Figures 2 and 3 show the concentration time series of pinonaldehyde and other measured trace gases together with MCM model results for the two experiments with and without OH scavenger, respectively.

Weather conditions were similar for both experiment days. The temperature inside the chamber increased over the course of each experiment from 305 to 315 K. The solar zenith angle at noon was 30° and maximum measured pinonaldehyde photolysis frequencies were approximately $3.5 \times 10^{-5}\,s^{-1}$ in both experiments.

In both experiments, the measured pinonaldehyde decay was significantly faster than predicted by the model once the chamber roof was opened. The predicted pinonaldehyde consumption rate was slower by 50 % and 25 % in the pure photolysis case and in the OH oxidation case, respectively. Potential wall loss of pinonaldehyde in the chamber was tested in separate experiments, in which pinonaldehyde was injected into the dark chamber. The loss of pinonaldehyde in this case is consistent with the dilution calculated from the replenishment flow.

The two measured major organic products, acetone and formaldehyde, are also not well reproduced by the model calculations. In the experiment with the OH scavenger, in which pinonaldehyde is removed by photolysis only, the modeled concentrations of formaldehyde and acetone are 60 % and 70 % higher compared to the measurements, although the photolysis frequency of pinonaldehyde is obviously underestimated. In contrast, in the experiment in which pinonaldehyde was photolyzed and oxidized by OH-modeled acetone concentrations are underestimated by 17 % compared to measurements. Modeled formaldehyde concentrations are 6 % smaller than measurements, which is within the measurement uncertainty. The smaller modeled acetone yield cannot be explained by the lower consumption of pinonaldehyde in the model alone. A sensitivity run that reproduces the pinonaldehyde consumption also underestimates the acetone concentrations.

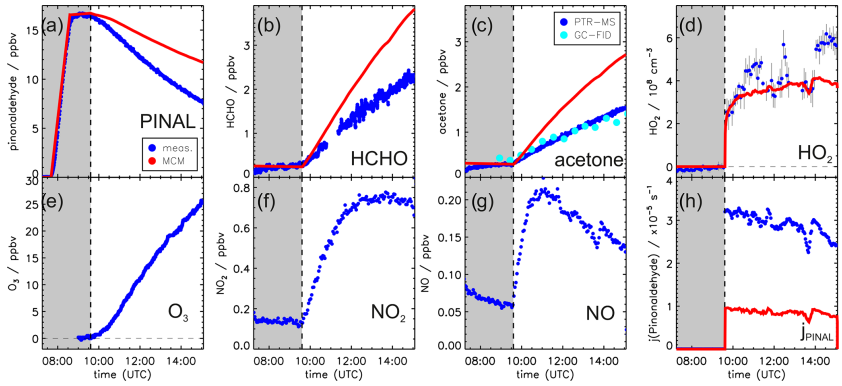

Figure 2. Measured and modeled trace gas concentrations and photolysis frequencies during photooxidation of pinonaldehyde in the presence of an OH scavenger. Pinonaldehyde is removed by photolysis only. Measured O_3, NO_2 and NO were used as constraints for the model. See the text for details of the pinonaldehyde photolysis frequency (h). Grey-shaded areas indicate times when the chamber roof was closed.

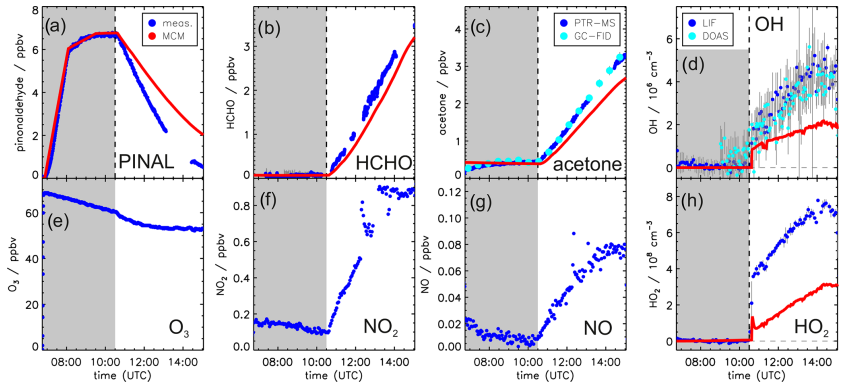

Figure 3. Measured and modeled trace gas concentrations during the photooxidation of pinonaldehyde without OH scavenger. In this experiment, pinonaldehyde is removed by photolysis and reaction with OH. Measured O_3, NO_2, and NO were used as constraints for the model. Grey-shaded areas indicate times when the chamber roof was closed.

In the experiment without scavenger, OH and HO_2 are both considerably underpredicted by the MCM. While OH shows an increasing discrepancy of up to a factor of 2, modeled HO_2 is a factor of 2–4 lower than measured. In the experiment with OH scavenger, measured and modeled HO_2 concentrations agree within the stated uncertainty during the first part of the experiment, but the model underestimates the HO_2 by 50 % in the last hour.

Measured time series of acetone and formaldehyde are used to determine the total yields of acetone and formaldehyde from the pinonaldehyde oxidation following the procedure described by Galloway et al. (2011), Kaminski et al. (2017), and Rolletter et al. (2019). In this approach, the measured time series of trace gases are corrected for loss and production that are not directly related to the chemical oxidation scheme of pinonaldehyde. This includes dilution of trace gases in the chamber, loss of formaldehyde due to photolysis, and a small production of formaldehyde and acetone in the sunlit chamber that is independent of the pinonaldehyde chemistry. If OH is also present, additional corrections

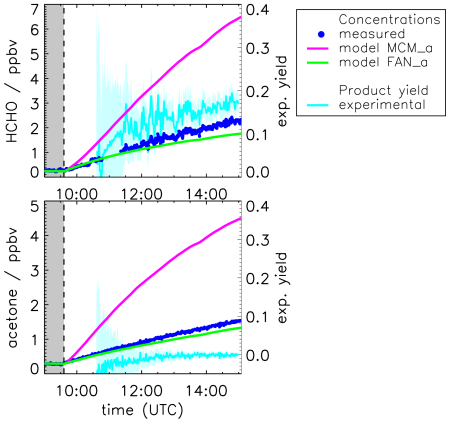

Figure 4. Measured and modeled formaldehyde and acetone mixing ratios for the experiment with OH scavenger. All model runs were done with measured photolysis frequencies for pinonaldehyde (see Fig. 6). Model runs include the MCM and the MCM with additions described in Fantechi et al. (2002). In addition, yields calculated from measured time series are shown (see text for details) with the 1σ error derived from measurements and errors of the applied correction. Colored areas give the uncertainty of this calculation. The additional error caused by the uncertainty of the chamber source is not included here.

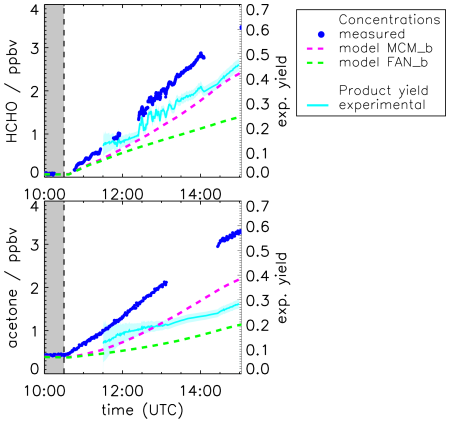

Figure 5. Measured and modeled formaldehyde and acetone mixing ratios for the experiment without OH scavenger. All model runs were done with measured photolysis frequencies for pinonaldehyde and with HO_2 constrained to measurements (see Fig. 7). Model runs were done using the MCM and the MCM with modifications described in Fantechi et al. (2002). In addition, yields calculated from measured time series are shown (see text for details) with the 1σ error derived from measurements and errors of the applied correction. Colored areas give the uncertainty of this calculation. The additional error caused by the uncertainty of the chamber source is not included here.

for the losses of formaldehyde and acetone due to their reactions with OH are applied. The corrected time series can then be used to calculate the ratio of a formed organic product and the consumed pinonaldehyde to derive the yield of the organic compound that is connected to the chemical degradation of pinonaldehyde. The main uncertainty in the calculated yields is caused by the uncertainty of the strength of the small chamber sources, which has to be taken from characterization experiments that were performed before and after the experiments with pinonaldehyde. Sensitivity studies in which the source strengths are systematically varied show that 1σ uncertainties of yields are 0.2 and 0.1 for formaldehyde and acetone, respectively.

Figure 4 shows the result of the yield calculations. The formaldehyde yield is (0.1 ± 0.2) in the beginning and increases to approximately (0.18 ± 0.2) at the end of the experiment. The acetone yield of the photolysis is zero within the uncertainty of 0.1.

The yields of acetone and formaldehyde are also calculated from the measured time series in the experiment when pinonaldehyde was oxidized by OH as described for the experiment with OH scavenger. Results are shown in Fig. 5. The yields of both species increase over the course of the experiment. The formaldehyde yield increases from approximately (0.15 ± 0.2) to values higher than (0.45 ± 0.2), and the acetone yield increases from approximately (0.2 ± 0.1) to (0.3 ± 0.1).

4 Discussion

4.1 Pinonaldehyde photolysis

In the presence of an OH scavenger, the pinonaldehyde decay observed in the chamber could be due to photolysis, wall loss, and dilution. As was shown by additional experiments in the dark chamber, wall loss is negligible on the timescale of a few hours. The effect of dilution was quantified from the measured dilution flow rate and the chamber volume and agreed with the results from the tracer (CO_2) measurements within 3 %. Without OH, the chemical degradation of pinonaldehyde depends only on the photolysis frequency of pinonaldehyde. In MCM, photolysis frequencies are generally calculated as a function of solar zenith angle χ using three parameters l, m, and n.

$$J = l \cdot (\cos(\chi))^m \cdot e^{(-n \cdot \sec(\chi))} \quad (2)$$

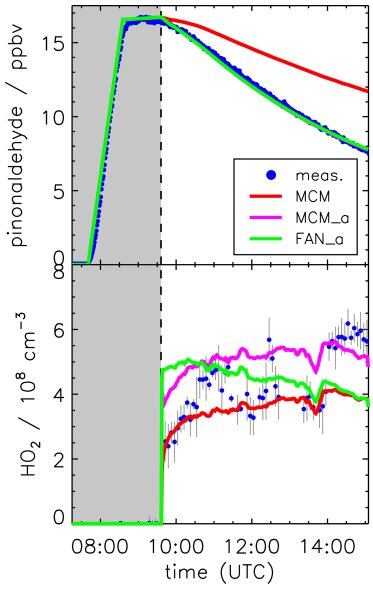

Figure 6. Pinonaldehyde and HO_2 time series during the experiment with OH scavenger. Model runs were done either using the MCM with parameterization of pinonaldehyde photolysis frequencies (MCM), with measured values for photolysis frequencies (MCM_a; see the text for details), or with modifications described in Fantechi et al. (2002) (FAN_a). The pinonaldehyde concentration time profile is the same for both model runs MCM_a and FAN_a. Grey-shaded areas indicate times when the chamber roof was closed.

For pinonaldehyde, MCM is using the parameters ($l = 2.792 \times 10^{-5} s^{-1}$, $m = 0.805$, $n = 0.338$; valid for clear sky conditions) for the photolysis of n-butanal. The parameterization is based on the absorption spectrum measured for n-butanal at 298 K by Martinez et al. (1992) and the quantum yield (0.21) for its dissociation to $n\text{-}C_3H_7 + HCO$ at 298 K and 1 atm by Tadić et al. (2001). For the evaluation of the chamber experiments, the clear sky values from the parameterization (Eq. 1) are corrected for the influence of cloud cover and chamber transmission by multiplying the clear sky value by the ratio of the measured to parameterized photolysis frequency of NO_2. Following this procedure, the simulated decay of pinonaldehyde in the base model (MCM) is considerably slower than the observed decay (Fig. 6).

As an alternative, the photolysis frequency of pinonaldehyde is calculated using the measured spectrally resolved solar actinic flux (Sect. 2.2) and the pinonaldehyde absorption spectrum (280–340 nm) measured at 300 K by Hallquist et al. (1997). Good agreement between the observed and simulated (MCM_a) pinonaldehyde decay is achieved if an effective quantum yield of 0.9 is assumed (Fig. 6, upper panel). Here, the mean decay rate of pinonaldehyde between 10:00 and 15:00 UTC is $3.9 \times 10^{-5} s^{-1}$, of which $2.9 \times 10^{-5} s^{-1}$ is caused by photolysis and $1.0 \times 10^{-5} s^{-1}$ by dilution. The experimentally derived photolysis frequencies are approximately a factor of 3 to 3.5 higher than the values from the parameterization in the MCM. The experimental error (20 %) of the effective quantum yield (0.9) is mainly determined by the uncertainties of the absorption spectrum (< 5 %; Hallquist et al., 1997) and the actinic flux measurement (10 %). Error contributions from wall loss and dilution are small (< 5 %).

The applied absorption cross sections by Hallquist et al. (1997) are the only published measurements and are recommended by IUPAC (Atkinson et al., 2006). The effective, wavelength-independent quantum yield determined in this work is significantly higher than in two other chamber studies, which report values of 0.14 ± 0.03 (Moortgat et al., 2002) and 0.4 (Jaoui and Kamens, 2003) for photolysis with natural sunlight. No recommendation for the quantum yield is given by IUPAC (Atkinson et al., 2006). Both chamber studies applied the absorption spectrum from Hallquist et al. (1997) for the calculation of photolysis frequencies. Jaoui and Kamens (2003) measured the solar radiation by a UV Eppley radiometer. The broadband instrument measures the spectrally integrated solar irradiance (spatially cosine-weighted photon flux density) from 300 to 400 nm. The nontrivial conversion to a actinic flux spectrum (spatially isotropically weighted photon-flux density) between 300 and 340 nm needed for the evaluation of the pinonaldehyde photolysis frequencies has not been documented by the authors. The conversion requires knowledge of the spatial distribution of the incident solar radiation, which is a function of solar zenith angle, wavelength, atmospheric aerosol, and clouds (Hofzumahaus, 2006). Furthermore, the wavelength range of pinonaldehyde photolysis (< 340 nm) strongly depends on the total atmospheric ozone column, while UV Eppley measurements (300–400 nm) are only weakly dependent on total ozone. Considerable errors may therefore be connected to the conversion of Eppley data to photolysis frequencies for pinonaldehyde.

In the study by Moortgat et al. (2002), solar actinic flux was directly measured by a spectroradiometer with good accuracy like in the present work. However, similar to Jaoui and Kamens (2003), Moortgat et al. (2002) had to apply large corrections for wall losses and dilution, each of which were of the same magnitude as the photolysis rate. The large difference by a factor of 7 in comparison to the present work is likely not explained by systematic errors of the correction.

The pinonaldehyde photolysis is faster than n-butanal because of its two carbonyl functions. This might be valid for other bi-carbonyl compounds that have non-conjugated car-

bonyl functions, so that the use of the n-butanal photolysis frequency could systematically underestimate the photolysis frequencies of these compounds. However, the high quantum yield close to unity could also be a specific property of pinonaldehyde that might not apply for the photolysis of other bicarbonyl species.

Figure 4 shows the time series of measured acetone and formaldehyde concentrations together with results from model calculations applying the MCM. In contrast to the base case model (MCM, Fig. 2), measured photolysis frequencies are used (MCM_a). As a consequence of the higher photolysis frequencies, the consumption of pinonaldehyde leads to even larger productions of formaldehyde and acetone (approximately three times higher than measured values) compared to the base case model.

For conditions of this experiment, 80 % of RO_2 radicals formed in the photolysis reaction of pinonaldehyde are reacting with NO and only 20 % are reacting with HO_2, so that carbonyl compounds are expected to be the main organic products (Fig. 1). Acetone measured in this experiment is solely formed by the chamber source. Initial acetone yield values are negative because of the high uncertainty in the corrections that are applied in the yield calculation. In the beginning of an experiment, only small amounts of products are formed, which leads to a large uncertainty, so that negative values are not significant. It has to be stressed here again that the parametrization of the chamber source is the main uncertainty in the yield calculation. If the chamber source was overestimated, the constant measured acetone yield could also include a small contribution from the pinonaldehyde photolysis.

In a sensitivity model run (FAN_a), the pinonaldehyde oxidation scheme suggested by Fantechi et al. (2002) is tested for the experiment with OH scavenger. While the initial photodissociation step and the reaction of C96O2 with NO are the same, the following decomposition of C96O yields considerably different organic products. No acetone and less formaldehyde are produced together with mainly 4-hydroxynorpinonaldehyde and norpinonaldehyde that were not measured in these experiments. Agreement between modeled and measured acetone is achieved within the accuracy of measurements of 10 %. Modeled formaldehyde concentrations are also only 20 % lower than measured values. Thus, the model description of acetone and formaldehyde products is greatly improved by the use of the Fantechi et al. (2002) mechanism compared to the MCM.

To our knowledge, there is only one other study by Jaoui and Kamens (2003), which investigated the product yields of pinonaldehyde photolysis. Products were measured by gas chromatography in that chamber study in the presence and absence of an OH scavenger. The measured norpinonaldehyde yield agrees within the stated uncertainty with the yield proposed by Fantechi et al. (2002). Formaldehyde and acetone yields were not measured by Jaoui and Kamens (2003).

Using the MCM with the measured photolysis frequency (MCM_a) leads to an increase in modeled HO_2 of about 25 % (Fig. 6, lower panel), which can be explained by the higher amount of consumed pinonaldehyde that is formed at the end of the radical reaction chain together with 3,4-dioxopentanal (CO23C4CHO). Unfortunately, between 11:30 and 14:00 UTC experimental problems occurred in the HO_2 measurements. Neither NO measurements nor photolysis frequencies showed any features that could explain the decrease in the HO_2 concentration. The exact reason for the HO_2 variations remains unclear and the uncertainty of HO_2 measurements is likely higher (50 %) for this period. Implementing the modifications by Fantechi et al. (2002) results in a HO_2 concentration time profile (FAN_a) that is different from both model runs done with the MCM mechanism. In the FAN_a model run HO_2 is formed more rapidly compared to the MCM, and concentrations decrease towards the end of the experiment. The rate determining step in radical chain reactions is the reaction of RO_2 with NO forming an alkoxy radical and NO_2. In the MCM, there are three $RO_2 + NO$ reactions before the radical chain is terminated and the stable product CO23C4CHO is formed together with HO_2. In contrast, in the Fantechi et al. (2002) mechanism only one $RO_2 + NO$ reaction occurs before the stable products are formed and HO_2 is regenerated. In addition, no subsequent chemistry of the formed product 4-hydroxynorpinonaldehyde is included in the model, which would produce additional HO_2, especially in later stages of the experiment.

4.2 Photooxidation by OH

In the photooxidation experiment without OH scavenger (Fig. 3), a much faster decay of pinonaldehyde is observed compared to the case with OH scavenger (Fig. 2). Without scavenger, 30 % of the decay in the beginning of the experiment is explained by photolysis and 5 % by dilution. The remaining 65 % are due to the removal of pinonaldehyde by OH. However, OH concentrations rise over the course of the experiment and the pinonaldehyde fraction reacting with OH increase to up to 80 %. Here and in the following analysis, experimental photolysis frequencies are used, which assume a quantum yield of 0.9 (see Sect. 4.1). The photolysis and the OH reaction of pinonaldehyde lead to a mix of peroxy radicals (Fig. 1), which react mainly with HO_2 or NO. During the experiment, the NO mixing ratio increases from about 10 pptv to 80 pptv. Accordingly, the fraction of RO_2 radicals reacting with NO increases from 20 % to 55 %, while the RO_2 fraction reacting with HO_2 decreases.

Applying the experimental pinonaldehyde photolysis frequency to the model (MCM_a) improves the simulation of the pinonaldehyde decay compared to the base model run (MCM), which uses a slower parameterized photolysis frequency. However, even with the faster photolysis rate, the consumption of pinonaldehyde is underestimated (Fig. 7, up-

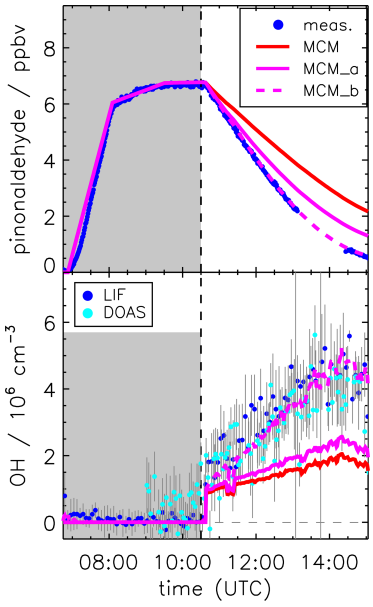

Figure 7. Pinonaldehyde and OH time series during the experiment without OH scavenger. Model runs were done either using the MCM with parameterization of pinonaldehyde photolysis frequencies (MCM) or with measured values for photolysis frequencies (MCM_a; see the text for details). The model MCM_b was additionally constrained to measured HO_2 concentration, resulting in an agreement between modeled and measured (LIF and DOAS) OH concentrations. Grey-shaded areas indicate times when the chamber roof was closed.

per panel). At the end of the experiment (15:00 UTC), the remaining modeled pinonaldehyde concentration is a factor of 2 larger than the measured value. This is due to the lower OH concentration in the model compared to measurements. If modeled OH concentrations are increased to match measured values, which can be achieved by constraining HO_2 in the model to measurements (MCM_b), modeled and measured pinonaldehyde concentrations agree within 10 % (Fig. 7). This demonstrates that missing OH production in the model is most likely due to the underestimation of HO_2, which forms OH by reaction with NO. This suggests that there is a HO_2 source missing in the model. In a sensitivity run (not shown here) artificial HO_2 sources were added to the model to quantify the required HO_2 source strength. The missing HO_2 source is increasing over the course of the experiment. A source strength between 0.8 and 1.5 ppbv h^{-1} would be required to explain observations. The consumption of pinonaldehyde during the experiment is up to 2.5 ppbv h^{-1}, and thus a comparably large HO_2 source would be required.

Implementation of the mechanism by Fantechi et al. (2002) does not improve the model–measurement agreement of OH and HO_2 (Fig. 8) compared to the MCM. As discussed above, the mechanism by Fantechi et al. (2002) is able to describe HO_2 concentrations as well as product formation of acetone and HCHO, if pinonaldehyde is only consumed by photolysis. In contrast, reaction pathways that are connected to the reaction of pinonaldehyde + OH are not correctly described.

Modeled HO_2 concentrations could be affected by the use of general reaction rate constants for reactions of RO_2 with HO_2 and NO (KRO2HO2 and KRO2NO), respectively. This might be an oversimplification for highly functionalized compounds. A sensitivity test (see the Supplement) with an enhanced reaction rate for $RO_2 + NO$ reactions of 2× KRO2NO in the modified mechanism by Fantechi et al. (2002) was performed. As a result, the fraction of RO_2 reacting with NO instead of HO_2 is increased. This leads to an enhanced HO_2 concentration of approximately 50 % compared to the model run FAN_a. However, HO_x concentrations are again underestimated compared to measurements, and the sensitivity run cannot reproduce the HO_2 concentration time behavior from observations.

Besides reactions with NO, new types of RO_2 reactions have been recognized in the last decade that can produce HO_x. These processes include unimolecular autoxidation reactions of RO_2 (e.g., Crounse et al., 2013) and reactions of RO_2 with HO_2 yielding OH (e.g., Hasson et al., 2004). The new types of reactions become potentially important when NO concentrations are below 1 ppbv. These reactions are especially favored when the RO_2 molecule contains functional groups, like carbonyl groups as in the case of pinonaldehyde peroxy radicals. For example, acetyl- and acetonyl-RO_2 can react with HO_2, forming alkoxy radicals and OH instead of terminating the radical reaction chain and forming hydroxyperoxides (Hasson et al., 2004; Dillon and Crowley, 2008). Other examples are reactions already included in the MCM, such as the photooxidation of methyl vinyl ketone (Praske et al., 2015; Fuchs et al., 2018). For pinonaldehyde, there have been no comparable reactions suggested so far, although pinonaldehyde and its degradation products have at least two carbonyl functions. Because 80 % to 45 % of RO_2 reacts with HO_2 for conditions of the experiment here, such reaction pathways have the potential to impact the OH production rate. A sensitivity test (not shown here) shows that $RO_2 + HO_2$ reactions of RO_2 included in the mechanism with a rate of 10× KRO2HO2 can reproduce measured OH concentrations. Nevertheless, the enhanced HO_2 consumption increases the model–measurement discrepancy of HO_2 even more.

Reported autoxidation reactions of RO_2, which produce HO_x without NO, involve isomerization and decomposi-

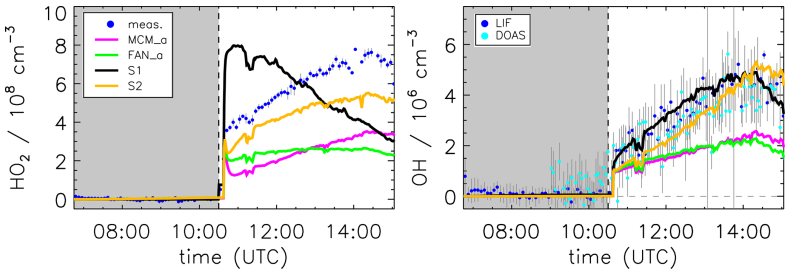

Figure 8. Model sensitivity study of the impact of potential additional HO_2 formation by unimolecular RO_2 reactions (S1) or photolysis of pinonaldehyde oxidation products (S2) compared to the model base case (MCM_a) and the case using the mechanism by Fantechi et al. (2002) (FAN_a). See Table 2 for differences in the model runs. Grey-shaded areas indicate times when the chamber roof was closed.

tion of organic peroxy radicals. These reactions play a role, for example, in the photooxidation of isoprene (e.g., Fuchs et al., 2013; Peeters et al., 2014; Novelli et al., 2020) and methacrolein (Crounse et al., 2012; Fuchs et al., 2014), where H-shift reactions in RO_2 species lead to decomposition into a radical (OH or HO_2) and a carbonyl compound. In general, rate coefficients of H-shift reactions are strongly enhanced by the presence of functional groups such as carbonyl groups, and can reach values on the order of $0.1\,s^{-1}$ at room temperature (Crounse et al., 2013; Otkjær et al., 2018). Depending on the specific RO_2 structure and its functional groups, either OH or HO_2 can be formed. The presence of hydroxyl or hydroperoxy groups in carbonyl peroxy radicals, for example, favors the elimination of HO_2.

In the chemical degradation of pinonaldehyde to its first-generation products (Fig. 1), a large number of multifunctional peroxy and alkoxy radicals are formed as intermediates. Thus, there is potential for additional HO_2 formation by unimolecular reactions. This possibility is explored in a model sensitivity run for the four oxidation branches I–IV (Fantechi et al., 2002), which follow OH addition to pinonaldehyde. The model run S1 (see the Supplement) assumes that each of the initially formed peroxy radicals (C96CO3, FAN_D1, PINALO2, and FAN_G1) is eventually converted to HO_2 with a rate coefficient of $0.1\,s^{-1}$. However, only FAN_D1, PINALO2, and FAN_G1 have an aldehyde group with a hydrogen that can be easily abstracted (see the Supplement). The model run (Fig. 8) shows a considerable enhancement of the HO_2 concentration level in the first period of the experiment compared to model runs MCM_a and FAN_a, leading to good agreement between modeled and measured OH. However, the temporal trend of the modeled HO_2 is not well described. While the observed HO_2 shows a steady increase from the beginning to the end of the experiment, the simulation S1 shows a continuous decrease that follows the concentration of the short-lived RO_2 radicals. The opposite temporal trend suggests that additional HO_2 formation by a fast process in the oxidation branches I–IV is not a likely explanation. It indicates that the additionally required HO_2 is slowly built up, probably from stable products of the pinonaldehyde oxidation.

One such possibility would be the photolysis of first-generation products. This idea is tested in model run S2 (Table 2, Fig. 8). All products of the pinonaldehyde photooxidation have either two or three carbonyl groups and therefore are likely to undergo photolysis. CO23C4CHO and C818CO even have conjugated carbonyl functions similar to glyoxal, which photolysis is up to 2 times faster than pinonaldehyde. However, using the photolysis frequency of glyoxal as an upper limit for the photolysis frequency of the products formed here, is not sufficient to significantly improve the HO_2 model–measurement agreement. Only if a strongly enhanced photolysis frequency equivalent to $0.2 \times j_{NO2}$ is applied, does modeled HO_2 comes close to the observed values. In this case, the temporal trend of the simulation is similar to the observed time behavior of HO_2 and also OH is reasonably well reproduced. This supports the hypothesis that the additional HO_2 is slowly formed from stable oxidation products. However, the value for the assumed photolysis frequency, which is 200 times larger than of pinonaldehyde, appears unrealistically high.

Another possibility is that the fast H-shift isomerization of RO_2 radicals (see the Supplement) leads to the formation of peroxy acids with additional carbonyl functions in high yields. As discussed above, these bi-functional compounds could photolyze faster than currently implemented in the mechanism. A sensitivity test (S1_mod_hv; see the Supplement) was performed that includes isomerization of RO_2 with a $-HCO$ group. Products are assumed to photolyze with a photolysis rate that is 2 times higher than that of glyoxal. Implementation of these reactions leads to HO_2 concentrations that are increased by up to 60 % compared to the sensitivity run that includes only isomerization reactions. Calculated HO_2 concentrations underestimate measurements by

factor of 2. The sensitivity test reproduces measured OH concentrations within the measurement uncertainty.

No subsequent chemistry of 4-hydroxynorpinonaldehyde is included in the mechanism so far. In the experiment here, 4-hydroxynorpinonaldehyde is formed with an overall yield of approximately 25 %. 4-hydroxynorpinonaldehyde is highly functionalized and RO_2 radicals formed in its degradation could undergo fast isomerization reactions. For a sensitivity run (S3; see the Supplement) a mechanism was deduced with the structure–activity relationship (SAR; Kwok and Atkinson, 1995; Vereecken and Peeters, 2009; Vereecken and Nozière, 2020) method. However, the impact of the tested 4-hydroxynorpinonaldehyde degradation scheme on the HO_2 formation was small (≤ 10 %) compared to the modified mechanism by Fantechi et al. (2002). Unfortunately, no measurements of stable oxidation products other than acetone and HCHO were available. Without further product measurements the whole analysis discussed here relies on product distribution prescribed by the models. Further experiments that measure oxidation products and yields could help to better constrain branching ratios in degradation mechanisms. In addition, theoretical studies could investigate subsequent degradation schemes of major products in more detail.

The continuous increase in the acetone and formaldehyde yields during the experiment (Fig. 5) indicates that both species are not only formed from the first reaction step of pinonaldehyde with OH but also from further oxidation of organic products.

The base model (Fig. 3, MCM) underestimates the pinonaldehyde consumption but shows a good model–measurement agreement with formaldehyde and acetone within the measurement uncertainty. In contrast, the model, which uses measured pinonaldehyde photolysis frequencies and is constrained to measured HO_2, produces up to 30 % less acetone and formaldehyde than measured (Fig. 5, MCM_b). The discrepancies increase quickly during the first 2 h of the experiment, when pinonaldehyde is the most important reaction partner for OH, and slow down when oxidation products gain importance at later times of the experiment. The elevated HO_2 concentrations change the product distribution compared to the base case with less formed formaldehyde and acetone because $RO_2 + HO_2$ reactions producing hydroxyperoxides become more important compared to the $RO_2 + NO$ pathway. In the chemical model, acetone and formaldehyde of this reaction pathway are formed by the slow photolysis (10 times slower than the photolysis of pinonaldehyde) of pinonic acid and perpinonic acid that are produced in the subsequent chemistry of hydroxyperoxides. Therefore, acetone and formaldehyde yields are smaller in the MCM model run, if HO_2 concentrations are correctly described compared to the base case MCM model, when HO_2 is significantly underestimated.

Implementation of the mechanism by Fantechi et al. (2002) with HO_2 concentrations and pinonaldehyde photolysis frequency also constrained to measurements (FAN_b) makes the model–measurement agreement for acetone and formaldehyde worse. Acetone and formaldehyde yields are lowered and 4-hydroxynorpinonaldehyde and norpinonaldehyde are produced instead. Acetone and formaldehyde time series agree for the photolysis experiment, when the mechanism by Fantechi et al. (2002) is applied. Similarly, the majority of consumed pinonaldehyde (approximately 65 %) forms the peroxy radical C96O2 either by photolysis or reaction pathway I (Fig. 1), when OH is also present. Therefore, it can be assumed that the C96O2 + NO reaction channel is not responsible for the underprediction of acetone and formaldehyde, at least for the early times of the experiments, when contributions from OH reactions of product species are small. However, because $RO_2 + HO_2$ reactions are more important in the experiment with OH oxidation (see above), additional HO_2 production from this reaction pathway has the potential to serve as an explanation for the observed discrepancies. In addition, minor pathways could produce additional formaldehyde and acetone to explain the model–measurement discrepancy right after the start of the pinonaldehyde oxidation. At later times of the experiment, additional production of acetone and formaldehyde from the further degradation of oxidation products need to be assumed to close the gap. For example, this could be due to a reaction channel of the alkoxy radical R′O8 that does not produce norpinonaldehyde but produces acetone and formaldehyde instead. However, the exact chemical mechanism that is responsible for the additional acetone and formaldehyde cannot be determined from measurements in these experiments.

Presently, there is only one work of Noziére et al. (1999) where acetone and formaldehyde were quantitatively measured for the reaction of pinonaldehyde with OH. The formaldehyde yield was determined to be 1.52 ± 0.56, significantly higher than the yield measured in this work. The acetone yield in Noziére et al. (1999) lies with 0.15 ± 0.07 in the range of the acetone yield determined here for the times of the experiment when pinonaldehyde is the dominant OH reactant. In the oxidation scheme of pinonaldehyde, acetone and formaldehyde are typically formed together so that similar yields would be expected. The high HCHO yield measured by Noziére et al. (1999) can be partially explained by additional fast photolysis of pinonaldehyde and possibly other products by the 254 nm lamps used to generate OH by photodissociation of H_2O_2 (Fantechi et al., 2002).

5 Summary and conclusions

The photooxidation of pinonaldehyde was investigated under natural sunlight at low NO concentrations (< 0.2 ppbv) in the presence and absence of an OH scavenger. Two experiments were conducted with maximum pinonaldehyde concentrations of 16.5 ppbv (with OH scavenger) and 6.5 ppbv (without OH scavenger). Measured times series were com-

pared to model calculations based on the recent version of the Master Chemical Mechanism (version 3.3.1).

Model results show that the pinonaldehyde consumption is underestimated in the experiment with OH scavenger. In contrast, the concentration of the measured products acetone and formaldehyde is overestimated by 60 % and 70 %, respectively. The observed decay of pinonaldehyde requires a quantum yield of 0.9 for the photolysis reaction. Previous investigations of the quantum yield determined lower yields of 0.15 (Moortgat et al., 2002) and ≤ 0.4 (Jaoui and Kamens, 2003). However, the solar actinic flux could not accurately be determined in these other chamber studies and large corrections for wall loss were applied. Calculations using the measured absorption spectrum (Hallquist et al., 1997) and a quantum yield of 0.9 give photolysis frequencies, which are a factor of 3.5 times higher than values calculated by the parameterization implemented in the MCM, and thus photolysis of pinonaldehyde is significantly underestimated if this parameterization is applied.

Similarly, the pinonaldehyde consumption is underestimated by the MCM model in the experiment, where the pinonaldehyde consumption is dominated by its reaction with OH radicals. Implementing the measured photolysis frequency improves model–measurement agreement. The remaining discrepancy is caused by underestimated OH radical concentrations leading to a slower pinonaldehyde consumption. Constraining HO_2 model concentrations to the measurements brings OH concentrations in model and measurement into agreement. As a consequence, the pinonaldehyde concentration profile is also reproduced within the measurement uncertainty. The closed OH budget indicates that a HO_2 source is missing in this mechanism. The additional HO_2 source would be at least half the rate at which pinonaldehyde is consumed. HO_2 would therefore need to be reproduced much faster than current chemical models suggest in one of the major oxidation pathways. Because a large fraction of RO_2 radicals (45 %–80 %) react with HO_2, potential reaction pathways that do not lead to the formation of hydroxyperoxide but reform radicals have the potential to contribute the regeneration of HO_2. If fast unimolecular RO_2 reactions existed that could compete with $RO_2 + NO$ and $RO_2 + HO_2$ reactions, they could also add to additional HO_2 production. Nevertheless, a fast degradation of first-generation product species forming HO_2 shows a better agreement with measured HO_2 concentration time profiles rather than reactions of RO_2 species.

The yield of formaldehyde in the pinonaldehyde photolysis with OH scavenger present is determined to be 0.18 ± 0.20. No acetone formation is observed. Model calculations based on the MCM constrained with the measured photolysis frequency overestimate formaldehyde and acetone concentrations by a factor of approximately 3. In the experiment with OH the yields of acetone and formaldehyde increase over the course of the experiment from (0.2 ± 0.1) to (0.3 ± 0.1) and from (0.15 ± 0.2) to (0.45 ± 0.2), respectively. The increasing yields indicate that both species are also formed by the subsequent chemistry of products formed in the first reaction steps.

Modifications of the degradation mechanism proposed by Fantechi et al. (2002), including a new product distribution and additional products for the initial attack of OH, reproduce measured acetone and formaldehyde concentrations within their uncertainty as long as the reaction with OH is suppressed. In the experiment with OH, the model–measurement agreement for both species decreases after implementing the modifications by Fantechi et al. (2002). This indicates that the pathways relevant when OH is dominating the fate of pinonaldehyde lack sources of acetone and formaldehyde in this case.

Field campaigns in environments dominated by monoterpene emissions like the Bio-hydro-atmosphere interactions of Energy, Aerosols, Carbon, H2O, Organics, and Nitrogen–Rocky Mountain Organic Carbon Study (BEACHON-ROCS; Kim et al., 2013) or the Hyytiälä United Measurements of Photochemistry and Particles in Air – Comprehensive Organic Precursor Emission and Concentration study (HUMPPA-COPEC; Hens et al., 2014) showed that OH and HO_2 radical concentrations were underestimated in model calculations by up to a factor of 2.5. Constraining modeled HO_2 concentrations to measurements allowed for reproducing OH radical concentrations. In addition, chamber studies on the photooxidation of α-pinene (Rolletter et al., 2019) and β-pinene (Kaminski et al., 2017) also confirmed that the current α-pinene and β-pinene mechanisms lack HO_2 sources. It is currently unknown if the missing source is part of reactions forming first-generation products or the subsequent chemistry of the degradation products. Here, it is shown that in the mechanism of the photooxidation of pinonaldehyde, a degradation product of α-pinene, a HO_2 source is also missing. However, the findings here cannot explain the discrepancies observed in the α-pinene chamber experiments and field campaigns because the pinonaldehyde yield in the α-pinene degradation is rather small (5 %, Rolletter et al. (2019)). Nevertheless, this result is an example for a second-generation species that produces significantly more HO_2 than suggested in current chemical models. Further experiments will be required to investigate whether other oxidation products from the degradation of monoterpenes could also explain observations of missing HO_2 sources.

Data availability. Data of the experiments in the SAPHIR chamber used in this work are available on the EUROCHAMP data homepage: https://doi.org/10.25326/G53K-WH75 (Fuchs et al., 2020a) and https://doi.org/10.25326/887C-F682 (Fuchs et al., 2020b).

Supplement. The supplement related to this article is available online at: https://doi.org/10.5194/acp-20-13701-2020-supplement.

Author contributions. MR analyzed the data and wrote the paper. HF and MK designed the experiments. HF conducted the HO_x radical measurements. BB conducted the radiation measurements. MK and RW were responsible for the GC measurements. RT was responsible for the PTR-TOF-MS measurements. XL was responsible for the HONO measurements and H-PD for the DOAS OH data. FR was responsible for the NO_x and O_3 data. All co-authors commented on the manuscript.

Competing interests. The authors declare that they have no conflict of interest.

Special issue statement. This article is part of the special issue "Simulation chambers as tools in atmospheric research (AMT/ACP/GMD inter-journal SI)". It is not associated with a conference.

Acknowledgements. This work was supported by the EU Horizon 2020 program Eurochamp2020 (grant agreement no. 730997). This project has received funding from the European Research Council (ERC) under the European Union's Horizon 2020 research and innovation programme (SARLEP grant agreement no. 681529). The authors thank Luc Vereecken for his help with the 4-hydroxynorpinonaldehyde mechanism.

Financial support. This research has been supported by the European Commission, H2020 Research Infrastructures (grant no. EUROCHAMP-2020 (730997)) and the European Commission, H2020 European Research Council (grant no. SARLEP (681529)).

The article processing charges for this open-access publication were covered by a Research Centre of the Helmholtz Association.

Review statement. This paper was edited by Jean-Francois Doussin and reviewed by William Carter and two anonymous referees.

References

Alves, C., Carvalho, A., and Pio, C.: Mass balance of organic carbon fractions in atmospheric aerosols, J. Geophys. Res.-Atmos., 107, ICC7-1–ICC7-9, https://doi.org/10.1029/2001jd000616, 2002.

Atkinson, R. and Arey, J.: Atmospheric degradation of volatile organic compounds, Chem. Rev., 103, 4605–4638, https://doi.org/10.1021/cr0206420, 2003.

Atkinson, R., Baulch, D. L., Cox, R. A., Crowley, J. N., Hampson, R. F., Hynes, R. G., Jenkin, M. E., Rossi, M. J., and Troe, J.: Evaluated kinetic and photochemical data for atmospheric chemistry: Volume I – gas phase reactions of O_x, HO_x, NO_x and SO_x species, Atmos. Chem. Phys., 4, 1461–1738, https://doi.org/10.5194/acp-4-1461-2004, 2004.

Atkinson, R., Baulch, D. L., Cox, R. A., Crowley, J. N., Hampson, R. F., Hynes, R. G., Jenkin, M. E., Rossi, M. J., Troe, J., and IUPAC Subcommittee: Evaluated kinetic and photochemical data for atmospheric chemistry: Volume II – gas phase reactions of organic species, Atmos. Chem. Phys., 6, 3625–4055, https://doi.org/10.5194/acp-6-3625-2006, 2006.

Bohn, B. and Zilken, H.: Model-aided radiometric determination of photolysis frequencies in a sunlit atmosphere simulation chamber, Atmos. Chem. Phys., 5, 191–206, https://doi.org/10.5194/acp-5-191-2005, 2005.

Bohn, B., Rohrer, F., Brauers, T., and Wahner, A.: Actinometric measurements of NO_2 photolysis frequencies in the atmosphere simulation chamber SAPHIR, Atmos. Chem. Phys., 5, 493–503, https://doi.org/10.5194/acp-5-493-2005, 2005

Boy, M., Petäjä, T., Dal Maso, M., Rannik, Ü., Rinne, J., Aalto, P., Laaksonen, A., Vaattovaara, P., Joutsensaari, J., Hoffmann, T., Warnke, J., Apostolaki, M., Stephanou, E. G., Tsapakis, M., Kouvarakis, A., Pio, C., Carvalho, A., Römpp, A., Moortgat, G., Spirig, C., Guenther, A., Greenberg, J., Ciccioli, P., and Kulmala, M.: Overview of the field measurement campaign in Hyytiälä, August 2001 in the framework of the EU project OSOA, Atmos. Chem. Phys., 4, 657–678, https://doi.org/10.5194/acp-4-657-2004, 2004.

Cahill, T. M., Seaman, V. Y., Charles, M. J., Holzinger, R., and Goldstein, A. H.: Secondary organic aerosols formed from oxidation of biogenic volatile organic compounds in the Sierra Nevada Mountains of California, J. Geophys. Res.-Atmos., 111, D16312, https://doi.org/10.1029/2006jd007178, 2006.

Calogirou, A., Larsen, B. R., and Kotzias, D.: Gas-phase terpene oxidation products: a review, Atmos. Environ., 33, 1423–1439, https://doi.org/10.1016/S1352-2310(98)00277-5, 1999.

Capouet, M., Peeters, J., Nozi'ere, B., and Müller, J.-F.: Alpha-pinene oxidation by OH: simulations of laboratory experiments, Atmos. Chem. Phys., 4, 2285–2311, https://doi.org/10.5194/acp-4-2285-2004, 2004.

Crounse, J. D., Knap, H. C., Ornso, K. B., Jorgensen, S., Paulot, F., Kjaergaard, H. G., and Wennberg, P. O.: On the atmospheric fate of methacrolein: 1. Peroxy radical isomerization following addition of OH and O_2, J. Phys. Chem. A, 116, 5756–5762, https://doi.org/10.1021/jp211560u, 2012.

Crounse, J. D., Nielsen, L. B., Jørgensen, S., Kjaergaard, H. G., and Wennberg, P. O.: Autoxidation of organic compounds in the atmosphere, J. Phys. Chem. Lett., 4, 3513–3520, https://doi.org/10.1021/jz4019207, 2013.

Dash, M. R. and Rajakumar, B.: Abstraction kinetics of H-atom by OH radical from pinonaldehyde ($C_{10}H_{16}O_2$): Ab initio and transition-state theory Calculations, J. Phys. Chem. A, 116, 5856–5866, https://doi.org/10.1021/jp209208e, 2012.

Daumont, D., Brion, J., Charbonnier, J., and Malicet, J.: Ozone UV spectroscopy I: Absorption cross-sections at room temperature, J. Atmos. Chem., 15, 145–155, https://doi.org/10.1007/bf00053756, 1992.

Dillon, T. J. and Crowley, J. N.: Direct detection of OH formation in the reactions of HO_2 with $CH_3C(O)O_2$ and other substituted peroxy radicals, Atmos. Chem. Phys., 8, 4877–4889, https://doi.org/10.5194/acp-8-4877-2008, 2008.

Dorn, H.-P., Brandenburger, U., Brauers, T., and Hausmann, M.: A new in-situ laser long-path absorption instrument for the mea-

surement of tropospheric OH radicals, J. Atmos. Sci., 52, 3373–3380, 1995a.

Dorn, H. P., Neuroth, R., and Hofzumahaus, A.: Investigation of OH absorption cross sections of rotational transitions in the $A^2\Sigma^+$, $\nu' = 0 \leftarrow X^2\Pi$, $\nu{-}0$ band under atmospheric conditions: Implications for tropospheric long-path absorption measurements, J. Geophys. Res., 100, 7397–7409, https://doi.org/10.1029/94jd03323, 1995b.

Fantechi, G., Vereecken, L., and Peeters, J.: The OH-initiated atmospheric oxidation of pinonaldehyde: Detailed theoretical study and mechanism construction, Phys. Chem. Chem. Phys., 4, 5795–5805, https://doi.org/10.1039/B205901K, 2002.

Fuchs, H., Bohn, B., Hofzumahaus, A., Holland, F., Lu, K. D., Nehr, S., Rohrer, F., and Wahner, A.: Detection of HO_2 by laser-induced fluorescence: calibration and interferences from RO_2 radicals, Atmos. Meas. Tech., 4, 1209–1225, https://doi.org/10.5194/amt-4-1209-2011, 2011.

Fuchs, H., Dorn, H.-P., Bachner, M., Bohn, B., Brauers, T., Gomm, S., Hofzumahaus, A., Holland, F., Nehr, S., Rohrer, F., Tillmann, R., and Wahner, A.: Comparison of OH concentration measurements by DOAS and LIF during SAPHIR chamber experiments at high OH reactivity and low NO concentration, Atmos. Meas. Tech., 5, 1611–1626, https://doi.org/10.5194/amt-5-1611-2012, 2012.

Fuchs, H., Hofzumahaus, A., Rohrer, F., Bohn, B., Brauers, T., Dorn, H.-P., Häseler, R., Holland, F., Kaminski, M., Li, X., Lu, K., Nehr, S., Tillmann, R., Wegener, R., and Wahner, A.: Experimental evidence for efficient hydroxyl radical regeneration in isoprene oxidation, Nat. Geosci., 6, 1023–1026, https://doi.org/10.1038/NGEO1964, 2013.

Fuchs, H., Acir, I. H., Bohn, B., Brauers, T., Dorn, H. P., Häseler, R., Hofzumahaus, A., Holland, F., Kaminski, M., Li, X., Lu, K., Lutz, A., Nehr, S., Rohrer, F., Tillmann, R., Wegener, R., and Wahner, A.: OH regeneration from methacrolein oxidation investigated in the atmosphere simulation chamber SAPHIR, Atmos. Chem. Phys., 14, 7895–7908, https://doi.org/10.5194/acp-14-7895-2014, 2014.

Fuchs, H., Albrecht, S., Acir, I., Bohn, B., Breitenlechner, M., Dorn, H.-P., Gkatzelis, G. I., Hofzumahaus, A., Holland, F., Kaminski, M., Keutsch, F. N., Novelli, A., Reimer, D., Rohrer, F., Tillmann, R., Vereecken, L., Wegener, R., Zaytsev, A., Kiendler-Scharr, A., and Wahner, A.: Investigation of the oxidation of methyl vinyl ketone (MVK) by OH radicals in the atmospheric simulation chamber SAPHIR, Atmos. Chem. Phys., 18, 8001–8016, https://doi.org/10.5194/acp-18-8001-2018, 2018.

Fuchs, H., Rolletter, M., Blocquet, M., Kaminski, M., Bohn, B., Dorn, H.-P., Hofzumahaus, A., Holland, F., Li, X., Rohrer, F., Tillmann, R., Wegener, R., Kiendler-Scharr, A., and Wahner, A.: Atmospheric simulation chamber study: pinonaldehyde + OH − Gas-phase oxidation − product study [Data set], AERIS, https://doi.org/10.25326/G53K-WH75, 2020a.

Fuchs, H., Rolletter, M., Blocquet, M., Kaminski, M., Bohn, B., Dorn, H.-P., Hofzumahaus, A., Holland, F., Li, X., Rohrer, F., Tillmann, R., Wegener, R., Kiendler-Scharr, A., and Wahner, A.: Atmospheric simulation chamber study: pinonaldehyde + OH − Gas-phase oxidation − product study [Data set], AERIS, https://doi.org/10.25326/887C-F682, 2020b.

Galloway, M. M., Huisman, A. J., Yee, L. D., Chan, A. W. H., Loza, C. L., Seinfeld, J. H., and Keutsch, F. N.: Yields of oxidized volatile organic compounds during the OH radical initiated oxidation of isoprene, methyl vinyl ketone, and methacrolein under high-NO_x conditions, Atmos. Chem. Phys., 11, 10779–10790, https://doi.org/10.5194/acp-11-10779-2011, 2011.

Gautrois, M. and Koppmann, R.: Diffusion technique for the production of gas standards for atmospheric measurements, J. Chromatography A, 848, 239–249, https://doi.org/10.1016/S0021-9673(99)00424-0, 1999.

Glasius, M., Calogirou, A., Jensen, J., Hjorth, J., and Nielsen, C. J.: Kinetic study of gas-phase reactions of pinonaldehyde and structurally related compounds, Int. J. Chem. Kin., 29, 527–533, https://doi.org/10.1002/(sici)1097-4601(1997)29:7<527::Aid-kin7>3.0.Co;2-w, 1997.

Guenther, A. B., Jiang, X., Heald, C. L., Sakulyanontvittaya, T., Duhl, T., Emmons, L. K., and Wang, X.: The Model of Emissions of Gases and Aerosols from Nature version 2.1 (MEGAN2.1): an extended and updated framework for modeling biogenic emissions, Geosci. Model Dev., 5, 1471–1492, https://doi.org/10.5194/gmd-5-1471-2012, 2012.

Hallquist, M., Wängberg, I., and Ljungström, E.: Atmospheric fate of carbonyl oxidation products originating from α-pinene and Δ^3-carene: determination of rate of reaction with OH and NO_3 radicals, UV absorption cross sections, and vapor pressures, Environ. Sci. Technol., 31, 3166–3172, https://doi.org/10.1021/es970151a, 1997.

Hasson, A. S., Tyndall, G. S., and Orlando, J. J.: A product yield study of the reaction of HO_2 radicals with ethyl peroxy ($C_2H_5O_2$), acetyl peroxy ($CH_3C(O)O_2$), and acetonyl peroxy ($CH_3C(O)CH_2O_2$) radicals, J. Phys. Chem. A, 108, 5979–5989, https://doi.org/10.1021/jp048873t, 2004.

Hausmann, M., Brandenburger, U., Brauers, T., and Dorn, H.-P.: Detection of tropospheric OH radicals by long-path differential-optical-absorption spectroscopy: Experimental setup, accuracy, and precision, J. Geophys. Res., 102, 16011–16022, https://doi.org/10.1029/97jd00931, 1997.

Hens, K., Novelli, A., Martinez, M., Auld, J., Axinte, R., Bohn, B., Fischer, H., Keronen, P., Kubistin, D., Nölscher, A. C., Oswald, R., Paasonen, P., Petäjä, T., Regelin, E., Sander, R., Sinha, V., Sipilä, M., Taraborrelli, D., Tatum Ernest, C., Williams, J., Lelieveld, J., and Harder, H.: Observation and modelling of HO_x radicals in a boreal forest, Atmos. Chem. Phys., 14, 8723–8747, https://doi.org/10.5194/acp-14-8723-2014, 2014.

Herckes, P., Engling, G., Kreidenweis, S. M., and Collett, J. L.: Particle size distributions of organic aerosol constituents during the 2002 Yosemite Aerosol Characterization Study, Environ. Sci. Technol., 40, 4554–4562, https://doi.org/10.1021/es0515396, 2006.

Hofzumahaus, A.: Measurement of Photolysis Frequencies in the Atmosphere, in: Analytical Techniques for Atmospheric Measurement, edited by: Heard, D. E., book section 9, pp. 406–500, https://doi.org/10.1002/9780470988510.ch9, 2006.

Holland, F., Hofzumahaus, A., Schäfer, J., Kraus, A., and Pätz, H. W.: Measurements of OH and HO_2 radical concentrations and photolysis frequencies during BERLIOZ, J. Geophys. Res., 108, 8246, https://doi.org/10.1029/2001JD001393, 2003.

Jacob, D. J., Field, B. D., Jin, E. M., Bey, I., Li, Q., Logan, J. A., and Yantosca, R. M.: Atmospheric acetone budget, J. Geophys. Res., 107, 4100, https://doi.org/10.1029/2001JD000694, 2002.

Jaoui, M. and Kamens, R. M.: Gas phase photolysis of pinonaldehyde in the presence of sunlight, Atmos. Environ., 37, 1835–1851, https://doi.org/10.1016/S1352-2310(03)00033-5, 2003.

Jenkin, M. E., Saunders, S. M., and Pilling, M. J.: The tropospheric degradation of volatile organic compounds: A protocol for mechanism development, Atmos. Environ., 31, 81–104, https://doi.org/10.1016/S1352-2310(96)00105-7, 1997.

Jordan, A., Haidacher, S., Hanel, G., Hartungen, E., Märk, L., Seehauser, H., Schottkowsky, R., Sulzer, P., and Märk, T. D.: A high resolution and high sensitivity proton-transfer-reaction time-of-flight mass spectrometer (PTR-TOF-MS), Int. J. Mass Spectrom., 286, 122–128, https://doi.org/10.1016/j.ijms.2009.07.005, 2009.

Kaminski, M., Fuchs, H., Acir, I.-H., Bohn, B., Brauers, T., Dorn, H.-P., Häseler, R., Hofzumahaus, A., Li, X., Lutz, A., Nehr, S., Rohrer, F., Tillmann, R., Vereecken, L., Wegener, R., and Wahner, A.: Investigation of the β-pinene photooxidation by OH in the atmosphere simulation chamber SAPHIR, Atmos. Chem. Phys., 17, 6631–6650, https://doi.org/10.5194/acp-17-6631-2017, 2017.

Kanakidou, M., Tsigaridis, K., Dentener, F. J., and Crutzen, P. J.: Human-activity-enhanced formation of organic aerosols by biogenic hydrocarbon oxidation, J. Geophys. Res., 105, 9243–9354, https://doi.org/10.1029/1999JD901148, 2000.

Karl, M., Dorn, H.-P., Holland, F., Koppmann, R., Poppe, D., Rupp, L., Schaub, A., and Wahner, A.: Product study of the reaction of OH radicals with isoprene in the atmosphere simulation chamber SAPHIR, J. Atmos. Chem., 55, 167–187, https://doi.org/10.1007/s10874-006-9034-x, 2006.

Kavouras, I. G., Mihalopoulos, N., and Stephanou, E. G.: Formation and gas/particle partitioning of monoterpenes photooxidation products over forests, Geophys. Res. Lett., 26, 55–58, https://doi.org/10.1029/1998gl900251, 1999.

Kim, S., Wolfe, G. M., Mauldin, L., Cantrell, C., Guenther, A., Karl, T., Turnipseed, A., Greenberg, J., Hall, S. R., Ullmann, K., Apel, E., Hornbrook, R., Kajii, Y., Nakashima, Y., Keutsch, F. N., DiGangi, J. P., Henry, S. B., Kaser, L., Schnitzhofer, R., Graus, M., Hansel, A., Zheng, W., and Flocke, F. F.: Evaluation of HO_x sources and cycling using measurement-constrained model calculations in a 2-methyl-3-butene-2-ol (MBO) and monoterpene (MT) dominated ecosystem, Atmos. Chem. Phys., 13, 2031–2044, https://doi.org/10.5194/acp-13-2031-2013, 2013.

Kwok, E. S. C. and Atkinson, R.: Estimation of hydroxyl radical reaction rate constants for gas-phase organic compounds using a structure-reactivity relationship: An update, Atmos. Environ., 29, 1685–1695, https://doi.org/10.1016/1352-2310(95)00069-B, 1995.

Larsen, B. R., Di Bella, D., Glasius, M., Winterhalter, R., Jensen, N. R., and Hjorth, J.: Gas-phase OH oxidation of monoterpenes: Gaseous and particulate products, J. Atmos. Chem., 38, 231–276, https://doi.org/10.1023/A:1006487530903, 2001.

Lew, M. M., Dusanter, S., and Stevens, P. S.: Measurement of interferences associated with the detection of the hydroperoxy radical in the atmosphere using laser-induced fluorescence, Atmos. Meas. Tech., 11, 95–109, https://doi.org/10.5194/amt-11-95-2018, 2018.

Li, X., Rohrer, F., Hofzumahaus, A., Brauers, T., Häseler, R., Bohn, B., Broch, S., Fuchs, H., Gomm, S., Holland, F., Jäger, J., Kaiser, J., Keutsch, F. N., Lohse, I., Lu, K., Tillmann, R., Wegener, R., Wolfe, G. M., Mentel, T. F., Kiendler-Scharr, A., and Wahner, A.: Missing gas-phase source of HONO inferred from Zeppelin measurements in the troposphere, Science, 344, 292–296, https://doi.org/10.1126/science.1248999, 2014.

Lindinger, W., Hansel, A., and Jordan, A.: On-line monitoring of volatile organic compounds at pptv levels by means of proton-transfer-reaction mass spectrometry (PTR-MS) – Medical applications, food control and environmental research, Int. J. Mass Spectrom., 173, 191–241, https://doi.org/10.1016/s0168-1176(97)00281-4, 1998.

Martinez, R. D., Buitrago, A. A., Howell, N. W., Hearn, C. H., and Joens, J. A.: The near U.V. absorption spectra of several aliphatic aldehydes and ketones at 300 K, Atmos. Environ., 26, 785–792, https://doi.org/10.1016/0960-1686(92)90238-G, 1992.

Matsumi, Y., Comes, F. J., Hancock, G., Hofzumahaus, A., Hynes, A. J., Kawasaki, M., and Ravishankara, A. R.: Quantum yields for production of $O(^1D)$ in the ultraviolet photolysis of ozone: Recommendation based on evaluation of laboratory data, J. Geophys. Res.-Atmos., 107, ACH1-1–ACH1-12, https://doi.org/10.1029/2001jd000510, 2002.

MCM: Master Chemical Mechanism, available at: http://mcm.leeds.ac.uk/MCM/ (last access: 4 March 2020), 2017.

Mérienne, M. F., Jenouvrier, A., and Coquart, B.: The NO_2 absorption spectrum. I: Absorption cross-sections at ambient temperature in the 300–500 nm region, J. Atmos. Chem., 20, 281–297, https://doi.org/10.1007/bf00694498, 1995.

Moortgat, G., Wirtz, K., Hjorth, J., Ljungstrom, E., Ruppert, L., Hayman, G., and Mellouki, W.: ''Evaluation of radical sources in atmospheric chemistry through chamber and laboratory studies'', Final report on the EU project "RADICAL", Report EUR 20254 EN, 2002.

Müller, K., Haferkorn, S., Grabmer, W., Wisthaler, A., Hansel, A., Kreuzwieser, J., Cojocariu, C., Rennenberg, H., and Herrmann, H.: Biogenic carbonyl compounds within and above a coniferous forest in Germany, Atmos. Environ., 40, 81–91, https://doi.org/10.1016/j.atmosenv.2005.10.070, 2006.

Novelli, A., Vereecken, L., Bohn, B., Dorn, H.-P., Gkatzelis, G. I., Hofzumahaus, A., Holland, F., Reimer, D., Rohrer, F., Rosanka, S., Taraborrelli, D., Tillmann, R., Wegener, R., Yu, Z., Kiendler-Scharr, A., Wahner, A., and Fuchs, H.: Importance of isomerization reactions for OH radical regeneration from the photooxidation of isoprene investigated in the atmospheric simulation chamber SAPHIR, Atmos. Chem. Phys., 20, 3333–3355, https://doi.org/10.5194/acp-20-3333-2020, 2020.

Noziére, B., Barnes, I., and Becker, K.-H.: Product study and mechanisms of the reactions of α-pinene and of pinonaldehyde with OH radicals, J. Geophys. Res., 104, 23645–23656, https://doi.org/10.1029/1999JD900778, 1999.

Otkjær, R. V., Jakobsen, H. H., Tram, C. M., and Kjaergaard, H. G.: Calculated Hydrogen Shift Rate Constants in Substituted Alkyl Peroxy Radicals, J. Phys. Chem. A,, 122, 8665–8673, https://doi.org/10.1021/acs.jpca.8b06223, 2018.

Peeters, J., Vereecken, L., and Fantechi, G.: The detailed mechanism of the OH-initiated atmospheric oxidation of α-pinene: a theoretical study, Phys. Chem. Chem. Phys., 3, 5489–5504, https://doi.org/10.1039/B106555F, 2001.

Peeters, J., Müller, J.-F., Stavrakou, T., and Nguyen, V. S.: Hydroxyl radical recycling in isoprene oxidation driven by hydrogen bonding and hydrogen tunneling: The upgraded

LIM1 mechanism, J. Phys. Chem. A, 118, 8625–8643, https://doi.org/10.1021/jp5033146, 2014.

Plewka, A., Gnauk, T., Bruggemann, E., and Herrmann, H.: Biogenic contributions to the chemical composition of airborne particles in a coniferous forest in Germany, Atmos. Environ., 40, S103–S115, https://doi.org/10.1016/j.atmosenv.2005.09.090, 2006.

Praske, E., Crounse, J. D., Bates, K. H., Kurten, T., Kjaergaard, H. G., and Wennberg, P. O.: Atmospheric fate of methyl vinyl ketone: Peroxy radical reactions with NO and HO_2, J. Phys. Chem. A, 119, 4562–4572, https://doi.org/10.1021/jp5107058, 2015.

Rissanen, T., Hyotylainen, T., Kallio, M., Kronholm, J., Kulmala, M., and Rikkola, M. L.: Characterization of organic compounds in aerosol particles from a coniferous forest by GC-MS, Chemosphere, 64, 1185–1195, https://doi.org/10.1016/j.chemosphere.2005.11.079, 2006.

Rohrer, F. and Brüning, D.: Surface NO and NO_2 mixing ratios measured between 30° N and 30° S in the Atlantic region, J. Atmos. Chem., 15, 253–267, https://doi.org/10.1029/97JD01853, 1992.

Rohrer, F., Bohn, B., Brauers, T., Brüning, D., Johnen, F.-J., Wahner, A., and Kleffmann, J.: Characterisation of the photolytic HONO-source in the atmosphere simulation chamber SAPHIR, Atmos. Chem. Phys., 5, 2189–2201, https://doi.org/10.5194/acp-5-2189-2005, 2005.

Rolletter, M., Kaminski, M., Acir, I.-H., Bohn, B., Dorn, H.-P., Li, X., Lutz, A., Nehr, S., Rohrer, F., Tillmann, R., Wegener, R., Hofzumahaus, A., Kiendler-Scharr, A., Wahner, A., and Fuchs, H.: Investigation of the α-pinene photooxidation by OH in the atmospheric simulation chamber SAPHIR, Atmos. Chem. Phys., 19, 11635–11649, https://doi.org/10.5194/acp-19-11635-2019, 2019.

Satsumabayashi, H., Nishizawa, H., Yokouchi, Y., and Ueda, H.: Pinonaldehyde and some other organics in rain and snow in central Japan, Chemosphere, 45, 887–891, https://doi.org/10.1016/s0045-6535(01)00024-8, 2001.

Saunders, S. M., Jenkin, M. E., Derwent, R. G., and Pilling, M. J.: Protocol for the development of the Master Chemical Mechanism, MCM v3 (Part A): tropospheric degradation of non-aromatic volatile organic compounds, Atmos. Chem. Phys., 3, 161–180, https://doi.org/10.5194/acp-3-161-2003, 2003.

Schlosser, E., Bohn, B., Brauers, T., Dorn, H.-P., Fuchs, H., Häseler, R., Hofzumahaus, A., Holland, F., Rohrer, F., Rupp, L. O., Siese, M., Tillmann, R., and Wahner, A.: Intercomparison of two hydroxyl radical measurement techniques at the atmosphere simulation chamber SAPHIR, J. Atmos. Chem., 56, 187–205, https://doi.org/10.1007/s10874-006-9049-3, 2007.

Schwantes, R. H., Emmons, L. K., Orlando, J. J., Barth, M. C., Tyndall, G. S., Hall, S. R., Ullmann, K., St. Clair, J. M., Blake, D. R., Wisthaler, A., and Bui, T. P. V.: Comprehensive isoprene and terpene gas-phase chemistry improves simulated surface ozone in the southeastern US, Atmos. Chem. Phys., 20, 3739–3776, https://doi.org/10.5194/acp-20-3739-2020, 2020.

Stutz, J., Kim, E. S., Platt, U., Bruno, P., Perrino, C., and Febo, A.: UV-visible absorption cross sections of nitrous acid, J. Geophys. Res.-Atmos., 105, 14585–14592, https://doi.org/10.1029/2000jd900003, 2000.

Tadić, J., Juranić, I., and Moortgat, G. K.: Pressure dependence of the photooxidation of selected carbonyl compounds in air: n-butanal and n-pentanal, J. Photochem. Photobiol. A, 143, 169–179, https://doi.org/10.1016/S1010-6030(01)00524-X, 2001.

Troe, J.: Are primary quantum yields of NO2 photolysis at $\lambda \leq$ 398 nm smaller than unity?, Z. Phys. Chem., 214, 573–581, https://doi.org/10.1524/zpch.2000.214.5.573, 2000.

Vereecken, L. and Nozière, B.: H migration in peroxy radicals under atmospheric conditions, Atmos. Chem. Phys., 20, 7429–7458, https://doi.org/10.5194/acp-20-7429-2020, 2020.

Vereecken, L. and Peeters, J.: Enhanced H-atom abstraction from pinonaldehyde, pinonic acid, pinic acid, and related compounds: theoretical study of C-H bond strengths, Phys. Chem. Chem. Phys., 4, 467–472, https://doi.org/10.1039/B109370C, 2002.

Vereecken, L. and Peeters, J.: Decomposition of substituted alkoxy radicals-part I: a generalized structure-activity relationship for reaction barrier heights, Phys. Chem. Chem. Phys., 11, 9062–9074, https://doi.org/10.1039/B909712K, 2009.

Vereecken, L., Müller, J. F., and Peeters, J.: Low-volatility poly-oxygenates in the OH-initiated atmospheric oxidation of α-pinene: impact of non-traditional peroxyl radical chemistry, Phys. Chem. Chem. Phys., 9, 5241–5248, https://doi.org/10.1039/B708023A, 2007.

Whalley, L. K., Blitz, M. A., Desservettaz, M., Seakins, P. W., and Heard, D. E.: Reporting the sensitivity of laser-induced fluorescence instruments used for HO2 detection to an interference from RO_2 radicals and introducing a novel approach that enables HO_2 and certain RO_2 types to be selectively measured, Atmos. Meas. Tech., 6, 3425–3440, https://doi.org/10.5194/amt-6-3425-2013, 2013.

Xu, L., Møller, K. H., Crounse, J. D., Otkjær, R. V., Kjaergaard, H. G., and Wennberg, P. O.: Unimolecular Reactions of Peroxy Radicals Formed in the Oxidation of α-Pinene and β-Pinene by Hydroxyl Radicals, J. Phys. Chem. A, 123, 1661–1674, https://doi.org/10.1021/acs.jpca.8b11726, 2019.

Yu, J. Z., Griffin, R. J., Cocker, D. R., Flagan, R. C., Seinfeld, J. H., and Blanchard, P.: Observation of gaseous and particulate products of monoterpene oxidation in forest atmospheres, Geophys. Res. Lett., 26, 1145–1148, https://doi.org/10.1029/1999gl900169, 1999.

6 Summary and discussion of BVOC studies

This chapter summarizes and discusses the three atmospheric simulation chamber studies presented in Chapters 3–5.

6.1 Overview of experiments

The photooxidation of three different BVOCs (MBO, α-pinene, and pinonaldehyde) was investigated and compared to model results. In total five experiments were analyzed. An overview of the experimental conditions is given in Table 6.1.

Table 6.1: Overview of experiments presented in Chapters 3–5. A selection of important experiment conditions is listed.

species	date	[NO] / pptv	max [VOC] / ppbv	$[O_3]^a$ / ppbv	T / K	SZA[b]
MBO	18.08.2012	< 200	4.8	32	310–320	38.0°
α-pinene	30.08.2012	< 100	2.9	42	306–318	42.3°
α-pinene	02.07.2014	< 120	3.8	37	293–303	28.0°
pinonaldehyde	17.07.2014	< 80	6.5	60	305–315	29.8°
pinonaldehyde[c]	18.07.2014	< 220	16.5	0	305–315	30.0°

[a] Initial concentration
[b] Solar zenith angle at noon
[c] 2500 ppbv cyclohexane was added as OH scavenger to study the photolysis

The main focus was to study the atmospheric degradation of BVOCs by OH under conditions that are typical for forested environments. Four experiments have been performed where injected VOCs are predominantly consumed by OH and NO concentrations are lower than 200 pptv. 30 to 60 ppbv O_3 were added to simulate conditions of forested environments. One experiment was conducted in

the presence of an OH scavenger (cyclohexane) to study the photodegradation of pinonaldehyde in the absence of OH (see experiment on 18.07.2014). Temperatures and solar radiation were typical for summertime in Central Europe. In each experiment, temperatures increased between morning and afternoon by approximately 10 K. The maximum solar zenith angles were in the range of 28–42°. In all experiments, initial water vapor mixing ratios were approximately 2 % and decreased over the course of an experiment due to the dilution with dry synthetic air.

For the analysis of experiments, a comprehensive set of measurements is available. Table 6.2 gives an overview of the availability of HO_x, OH reactivity, and VOC measurements for all conducted experiments. For each experiment, OH and HO_2 concentration measurements by LIF were used for the evaluation. In addition, independent OH measurements by DOAS were available for validation of LIF OH measurements. OH measurements by LIF and DOAS agree on average within 15 %. Hence, measurement interferences can be excluded. The concentrations of injected VOC were monitored by PTR–TOF–MS. In addition, concentrations of the formed products acetone and formaldehyde were measured. In the experiments in 2012, the concentration of injected VOCs in the model was adjusted to match the increase in OH reactivity. In 2014, data from the OH lifetime instrument could not be used due to an instrumental failure. For those experiments, PTR–TOF–MS data were used to determine the injected VOC concentrations.

Table 6.2: Availability of measurements in the experiments presented in Chapters 3–5. Measurements that were available are indicated with a "x" and measurements that were not available are indicated with a "-".

species	date	OH_{LIF}	OH_{DOAS}	HO_2	k_{OH}	VOC	Acetone	HCHO
MBO	18.08.2012	x	x	x	x	x[a]	x	x
α-pinene	30.08.2012	x	x	x	x	x[b]	x	x
α-pinene	02.07.2014	x	x	x	-	x[c]	x	x
pinonaldehyde	17.07.2014	x	x	x	-	x[d]	x	x
pinonaldehyde[e]	18.07.2014	x	-	x	-	x[d]	x	x

[a] MBO was measured
[b] α-pinene was measured
[c] α-pinene and pinonaldehyde were measured
[d] Pinonaldehyde was measured
[e] 2500 ppbv cyclohexane was added as OH scavenger

6.2 Product yields

The effective yields of acetone and formaldehyde were determined by their concentration increases during the photooxidation of α-pinene and pinonaldehyde. In addition, the pinonaldehyde yield was determined in the photooxidation of α-pinene in the 2012 experiment. The yield calculation follows the procedure described by Galloway et al. (2011) (see Appendix A.2 for details). In this approach, the measured time series of trace gases are corrected for loss and production, which are not directly related to the chemical oxidation scheme of α-pinene or pinonaldehyde. This includes dilution of trace gases in the chamber, loss of formaldehyde due to photolysis, and a small production of formaldehyde and acetone in the sunlit chamber that is independent of the α-pinene and pinonaldehyde chemistry. If OH is also present, additional corrections for the losses of formaldehyde and acetone due to their reactions with OH are applied. The corrected time series were used to calculate the ratio of a formed organic product and the amount of consumed α-pinene and pinonaldehyde, respectively, to derive the effective yield of the organic compound. The measured yields are given in Table 6.3.

Table 6.3: Overview of experimental product yields in the experiments presented in Chapters 4–5. Given uncertainties are 1 σ.

VOC experiment	experimental yield		
	pinonaldehyde	acetone	HCHO
α-pinene	$(0.05 \pm 0.03)^{a}$	$(0.19 \pm 0.06)^{b}$	$(0.11 \pm 0.05)^{b}$
pinonaldehyde ($h\nu$)	-	0 ± 0.1	$(0.1^{c}$ to $0.18^{d}) \pm 0.2$
pinonaldehyde (OH)	-	$(0.2^{c}$ to $0.3^{d}) \pm 0.1$	$(0.15^{c}$ to $0.45^{d}) \pm 0.2$

[a] Yield determined in the 2014 experiment
[b] Combined yield from experiments in 2012 and 2014
[c] Yield determined at the beginning of the experiment
[d] Yield determined at the end of the experiment

The determined effective pinonaldehyde yield was constant over the whole experiment, indicating that pinonaldehyde is a primary oxidation product. In contrast, acetone and formaldehyde yields increased over the course of the experiments indicating that both species are not only formed from the first degradation step but also from further oxidation of organic products. The yield at the early stage of

the experiments, when only little injected VOC reacted away, best reflects their formation yield directly from the VOC reaction with OH or photolysis, whereas the yield at later times gives the overall yield of the VOC degradation.

The uncertainties in the yield calculation are caused by measurement errors for reagents and products, quantification of chamber sources for acetone and HCHO, and corrections for losses by dilution, reaction with OH, and photolysis. More details can be found in the corresponding Chapters.

In the α-pinene study, measured acetone and formaldehyde yields were 0.19 ± 0.06 and 0.11 ± 0.05, respectively. These yields agreed with literature data and can be reproduced by the MCM. However, the measured pinonaldehyde yield of 0.05 ± 0.03 was at the low side of yields measured in previous laboratory studies ranging from 0.06 to 0.87 (Larsen et al., 2001; Noziere et al., 1999). Pinonaldehyde measurements based on fourier-transform infrared spectroscopy (FT-IR; Hatakeyama et al., 1991; Noziere et al., 1999) may suffer from interferences from other carbonyl compounds, which could have led to overestimated yields (Eddingsaas et al., 2012). Studies measuring pinonaldehyde with GC–FID (Arey et al., 1990; Hakola et al., 1994; Jaoui and Kamens, 2001; Aschmann et al., 2002) and PTR–MS (Lee et al., 2006; Wisthaler et al., 2001) gave similar yields that are in the range of 28 % to 34 %. In the experiment described here, the production rates of acetone and formaldehyde from chamber sources were 0.04 and between 0.11 and 0.27 ppbv h^{-1}, respectively. For acetone the chamber source contributed only 10 % to the overall formed acetone. In contrast, up to 60 % of the total measured HCHO was formed on the chamber walls, which could lead to an additional bias of the determined yield. It has to be stressed here that the chamber study in this work is the first one using atmospheric conditions of reactant concentrations. In contrast to studies with highly elevated reactant concentrations, only small corrections were applied here.

Measured acetone and HCHO yields in the photolysis of pinonaldehyde are the first ones published. No reference data are available. For the reaction of pinonaldehyde with OH, there is only one study by Noziere et al. (1999) available that measured acetone and HCHO yields. The formaldehyde yield of 1.52 ± 0.56 is significantly higher than the yield measured in this work. The acetone yield of 0.15 ± 0.07 reported by Noziere et al. (1999) is in the range of the acetone yield determined here for the times of the experiment when pinonaldehyde is the dominant OH reactant. The high HCHO yield measured by Noziere et al. (1999) can

be partially explained by additional fast photolysis of pinonaldehyde and possibly other products by the 254 nm lamps used to generate OH by photodissociation of H_2O_2 (Fantechi et al., 2002).

6.3 Comparison of trace-gas measurements with model calculations

The measured data for radicals, organic compounds, and k_{OH} listed in Table 6.2 were compared to chemical box model simulations (see Section 2.5) in order to test how well the chemical mechanism MCM 3.3.1 describes important intermediates and products in the photooxidation of MBO, α-pinene, and pinonaldehyde.

Table 6.4 provides an overview of the average ratio of measured to modeled radical concentrations in all experiments.

Table 6.4: Ratios of measured to modeled OH and HO_2 concentrations in experiments presented in Chapters 3–5. Model results were calculated with the MCM. Ratios are averaged over the experiment period where VOCs were injected and the chamber roof was opened. Values are given with 1 σ standard deviation.

parent compound	date	$\text{avg.}\frac{[\text{OH}]_{\text{meas}}}{[\text{OH}]_{\text{model}}}$	$\text{avg.}\frac{[\text{HO}_2]_{\text{meas}}}{[\text{HO}_2]_{\text{model}}}$
MBO	18.08.2012	1.0 ± 0.2	0.9 ± 0.1
α-pinene	30.08.2012	1.7 ± 0.4	1.7 ± 0.2
α-pinene	02.07.2014	1.6 ± 0.3	1.3 ± 0.1
pinonaldehyde	17.07.2014	2.0 ± 0.5	2.5 ± 0.3

Ratios are averaged over the experiment period where VOCs were present in the chamber and the chamber roof was opened. Then, OH losses are dominated by chemical reactions with VOCs and the unknown chemical nature of the background reactivity that is important in the zero-air phase can be neglected (see page 39).

Similarly, Table 6.5 gives an overview of the average ratio of measured to modeled VOC concentrations. Again, the time period when the chamber roof was open was used to assure that acetone and HCHO formation is dominated by chemical sources.

Table 6.5: Ratios of measured to modeled acetone, formaldehyde, and pinonaldehyde concentrations in experiments presented in Chapters 3–5. Ratios are averaged over the experiment period where VOCs were injected and the chamber roof was opened. Values are given with 1 σ standard deviation.

parent compound	date	avg. $[X]_{meas}/[X]_{model}$		
		acetone	HCHO	pinonaldehyde
MBO	18.08.2012	1.0 ± 0.1	1.0 ± 0.1	–
α-pinene[a]	30.08.2012	1.1 ± 0.1	0.9 ± 0.2	–[b]
α-pinene[a]	02.07.2014	1.0 ± 0.1	1.0 ± 0.1	0.2 ± 0.1
pinonaldehyde[a]	17.07.2014	1.3 ± 0.1	1.2 ± 0.1	0.8 ± 0.2
pinonaldehyde[a]	18.07.2014	0.6 ± 0.2	0.6 ± 0.2	1.00 ± 0.01

[a] MCM model with measured pinonaldehyde photolysis frequency
[b] not measured

The main results presented in the photooxidation studies are summarized in the following sections for each parent compound.

6.3.1 MBO

The first study (Chapter 3) that investigated the photooxidation of MBO showed a good overall model-measurement agreement. Measured and modeled OH and HO_2 concentrations agreed within 10 % (see Figure 2, page 40). Experimental OH and HO_2 budgets were calculated to analyze the completeness of radical formation and loss terms.

The OH concentration is determined by the OH production rate P_{OH} and the total OH loss rate L_{OH}. It can be expressed as the OH budget equation (Equation 6.1). On the timescale of the OH lifetime, P_{OH} and L_{OH} are constant. Therefore, OH concentrations are in quasi steady-state conditions and the net change of OH concentrations is 0.

$$\frac{d[OH]}{dt} = P_{OH} - L_{OH} \approx 0 \tag{6.1}$$

Measured P_{OH} include OH production from HONO and ozone photolysis, reaction of HO_2 with NO, and reaction of HO_2 with O_3. L_{OH} is the sum of all losses from species reacting with OH and can be calculated from measured OH concentrations

and measurements of OH reactivity.

$$L_{\mathrm{OH}} = [\mathrm{OH}]k_{\mathrm{OH}} \tag{6.2}$$

The calculated radical budget in the MBO experiment was closed, which indicates that the MCM includes all relevant sinks or sources for OH and HO_2 (see Figures 3 and 4, page 42) The MBO degradation is initiated by the OH attack, forming two RO_2 isomers. Under described experimental conditions, these RO_2 dominantly react with NO forming glycoaldehyde, acetone, and HO_2 or hydroxymethylpropanal, HCHO, and HO_2. This simple mechanism is well described in the MCM for experimental conditions showing a good agreement for radicals (see Table 6.4) and measured oxidation products acetone and HCHO (see Table 6.5). The correct product distribution indicates that the branching ratio of initial formed RO_2 is correctly described by the MCM.

The good model–measurement agreement also demonstrate that the concept of simulation chamber experiments and used instrumentation are suitable to examine complete chemical mechanisms under atmospheric conditions. A similarly good agreement has been shown for the simple reaction systems of CH_4 and CO (e.g. Fuchs et al., 2013, Figure 2).

The impact of suggestions by Knap et al. (2016) on model results was investigated in the photooxidation of MBO. The authors suggest hydrogen shift reactions in the peroxy radicals originated after photooxidation of four different methyl-buten-ol isomers. In a sensitivity study, three H-shift reactions were added in the MCM model that directly form stable products without considering formation of any intermediates. As expected from the low reaction rates for these reactions, the impact of these modifications is very small with a change of less than 1 % on any of the modeled trace gases. In conclusion, implementation of modifications by Knap et al. (2016) does not improve the already good model–measurement agreement. This is consistent with the study by Knap et al. (2016), in which the authors concluded that H-shift reactions are not relevant for the oxidation scheme of MBO even for low NO conditions (< 50 pptv). Then, the reaction with HO_2 remains the dominant loss process for RO_2 that originates from MBO. In the chemistry of isoprene and methacrolein, fast H-shift reactions have been observed that are favored by conjugated carbon–carbon double bonds (Peeters and Nguyen, 2012). In contrast, MBO has only one double bond and such fast H-shift

reactions are not expected.

6.3.2 α-pinene

In contrast to the MBO study, the model–measurement comparison in the α-pinene (Chapter 4) experiments showed large discrepancies in respect to radical concentrations and product formation.

In the MCM, the α-pinene photooxidation is initiated by the OH attack forming three RO_2 isomers in total. Two RO_2 isomers that retain the four-membered ring structure are predominantly formed. Under experiment conditions, they mainly react with NO and eventually form pinonaldehyde and HO_2. In the formation of the third initial RO_2 isomer, the four-membered ring is opened, and after reaction with NO acetone, a cyclic β-hydroxyketone, and HO_2 are formed.

OH and HO_2 concentrations were significantly underestimated by model calculations in α-pinene experiments (see Figure 4, page 58 and Figure 5, page 60). Average ratios of measured to modeled OH concentrations were (1.7 ± 0.4) and (1.6 ± 0.3) (see Table 6.4). Similarly, average ratios of measured to modeled HO_2 concentrations were (1.7 ± 0.2) and (1.3 ± 0.1).

However, the measured OH concentrations could be simulated when the HO_2 concentrations in the model were constrained to the measured HO_2 data. The OH budget is closed, and the main OH source is the reaction of HO_2 with NO. Therefore, underestimated HO_2 concentrations directly lead to underpredicted OH concentrations. In conclusion, a HO_2 source is needed in the model of the α-pinene degradation to explain observed radical concentrations.

Modeled pinonaldehyde mixing ratios were overestimated by at least a factor of 4 compared to measurements (see Figure 4, page 58). In addition, the calculated α-pinene consumption is approximately 10 % slower than observed, which is consistent with the lower modeled OH compared to observations. Similarly, a slower decrease in the modeled OH reactivity is observed compared to measurements carried out in the experiment in 2012. The production of acetone in the model matches the observations within the stated errors. In contrast, the formation of formaldehyde is slightly overestimated by around 10 % (see Table 6.5).

In the α-pinene study, the MCM model was modified based on propositions by Vereecken et al. (2007) that include a change of the initial RO_2 distribution and additional H-shift reactions (M1, see Figure 4, page 58 and Figure 5, page 60).

The modifications reduce the model–measurement discrepancies for radicals, OH reactivity, α-pinene, and pinonaldehyde without changing the reasonable agreement for formaldehyde and acetone, but measured pinonaldehyde concentrations are still significantly lower than predicted by the model. In an additional sensitivity study, the initial RO_2 branching ratio was further adjusted such as the pathway that does not form pinonaldehyde is increased. A similar shift in the RO_2 distribution was proposed by Xu et al. (2019). Implementing these model modifications increase HO_2 concentrations by up to 30 %, giving reasonable model–measurement agreement within the stated uncertainties. The increased HO_2 together with a reduced OH loss rate due to the decreased pinonaldehyde concentration result in up to 30 % higher modeled OH radical concentrations compared to M1, which agree with measurements within the stated uncertainty.

In contrast to the MBO study, the MCM mechanism is not able to reproduce the initial RO_2 distribution, thus predicting a different product distribution compared to observations.

6.3.3 Pinonaldehyde

In the MCM mechanism, the the photolysis of pinonaldehyde forms a single RO_2 that reacts under experiment conditions with NO and eventually leads to the formation of 3,4-dioxopentanal, acetone, formaldehyde, and HO_2.

When pinonaldehyde is oxidized by OH, two RO_2 isomers are formed in the MCM mechanism. The main RO_2 isomer reacts with NO to eliminate CO_2 and form the same RO_2 that is obtained by the pinonaldehyde photolysis. The other initially formed RO_2 isomer reacts multiple times with NO and eventually forms 3-oxopentanedial, acetone, formaldehyde, and HO_2.

The pinonaldehyde degradation was analyzed in the presence and absence of an OH scavenger (cyclohexane). In the first case, pinonaldehyde was exclusively removed by photolysis. In contrast, without OH scavenger pinonaldehyde was mainly consumed in the reaction with OH. In both cases, the observed pinonaldehyde consumption rate was faster than predicted by the MCM. In the pure photolysis experiment (see Figure 2, page 73), the pinonaldehyde consumption could be reproduced by the model if an experimentally determined photolysis frequency was used instead of the parameterization in the MCM that is based on the photolysis of n-butanal. For this purpose, the photolysis frequency was cal-

culated from measured solar actinic flux spectrum and absorption cross sections of pinonaldehyde published by Hallquist et al. (1997). The best fit was achieved with an effective quantum yield of 0.9. When pinonaldehyde is consumed by OH, the pinonaldehyde decay could be correctly described by application of measured photolysis frequency and constraining of HO_2 concentrations to measurements in order to correctly predict OH concentrations.

The pinonaldehyde photolysis frequency was calculated based on absorption cross sections by Hallquist et al. (1997). These are the only published measurements and recommended by IUPAC (Atkinson et al., 2006). The effective, wavelength-independent quantum yield of 0.9 determined in this work is significantly higher than those in two other chamber studies that also used natural sunlight and reported quantum yields of 0.14 ± 0.03 (Moortgat et al., 2002) and 0.4 (Jaoui and Kamens, 2003) for pinonaldehyde photolysis. However, the solar actinic flux could not accurately be determined in the study by Jaoui and Kamens (2003). In the study by Moortgat et al. (2002), measurements were performed with a spectroradiometer that allows solar actinic flux measurements with a good accuracy like in the work presented here. In both studies, large corrections for wall losses and dilution that were of the same magnitude as the photolysis rate were applied. However, the large difference by a factor of 7 in the study of Moortgat et al. (2002) compared to results in this thesis is likely not explained by systematic errors of the correction.

In the MCM, the parameterization based on n-butanal is also used for other species than pinonaldehyde that similarly have two or more carbonyl functions. The chemical structures of n-butanal and pinonaldehyde can bee seen in Figure 6.1. In comparison to pinonaldehyde, n-butanal is a simple linear aldehyde with no additional functional group. The measured photolysis frequency was 3.5 times faster than the parameterization applied for pinonaldehyde in the MCM be-

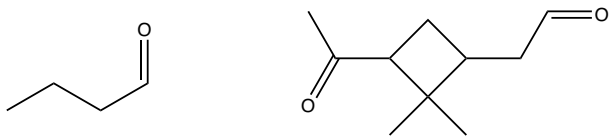

n-butanal pinonaldehyde

Figure 6.1: Chemical structures of n-butanal and pinonaldehyde.

cause of its two carbonyl functions. This might be valid for other bi-carbonyl compounds that have non-conjugated carbonyl functions. This means that the use of the n-butanal photolysis frequency could systematically underestimate the photolysis frequencies of these compounds. However, the high quantum yield close to unity could also be a specific property of pinonaldehyde that might not apply for the photolysis of other bi-carbonyl species.

When pinonaldehyde is mainly oxidized by OH (see Figure 3, page 73), modeled OH and HO_2 concentrations are underestimated on average by a factor of (2.0 ± 0.5) and (2.5 ± 0.3), respectively, compared to observations (see Table 6.4). Similarly to the results from α-pinene experiments, the OH budget was closed, and measured OH concentrations could be reproduced when HO_2 concentrations in the model were constrained to measurements. This demonstrates that current atmospheric chemical models also lack a HO_2 source in the degradation scheme of pinonaldehyde.

Pinonaldehyde is an oxidation product in the photooxidation of α-pinene. However, the missing HO_2 source cannot explain the discrepancies observed in the α-pinene chamber experiments and field campaigns because the pinonaldehyde yield in the α-pinene degradation is rather small (5 %).

The MCM model for the degradation of pinonaldehyde was extended by reactions based on quantum chemical calculations by Fantechi et al. (2002). Additions to the model include the initial formation of additional RO_2, change in branching ratios, and new H-shift reactions. In the experiment with added OH scavenger, in which the pinonaldehyde consumption is dominated by photolysis, the HO_2 concentration time profile is changed compared to the MCM model (see Figure 8, page 78). Typically, the rate determining step in radical chain reactions is the reaction of RO_2 with NO, forming an alkoxy radical and NO_2. In the MCM mechanism, there are three $RO_2 + NO$ reactions before the radical chain is terminated and the stable product 3,4-dioxopentanal is formed together with HO_2. In contrast, in the degradation scheme by Fantechi et al. (2002), only one $RO_2 + NO$ reaction occurs before the stable products are formed, and HO_2 is regenerated faster compared to the MCM. However, the HO_2 model–measurement agreement is good for both MCM and the meachansim by Fantechi et al. (2002). In addition, no acetone and less formaldehyde are formed compared to the pure MCM model, thus increasing model–measurement agreement. Modeled acetone concentrations agree with observations within the stated uncertainty, and mod-

eled formaldehyde concentrations are only 20 % lower than measurements. In the modified model, 4-hydroxynorpinonaldehyde and norpinonaldehyde are formed instead. However, measurements of these compounds were not available.

Implementation of modifications suggested by Fantechi et al. (2002) does not improve model–measurement agreement for OH and HO_2 in the experiment where pinonaldehyde is dominantly consumed in the reaction with OH. Various sensitivity studies were performed to test, if the missing radical source can be explained by either unimolecular reactions of RO_2 or by photolysis and decomposition reactions of oxidation products. The strength of the missing HO_2 source is increasing over the course of the experiment. Sensitivity runs that investigate the HO_2 production by processes involving RO_2 show an opposite time behavior, forming more HO_2 in the beginning than at the end of the experiment, following the concentration time profile of the short-lived RO_2 radicals. In contrast, HO_2 sources that are connected to further degradation of oxidation products become more important over the course of an experiment when more oxidation products have been formed. Results of the sensitivity studies indicate that the missing HO_2 source is connected to subsequent chemistry of formed oxidation products rather than connected to RO_2 reactions. However, without further possibilities to constrain the mechanism, it was not possible to find the source that would explain the model–measurement discrepancy.

Overall, the investigated systems of α-pinene and pinonaldehyde follow the general trend that radical regeneration in the photooxidation of BVOCs is not well understood by currently available atmospheric chemical models.

6.4 Comparison with field studies

Many field campaigns were conducted in environments that are dominated by BVOC emissions. Here we compare results of our chamber study to field campaigns that measured HO_x and were conducted in forested regions with MBO and α-pinene emissions.

The Biosphere Effects on Aerosols and Photochemisty Experiment II (BEARPEX09) campaign was conducted in a Ponderosa pine plantation near the Blodgett Forest Research Station in the California Sierra Nevada Mountains (USA). MBO was the most abundant BVOC with daily average concentrations of 3000 pptv,

followed by isoprene (daily average 1700 pptv) and monoterpenes (α-pinene, daily average 100 pptv and β-pinene, daily average 70 pptv). Daytime OH concentrations showed an average measurement to model ratio of 1.4 ± 0.3. Modeled HO_2 concentrations are overestimated by a factor of up to 1.3, which is within the stated 2σ uncertainty of 40 % for HO_2 measurements (Mao et al., 2012). This is in agreement with the MBO chamber study, in which the MCM was able to correctly reproduce measured radical and VOC concentrations. Maximum MBO concentrations of 4.8 ppbv in the chamber study were similar to observations in the BEARPEX09 campaign. In addition, NO concentrations in the chamber experiment were below 200 pptv, which is comparable to the daytime average value of 74 ± 240 pptv observed in the field campaign.

In the BEACHON-ROCS (Ortega et al., 2014) campaign, BVOC emissions were dominated by MBO (daily average $\sim$ 1600 pptv) followed by monoterpenes (daily average $\sim$ 500 pptv) (Kim et al., 2013). Model results underestimated HO_2 radical concentrations by up to a factor of 3 and OH concentrations could only be reproduced by the model if HO_2 was constrained to measurements. Figure 6.2 shows the averaged diurnal cycles of measured and modeled HO_2.

Kim et al. (2013) suggested an unidentified HO_2 source that may be due to photolysis of oxidized VOCs (OVOCs) or reactions of RO_2. However, sources from

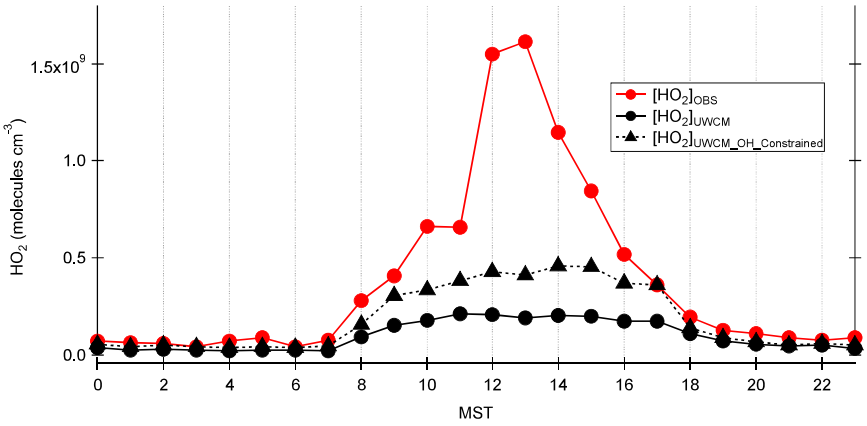

Figure 6.2: The averaged diurnal cycles of observed and modeled HO_2 concentrations in the BEACHON-ROCS campaign. See text for details. Figure modified from Kim et al. (2013).

photolysis reactions of OVOCs would either require large sources of OVOCs or very fast photolysis rates. Similar results are found in the pinonaldehyde photooxidation experiment in this work. Here, a photolysis frequency of $0.2 \times j_{NO2}$ for first generation oxidation products was needed to explain observed HO_2 concentrations. The missing HO_2 production rate in the BEACHON-ROCS campaign was in the order of 1–7 ppbv h^{-1}, which is large compared to an estimated MBO and monoterpene consumption by OH of up to 2 ppbv h^{-1}. The BVOC turnover rate is an upper limit and is estimated by the given BVOC concentrations and maximum OH concentrations at noon time. The missing HO_2 production rate in the α-pinene chamber experiment in this work was increasing over the course of the experiment from 0.2 ppbv h^{-1} to 0.8 ppbv h^{-1} with a maximum α-pinene consumption of 1.4 ppbv h^{-1}. In the pinonaldehyde chamber study, the missing HO_2 source strength was in the order of 0.8 ppbv h^{-1} to 1.5 ppbv h^{-1} with a pinonaldehyde consumption of up to 2.5 ppbv h^{-1}. The HO_2 source strengths normalized to the amount of consumed VOC per hour are 0.2 ppbv h^{-1} to 1.5 ppbv h^{-1} and 0.2 ppbv h^{-1} to 0.6 ppbv h^{-1} for the pinonaldehyde and α-pinene experiment, respectively. Both chamber studies show a HO_2 source strength that is comparable to the observations in the BEACHON-ROCS campaign but at the lower range of reported values.

In the field campaign, OH consumption is controlled by mixtures of MBO, monoterpenes, and their oxidation products. In contrast, at the beginning of the simulation chamber experiments, only pure monoterpene species and pinonaldehyde were injected into the chamber and dominated the consumption of OH radicals. Therefore, conditions at later times of the chamber experiment better represent an ambient environment with mixtures of emitted species and oxidation products. The needed HO_2 source strength increased towards the end of the α-pinene and pinonaldehyde experiments from 0.2 ppbv h^{-1} to 0.8 ppbv h^{-1} and 0.8 ppbv h^{-1} to 1.5 ppbv h^{-1}, respectively.

The HUMPPA-COPEC field campaign, measured α-pinene mixing ratios peaked around 1 ppbv, which is comparable to α-pinene concentrations in the chamber experiments discussed here of up to 3.8 ppbv. The field campaign showed similar results as reported by Kim et al. (2013). The OH budget was balanced but k_{OH} and HO_2 concentrations were both underestimated by model calculations. Hens et al. (2014) attributed this to a missing HO_2 source. Figure 6.3 shows the ratio of measured to modeled HO_2 using the Mainz Isoprene Mechanism (MIM). Modeled

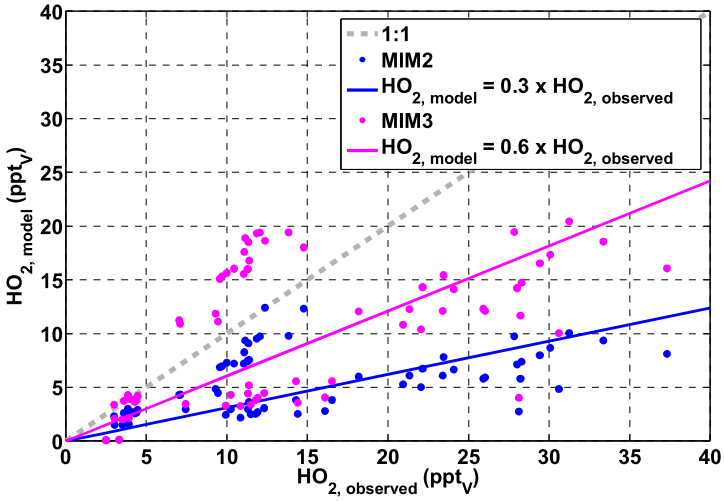

Figure 6.3: Measured vs modeled HO_2 mixing ratios in the HUMPPA-COPEC campaign. Modelled concentrations were derived by applying the MIM2 chemistry scheme and the proposed MIM3 including additions in the isoprene chemistry. Figure modified from Hens et al. (2014).

HO_2 concentrations are 70 % smaller compared to observations. A second model run (MIM3) using an extended mechanism that includes new additions that are based on radical regeneration mechanisms found for isoprene (Taraborrelli et al., 2012) improved the model-measurement agreement. However, for most of the modeled data, HO_2 concentrations are 40 % lower than observations.

Comparing simulated contributions to the observed total OH reactivity showed that the main OH consumption is due to the reaction with oxidation products (34 %) and monoterpenes (4 %). However, a large fraction of 45 % of the total reactivity cannot be explained by species in the model. The missing reactivity is likely caused by unmeasured primary emissions and oxidation products. Replacing the fraction of unknown reactivity with a surrogate which behaves chemically identically to α-pinene was not sufficient to bring model and measurements into agreement. Similar to the results in this work, more efficient radical regeneration is needed to explain observations.

Results from the BEACHON-ROCS and HUMPPA-COPEC field campaigns agree with the results of the α-pinene chamber study discussed here and with results of

the β-pinene study by Kaminski et al. (2017). All studies report a balanced radical budget in combination with an unknown HO_2 source. MBO was also an important OH reactant during the BEACHON-ROCS campaign but is likely not responsible for the observed model–measurement discrepancies. Findings from the pinonaldehyde study are not sufficient to explain model–measurement discrepancies because the pinonaldehyde yield in the photooxidation of α-pinene is too small. However, the missing HO_2 source in the pinonaldehyde experiments might be similar for other α- and β-pinene oxidation products. This might also be valid for degradation products from other monoterpene species. However, the exact nature of the HO_2 source cannot be determined based on the conducted SAPHIR experiments. Therefore, additional experiments are needed in the future.

6.5 Implication for atmospheric chemistry

The SAPHIR studies presented in this work showed that the chemical degradation of α-pinene and pinonaldehyde by OH is considerably more complex than currently implemented in state-of-the-art chemical mechanisms like the MCM. Similar results have been previously reported for the degradation schemes of β-pinene and isoprene. There is a lack of knowledge concerning the photolysis of OVOCs (see pinonaldehyde). In addition, this thesis shows that branching ratios of initially formed RO_2 isomers and their subsequent reactions that impact HO_x regeneration and the formation of partially oxidized VOCs are not correctly implemented in the MCM. Similar to previously published studies of isoprene and MACR, unimoelecular reactions of RO_2 that are not included in the chemical models so far become important.

In the photooxidation experiments of all three investigated VOCs, OH budgets were closed. Similarly, as previously reported in the photooxidation of β-pinene, the HO_2 regeneration in the degradation schemes of α-pinene and pinonaldehyde was underestimated, resulting in underestimated OH concentrations. Atmospheric OH concentrations control the daytime composition of the atmosphere. When models underestimate OH concentrations, the oxidative capacity of the atmosphere is underestimated and modeled VOC lifetimes are extended. This applies to greenhouse gases like methane, thus enhancing the predicted radiative forcing and contribution to climate change. In addition, underestimated

HO_2 concentrations lead to an underestimation of the photochemical ozone formation, impacting local air quality. The lack of understanding of RO_2 distributions and OVOC formation directly translate to an uncertainty in the prediction of formed organic particles.

In the experiments presented here, analysis of different reaction pathways was limited by the availability of measurements of intermediates and product species. Further progress in determining the details of reaction mechanisms could be achieved, if different oxygenated organic compounds and reaction intermediates were identified and quantified. In future SAPHIR studies, additional measurements of oxidation products, nitrate species, and speciated RO_2 with chemical ionization mass spectrometers (CIMS) and PTR–TOF–MS could help to better constrain reaction mechanisms.

The data of experiments discussed in this work are available on the EUROCHAMP data home page (Eurochamp) and can be used as constraints for future works. Concentration times series and measured yields can be used for the validation of theory based studies. In addition, developed mechanisms from this work can be used for the evaluation of new experimental studies. Furthermore, tested mechanisms from this thesis could be used for model studies to investigate the global impact of additional HO_2 sources in the α-pinene and pinonaldehyde degradation on OH concentrations and O_3 formation.

Part II

Spectroscopic and kinetic measurements of acetylperoxy radicals

7 Introduction

As described in Chapter 1, the reaction of acetylperoxy radicals with HO_2 can regenerate OH radicals without the participation of NO.

The simplest acylperoxy radical is the acetylperoxy radical ($CH_3C(O)O_2$), which is formed in the troposphere by the photooxidation of a large variety of different, highly abundant carbonyl compounds. The main sources for the formation of $CH_3C(O)O_2$ in the atmosphere are the oxidation of acetaldehyde and the photolysis of methylglyoxal (CH_3COCHO) and acetone (Fischer et al., 2014). An overview of relative contributions to the annual global $CH_3C(O)O_2$ formation calculated with the Goddard Earth Observing System chemical transport model (GEOS-chem) is shown in Figure 7.1. $CH_3C(O)O_2$ precursors are formed in the oxidation of BVOCs or are directly emitted.

Recent studies (Hasson et al., 2004; Jenkin et al., 2007; Winiberg et al., 2016; Hui et al., 2019) of the reaction of acetylperoxy radicals with HO_2 showed that this reaction is not only terminating the radical reaction chain (R 7.1a & R 7.1b) but can also regenerate OH radicals (R 7.1c).

$$CH_3C(O)O_2 + HO_2 \longrightarrow CH_3C(O)OOH + O_2 \quad \text{(R 7.1a)}$$

$$\longrightarrow CH_3C(O)OH + O_3 \quad \text{(R 7.1b)}$$

$$\longrightarrow CH_3C(O)O + OH + O_2 \quad \text{(R 7.1c)}$$

Earlier studies (Niki et al., 1985; Moortgat et al., 1989; Horie and Moortgat, 1992; Tomas et al., 2001) of the $CH_3C(O)O_2 + HO_2$ reaction only observed the formation of stable products peracetic acid (R 7.1a) and acetic acid (R 7.1b). Theoretical studies (Hasson et al., 2005; Le Crâne et al., 2006) showed that the reaction either proceeds via hydrogen atom transfer (R 7.1a) or a hydrotetroxide intermediate (R 7.1b & R 7.1c). In the case of simple alkylperoxy species, no product channels are accessible for the hydrotetroxide intermediate, and it decomposes back to reactants.

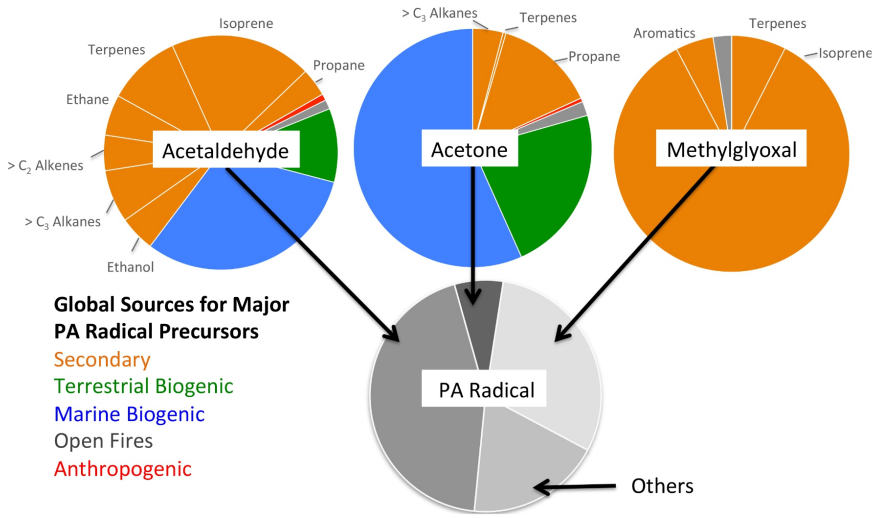

Figure 7.1: Overview of the relative global contributions of emitted VOCs to the main carbonyl species (acetaldehyde, acetone, methylglyoxal) that form peroxyacetyl (PA) radicals. In addition, the relative contributions of the carbonyl species to PA formation are shown. Contributions were calculated with GEOS-chem. Figure from Fischer et al. (2014).

The detection of $CH_3C(O)O_2$ in previous kinetic laboratory studies was mainly done in the UV region. The absorption spectra of different peroxy radicals and reaction products overlap in this region (Figure 7.2) which could lead to systematic errors if not properly accounted for.

This thesis presents new spectroscopic and kinetic measurements of $CH_3C(O)O_2$ radicals by cavity ring-down spectroscopy (CRDS) in the near infrared (NIR). The A←X electronic transition of RO_2 in the NIR shows more structured spectra compared to the UV region, thus allowing a more selective identification of RO_2 radicals. However, the A←X transition is weaker than the B←X transition in the UV (Onel et al., 2020).

Investigated radical reactions in this work are second-order. Therefore, it is not sufficient to measure relative concentration time profiles for the determination of reaction rate constants. Instead, the knowledge of absolute concentrations is needed. This requires well known absorption cross sections, which are measured in this work at different NIR wavelengths for the first time (Chapter 9).

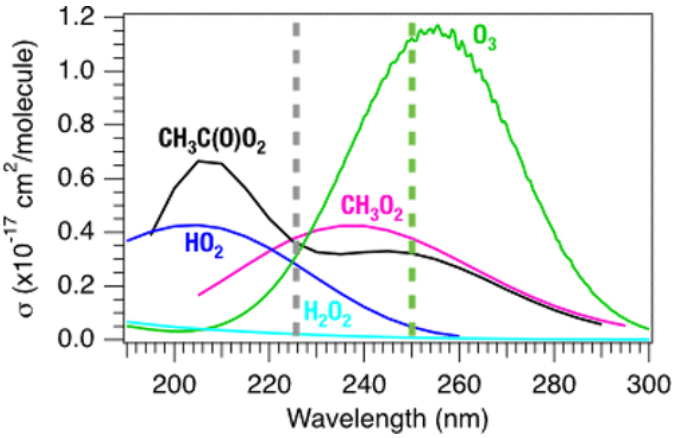

Figure 7.2: UV absorption cross sections of $CH_3C(O)O_2$ and other relevant species. Reprint (adapted) with permission from Hui et al. (2019). Copyright (2020) American Chemical Society.

In Chapter 10 the reaction rate constant of the $CH_3C(O)O_2$ self-reaction is measured to validate the newly measured absorption cross section of $CH_3C(O)O_2$.

8 Methods

In the following part, the experimental setup used for the detection of acetylperoxy radicals in the near infrared is described. Experiments were conducted at the Université Lille 1: PhysicoChimie des Processus de Combustion et de l'Atmopshère (France).

8.1 Radical detection by cavity ring-down spectroscopy

Continous-wave cavity ring-down spectroscopy (cw-CRDS) is a highly sensitive measurement technique. It has been developed by Anthony O'Keefe and David A. G. Deacon (O'Keefe and Deacon, 1988). The technique is inherently calibration-free, because analytes can be directly measured by absorption if the corresponding absorption cross-section is known. The details of the instruments used in this study can be found in previous publications (Thiebaud and Fittschen, 2006; Parker et al., 2011; Jain et al., 2011; Votava et al., 2012). Only the general CRDS principle is explained here.

The main difference to the conventional absorption spectroscopy is that CRDS contains an optical cavity which consists of two highly reflective mirrors with the reflectivity R. Laser light is focused into the optical cavity and is reflected back and forth between the mirrors. Intensity builds up in the cavity when the continuous light source is in resonance with a cavity mode. Once an intensity threshold is reached, the light source is turned off or the incident beam is deviated. For example, a continuous wave (cw) light source can be used in combination with an acousto optic modulator (AOM) to deviate the beam. Then, the intensity decay is monitored by a detector behind the rear cavity mirror. A schematic of a CRDS setup is shown in Fig. 8.1. Due to the cavity design, CRDS systems can achieve pathlengths of several km. For example, the effective pathlengths in the CRDS instrument discussed here are up to 2 km. Therefore, high sensitivities can be

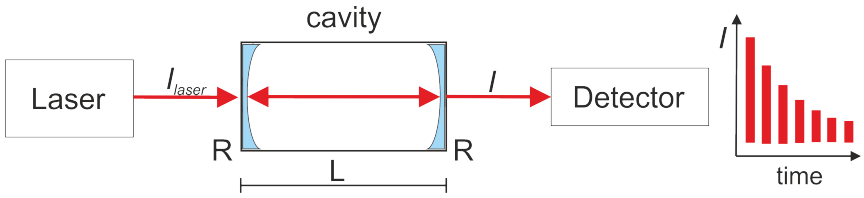

Figure 8.1: Schematic of a CRDS setup and a time dependent signal of intensity. I_{laser}: Intensity of incident beam; I: intensity leaking out of the cavity; L: cavity length; R: mirror reflectivity.

reached. In contrast to the conventional absorption spectroscopy, CRDS measures the decay time constant of intensity instead of the intensity difference between light source and detector. Therefore, CRDS is not affected by fluctuations of the light source.

The intensity decay depends on cavity length L, the transmission and scattering losses at the mirrors with a reflectivity R, and the absorption coefficient α in the cavity. The intensity at time t can be expressed as:

$$I(t) = I_0 \exp\left\{-t\left(\frac{c(1-R)}{L} + c[A]\sigma_A(\lambda) + cN_{RS}\sigma_{RS}\right)\right\} \tag{8.1}$$

where c speed of light in vacuum, $[A]$ the concentration of an absorbing species A, σ_A the absorption cross section of species A, N_{RS} concentration of centers for Rayleigh scattering, and σ_{RS} Rayleigh scattering cross section. Rayleigh scattering can limit the CRDS sensitivity at ambient pressure but becomes less important at reduced pressures. The time after the intensity ratio I/I_0 decays to 1/e is referred to as ring-down time τ.

$$I(t) = I_0 \exp\left(-\frac{t}{\tau}\right) \tag{8.2}$$

The ring-down time is derived by fitting the measured time-dependent intensity decay by a single-exponential function.

To separate absorption from other losses (mirror losses and light scatter), measurement of a zero decay time constant τ_0 without an absorber present is neces-

sary. The absolute concentration can be calculated according to:

$$[A] = \frac{1}{c\sigma_A}\left(\frac{1}{\tau} - \frac{1}{\tau_0}\right) \tag{8.3}$$

8.2 Experimental setup

A schematic view of the setup used to measure spectrum and kinetics of $CH_3C(O)O_2$ at the Université Lille 1 is shown in Figure 8.2. Further descriptions can be found in previously published studies (Thiebaud and Fittschen, 2006; Parker et al., 2011; Jain et al., 2011; Votava et al., 2012).

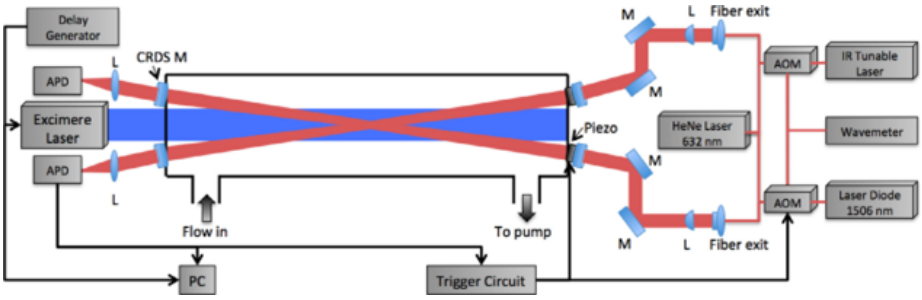

Figure 8.2: Schematic view of the used experimental setup: AOM, Acousto-Optic Modulator; APD, Avalanche Photo Diode; M, Mirror; L, Lens. Both cw-CRDS systems are equipped with identical trigger circuits and data acquisition systems. Figure from Rolletter et al. (2020a).

The beam of a pulsed Excimer laser (Lambda Physik LPX 202i) is passed longitudinally through a 0.70 m long flow reactor made of stainless steel. The reactor is equipped with two identical continuous-wave cavity ring-down spectroscopy absorption pathways, which are installed in a small angle with respect to the photolysis path. An overlap with the photolysis beam of 0.377 m is achieved (Assaf et al., 2016). The volumes in front of the mirrors are continuously purged with a small helium flow to prevent impurities. A distributed feedback (DFB) laser diode (Fitel Furukawa) and a tunable laser module (Agilent 81680A) are used as near-infrared light sources for the cw-CRDS systems. The laser module can be tuned within a wavelength range of 6329-6849 cm^{-1}. The DFB diode has a wavelength range of 6627-6653 cm^{-1}. Wavelengths can be tuned by either changing the DFB

diode temperature or the applied current, which are controlled by the power supply (Thorlabs ITC 502). The choice of light sources allows detecting $CH_3C(O)O_2$ and HO_2 at absorption lines at wavenumbers of 6510.74 cm^{-1} and 6638.205 cm^{-1}, respectively. To calculate concentrations, HO_2 absorption cross sections of σ_{HO2} = (2.72 $\pm$ 0.27) $\times$ 10^{-19} cm^{-2} (Assaf et al., 2017) are used. The cavity lengths are modulated by moving the front mirror mount with a piezoelectric transducer until the resonance condition is fulfilled (Votava et al., 2012) and intensity builds up in the cavity. The fiber output of each used laser source is connected to an acousto-optic modulator (AOM, AA OPTO-ELECTRONIC), which allows to rapidly stop light reaching the cavity as soon a preset intensity threshold is reached. In the following ring-down event, the decay of intensity in the cavity is measured by avalanche photodiodes (APDs) and recorded by a data aquisition card (PCI-6259, National Instruments). Measured time series are fitted with an exponentional function to retrieve the ring-down time τ. The 0^{th} order beam from the AOM is connected to a wavemeter (Burleigh WA-1100) to determine the wavelength of the DFB diodes. The wavelength of the Agilent laser module was directly recorded internally.

8.3 Radical generation

$CH_3C(O)O_2$ radicals were generated by pulsed photolysis of acetaldehyde/oxygen (O_2)/ chlorine (Cl_2) mixtures at 351 nm using an Excimer laser (Lambda Physik LPX 201) with a repetition rate of 0.5 Hz.

$$Cl_2 + h\nu \longrightarrow 2\,Cl \qquad \text{(R 8.2)}$$

$$CH_3CHO + Cl \longrightarrow CH_3CO + HCl \qquad \text{(R 8.3)}$$

$$CH_3CO + O_2 + M \longrightarrow CH_3C(O)O_2 + M \qquad \text{(R 8.4)}$$

Acetaldehyde from a diluted mixture in a glass bulb was added and the flow was monitored with a calibrated flow meter. Acetaldehyde concentrations in the experiments reported here were 2.5×10^{14} cm^{-3}. Experiments were conducted at 298 K and 67 hPa total pressure. The kinetic experiments were all performed in synthetic air.

8.4 Experiment procedure

8.4.1 Kinetic measurements

Two cw-CRDS absorption pathways allow the simultaneous detection of $CH_3C(O)O_2$, CH_3O_2, and HO_2 at 6510.74 cm^{-1}, 7489.16 cm^{-1}, and 6638.21 cm^{-1}, respectively. It is assured that both absorption pathways probe the same volume in which the radicals are photolytically generated at the start of the experiment. For this purpose, both cw-CRDS instruments measured HO_2 radicals simultaneously and showed an agreement within 5 %.

For the kinetic measurements, the laser output wavelengths were set to the individual absorption lines of the investigated species. The ring-down events were recorded 0.5 s before and after the photolysis pulse that generated Cl atoms and subsequently $CH_3C(O)O_2$ radicals. The derived ring-down time τ and the time delay with respect to the photolysis shot were recorded. A typical times series of ring-down events is shown in Figure 8.3.
Ring-down events that occurred before the photolysis shot when no radicals were present were averaged to one value for τ_0. Equation 8.3 describes an ideal case where the total length of the cavity is filled by an absorber. Here, we have to account for the geometry of the CRDS beam that does not overlap with the photolyzed volume over its full length. Therefore, a correction term, R_L, is introduced that corresponds to the ratio between total cavity length and effective absorption length.

$$[A]_t = \frac{\alpha_t}{\sigma_A} = \frac{R_\mathrm{L}}{c\sigma_A}\left(\frac{1}{\tau_t} - \frac{1}{\tau_0}\right) \tag{8.4}$$

With Eqn. 8.4, the ring-down times can be converted to absolute concentrations with the known absorption cross section σ. Each measured ring-down time is converted into concentration to derive a concentration time series. Since ring-down events occur randomly in time before and after a photolysis pulse, ring-down events from multiple photolysis pulses are accumulated to achieve a good coverage over the whole time range of an experiment.

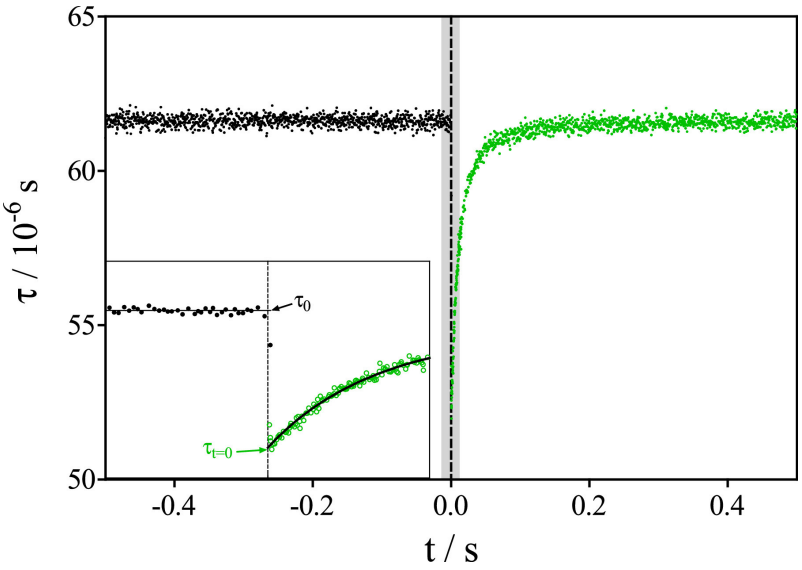

Figure 8.3: Typical series of ring-down times for $CH_3C(O)O_2$. The insert shows the zoom of the gray-shaded area ($\pm$ 15 ms). The dashed line represents the time of the photolysis pulse (t = 0 s). Ring-down events before the photolysis pulse (black) are used to determine τ_0. Extrapolation to t = 0 s of a bi-exponential fit of the ring-down times occurring during the first 50 ms after the photolysis pulse (black line in the insert) are used to determine τ. Figure from Rolletter et al. (2020a).

8.4.2 Measurement of spectrum and absorption cross sections

The procedure to measure absorption spectra with the given setup has been described before (Jain et al., 2011; Faragó et al., 2013; Assaf and Fittschen, 2016), and only a short description is given here. The laser wavelength is changed in 0.1 cm^{-1} and 0.2 cm^{-1} increments by tuning the electrical current applied to the DFB diode. For each wavelength, a time series of ring-down events such as described for the kinetic measurements, is recorded while keeping the concentration of initially generated $CH_3C(O)O_2$ radicals constant. Similar to the kinetic measurements, ring-down events from multiple photolysis shots were accumulated for each wavelength to get a better statistic. The values for τ_0 were derived from the average of all ring-down events before the photolysis pulse when no $CH_3C(O)O_2$ is present. The initial $CH_3C(O)O_2$ concentration is not distorted due to reactions with other radicals that could bias the measured absorption coefficient.

Ring-down times in the first 50 ms after $CH_3C(O)O_2$ was formed were fitted to a bi-exponential function and extrapolated to $t = 0\,\mathrm{s}$ to obtain the ring-down time of the initial radical concentration. Tests of different fitting procedures showed the best results when the bi-exponential fit was used. The decay constant from the fit has no physical meaning and was only used to achieve a reliable extrapolation to $t = 0\,\mathrm{s}$. The absorption coefficient at time $t = 0\,\mathrm{s}$ is calculated with:

$$\alpha_{t=0} = \frac{R_\mathrm{L}}{c}\left(\frac{1}{\tau_{t=0}} - \frac{1}{\tau_0}\right) \tag{8.5}$$

9 Absorption spectrum and absolute absorption cross sections of acetylperoxy radicals

The content of this chapter was published as “The Absorption Spectrum and Absolute Absorption Cross Sections of Acetylperoxy Radicals, $CH_3C(O)O_2$ in the near IR” by M. Rolletter, E. Assaf, M. Assali, H. Fuchs, and C. Fittschen in Journal of Quantitative Spectroscopy & Radiative Transfer, 245, 106877, 2020. The article is licensed under the Elsevier user license and the final published version can be found at:
https://www.sciencedirect.com/science/article/abs/pii/S0022407319309732
The supplementary material is provided in Appendix A.4.

Journal of Quantitative Spectroscopy & Radiative Transfer 245 (2020) 106877

Contents lists available at ScienceDirect

Journal of Quantitative Spectroscopy & Radiative Transfer

journal homepage: www.elsevier.com/locate/jqsrt

The absorption spectrum and absolute absorption cross sections of acetylperoxy radicals, $CH_3C(O)O_2$ in the near IR

Michael Rolletter[a], Emmanuel Assaf[b,#], Mohamed Assali[b], Hendrik Fuchs[a,*], Christa Fittschen[b,*]

[a] Institute of Energy and Climate Research, IEK-8: Troposphere, Forschungszentrum Jülich GmbH, D-52428 Jülich, Germany
[b] Université Lille, CNRS, UMR 8522 - PC2A - Physicochimie des Processus de Combustion et de l'Atmosphère, F-59000 Lille, France

ARTICLE INFO

Article history:
Received 11 December 2019
Revised 31 January 2020
Accepted 31 January 2020
Available online 3 February 2020

ABSTRACT

The $\tilde{A}$-$\tilde{X}$ electronic transition of acetylperoxy radicals ($CH_3C(O)O_2$) in the near-infrared was measured at 67hPa synthetic air in the spectral ranges from 6094 cm^{-1} to 6180 cm^{-1} and 6420 cm^{-1} to 6600 cm^{-1}. $CH_3C(O)O_2$ radicals were generated by the pulsed photolysis of a acetaldehyde/Cl_2/O_2 mixture at 351 nm and subsequently measured by time-resolved continuous-wave cavity ring-down spectroscopy (cw-CRDS). The absorption cross sections of eight discrete absorption lines were determined relative to the absorption cross section of HO_2, which has previously been reported. The strongest absorption cross section was found at 6510.73 cm^{-1} and was determined to be $(4.9 \pm 2.5) \times 10^{-20}$ cm^2.

1. Introduction

In the troposphere, the oxidation of volatile organic compounds (VOCs) is mainly driven by hydroxyl (OH) radicals and leads to the formation of organic peroxy radicals (RO_2). The fate of these RO_2 radicals depends on the chemical composition of the environment. In a polluted atmosphere they react mainly with nitric oxide (NO) to form alkoxy radicals or react with nitrogen dioxide (NO_2) to form peroxynitrates (RO_2NO_2). Subsequent to the reaction with NO, alkoxy radicals react with O_2 to form hydroperoxy (HO_2) radicals. HO_2 radicals further oxidize NO to NO_2 and regenerate OH closing the quasi-catalytic cycle. The photolysis of produced NO_2 is the only relevant chemical source of tropospheric ozone. In clean environments with low NO_x ($NO_x = NO + NO_2$) concentrations, the dominant loss of RO_2 is due to its reaction with HO_2 forming hydroperoxides ROOH and terminating the radical reaction chain. In addition, RO_2 radicals can react either with other RO_2 as self- ($RO_2 + RO_2$) or cross-reaction ($RO_2 + R'O_2$) or with OH radicals ($RO_2 + OH$) [1–3].

The majority of emitted biogenic non methane hydrocarbons are isoprene (53%) and monoterpene species (16%) [4]. The photooxidation of these highly abundant compounds and their oxidation products form among other products also significant amounts of acetylperoxy radicals ($CH_3C(O)O_2$). In the reaction with NO_2, $CH_3C(O)O_2$ form peroxyacetyl nitrate (PAN) which is a toxic secondary air pollutant. In addition, PAN acts as the principal tropospheric reservoir species for NO_x [5]. The only relevant source in the troposphere is this photochemical process, so that PAN is an indicator for photochemical oxidation. Its relatively long atmospheric lifetime of approximately two weeks allows for transport over long distances.

Model calculations of measured radical concentrations in different field studies underestimate HO_x ($HO_x = OH + HO_2$) radical concentrations in remote regions with high emissions of VOCs from biogenic sources [6–9]. Because acetylperoxy radicals are formed from biogenic precursors and serve as source for HO_2, understanding of its properties is of importance.

Recent studies show that the $CH_3C(O)O_2 + HO_2$ reaction, which is the most important tropospheric reaction in regions that are dominated by biogenic emissions (low NO emissions), does not only lead to radical chain terminating products (R1, R2), but can also regenerate OH (R3) [10–12]:

$$CH_3C(O)O_2 + HO_2 \rightarrow CH_3C(O)OOH + O_2 \quad (R1)$$

$$\rightarrow CH_3C(O)OH + O_3 \quad (R2)$$

$$\rightarrow CH_3C(O)O + OH + O_2 \quad (R3)$$

* Corresponding authors.
E-mail addresses: h.fuchs@fz-juelich.de (H. Fuchs), christa.fittschen@univ-lille.fr (C. Fittschen).
now at Earth System Research Laboratory, Chemical Sciences Division, National Oceanic and Atmospheric Administration, Boulder, Colorado 80305, United States

https://doi.org/10.1016/j.jqsrt.2020.106877
0022-4073/

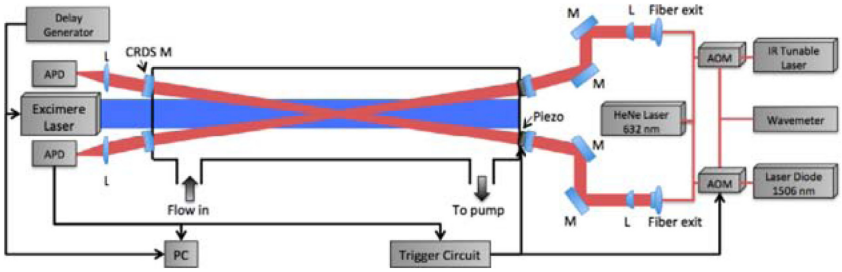

Fig. 1. Schematic view of the used experimental setup: AOM, Acousto-Optic Modulator; APD, Avalanche Photo Diode; M, Mirror; L, Lens. Both cw-CRDS systems are equipped with identical trigger circuits and data acquisition systems.

This additional OH radical regeneration could improve the model-measurement agreement in low NO_x environments with high VOC emission rates.

For an accurate understanding of the $CH_3C(O)O_2 + HO_2$ reaction, it is necessary to understand the secondary chemistry. For example, the $CH_3C(O)O_2$ self-reaction (R4) competes with the reaction with HO_2, forming the same product $CH_3C(O)O$ as (R3) making it hard to distinguish between both reactions.

$$2\ CH_3(O)O_2 \rightarrow 2\ CH_3C(O)O + O_2 \quad \text{(R4)}$$

In addition, reaction rate constants of the self-reaction ($k_4 = 2.9 \times 10^{-12}$ exp(500/T) cm^3 $molecule^{-1}$ s^{-1} [13]) and of the reaction with HO_2 ($k_{1\text{-}3} = 3.14 \times 10^{-12}$ exp(580/T) cm^3 $molecule^{-1}$ s^{-1} [13]) are in the same order of magnitude which makes it complicated to study those reaction kinetics.

The detection of RO_2 in previous kinetic laboratory studies was mainly done in the UV region. The spectral overlap of different peroxy species in this region is prone to systematic errors in the quantitative detection [14–18]. Therefore, experiments analysing different RO_2 are difficult to evaluate, if they are detected by UV absorption.

Here, we use absorption of $CH_3C(O)O_2$ in the $\tilde{A}$-$\tilde{X}$ electronic transition located in the near infrared region. This results in absorption cross sections that are up to several orders of magnitude smaller compared to values in the UV, but the detection is more selective due to less spectral overlap with formed products. In order to measure these small absorption cross sections, very sensitive detection methods need to be used, in our case continuous wave-Cavity Ring Down Spectroscopy (cw-CRDS). While the relative spectrum has already been measured by Zalyubovsky et al. [19] in a large wavelength range and the absolute absorption cross section of the strongest band at 5582 cm^{-1} has been estimated, we present here the determination of absolute absorption cross sections in two ranges from 6094 cm^{-1} - 6180 cm^{-1} and from 6420 cm^{-1} - 6600 cm^{-1}, corresponding to the COO bend and to the OO stretch transition, respectively, relative to the absorption cross section of HO_2. These cross sections can be used in future works for the quantitative detection of this radical.

2. Experimental

2.1. Experimental setup

The setup has been described in detail before [20–23] and is briefly discussed here (Fig. 1).

The setup consisted of a 0.79 m long flow reactor made of stainless steel. The beam of a pulsed excimer laser (Lambda Physik LPX 202i) passed the reactor longitudinally. The flow reactor contained two identical continuous wave cavity ring-down spectroscopy (cw-CRDS) absorption paths, which were installed in a small angle with respect to the photolysis path. An overlap with the photolysis beam of 0.377 m is achieved. Both beam paths were tested for a uniform overlap with the photolysis beam before experiments were done. For this purpose, both cw-CRDS instruments were operated to simultaneously measure HO_2 concentrations. Deviations between HO_2 concentrations were less than 5% demonstrating that the photolysis laser was very well aligned, *i.e.* both light paths probed a very similar photolysed volume in the reactor. A small helium purge flow prevented the mirrors from being contaminated. For measuring the $CH_3C(O)O_2$ spectrum, a tunable laser source (Agilent 81680A) was coupled into one of the cavities by systems of lenses and mirrors. On the other path, a DFB laser was coupled into the cavity for the detection of HO_2 radicals during the calibration measurements. The calibration of the acetylperoxy absorption cross section at 6497.94 and 6638.30 cm^{-1} in 67 hPa helium has also been carried out using a DFB laser instead of the Agilent module. Each probe beam passed an acousto-optic modulator (AOM, AAoptoelectronic) to rapidly turn off the 1st order beam once a threshold for light intensity in the cavity was reached, in order to measure the ring-down event. Then, the decay of light intensity was recorded and an exponential fit is applied to retrieve the ring-down time. The absorption coefficient α is derived from Eq. (1).

$$\alpha = [A] * \sigma_A = \frac{R_L}{c}\left(\frac{1}{\tau} - \frac{1}{\tau_0}\right) \quad (1)$$

where τ is the ring-down time with an absorber present; τ_0 is the ring-down time with no absorber present; σ_A is the absorption cross section of the absorbing species A; R_L is the ratio between cavity length (79 cm) and effective absorption path (37.7 cm); c is the speed of light. To calculate the absorption cross section it is necessary to know the absorber concentration.

Acetylperoxy radicals were generated by pulsed 351 nm photolysis of acetaldehyde (CH_3CHO) / Cl_2 / O_2 mixtures:

$$Cl_2 + h\nu \rightarrow 2\ Cl \quad \text{(R5)}$$

$$CH_3CHO + Cl \rightarrow CH_3CO + HCl \quad \text{(R6)}$$

$$CH_3CO + O_2 + M \rightarrow CH_3C(O)O_2 + M \quad \text{(R7)}$$

The Cl radical concentration for the measurement of the spectrum was around 1.7×10^{12} cm^{-3} and was varied for the calibration measurements between (1 and 8) $\times$ 10^{12} cm^{-3}. Acetaldehyde was prepared as a diluted mixture in a glass bulb. A small flow was added to the mixture through a calibrated flow meter giving a concentration of 2.5 $\times$ 10^{14} cm^{-3}. Nearly all experiments were performed in synthetic air, at 298 K and 67 hPa total pressure,

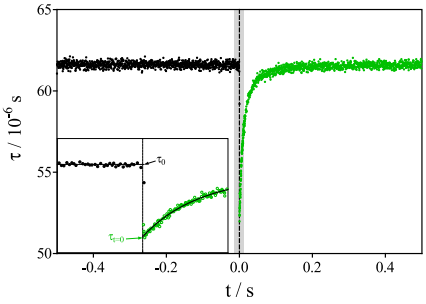

Fig. 2. Typical series of ring-down times for $CH_3C(O)O_2$, the insert shows the zoom of the gray-shaded area (+/−15 ms). The dashed line represents the time of the photolysis pulse ($t = 0$ s). Ring-down events before the photolysis pulse (black) are used to determine τ_0, extrapolation to $t = 0$ s of a bi-exponential fit of the ring-down times occurring during the first 50 ms after the photolysis pulse (black line in the insert) are used to determine τ.

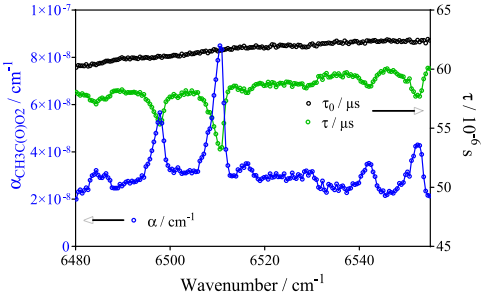

Fig. 3. Portion of the relative absorption spectrum: each dot, corresponding to one wavelength, is extracted from a kinetic decay such as shown in Fig. 2. Black dots represent baseline (τ_0), green dots obtained from extrapolation of bi-exponential fitting such as shown in Fig. 2 ($\tau_{t=0}$), blue dots (α) obtained by applying equation (Eq. (1)).

the absorption cross sections at 6697.94 and 6638.30 cm^{-1} were also determined at 67 hPa helium. N_2 (Praxair, 4.5), He (Praxair 4.5) and O_2 (Praxair, 4.5) were used without further purification. All gas flows were controlled by calibrated mass flow controllers (Bronkhorst, Tylan).

2.2. Absorption spectra measurements

The procedure to measure absorption spectra has been described before [24,25] and is only briefly discussed here. The spectrum was measured with a point spacing of 0.1 cm^{-1} for the wavelength range from 6094 - 6180 cm^{-1} and 0.2 cm^{-1} for the wavelength range from 6420 - 6600 cm^{-1}, corresponding to the COO bend and the OO stretch, respectively [19]. Both wavelength regions have been sampled by changing incrementally the wavelength of the laser while a constant amount of $CH_3C(O)O_2$ was generated in the reactor.

For each wavelength, a time series of ring-down measurements testing the acetyperoxy radical absorption was recorded. After the data acquisition was triggered ring-down events were usually recorded 0.5 s each before and after the photolysis laser shot which led to the formation of acetylperoxy radicals. A typical trace is shown in Fig. 2, where ring-down times from ring-down events occurring before the photolysis pulse are shown in black, and those after the photolysis pulse are shown in green. The loss of $CH_3C(O)O_2$ radicals is for the first tens of ms mostly due to self-reaction and to the reaction with the radical products of this self-reaction (CH_3O_2 and HO_2). With decreasing radical concentrations on the longer time scale, diffusion out of the photolysis volume becomes the major loss process. To derive the absorbance of the initially produced acetylperoxy radicals, the time-resolved series of ring-down events was extrapolated to the moment of the photolysis pulse (t = 0 s). Different fitting procedures were tested, and it turned out that a bi-exponentiel fit over the first 50 ms following the photolysis pulse reproduced the data very well and allowed a reliable extrapolation to t = 0 s. However, it has to be kept in mind that the decay of the $CH_3C(O)O_2$ concentration is due to a complex reaction scheme, and the decay constants from the fit have no physical meaning. The quality of the fit is shown as a black line in the insert of Fig. 2. τ_0, that is required to calculate the absorbance (Eq. (1)), was derived from the average of all detected ring-down events that occurred before the photolysis pulse when no $CH_3C(O)O_2$ was present. The ring-down events are randomly distributed in time at each photolysis shot because of the random nature of when exactly an efficient coupling of the laser into the cavity was achieved. Ring-down events were therefore accumulated over several laser pulses (10 – 20 generally) to get a better coverage of the whole time range.

3. Results and discussion

A portion of the relative absorption spectrum of the OO stretch region is shown in Fig. 3. For each wavenumber, measurements were evaluated as shown in Fig. 2. Ring-down times extrapolated to t = 0 s (green) and τ_0 as the average of all ring-down times before the photolysis pulse (black) are shown for each wavenumber in Fig. 3. The absorption coefficients (blue) are calculated by applying equation (Eq. (1)) to each data pair τ and τ_0.

In order to convert the absorption coefficient α into absolute cross sections σ, the knowledge of the exact $CH_3C(O)O_2$ concentration is necessary. Therefore, a series of experiments was conducted to quantify the initial amount of radicals. This was achieved by quantitatively converting all Cl-atoms to HO_2 radicals, which can be reliably measured by cw-CRDS on a strong absorption line at 6638.205 cm^{-1} [23,26–29]. The measurement of the HO_2 absorption cross section is based on the measurement of HO_2 decays during self-reaction, which allows for retrieval of the initial concentration, and thus the absorption cross section, if the rate constant is known. While the uncertainty of the measured HO_2 decays itself is small (<10%), the uncertainty of the rate constant is currently recommended by the IUPAC committee to ±40%. This same uncertainty has to be considered for the absorption cross sections obtained in this work, as they are measured relative to the HO_2 absorption cross section. The quantitative conversion of Cl-atoms to HO_2 is done by photolysing a Cl_2 / methanol (CH_3OH) mixture:

$$Cl + CH_3OH \rightarrow HCl + CH_2OH \quad (R9)$$

$$CH_2OH + O_2 \rightarrow CH_2O + HO_2 \quad (R10)$$

Then, CH_3OH is substituted by CH_3CHO to form $CH_3C(O)O_2$ following reactions (R11) and (R12), while keeping conditions for the generation of Cl radicals constant.

$$Cl + CH_3CHO \rightarrow HCl + CH_3CO \quad (R11)$$

$$CH_3CO + O_2 \rightarrow CH_3C(O)O_2 \quad (R12a)$$

Assuming that the concentration of HO_2 radicals corresponds to the concentration of Cl atoms, the ratio of absorbance measured

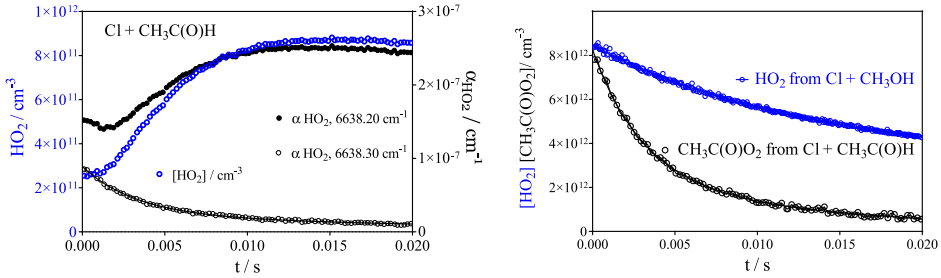

Fig. 4. Left plot shows HO_2 absorption coefficient online (6638.20 cm^{-1}, black dots) and offline (6638.30 cm^{-1}, open black symbols, right y-axis apply for both) and HO_2 concentration (blue symbols, left y-axis) measured after photolysing a Cl_2 / CH_3CHO / O_2 mixture. Right graph shows the HO_2 concentration from the photolysis of Cl_2 / CH_3OH / O_2 mixture (blue symbols) and the $CH_3C(O)O_2$ concentration time profile from the photolysis of the Cl_2 / CH_3CHO/ O_2 mixture (black symbols). Both experiments used the same Cl_2 concentration.

for $CH_3C(O)O_2$ and HO_2 can be used to calculate the $CH_3C(O)O_2$ absorption cross section relative to the well known HO_2 absorption cross section according to:

$$\sigma_{CH_3C(O)O_2} = \alpha_{CH_3C(O)O_2} \frac{\sigma_{HO_2}}{\alpha_{HO_2}} \quad (2)$$

However, the assumption does not entirely apply, because the reaction of $CH_3CO + O_2$ leads also to the formation of some OH radicals, the yield depending on pressure and nature of the CH_3CO precursor [30–32]. An OH yield of 0.25 is expected in nitrogen at 67 hPa [30].

$$CH_3CO + O_2 \rightarrow OH + \text{products} \quad (R12b)$$

OH radical concentrations can in principle be measured by cw-CRDS in the experimental set-up [33]. However, concentrations in these experiments were below the limit of detection likely due to the fast reaction with acetaldehyde [13]:

$$CH_3CHO + OH \rightarrow CH_3CO + H_2O \quad (R13)$$

Because under our experimental conditions ($[CH_3CHO] = 2.5 \times 10^{14}$ cm^{-3}), (R13) is leading with $k_{13} = 1.5 \times 10^{-11}$ cm^3 s^{-1} to an OH lifetime of 250 µs, and can thus, in absence of other potential reaction partners, be considered as the nearly exclusive fate of OH radicals. And because (R13) leads to formation of another CH_3CO radical, this reaction does not introduce an error in the calculation of the absorption cross section using equation (Eq. (2)).

However, it was observed in our experiments that small amounts of HO_2 radicals are formed immediately from the initial reaction of $CH_3CHO + Cl$. Radical concentrations measured in a typical experiment are shown in Fig. 4: the left graph shows the HO_2 signal obtained from photolysis of Cl_2 / CH_3CHO / O_2 mixture. Because $CH_3C(O)O_2$ has a broad absorption spectrum [19], it still absorbs in the wavelength range where HO_2 is detected (6638.2 cm^{-1}). Therefore, absolute HO_2 concentrations (blue symbols) are obtained from the difference of the online (6638.2 cm^{-1}) and the offline (6638.3 cm^{-1}) absorption signal. It can be seen that the HO_2 concentration immediately after the photolysis pulse is not zero. The blue symbols on the right graph show the HO_2 concentration time profile under the same conditions, but with CH_3OH instead of CH_3CHO. Comparing the HO_2 concentrations measured from methanol mixtures ($[HO_2]_{CH_3OH}$) and acetaldehyde mixtures ($[HO_2]_{CH_3C(H)O}$) shows that around 3% of the Cl-atoms are converted to HO_2 (δ_{HO_2}) in the presence of CH_3CHO.

$$\delta_{HO_2} = \frac{[HO_2]_{CH_3CHO}}{[HO_2]_{CH_3OH}} \quad (3)$$

This small correction of the initial $CH_3C(O)O_2$ concentration was taken into account when converting the absorption coefficient of $CH_3C(O)O_2$ into absorption cross sections:

$$\sigma_{CH_3C(O)O_2} = \alpha_{CH_3C(O)O_2} \frac{\sigma_{HO_2}}{\alpha_{HO_2}} \times \frac{1}{(1 - \delta_{HO_2})} \quad (4)$$

The origin of this rapid HO_2 formation is not clear, but is formed possibly through the reaction

$$CH_3CO + O_2 \rightarrow CH_2CO + HO_2 \quad (R12c)$$

Such a rapid HO_2 formation with similar yields had already been observed by Morajkar et al. [34]. with a yield of around 7%, independent of pressure between 10 and 90 Torr helium, following the 248 nm photolysis of CH_3CHO, and also by Hui et al. [35]. with a yield of 2–3% following the reaction of Cl-atoms with CH_3CHO at 100 Torr N_2. HO_2 concentrations at 67 hPa N_2 have been calculated using an absorption cross section of $\sigma_{HO_2,6638.20cm\text{-}1} = 2.01 \times 10^{-19}$ cm^2, obtained from the empirical expression of Assaf et al. [27].

This way, absorption cross sections σ were measured for 8 wavenumbers in synthetic air and for 2 wavenumbers in helium, given in Table 1 together with the absorption coefficients α for the same wavelengths in synthetic air, such as found during the measurement of the full spectrum. Also given in Table 1 are the absorption cross sections for two wavenumbers, obtained in 67 hPa

Table 1
Absorption coefficient α for $CH_3C(O)O_2$ from the measurement of the full spectrum for eight wavenumbers (marked by lines in the full spectrum of Fig. 6) and absorption cross sections σ for the same lines, determined relative to the HO_2 cross section at 67 hPa N_2 and for two wavenumbers at 67 hPa helium.

Wavenumber / cm^{-1}	α / 10^{-8} cm^{-1}	σ / 10^{-20} cm^2
6121.08	5.65 ± 0.28	3.4 ± 1.7
6164.75	2.75 ± 0.14	1.7 ± 0.8
6108.74	4.01 ± 0.20	2.2 ± 1.1
6114.53	1.59 ± 0.08	0.9 ± 0.5
6497.94	5.35 ± 0.27	3.2 ± 1.6
6697.94 (helium)		3.3 ± 1.7
6502.80	3.03 ± 0.15	1.7 ± 0.9
6552.76	4.29 ± 0.21	2.5 ± 1.3
6510.74	8.49 ± 0.42	4.9 ± 2.4
6638.30 (helium)		0.8 ± 0.4

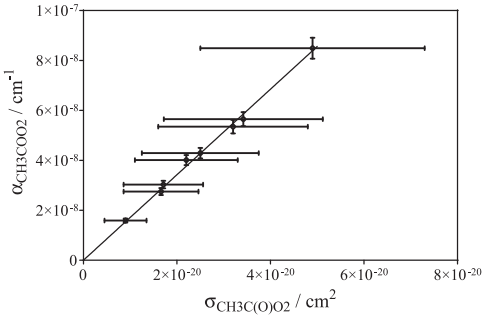

Fig. 5. Absorption coefficients α as a function of the absorption cross sections σ from Table 1. Error bars are statistical for absorption coefficients α (5%), and an uncertainty of 45% is added for the absorption cross section σ, taking into account the uncertainty in the absorption cross section for HO_2.

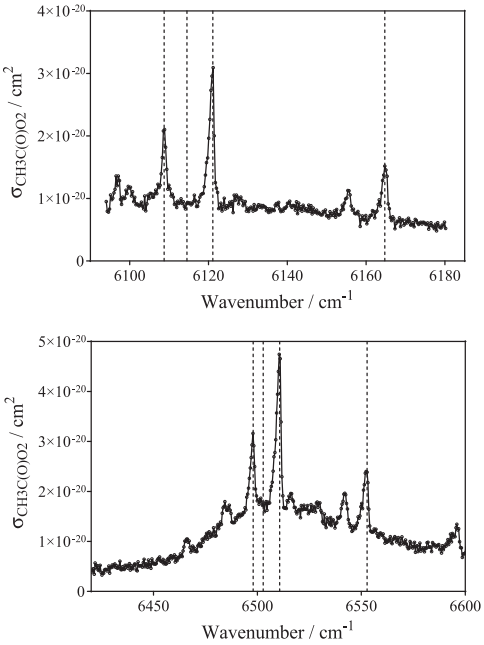

Fig. 6. Absolute absorption spectrum of $CH_3C(O)O_2$. Vertical lines indicate the wavelengths where absolute absorption cross sections have been determined relative to the absorption cross section of HO_2 (see Table 1). The data can be downloaded as supplementary data.

helium: 6697.94 cm^{-1} corresponds to one peak of the OO-stretch transition band, while 6638.30 cm^{-1} corresponds to the wavenumber that we commonly use for the measurement of the HO_2-offline signal, i.e. the open circles in Fig. 4. The error bars of the absorption coefficients α are statistical only and are given with ±5%, obtained from the 95% confidence interval of the extrapolation of the bi-exponential fit to $t = 0$ s (black curve in the insert of Fig. 2, typically below 4%) as well as the τ_0 (average of all ring down events before the photolysis pulse: typically less than 1%). The error bars for the absorption cross sections are given with ±50% and are composed of twice the uncertainty of extrapolating α to $t = 0$ s (once for $\alpha_{CH_3C(O)O_2}$ and once for α_{HO_2}) and the 40% uncertainty given by the IUPAC committee [36] for the rate constant of the HO_2 self-reaction, that was used to determine the absorption cross section of HO_2.

In Fig. 5 the absorption coefficients are plotted for all eight wavenumbers as a function of the absorption cross sections σ. A good linearity is found, assuring that the $CH_3C(O)O_2$ concentration was stable during the measurement of the full spectrum.

The slope from the linear regression of Fig. 5 leads to the concentration of $CH_3C(O)O_2$ radicals that was generated during the measurement of the full spectrum: 1.7×10^{12} cm^{-3}. This value was used for the conversion of the absorption coefficients from the relative spectra (blue line in Fig. 3) of the two wavelength ranges into absolute absorption cross sections, shown in Fig. 6. A comparison with a previously published spectrum [19] shows an excellent agreement of the positions and relative intensities of the different absorption maxima.

Zalyubovsky et al. [19] determined an absorption cross section of $\sigma = (1 \pm 0.5) \times 10^{-19}$ cm^2 at 5582.5 cm^{-1}. This is consistent with our absorption cross section of $(4.9 \pm 2.4) \times 10^{-20}$ cm^2 at the absorption maximum 6510.71 cm^{-1}, which has in the spectrum of Zalyubovsky et al. a relative intensity of approximately a factor 2 less than the absorption maximum at 5582.5 cm^{-1}.

The results obtained in this work will be used in future studies on the reaction kinetics of $CH_3C(O)O_2$ radicals. Depending on the quality of alignment, cleanliness of mirrors, etc. a decrease of the ring-down time of $\Delta\tau = 0.5$ µs on a typical $\tau_0 = 50$ µs can be achieved in time-resolved experiments, leading to a limit of detection below $[CH_3C(O)O_2] = 4 \times 10^{11}$ cm^{-3}, making this technique more sensitive than typical UV-absorption measurements. And even though the spectrum features a rather broad background, *i.e.* lacks the high selectivity that can be achieved for HO_2 or OH measurements, its main absorption peaks are red-shifted compared to other small peroxy radicals such as HO_2, CH_3O_2 [24,37,38], $C_2H_5O_2$ [37] and should thus allow a selective detection for measuring the rate constants and branching ratios of self- and cross-reactions.

4. Conclusion

We measured the $CH_3C(O)O_2$ absorption spectrum in the ranges from 6094 cm^{-1} - 6180 cm^{-1} and 6420 cm^{-1} - 6600 cm^{-1}. Measurements were performed in 67 hPa synthetic air or helium total pressure. Radicals were generated by the pulsed photolysis of acetaldehyde / Cl_2 / O_2 mixtures at 351 nm.

Some large peaks on top of a broad absorption spectrum were obtained, in good agreement with an earlier measurement by Zalyubovsky et al. [19]. Absolute absorption cross sections were measured for eight different wavelengths and are in good agreement relative to the only available measurement by Zalyubovsky et al. [19] performed at a lower wavenumber.

Declaration of Competing Interest

The authors declare that they have no known competing financial interests or personal relationships that could have appeared to influence the work reported in this paper.

CRediT authorship contribution statement

Michael Rolletter: Data curation, Writing - original draft. **Emmanuel Assaf:** Investigation, Data curation, Resources.

Mohamed Assali: Investigation, Data curation. **Hendrik Fuchs:** Conceptualization, Writing - review & editing, Supervision, Funding acquisition. **Christa Fittschen:** Conceptualization, Writing - original draft, Supervision, Project administration, Funding acquisition.

Acknowledgments

This project was supported by the French ANR agency under contract No. ANR-11-Labx-0005-01 CaPPA (Chemical and Physical Properties of the Atmosphere), the Région Hauts-de-France, the Ministère de l'Enseignement Supérieur et de la Recherche (CPER Climibio) and the European Fund for Regional Economic Development. This project has received funding from the European Research Council (ERC) under the European Union's Horizon 2020 research and innovation program (SARLEP grant agreement No. 681529) and from the exchange program of the Deutscher Akademischer Austauschdienst (DAAD) (project number 57316518) and PHC Procope project no. 37666WA.

Supplementary materials

Supplementary material associated with this article can be found, in the online version, at doi:10.1016/j.jqsrt.2020.106877.

References

[1] Orlando JJ, Tyndall GS. Laboratory studies of organic peroxy radical chemistry: an overview with emphasis on recent issues of atmospheric significance. Chem Soc Rev 2012;41:6294–317.
[2] Fittschen C. The reaction of peroxy radicals with OH radicals. Chem Phys Lett 2019;725:102–8.
[3] Assaf E, Song B, Tomas A, Schoemaecker C, Fittschen C. Rate constant of the reaction between CH_3O_2 radicals and OH radicals revisited. J Phys Chem A 2016;120:8923–32.
[4] Guenther AB, Jiang X, Heald CL, Sakulyanontvittaya T, Duhl T, Emmons LK, et al. The model of emissions of gases and aerosols from nature version 2.1 (MEGAN2. 1): an extended and updated framework for modeling biogenic emissions. Geosci Model Dev 2012;5:1471–92.
[5] Fischer EV, Jacob DJ, Yantosca RM, Sulprizio MP, Millet DB, Mao J, et al. Atmospheric peroxyacetyl nitrate (PAN): a global budget and source attribution. Atmos Chem Phys 2014;14:2679–98.
[6] Tan D, Faloona I, Simpas JB, Brune W, Shepson PB, Couch TL, et al. HO_x budgets in a deciduous forest: results from the PROPHET summer 1998 campaign. J Geophys Res Atmos 2001;106:24407–27.
[7] Lelieveld J, Butler TM, Crowley JN, Dillon TJ, Fischer H, Ganzeveld L, et al. Atmospheric oxidation capacity sustained by a tropical forest. Nature 2008;452:737–40.
[8] Hofzumahaus A, Rohrer F, Lu K, Bohn B, Brauers T, Chang CC, et al. Amplified trace gas removal in the troposphere. Science 2009;324:1702–4.
[9] Wolfe GM, Thornton JA, Bouvier-Brown NC, Goldstein AH, Park JH, McKay M, et al. The Chemistry of Atmosphere-Forest Exchange (CAFE) model - Part 2: application to BEARPEX-2007 observations. Atmos Chem Phys 2011;11:1269–94.
[10] Hasson AS, Tyndall GS, Orlando JJ. A product yield study of the reaction of HO_2 radicals with ethyl peroxy ($C_2H_5O_2$), acetyl peroxy ($CH_3C(O)O_2$), and acetonyl peroxy ($CH_3C(O)CH_2O_2$) radicals. J Phys Chem A 2004;108:5979–89.
[11] Winiberg FAF, Dillon TJ, Orr SC, Groß CBM, Bejan I, Brumby CA, et al. Direct measurements of oh and other product yields from the $HO_2 + CH_3C(O)O_2$ reaction. Atmos Chem Phys 2016;16:4023–42.
[12] Hui AO, Fradet M, Okumura M, Sander SP. Temperature dependence study of the kinetics and product yields of the $HO_2 + CH_3C(O)O_2$ reaction by direct detection of OH and HO_2 radicals using 2f-IR wavelength modulation spectroscopy. J Phys Chem A 2019;123:3655–71.
[13] Atkinson R, Baulch DL, Cox RA, Crowley JN, Hampson RF, Hynes RG, et al. Evaluated kinetic and photochemical data for atmospheric chemistry: volume ii - gas phase reactions of organic species. Atmos Chem Phys 2006;6:3625–4055.
[14] Addison MC, Burrows JP, Cox RA, Patrick R. Absorption-Spectrum and kinetics of the acetylperoxy radical. Chem Phys Lett 1980;73:283–7.
[15] Moortgat G, Veyret B, Lesclaux R. Absorption-Spectrum and kinetics of reactions of the acetylperoxy radical. J Phys Chem 1989;93:2362–8.
[16] Lightfoot P.D., Cox R.A., Crowley J.N., Destriau M., Hayman G.D., Jenkin M.E., et al. Organic peroxy-radicals - Kinetics, spectroscopy and tropospheric chemistry. atmospheric environment part a-General topics. 1992;26:1805–961.
[17] Roehl CM, Bauer D, Moortgat GK. Absorption spectrum and kinetics of the acetylperoxy radical. J Phys Chem 1996;100:4038–47.
[18] Maricq MM, Szente JJ. The $CH_3C(O)O_2$ radical. its uv spectrum, self-reaction kinetics, and reaction with CH_3O_2. J Phys Chem 1996;100:4507–13.
[19] Zalyubovsky SJ, Glover BG, Miller TA. Cavity ringdown spectroscopy of the $\tilde{A}-\tilde{X}$ electronic transition of the $CH_3C(O)O_2$ radical. J Phys Chem A 2003;107:7704–12.
[20] Thiebaud J, Fittschen C. Near infrared cw-CRDS coupled to laser photolysis: spectroscopy and kinetics of the HO_2 radical. Appl Phys B 2006;85:383–9.
[21] Parker AE, Jain C, Schoemaecker C, Szriftgiser P, Votava O, Fittschen C. Simultaneous, time-resolved measurements of OH and HO_2 radicals by coupling of high repetition rate lif and cw-CRDS techniques to a laser photolysis reactor and its application to the photolysis of H_2O_2. Appl Phys B 2011;103:725–33.
[22] Votava O, Mašát M, Parker AE, Jain C, Fittschen C. Microcontroller based resonance tracking unit for time resolved continuous wave cavity-ringdown spectroscopy measurements. Rev Sci Instrum 2012;83:043110.
[23] Assaf E, Asvany O, Votava O, Batut S, Schoemaecker C, Fittschen C. Measurement of line strengths in the $\tilde{A}$ $2A' \leftarrow$ x $2A''$ transition of HO_2 and DO_2. J Quant Spectrosc Radiat Transfer 2017;201:161–70.
[24] Faragó EP, Viskolcz B, Schoemaecker C, Fittschen C. Absorption spectrum and absolute absorption cross sections of CH_3O_2 radicals and CH3I molecules in the wavelength range 7473–7497 cm–1. J Phys Chem A 2013;117:12802–11.
[25] Jain C, Morajkar P, Schoemaecker C, Viskolcz B, Fittschen C. Measurement of absolute absorption cross sections for nitrous acid (HONO) in the near-infrared region by the continuous wave cavity ring-down spectroscopy (cw-CRDS) technique coupled to laser photolysis. J Phys Chem A 2011;115:10720–8.
[26] Thiebaud J, Crunaire S, Fittschen C. Measurements of line strengths in the $2\nu 1$ band of the HO_2 radical using laser photolysis/continuous wave cavity ring–down spectroscopy (cw-CRDS). J Phys Chem A 2007;111:6959–66.
[27] Assaf E, Liu L, Schoemaecker C, Fittschen C. Absorption spectrum and absorption cross sections of the $2\nu_1$ band of HO_2 between 20 and 760 Torr air in the range 6636 and 6639 cm^{-1}. J Quant Spectrosc Radiat Transf 2018;211:107–14.
[28] Onel L, Brennan A, Gianella M, Ronnie G, Lawry Aguila A, Hancock G, et al. An intercomparison of HO_2 measurements by fluorescence assay by gas expansion and cavity ring-down spectroscopy within HIRAC (Highly instrumented reactor for atmospheric chemistry). Atmos Meas Tech 2017;10:4877–94.
[29] Tang Y, Tyndall GS, Orlando JJ. Spectroscopic and kinetic properties of HO_2 radicals and the enhancement of the HO_2 self reaction by CH_3OH and H_2O. J Phys Chem A 2010;114:369–78.
[30] Groß CBM, Dillon TJ, Crowley JN. Pressure dependent oh yields in the reactions of CH_3CO and $HOCH_2CO$ with O_2. Phys Chem Chem Phys 2014;16:10990–8.
[31] Carr SA, Baeza-Romero MT, Blitz MA, Pilling MJ, Heard DE, Seakins PW. OH yields from the CH_3CO+O_2 reaction using an internal standard. Chem Phys Lett 2007;445:108–12.
[32] Devolder P, Dusanter S, Lemoine B, Fittschen C. About the co-product of the OH radical in the reaction of acetyl with O_2 below atmospheric pressure. Chem Phys Lett. 2006;417:154–8.
[33] Assaf E, Fittschen C. Cross section of oh radical overtone transition near 7028 cm^{-1} and measurement of the rate constant of the reaction of OH with HO_2 radicals. J Phys Chem A 2016;120:7051–9.
[34] Morajkar P, Bossolasco A, Schoemaecker C, Fittschen C. Photolysis of CH_3CHO at 248 nm: evidence of triple fragmentation from primary quantum yield of CH_3 and HCO radicals and h atoms. J Chem Phys 2014;140:214308.
[35] Hui AO, Fradet M, Okumura M, Sander SP. Temperature dependence study of the kinetics and product yields of the $HO_2 + CH_3C(O)O_2$ reaction by direct detection of oh and HO_2 radicals using 2f-IR wavelength modulation spectroscopy. J Phys Chem A 2019;123:3655–71.
[36] Atkinson R, Baulch DL, Cox RA, Crowley JN, Hampson RF, Hynes RG, et al. Evaluated kinetic and photochemical data for atmospheric chemistry: volume 1 – Gas Phase reactions of O_x, HO_x, NO_x, and SO_x, species, IUPAC task group on atmospheric chemical kinetic data evaluation. Atmos Chem Phys. 2004;2(4):1461–738. http://iupac.pole-ether.fr.
[37] Atkinson DB, Hudgens JW. Chemical kinetic studies using ultraviolet cavity ring-down spectroscopic detection: self-reaction of ethyl and ethylperoxy radicals and the reaction $O_2 + C_2H_5 \rightarrow C_2H_5O_2$. J Phys Chem A 1997;101:3901–9.
[38] Chung C-Y, Cheng C-W, Lee Y-P, Liao H-Y, Sharp EN, Rupper P, et al. Rovibronic bands of the $\tilde{A} \leftarrow \tilde{X}$ transition of CH_3OO and CD_3OO detected with cavity ring-down absorption near 1.2–1.4μm. J Chem Phys 2007;127:044311.

10 Kinetic study of acetylperoxy radical reactions

This Chapter describes additional laboratory kinetic experiments that have been performed at the Université Lille 1. Measurements of the reaction rate constant of the $CH_3C(O)O_2$ self-reaction are used to validate the newly determined absorption cross section in the near-infrared (Chapter 9).

10.1 The $CH_3C(O)O_2$ self-reaction

It is complicated to perform kinetic studies of the $CH_3C(O)O_2 + HO_2$ reaction because of side reactions that are difficult to avoid. One important competing reaction is the self-reaction of $CH_3C(O)O_2$ radicals:

$$CH_3C(O)O_2 + CH_3C(O)O_2 \longrightarrow 2\,CH_3C(O)O + 2\,O_2 \qquad \text{(R 10.1)}$$

$CH_3C(O)O$ from reactions (R 7.1c) and (R 10.1) rapidly decomposes to methyl radicals (CH_3), and subsequently methylperoxy radicals (CH_3O_2) are formed by the addition of oxygen.

$$CH_3C(O)O \xrightarrow{M} CH_3 + CO_2 \qquad \text{(R 10.2)}$$

$$CH_3 + O_2 \xrightarrow{M} CH_3O_2 \qquad \text{(R 10.3)}$$

Furthermore, formed CH_3O_2 can react with $CH_3C(O)O_2$ in a peroxy radical cross-reaction:

$$CH_3C(O)O_2 + CH_3O_2 \longrightarrow CH_3O + CH_3C(O)O + O_2 \qquad \text{(R 10.4a)}$$

$$\longrightarrow CH_3C(O)OH + HCHO + O_2 \qquad \text{(R 10.4b)}$$

Reaction (R 10.4a) regenerates one CH_3O_2 radical and additionally forms one HO_2 by:

$$CH_3O + O_2 \longrightarrow HO_2 + CH_2O \qquad \text{(R 10.5)}$$

Other relevant peroxy radical reactions are

$$CH_3O_2 + HO_2 \longrightarrow CH_3OOH + O_2 \qquad \text{(R 10.6a)}$$
$$\longrightarrow CH_2O + H_2O + O_2 \qquad \text{(R 10.6b)}$$

and the HO_2 self-reaction (see R 1.18). CH_3O_2 is coincidentally formed as a product from reactions R 7.1c and R 10.1. Over the course of the experiment, CH_3O_2 concentrations rise and stronger affect $CH_3C(O)O_2$ and HO_2 concentrations by reactions R 10.4 and R 10.6, respectively.

To study the self-reaction, $Cl_2/CH_3CHO/O_2$ mixtures were photolysed with different Cl_2 concentrations (see reactions R 8.2 to R 8.4). Initially formed Cl radical concentrations ($[Cl]_0$) were in the range of (0.4-3.1) x 10^{13} cm^{-3}.

In the first few ms after the photolysis pulse, the $CH_3C(O)O_2$ consumption is dominated by the self-reaction. The self-reaction is a second order reaction, and its concentration change by time can be described in a general form as

$$-\frac{d[\mathrm{A}]}{dt} = k[\mathrm{A}]^2 \qquad (10.1)$$

where [A] is the concentration of reactant A, *k* is the reaction rate constant, and *t* the time. Rearrangement and integration from $[A]_0$ at $t = 0$ to $[A]_t$ at time *t*, leads to:

$$\int_{[\mathrm{A}]_0}^{[\mathrm{A}]_t} \frac{d[\mathrm{A}]}{[\mathrm{A}]^2} = -\int_0^t k dt \qquad (10.2)$$

The integrated rate expression is then:

$$\frac{1}{[\mathrm{A}]_t} = \frac{1}{[\mathrm{A}]_0} + kt \qquad (10.3)$$

For a second order reaction, the plot 1/[A] versus the time results in a straight line with slope *k*.

In total, four experiments were performed with initial Cl radical concentrations of 0.4×10^{13} cm^{-3}, 1.9×10^{13} cm^{-3}, 2.5×10^{13} cm^{-3}, and 3.1×10^{13} cm^{-3}. A function was adjusted to experimental data with the LINFIT function that fits input data by minimizing the chi-square error statistic. An example recorded at initial Cl concentration of 0.4×10^{13} cm^{-3} can be seen in Figure 10.1.

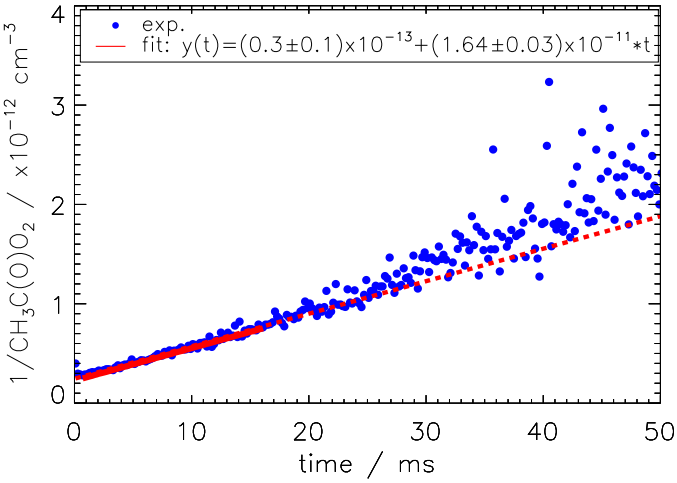

Figure 10.1: Measured $1/CH_3C(O)O_2$ concentration time profile derived for $[Cl]_0$ = 4.0×10^{12} cm^{-3}. The dashed line shows the derived fit function and the solid red line indicates the time range that was used for fitting the experimental data.

At $t = 0$, $CH_3C(O)O_2$ was generated by the photolysis pulse together with small amounts of HO_2 ($\leq 3\,\%$). The first few points where $CH_3C(O)O_2$ concentrations are still increasing were excluded from the fit. In the beginning, $CH_3C(O)O_2$ is exclusively removed by the self-reaction. In the course of the experiment, product concentrations of CH_3O_2 and HO_2 increase. As a result, the contribution of the self-reaction to the overall $CH_3C(O)O_2$ consumption is decreasing. To assure that the fit is not influenced too much by competing reactions, only the initial phase of the experiments was used when the $CH_3C(O)O_2$ self-reaction accounted for $\geq 80\,\%$ (see fit in Figure 10.1). The average reaction rate constant and standard deviation of the $CH_3C(O)O_2$ self-reaction derived by the fits of all experiments is $(1.7 \pm 0.1) \times 10^{-11}$ cm^3 s^{-1}. This is in agreement with the current IUPAC recommendation (Atkinson et al., 2006) of $(1.6^{+1.4}_{-0.8}) \times 10^{-11}$ cm^3 s^{-1}. If the fit function is applied to a larger time interval, larger values for the reaction rate constants are

derived. In Figure 10.1, it can be seen that the extrapolated fit is underestimating the $CH_3C(O)O_2$ consumption. This is caused by the additional $CH_3C(O)O_2$ consumption by reactions with CH_3O_2 (see R 10.4) and HO_2 (R 7.1), which become more important when these products have been formed.

The discussion here relies on the absorption cross sections used to transform the absorption time profiles into absolute concentrations, and any error in the absorption cross section would directly translate into a proportional error in the rate constant. If the absorption cross section was too large, it would convert measured absorbance into too small concentration and thus too high reaction rate constant. Therefore, reproducing literature recommendations is an indication that concentrations, which were derived by using determined $CH_3C(O)O_2$ absorption cross section are correct.

10.2 Outlook

It has been shown that the measured absorption cross-section in this work can be used for the quantitative detection of $CH_3C(O)O_2$. In a next step, the experimental setup described in Section 8.2 can be used to investigate the reaction system of $CH_3C(O)O_2$ with HO_2.

Two cw-CRDS absorption pathways allow the simultaneous detection of $CH_3C(O)O_2$, CH_3O_2, and HO_2 at 6510.74 cm^{-1}, 7489.16 cm^{-1}, and 6638.21 cm^{-1}, respectively. In addition, OH measurements by LIF and CRDS are available to determine the OH yield of the reaction of $CH_3C(O)O_2$ with HO_2. OH measurements by CRDS at 7028.83 cm^{-1} can be used to calibrate the LIF, which is a more sensitive detection technique compared to CRDS. By adding methanol to the acetaldehyde/O_2/Cl_2 mixtures, $CH_3C(O)O_2$ and HO_2 radicals are formed at the same time by photolysis. Subsequently, the $CH_3C(O)O_2$ degradation and the formation of CH_3O_2 and OH can be observed. In order to account for the secondary chemistry a zero-dimensional box model was used. The model was based on current literature recommendations and included all relevant reactions.

The chemical model was used to analyze measured concentration times series of $CH_3C(O)O_2$, CH_3O_2, and HO_2 in experiments of the $CH_3C(O)O_2$ self-reaction and the $CH_3C(O)O_2$ + HO_2 reaction. In the $CH_3C(O)O_2$ self-reaction, formed CH_3O_2 and HO_2 from Reactions R 10.1–R 10.3 and R 10.4a–R 10.5, respectively, were

overestimated by model calculations compared to observations. Therefore, the $CH_3C(O)O_2$ consumption was overestimated by Reactions R 10.4 and R 7.1. Similarly, first experiments of the $CH_3C(O)O_2$ + HO_2 reaction system showed that calculated CH_3O_2 concentration time profiles overestimated measurements by a factor of up to 3 compared to measurements.

The CH_3O_2 absorption cross section has been determined by two independent groups (Fittschen, 2019; Onel et al., 2020) and is most likely not the explanation for the discrepancy between measured and modelled CH_3O_2 concentrations. Several sensitivity studies were conducted to find an explanation for the enhanced CH_3O_2 formation in the model compared to observations. For example, a change in the branching ratio of Reaction R 10.4 towards channel b) was tested as suggested by Maricq and Szente (1996) and Roehl et al. (1996). As a result, the model–measurement agreement for $CH_3C(O)O_2$ and CH_3O_2 was improved. However, calculated CH_3O_2 concentrations were still overestimated by up to 40 %. In addition, calculated HO_2 concentrations were significantly underestimated by the model. This was caused by disabling the formation of CH_3O in the sensitivity study by changing the branching ratio towards other products.

Unfortunately, the exact nature of the reduced CH_3O_2 formation compared to literature data cannot be solved based on the current set of experiments. Therefore, it was not possible to determine the OH yield in the reaction of $CH_3C(O)O_2$ with HO_2. Further experiments and quantum based theoretical calculations are necessary to understand the chemistry. Especially, kinetic experiments of the $CH_3C(O)O_2$ + CH_3O_2 reaction could add valuable information to pin down the reaction responsible for the reduced CH_3O_2 formation compared to literature recommendations.

Part III

Conclusions

The aim of this thesis was to investigate the photochemical degradation mechanisms of selected BVOCs with a focus on explaining observed OH and HO_2 radical concentrations. In the presence of BVOCs, OH concentrations are suppressed due to their consumption in the oxidation reactions. However, several field campaigns showed that OH radicals are regenerated faster during the BVOC oxidation processes than is explained by the current knowledge of tropospheric chemistry, hence reducing the suppression of OH radicals.

In this work, the chemical mechanism of BVOC photooxidation was investigated in simulation experiments in the atmospheric simulation chamber SAPHIR. In addition, spectroscopic basics were provided to further investigate reaction kinetics of $CH_3C(O)O_2$ in the NIR.

The experiment with MBO validated that the MCM as state-of-the-art atmospheric mechanism is capable of reproducing observed concentration time profiles for OH and HO_2 radicals as well as for oxidation products. In this example, the traditional chemistry can explain observation without the need of novel RO_2 chemistry. In contrast, measured OH and HO_2 concentrations were systematically underestimated by a factor of up to 2 by model calculations in the α-pinene and pinonaldehyde experiments. As a consequence, in atmospheric models, the predicted lifetime of greenhouse gases like methane is increased in the troposphere, and thereby the radiative forcing is overestimated. In both studies, OH concentrations could be explained by constraining HO_2 concentrations in the model to observations. This indicates that both α-pinene and pinonaldehyde mechanisms lack a HO_2 source under investigated conditions. This result elucidates the need of the experimental investigation of oxidation of BVOC species in this work to improve the knowledge of radical regeneration in current chemical models.

In addition to the model–measurement discrepancies for radical species, the MCM mechanism was not able to correctly reproduce the observed pinonaldehyde concentrations in the α-pinene and pinonaldehyde experiment. In the first case, measured pinonaldehyde concentrations are strongly overestimated by at least a factor of 4. Sensitivity studies showed that measured pinonaldehyde concentrations can be explained by a shift in the initial RO_2 distribution towards reaction channels that do not form pinonaldehyde. In the pinonaldehyde experiments, model calculations underestimated the observed pinonaldehyde consumption. This could be partly explained by the parameterization of the photolysis rates in the MCM, which is lower than values that are calculated using measured ab-

sorption cross sections and a solar actinic flux spectrum. The large discrepancy of a factor of 3 between measured pinonaldehyde photolysis frequency and the parameterization that is used by the MCM illustrates the need for individual laboratory data to validate current atmospheric mechanisms. Similarly to pinonaldehyde, the MCM might also underestimate photolysis frequencies for other bi-carbonyl compounds.

Sensitivity runs were performed in the pinonaldehyde experiment to investigate the nature of the missing HO_2 source. A photolytic HO_2 source could close the model–measurement discrepancies in the experiment with pinonaldehyde. However a very fast photolysis frequency would be necessary. Performed sensitivity tests indicate that the HO_2 source is more likely connected to subsequent chemistry of oxidation products instead of chemistry that is connected to pinonaldehyde RO_2 radicals.

The comparison of the results from our chamber studies with BEACHON-ROCS and HUMPPA-COPEC field campaigns showed similarities for BVOC oxidation in coniferous forests. OH and HO_2 concentrations in MBO and monoterpene dominated environments were underestimated by model calculations. Results from this work help to explain why current chemical models calculations fail to reproduce observations of radical concentrations in field campaigns. Results are consistent with the hypothesis that additional HO_2 is photolytically produced as suggested by Kim et al. (2013).

In addition to the simulation chamber experiments, kinetic experiments were conducted to analyze the OH regeneration potential of the reaction of $CH_3C(O)O_2$ with HO_2. For that reason, the $CH_3C(O)O_2$ spectrum in the near-IR was measured and absorption cross sections determined.

It has been recently found that the reaction of $CH_3C(O)O_2$ + HO_2 can significantly regenerate OH in contrast to the expectation that radical recombination reactions terminate the radical chain. However, precise and accurate measurements of $CH_3C(O)O_2$ are required in order to investigate the kinetic parameters of this reaction. Measurements of the near-IR spectrum in this work will allow for more accurate detection of $CH_3C(O)O_2$ in future laboratory investigations of its reactions to better constrain the OH regeneration rate.

Unfortunately, the interpretation of further experiments investigating the $CH_3C(O)O_2 + HO_2$ reaction kinetics, in which the new absorption cross section was applied, was not conclusive because unexplained high CH_3O_2 concentrations

were predicted by current literature data compared to observations. Further experiments and quantum based theoretical calculations might help to improve the understanding of the involved chemistry. Especially kinetic experiments of the $CH_3C(O)O_2 + CH_3O_2$ reaction could add valuable information to identify the reasons for reduced CH_3O_2 formation compared to literature recommendations.

In summary, the investigation of the BVOC photooxidation in SAPHIR shows that there is a lack of understanding in the radical chemistry connected to the degradation of globally abundant compounds. The intercomparison of model results and observations shows large discrepancies for oxidation products and radical concentrations. This thesis improves the understanding of field campaigns in monoterpene dominated environments and helps to determine reaction mechanisms of BVOC species that have been found to have high emission rates in forest areas. In addition, it provides valuable information for future experiments that investigate radical regeneration in similar environments.

Further progress in determining the details of the reaction mechanism could be achieved, if the number of different oxygenated organic compounds and reaction intermediates that are produced in the different reaction pathways were quantified. Measured products acetone and formaldehyde are formed in many reaction branches, and it is therefore difficult to determine unambiguous reaction pathways from their measurement alone. A reliable identification and quantification of oxidation products, nitrate species, and speciated RO_2 with chemical ionization mass spectrometers (CIMS) and PTR-TOF-MS would help to constrain reaction mechanisms in future experiments.

References

The following list includes all references used within the main part of this PhD thesis. For references within each journal article and the corresponding supplementary material, please refer to their respective reference list.

Alicke, B., Geyer, A., Hofzumahaus, A., Holland, F., Konrad, S., Pätz, H. W., Schäfer, J., Stutz, J., Volz-Thomas, A., and Platt, U.: OH formation by HONO photolysis during the BERLIOZ experiment, J. Geophys. Res. Atmos., 108, PHO 3–1–PHO 3–17, doi:10.1029/2001JD000579, 2003.

Archibald, A. T., Petit, A. S., Percival, C. J., Harvey, J. N., and Shallcross, D. E.: On the importance of the reaction between OH and RO_2 radicals, Atmos. Sci. Lett., 10, 102–108, doi:10.1002/asl.216, 2009.

Arey, J., Atkinson, R., and Aschmann, S. M.: Product Study of the Gas-Phase Reactions of Monoterpenes With the OH Radical in the Presence of NO_x, J. Geophys. Res. Atmos., 95, 18 539–18 546, doi:10.1029/JD095iD11p18539, 1990.

Arey, J., Aschmann, S. M., Kwok, E. S. C., and Atkinson, R.: Alkyl nitrate, hydroxyalkyl nitrate, and hydroxycarbonyl formation from the NO_x-air photooxidations of C_5-C_8 n-alkanes, J. Phys. Chem. A, 105, 1020–1027, doi:10.1021/jp003292z, 2001.

Aschmann, S. M., Atkinson, R., and Arey, J.: Products of reaction of OH radicals with α-pinene, J. Geophys. Res. Atmos., 107, ACH 6–1–ACH 6–7, doi:10.1029/2001jd001098, 2002.

Assaf, E. and Fittschen, C.: Cross Section of OH Radical Overtone Transition near 7028 cm^{-1} and Measurement of the Rate Constant of the Reaction of OH with HO_2 Radicals, J. Phys. Chem. A, 120, 7051–7059, doi:10.1021/acs.jpca.6b06477, 2016.

Assaf, E., Song, B., Tomas, A., Schoemaecker, C., and Fittschen, C.: Rate Constant of the Reaction between CH_3O_2 Radicals and OH Radicals Revisited, J. Phys. Chem. A, 120, 8923–8932, doi:10.1021/acs.jpca.6b07704, 2016.

Assaf, E., Tanaka, S., Kajii, Y., Schoemaecker, C., and Fittschen, C.: Rate constants of the reaction of C_2-C_4 peroxy radicals with OH radicals, Chem. Phys. Lett., 684, 245–249, doi:10.1016/j.cplett.2017.06.062, 2017.

Assaf, E., Schoemaecker, C., Vereecken, L., and Fittschen, C.: Experimental and theoretical investigation of the reaction of RO_2 radicals with OH radicals: Dependence of the HO_2 yield on the size of the alkyl group, Int. J. Chem. Kinet., 50, 670–680, 2018.

Atkinson, R.: Gas-Phase Tropospheric Chemistry of Volatile Organic Compounds: 1. Alkanes and Alkenes, J. Phys. Chem. Ref. Data, 26, 215–290, doi:10.1063/1.556012, 1997.

Atkinson, R. and Arey, J.: Gas-phase tropospheric chemistry of biogenic volatile organic compounds: a review, Atmos. Environ., 37, 197–219, doi:10.1016/S1352-2310(03)00391-1, 2003.

Atkinson, R., Baulch, D. L., Cox, R. A., Crowley, J. N., Hampson, R. F., Hynes, R. G., Jenkin, M. E., Rossi, M. J., Troe, J., and Subcommittee, I.: Evaluated kinetic and photochemical data for atmospheric chemistry: Volume II - gas phase reactions of organic species, Atmos. Chem. Phys., 6, 3625–4055, doi:10.5194/acp-6-3625-2006, 2006.

Bianchi, F., Kurtén, T., Riva, M., Mohr, C., Rissanen, M. P., Roldin, P., Berndt, T., Crounse, J. D., Wennberg, P. O., Mentel, T. F., Wildt, J., Junninen, H., Jokinen, T., Kulmala, M., Worsnop, D. R., Thornton, J. A., Donahue, N., Kjaergaard, H. G., and Ehn, M.: Highly Oxygenated Organic Molecules (HOM) from Gas-Phase Autoxidation Involving Peroxy Radicals: A Key Contributor to Atmospheric Aerosol, Chem. Rev., 119, 3472–3509, doi:10.1021/acs.chemrev.8b00395, 2019.

Bohn, B. and Zilken, H.: Model-aided radiometric determination of photolysis frequencies in a sunlit atmosphere simulation chamber, Atmos. Chem. Phys., 5, 191–206, doi:10.5194/acp-5-191-2005, 2005.

Bohn, B., Rohrer, F., Brauers, T., and Wahner, A.: Actinometric measurements of NO_2 photolysis frequencies in the atmosphere simulation chamber SAPHIR, Atmos. Chem. Phys., 5, 493–503, doi:10.5194/acp-5-493-2005, 2005.

Borck, R. and Schrauth, P.: Population density and urban air quality, Report, Center for Economic Policy Analysis, doi:0.25932/publishup-42771, 2019.

Bossolasco, A., Faragó, E. P., Schoemaecker, C., and Fittschen, C.: Rate constant of the reaction between CH_3O_2 and OH radicals, Chem. Phys. Lett., 593, 7–13, doi:10.1016/j.cplett.2013.12.052, 2014.

Boyd, A. A., Flaud, P.-M., Daugey, N., and Lesclaux, R.: Rate Constants for RO_2 + HO_2 Reactions Measured under a Large Excess of HO_2, J. Phys. Chem. A, 107, 818–821, doi:10.1021/jp026581r, 2003.

Brauers, T. and Rohrer, F.: Easy AtmoSpheric chemistrY (Ver.2), Report, Forschungszentrum Jülich, 1999.

Browne, E. C., Min, K. E., Wooldridge, P. J., Apel, E., Blake, D. R., Brune, W. H., Cantrell, C. A., Cubison, M. J., Diskin, G. S., Jimenez, J. L., Weinheimer, A. J., Wennberg, P. O., Wisthaler, A., and Cohen, R. C.: Observations of total $RONO_2$ over the boreal forest: NO_x sinks and HNO_5 sources, Atmos. Chem. Phys., 13, 4543–4562, doi:10.5194/acp-13-4543-2013, 2013.

Burke, M., Driscoll, A., Heft-Neal, S., Xue, J., Burney, J., and Wara, M.: The changing risk and burden of wildfire in the United States, Proc. Natl. Acad. Sci. U.S.A, 118, e2011048 118, doi:10.1073/pnas.2011048118, 2021.

Calogirou, A., Larsen, B. R., and Kotzias, D.: Gas-phase terpene oxidation products: a review, Atmos. Environ., 33, 1423–1439, doi:10.1016/S1352-2310(98)00277-5, 1999.

Cox, R. A. and Cole, J. A.: Chemical aspects of the autoignition of hydrocarbon–air mixtures, Combust. Flame, 60, 109–123, doi:10.1016/0010-2180(85)90001-X, 1985.

Crounse, J. D., Paulot, F., Kjaergaard, H. G., and Wennberg, P. O.: Peroxy radical isomerization in the oxidation of isoprene, Phys. Chem. Chem. Phys., 13, 13 607–13 613, doi:10.1039/C1CP21330J, 2011.

Crounse, J. D., Knap, H. C., Ørnsø, K. B., Jørgensen, S., Paulot, F., Kjaergaard, H. G., and Wennberg, P. O.: Atmospheric Fate of Methacrolein. 1. Peroxy Radical Isomerization Following Addition of OH and O_2, J. Phys. Chem. A, 116, 5756–5762, doi:10.1021/jp211560u, 2012.

Crounse, J. D., Nielsen, L. B., Jørgensen, S., Kjaergaard, H. G., and Wennberg, P. O.: Autoxidation of Organic Compounds in the Atmosphere, J. Phys. Chem. Lett., 4, 3513–3520, doi:10.1021/jz4019207, 2013.

Crutzen, P. J.: Geology of mankind, Nature, 415, 23–23, doi:10.1038/415023a, 2002.

Czader, B. H., Rappenglück, B., Percell, P., Byun, D. W., Ngan, F., and Kim, S.: Modeling nitrous acid and its impact on ozone and hydroxyl radical during the Texas Air Quality Study 2006, Atmos. Chem. Phys., 12, 6939–6951, doi:10.5194/acp-12-6939-2012, 2012.

da Silva, G.: Hydroxyl radical regeneration in the photochemical oxidation of glyoxal: kinetics and mechanism of the HC(O)CO + O_2 reaction, Phys. Chem. Chem. Phys., 12, 6698–6705, doi:10.1039/B927176G, 2010.

da Silva, G., Graham, C., and Wang, Z.-F.: Unimolecular β-Hydroxyperoxy Radical Decomposition with OH Recycling in the Photochemical Oxidation of Isoprene, Environ. Sci. Technol., 44, 250–256, doi:10.1021/es900924d, 2010.

Daumont, D., Brion, J., Charbonnier, J., and Malicet, J.: Ozone UV spectroscopy I: Absorption cross-sections at room temperature, J. Atmos. Chem., 15, 145–155, doi:10.1007/bf00053756, 1992.

Dillon, T. J. and Crowley, J. N.: Direct detection of OH formation in the reactions of HO_2 with $CH_3C(O)O_2$ and other substituted peroxy radicals, Atmos. Chem. Phys., 8, 4877–4889, doi:10.5194/acp-8-4877-2008, 2008.

Dorn, H.-P., Brandenburger, U., Brauers, T., and Hausmann, M.: A New In Situ Laser Long-Path Absorption Instrument for the Measurement of Tropospheric OH Radicals, J. Atmos. Sci., 52, 3373–3380, doi:10.1175/1520-0469(1995)052<3373:Anisll>2.0.Co;2, 1995.

Eddingsaas, N. C., Loza, C. L., Yee, L. D., Seinfeld, J. H., and Wennberg, P. O.: α-pinene photooxidation under controlled chemical conditions - Part 1: Gas-phase composition in low- and high-NO_x environments, Atmos. Chem. Phys., 12, 6489–6504, doi:10.5194/acp-12-6489-2012, 2012.

Ehhalt, D. H.: Photooxidation of trace gases in the troposphere Plenary Lecture, Phys. Chem. Chem. Phys., 1, 5401–5408, doi:10.1039/a905097c, 1999.

Ehn, M., Thornton, J. A., Kleist, E., Sipilä, M., Junninen, H., Pullinen, I., Springer, M., Rubach, F., Tillmann, R., Lee, B., Lopez-Hilfiker, F., Andres, S., Acir, I.-H., Rissanen, M., Jokinen, T., Schobesberger, S., Kangasluoma, J., Kontkanen, J., Nieminen, T., Kurtén, T., Nielsen, L. B., Jørgensen, S., Kjaergaard, H. G., Canagaratna, M., Maso, M. D., Berndt, T., Petäjä, T., Wahner, A., Kerminen, V.-M., Kulmala, M., Worsnop, D. R., Wildt, J., and Mentel, T. F.: A large source of low-volatility secondary organic aerosol, Nature, 506, 476–479, doi:10.1038/nature13032, 2014.

Eurochamp: Database of Atmospheric Simulation Chamber Studies, URL https://data.eurochamp.org/.

Fantechi, G., Vereecken, L., and Peeters, J.: The OH-initiated atmospheric oxidation of pinonaldehyde: Detailed theoretical study and mechanism construction, Phys. Chem. Chem. Phys., 4, 5795–5805, doi:10.1039/b205901k, 2002.

Faragó, E. P., Viskolcz, B., Schoemaecker, C., and Fittschen, C.: Absorption Spectrum and Absolute Absorption Cross Sections of CH_3O_2 Radicals and CH_3I Molecules in the Wavelength Range 7473-7497 cm^{-1}, J. Phys. Chem. A, 117, 12 802–12 811, doi:10.1021/jp408686s, 2013.

Faragó, E. P., Schoemaecker, C., Viskolcz, B., and Fittschen, C.: Experimental determination of the rate constant of the reaction between $C_2H_5O_2$ and OH radicals, Chem. Phys. Lett., 619, 196–200, doi:10.1016/j.cplett.2014.11.069, 2015.

Finlayson-Pitts, B. J. and Pitts, Jr., J. N.: Chemistry of the Upper and Lower Atmosphere, Academic Press, San Diego, doi:10.1016/B978-012257060-5/50007-1, 2000.

Fischer, E. V., Jacob, D. J., Yantosca, R. M., Sulprizio, M. P., Millet, D. B., Mao, J., Paulot, F., Singh, H. B., Roiger, A., Ries, L., Talbot, R. W., Dzepina, K., and Pandey Deolal, S.: Atmospheric peroxyacetyl nitrate (PAN): a global budget and source attribution, Atmos. Chem. Phys., 14, 2679–2698, doi:10.5194/acp-14-2679-2014, 2014.

Fisher, J. A., Jacob, D. J., Travis, K. R., Kim, P. S., Marais, E. A., Chan Miller, C., Yu, K., Zhu, L., Yantosca, R. M., Sulprizio, M. P., Mao, J., Wennberg, P. O., Crounse, J. D., Teng, A. P., Nguyen, T. B., St. Clair, J. M., Cohen, R. C., Romer, P., Nault, B. A., Wooldridge, P. J., Jimenez, J. L., Campuzano-Jost, P., Day, D. A., Hu, W., Shepson, P. B., Xiong, F., Blake, D. R., Goldstein, A. H., Misztal, P. K., Hanisco, T. F., Wolfe, G. M., Ryerson, T. B., Wisthaler, A., and Mikoviny, T.: Organic nitrate chemistry and its implications for nitrogen budgets in an isoprene- and monoterpene-rich atmosphere: constraints from aircraft (SEAC4RS) and ground-based (SOAS) observations in the Southeast US, Atmos. Chem. Phys., 16, 5969–5991, doi:10.5194/acp-16-5969-2016, 2016.

Fittschen, C.: The reaction of peroxy radicals with OH radicals, Chem. Phys. Lett., 725, 102–108, doi:10.1016/j.cplett.2019.04.002, 2019.

Fuchs, H., Bohn, B., Hofzumahaus, A., Holland, F., Lu, K. D., Nehr, S., Rohrer, F., and Wahner, A.: Detection of HO_2 by laser-induced fluorescence: calibration and interferences from RO_2 radicals, Atmos. Meas. Tech., 4, 1209–1225, doi:10.5194/amt-4-1209-2011, 2011.

Fuchs, H., Dorn, H. P., Bachner, M., Bohn, B., Brauers, T., Gomm, S., Hofzumahaus, A., Holland, F., Nehr, S., Rohrer, F., Tillmann, R., and Wahner, A.: Comparison of OH concentration measurements by DOAS and LIF during SAPHIR chamber experiments at high OH reactivity and low NO concentration, Atmos. Meas. Tech., 5, 1611–1626, doi:10.5194/amt-5-1611-2012, 2012.

Fuchs, H., Hofzumahaus, A., Rohrer, F., Bohn, B., Brauers, T., Dorn, H. P., Haseler, R., Holland, F., Kaminski, M., Li, X., Lu, K., Nehr, S., Tillmann, R., Wegener, R., and Wahner, A.: Experimental evidence for efficient hydroxyl radical regeneration in isoprene oxidation, Nat. Geosci., 6, 1023–1026, doi:10.1038/NGEO1964, 2013.

Fuchs, H., Acir, I. H., Bohn, B., Brauers, T., Dorn, H. P., Haseler, R., Hofzumahaus, A., Holland, F., Kaminski, M., Li, X., Lu, K., Lutz, A., Nehr, S., Rohrer, F., Tillmann, R., Wegener, R., and Wahner, A.: OH regeneration from methacrolein oxidation investigated in the atmosphere simulation chamber SAPHIR, Atmos. Chem. Phys., 14, 7895–7908, doi:10.5194/acp-14-7895-2014, 2014.

Fuchs, H., Tan, Z., Hofzumahaus, A., Broch, S., Dorn, H. P., Holland, F., Künstler, C., Gomm, S., Rohrer, F., Schrade, S., Tillmann, R., and Wahner, A.: Investigation of potential interferences in the detection of atmospheric RO_x radicals by laser-induced fluorescence under dark conditions, Atmos. Meas. Tech., 9, 1431–1447, doi:10.5194/amt-9-1431-2016, 2016.

Fuchs, H., Novelli, A., Rolletter, M., Hofzumahaus, A., Pfannerstill, E. Y., Kessel, S., Edtbauer, A., Williams, J., Michoud, V., Dusanter, S., Locoge, N., Zannoni, N., Gros, V., Truong, F., Sarda-Esteve, R., Cryer, D. R., Brumby, C. A., Whalley, L. K., Stone, D., Seakins, P. W., Heard, D. E., Schoemaecker, C., Blocquet, M., Coudert, S., Batut, S., Fittschen, C., Thames, A. B., Brune, W. H., Ernest, C., Harder, H., Muller, J. B. A., Elste, T., Kubistin, D., Andres, S., Bohn, B., Hohaus, T., Holland, F., Li, X., Rohrer, F., Kiendler-Scharr, A., Tillmann, R., Wegener, R., Yu, Z., Zou, Q., and Wahner, A.: Comparison of OH reactivity measurements in the atmospheric simulation chamber SAPHIR, Atmos. Meas. Tech., 10, 4023–4053, doi:10.5194/amt-10-4023-2017, 2017.

Galloway, M. M., Huisman, A. J., Yee, L. D., Chan, A. W. H., Loza, C. L., Seinfeld, J. H., and Keutsch, F. N.: Yields of oxidized volatile organic compounds during the OH radical initiated oxidation of isoprene, methyl vinyl ketone, and methacrolein under high-NO_x conditions, Atmos. Chem. Phys., 11, 10 779–10 790, doi:10.5194/acp-11-10779-2011, 2011.

Gautrois, M. and Koppmann, R.: Diffusion technique for the production of gas standards for atmospheric measurements, J. Chromatogr. A, 848, 239–249, doi:10.1016/S0021-9673(99)00424-0, 1999.

Glasius, M. and Goldstein, A. H.: Recent Discoveries and Future Challenges in Atmospheric Organic Chemistry, Environ. Sci. Technol., 50, 2754–2764, doi:10.1021/acs.est.5b05105, 2016.

Glowania, M., Rohrer, F., Dorn, H. P., Hofzumahaus, A., Holland, F., Kiendler-Scharr, A., Wahner, A., and Fuchs, H.: Comparison of formaldehyde measurements by Hantzsch, CRDS and DOAS in the SAPHIR chamber, Atmos. Meas. Tech. Discuss., 2021, 1–23, doi:10.5194/amt-2021-10, 2021.

Groß, C. B. M., Dillon, T. J., Schuster, G., Lelieveld, J., and Crowley, J. N.: Direct Kinetic Study of OH and O3 Formation in the Reaction of CH3C(O)O2 with HO2, J. Phys. Chem. A, 118, 974–985, doi:10.1021/jp412380z, 2014.

Guenther, A. B., Jiang, X., Heald, C. L., Sakulyanontvittaya, T., Duhl, T., Emmons, L. K., and Wang, X.: The Model of Emissions of Gases and Aerosols from Nature version 2.1 (MEGAN2. 1): an extended and updated framework for modeling biogenic emissions, Geosci. Model Dev., 5, 1471–1492, doi:10.5194/gmd-5-1471-2012, 2012.

Hakola, H., Arey, J., Aschmann, S. M., and Atkinson, R.: Product formation from the gas-phase reactions of OH radicals and O_3 with a series of monoterpenes, J. Atmos. Chem., 18, 75–102, doi:10.1007/bf00694375, 1994.

Hallquist, M., Wängberg, I., and Ljungström, E.: Atmospheric Fate of Carbonyl Oxidation Products Originating from α-Pinene and Δ^3-Carene: Determination of Rate of Reaction with OH and NO_3 Radicals, UV Absorption Cross Sections, and Vapor Pressures, Environ. Sci. Technol., 31, 3166–3172, doi:10.1021/es970151a, 1997.

Hantson, S., Knorr, W., Schurgers, G., Pugh, T. A. M., and Arneth, A.: Global isoprene and monoterpene emissions under changing climate, vegetation, CO_2 and land use, Atmos. Environ., 155, 35–45, doi:10.1016/j.atmosenv.2017.02.010, 2017.

Hard, T. M., O'Brien, R. J., Chan, C. Y., and Mehrabzadeh, A. A.: Tropospheric Free Radical Determination by Fluorescence Assay with Gas Expansion, Environ. Sci. Technol., 18, 768–777, 1984.

Hasson, A. S., Tyndall, G. S., and Orlando, J. J.: A Product Yield Study of the Reaction of HO_2 Radicals with Ethyl Peroxy ($C_2H_5O_2$), Acetyl Peroxy ($CH_3C(O)O_2$), and Acetonyl Peroxy ($CH_3C(O)CH_2O_2$) Radicals, J. Phys. Chem. A, 108, 5979–5989, doi:10.1021/jp048873t, 2004.

Hasson, A. S., Kuwata, K. T., Arroyo, M. C., and Petersen, E. B.: Theoretical studies of the reaction of hydroperoxy radicals (HO_2) with ethyl peroxy ($CH_3CH_2O_2$), acetyl peroxy ($CH_3C(O)O_2$), and acetonyl peroxy ($CH_3C(O)CH_2O_2$) radicals, J. Photochem. Photobiol. A, 176, 218–230, doi:10.1016/j.jphotochem.2005.08.012, 2005.

Hasson, A. S., Tyndall, G. S., Orlando, J. J., Singh, S., Hernandez, S. Q., Campbell, S., and Ibarra, Y.: Branching Ratios for the Reaction of Selected Carbonyl-Containing Peroxy Radicals with Hydroperoxy Radicals, J. Phys. Chem. A, 116, 6264–6281, doi:10.1021/jp211799c, 2012.

Hatakeyama, S., Izumi, K., Fukuyama, T., Akimoto, H., and Washida, N.: Reactions of OH With Alpha-pinene and Beta-pinene in Air - Estimate of Global CO Production From the Atmospheric Oxidation of Terpenes, J. Geophys. Res. Atmos., 96, 947–958, doi:10.1029/90jd02341, 1991.

Hausmann, M., Brandenburger, U., Brauers, T., and Dorn, H.-P.: Detection of tropospheric OH radicals by long-path differential-optical-absorption spectroscopy: Experimental setup, accuracy, and precision, J. Geophys. Res. Atmos., 102, 16 011–16 022, doi:10.1029/97jd00931, 1997.

Hens, K., Novelli, A., Martinez, M., Auld, J., Axinte, R., Bohn, B., Fischer, H., Keronen, P., Kubistin, D., Nölscher, A. C., Oswald, R., Paasonen, P., Petäjä, T., Regelin, E., Sander, R., Sinha, V., Sipilä, M., Taraborrelli, D., Tatum Ernest, C., Williams, J., Lelieveld, J., and Harder, H.: Observation and modelling of HO_x radicals in a boreal forest, Atmos. Chem. Phys., 14, 8723–8747, doi:10.5194/acp-14-8723-2014, 2014.

Hofzumahaus, A., Rohrer, F., Lu, K., Bohn, B., Brauers, T., Chang, C.-C., Fuchs, H., Holland, F., Kita, K., Kondo, Y., Li, X., Lou, S., Shao, M., Zeng, L., Wahner, A., and Zhang, Y.: Amplified Trace Gas Removal in the Troposphere, Science, 324, 1702–1704, doi:10.1126/science.1164566, 2009.

Holland, F., Hessling, M., and Hofzumahaus, A.: In Situ Measurement of Tropospheric OH Radicals by Laser-Induced Fluorescence—A Description of the KFA Instrument, J. Atmos. Sci., 52, 3393–3401, doi:10.1175/1520-0469(1995)052<3393:ismoto>2.0.co;2, 1995.

Horie, O. and Moortgat, G. K.: Reactions of $CH_3C(O)O_2$ radicals with CH_3O_2 and HO_2 between 263 and 333 K. A product study, J. Chem. Soc.-Faraday Trans., 88, 3305–3312, doi:10.1039/ft9928803305, 1992.

Hui, A. O., Fradet, M., Okumura, M., and Sander, S. P.: Temperature Dependence Study of the Kinetics and Product Yields of the HO_2 + $CH_3C(O)O_2$ Reaction by Direct Detection of OH and HO_2 Radicals Using 2f-IR Wavelength Modulation Spectroscopy, J. Phys. Chem. A, 123, 3655–3671, doi:10.1021/acs.jpca.9b00442, 2019.

IPCC: Global warming of 1.5°C. An IPCC Special Report on the impacts of global warming of 1.5°C above pre-industrial levels and related global greenhouse gas emission pathways, in the context of strengthening the global response to the threat of climate change, sustainable development, and efforts to eradicate poverty, Masson-Delmotte, V., P. Zhai, H.-O. Pörtner, D. Roberts, J. Skea, P.R. Shukla, A. Pirani, W. Moufouma-Okia, C. Péan, R. Pidcock, S. Connors, J.B.R. Matthews, Y. Chen, X. Zhou, M.I. Gomis, E. Lonnoy, T. Maycock, M. Tignor, and T. Waterfield (eds.), Report, 2018.

Iyer, S., Reiman, H., Møller, K. H., Rissanen, M. P., Kjaergaard, H. G., and Kurtén, T.: Computational Investigation of RO_2 + HO_2 and RO_2 + RO_2 Reactions of Monoterpene Derived First-Generation Peroxy Radicals Leading to Radical Recycling, J. Phys. Chem. A, 122, 9542–9552, doi:10.1021/acs.jpca.8b09241, 2018.

Jain, C., Morajkar, P., Schoemaecker, C., Viskolcz, B., and Fittschen, C.: Measurement of Absolute Absorption Cross Sections for Nitrous Acid (HONO) in the Near-Infrared Region by the Continuous Wave Cavity Ring-Down Spectroscopy (cw-CRDS) Technique Coupled to Laser Photolysis, J. Phys. Chem. A, 115, 10 720–10 728, doi:10.1021/jp203001y, 2011.

Jaoui, M. and Kamens, R. M.: Mass balance of gaseous and particulate products analysis from α-pinene/NO_x/air in the presence of natural sunlight, J. Geophys. Res. Atmos., 106, 12 541–12 558, doi:10.1029/2001JD900005, 2001.

Jaoui, M. and Kamens, R. M.: Gas phase photolysis of pinonaldehyde in the presence of sunlight, Atmos. Environ., 37, 1835–1851, doi:10.1016/s1352-2310(03)00033-5, 2003.

Jenkin, M. E., Saunders, S. M., and Pilling, M. J.: The tropospheric degradation of volatile organic compounds: a protocol for mechanism development, Atmos. Environ., 31, 81–104, doi:10.1016/S1352-2310(96)00105-7, 1997.

Jenkin, M. E., Hurley, M. D., and Wallington, T. J.: Investigation of the radical product channel of the $CH_3C(O)O_2 + HO_2$ reaction in the gas phase, Phys. Chem. Chem. Phys., 9, 3149–3162, doi:10.1039/B702757E, 2007.

Jorand, F., Heiss, A., Sahetchian, K., Kerhoas, L., and Einhorn, J.: Identification of an unexpected peroxide formed by successive isomerization reactions of the n-butoxy radical in oxygen, J. Chem. Soc. Faraday Trans., 92, 4167–4171, doi:10.1039/FT9969204167, 1996.

Jordan, A., Haidacher, S., Hanel, G., Hartungen, E., Märk, L., Seehauser, H., Schottkowsky, R., Sulzer, P., and Märk, T. D.: A high resolution and high sensitivity proton-transfer-reaction time-of-flight mass spectrometer (PTR-TOF-MS), Int. J. Mass Spectrom., 286, 122–128, doi:10.1016/j.ijms.2009.07.005, 2009.

Kalafut-Pettibone, A. J., Klems, J. P., Burgess, D. R., and McGivern, W. S.: Alkylperoxy Radical Photochemistry in Organic Aerosol Formation Processes, J. Phys. Chem. A, 117, 14 141–14 150, doi:10.1021/jp4094996, 2013.

Kaminski, M.: Untersuchung des photochemischen Terpenoidabbaus in der Atmosphärensimulationskammer SAPHIR, PhD thesis, 2014.

Kaminski, M., Fuchs, H., Acir, I. H., Bohn, B., Brauers, T., Dorn, H. P., Haseler, R., Hofzumahaus, A., Li, X., Lutz, A., Nehr, S., Rohrer, F., Tillmann, R., Vereecken, L., Wegener, R., and Wahner, A.: Investigation of the β-pinene photooxidation by OH in the atmosphere simulation chamber SAPHIR, Atmos. Chem. Phys., 17, 6631–6650, doi:10.5194/acp-17-6631-2017, 2017.

Kim, S., Wolfe, G. M., Mauldin, L., Cantrell, C., Guenther, A., Karl, T., Turnipseed, A., Greenberg, J., Hall, S. R., Ullmann, K., Apel, E., Hornbrook, R., Kajii, Y., Nakashima, Y., Keutsch, F. N., DiGangi, J. P., Henry, S. B., Kaser, L., Schnitzhofer, R., Graus, M., Hansel, A., Zheng, W., and Flocke, F. F.: Evaluation of HO_x sources and cycling using measurement-constrained model calculations in a 2-methyl-3-butene-2-ol (MBO) and monoterpene (MT) dominated ecosystem, Atmos. Chem. Phys., 13, 2031–2044, doi:10.5194/acp-13-2031-2013, 2013.

Knap, H. C., Schmidt, J. A., and Jørgensen, S.: Hydrogen shift reactions in four methyl-buten-ol (MBO) peroxy radicals and their impact on the atmosphere, Atmos. Environ., 147, 79–87, doi:10.1016/j.atmosenv.2016.09.064, 2016.

Kwok, E. S. C. and Atkinson, R.: Estimation of hydroxyl radical reaction rate constants for gas-phase organic compounds using a structure-reactivity relationship: An update, Atmos. Environ., 29, 1685–1695, doi:10.1016/1352-2310(95)00069-B, 1995.

Larsen, B. R., Di Bella, D., Glasius, M., Winterhalter, R., Jensen, N. R., and Hjorth, J.: Gas-Phase OH Oxidation of Monoterpenes: Gaseous and Particulate Products, J. Atmos. Chem., 38, 231–276, doi:10.1023/a:1006487530903, 2001.

Le Crâne, J.-P., Rayez, M.-T., Rayez, J.-C., and Villenave, E.: A reinvestigation of the kinetics and the mechanism of the $CH_3C(O)O_2 + HO_2$ reaction using both experimental and theoretical approaches, Phys. Chem. Chem. Phys., 8, 2163–2171, doi:10.1039/B518321A, 2006.

Lee, A., Goldstein, A. H., Kroll, J. H., Ng, N. L., Varutbangkul, V., Flagan, R. C., and Seinfeld, J. H.: Gas-phase products and secondary aerosol yields from the photooxidation of 16 different terpenes, J. Geophys. Res. Atmos., 111, doi:10.1029/2006JD007050, 2006.

Lelieveld, J., Butler, T. M., Crowley, J. N., Dillon, T. J., Fischer, H., Ganzeveld, L., Harder, H., Lawrence, M. G., Martinez, M., Taraborrelli, D., and Williams, J.: Atmospheric oxidation capacity sustained by a tropical forest, Nature, 452, 737–740, doi:10.1038/nature06870, 2008.

Lelieveld, J., Pozzer, A., Pöschl, U., Fnais, M., Haines, A., and Münzel, T.: Loss of life expectancy from air pollution compared to other risk factors: a worldwide perspective, Cardiovasc. Res., 116, 1910–1917, doi:10.1093/cvr/cvaa025, 2020.

Lindinger, W., Hansel, A., and Jordan, A.: On-line monitoring of volatile organic compounds at pptv levels by means of proton-transfer-reaction mass spectrometry (PTR-MS) medical applications, food control and environmental research, Int. J. Mass Spectrom., 173, 191–241, doi:10.1016/S0168-1176(97)00281-4, 1998.

Lou, S., Holland, F., Rohrer, F., Lu, K., Bohn, B., Brauers, T., Chang, C. C., Fuchs, H., Häseler, R., Kita, K., Kondo, Y., Li, X., Shao, M., Zeng, L., Wahner, A., Zhang, Y., Wang, W., and Hofzumahaus, A.: Atmospheric OH reactivities in the Pearl River Delta – China in summer 2006: measurement and model results, Atmos. Chem. Phys., 10, 11 243–11 260, doi:10.5194/acp-10-11243-2010, 2010.

Mao, J., Ren, X., Zhang, L., Van Duin, D. M., Cohen, R. C., Park, J. H., Goldstein, A. H., Paulot, F., Beaver, M. R., Crounse, J. D., Wennberg, P. O., DiGangi, J. P., Henry, S. B., Keutsch, F. N., Park, C., Schade, G. W., Wolfe, G. M., Thornton, J. A., and Brune, W. H.: Insights into hydroxyl measurements and atmospheric oxidation in a California forest, Atmos. Chem. Phys., 12, 8009–8020, doi:10.5194/acp-12-8009-2012, 2012.

Maricq, M. M. and Szente, J. J.: The $CH_3C(O)O_2$ Radical. Its UV Spectrum, Self-Reaction Kinetics, and Reaction with CH_3O_2, The Journal of Physical Chemistry, 100, 4507–4513, doi:10.1021/jp9533234, 1996.

Matsumi, Y., Comes, F. J., Hancock, G., Hofzumahaus, A., Hynes, A. J., Kawasaki, M., and Ravishankara, A. R.: Quantum yields for production of $O(^1D)$ in the ultraviolet photolysis of ozone: Recommendation based on evaluation of laboratory data, J. Geophys. Res. Atmos., 107, ACH 1–1–ACH 1–12, doi:10.1029/2001jd000510, 2002.

MCM: Master Chemical Mechanism, v3.3.1, URL: http://mcm.leeds.ac.uk/MCM/, last access: 04 March 2020, 2017.

Mérienne, M. F., Jenouvrier, A., and Coquart, B.: The NO_2 absorption spectrum. I: Absorption cross-sections at ambient temperature in the 300-500 nm region, J. Atmos. Chem., 20, 281–297, doi:10.1007/bf00694498, 1995.

Moortgat, G. K. and Ravishankara, A. R.: Ozone Depletion and Related Topics | Photochemistry of Ozone, pp. 370–379, Academic Press, Oxford, doi:10.1016/B978-0-12-382225-3.00292-9, 2015.

Moortgat, G. K., Veyret, B., and Lesclaux, R.: Kinetics of the reaction of HO_2 with $CH_3C(O)O_2$ in the temperature range 253–368 K, Chem. Phys. Lett., 160, 443–447, doi:10.1016/0009-2614(89)87624-9, 1989.

Moortgat, G. K., Wirtz, K., Hjorth, J., Ljungstrom, E., Ruppert, L., Hayman, G., and Mellouki, W.: 'Evaluation of radical sources in atmospheric chemistry through chamber and laboratory studies', Final report on the EU project 'RADICAL', Report EUR 20254 EN., 2002.

Møller, K. H., Bates, K. H., and Kjaergaard, H. G.: The Importance of Peroxy Radical Hydrogen-Shift Reactions in Atmospheric Isoprene Oxidation, J. Phys. Chem. A, 123, 920–932, doi:10.1021/acs.jpca.8b10432, 2019.

Nehr, S., Bohn, B., Dorn, H. P., Fuchs, H., Haseler, R., Hofzumahaus, A., Li, X., Rohrer, F., Tillmann, R., and Wahner, A.: Atmospheric photochemistry of aromatic hydrocarbons: OH budgets during SAPHIR chamber experiments, Atmos. Chem. Phys., 14, 6941–6952, doi:10.5194/acp-14-6941-2014, 2014.

Niki, H., Maker, P. D., Savage, C. M., and Breitenbach, L. P.: FTIR study of the kinetics and mechanism for chlorine-atom-initiated reactions of acetaldehyde, J. Phys. Chem, 89, 588–591, doi:10.1021/j100250a008, 1985.

Novelli, A., Hens, K., Tatum Ernest, C., Kubistin, D., Regelin, E., Elste, T., Plass-Dülmer, C., Martinez, M., Lelieveld, J., and Harder, H.: Characterisation of an inlet pre-injector laser-induced fluorescence instrument for the measurement of atmospheric hydroxyl radicals, Atmos. Meas. Tech., 7, 3413–3430, doi:10.5194/amt-7-3413-2014, 2014.

Novelli, A., Kaminski, M., Rolletter, M., Acir, I. H., Bohn, B., Dorn, H. P., Li, X., Lutz, A., Nehr, S., Rohrer, F., Tillmann, R., Wegener, R., Holland, F., Hofzumahaus, A., Kiendler-Scharr, A., Wahner, A., and Fuchs, H.: Evaluation of OH and HO2 concentrations and their budgets during photooxidation of 2-methyl-3-butene-2-ol (MBO) in the atmospheric simulation chamber SAPHIR, Atmos. Chem. Phys., 18, 11 409–11 422, doi:10.5194/acp-18-11409-2018, 2018.

Novelli, A., Vereecken, L., Bohn, B., Dorn, H. P., Gkatzelis, G. I., Hofzumahaus, A., Holland, F., Reimer, D., Rohrer, F., Rosanka, S., Taraborrelli, D., Tillmann, R., Wegener, R., Yu, Z., Kiendler-Scharr, A., Wahner, A., and Fuchs, H.: Importance of isomerization reactions for OH radical regeneration from the photo-oxidation of isoprene investigated in the atmospheric simulation chamber SAPHIR, Atmos. Chem. Phys., 20, 3333–3355, doi:10.5194/acp-20-3333-2020, 2020.

Noziere, B., Barnes, I., and Becker, K. H.: Product study and mechanisms of the reactions of alpha-pinene and of pinonaldehyde with OH radicals, J. Geophys. Res. Atmos., 104, 23 645–23 656, doi:10.1029/1999jd900778, 1999.

Onel, L., Brennan, A., Gianella, M., Hooper, J., Ng, N., Hancock, G., Whalley, L., Seakins, P. W., Ritchie, G. A. D., and Heard, D. E.: An intercomparison of CH_3O_2 measurements by fluorescence assay by gas expansion and cavity ring-down spectroscopy within HIRAC (Highly Instrumented Reactor for Atmospheric Chemistry), Atmos. Meas. Tech., 13, 2441–2456, doi:10.5194/amt-13-2441-2020, 2020.

Ortega, J., Turnipseed, A., Guenther, A. B., Karl, T. G., Day, D. A., Gochis, D., Huffman, J. A., Prenni, A. J., Levin, E. J. T., Kreidenweis, S. M., DeMott, P. J., Tobo, Y., Patton, E. G., Hodzic, A., Cui, Y. Y., Harley, P. C., Hornbrook, R. S., Apel, E. C., Monson, R. K., Eller, A. S. D., Greenberg, J. P., Barth, M. C., Campuzano-Jost, P., Palm, B. B., Jimenez, J. L., Aiken, A. C., Dubey, M. K., Geron, C., Offenberg, J., Ryan, M. G., Fornwalt, P. J., Pryor, S. C., Keutsch, F. N., DiGangi, J. P., Chan, A. W. H., Goldstein, A. H., Wolfe, G. M., Kim, S., Kaser, L., Schnitzhofer, R., Hansel, A., Cantrell, C. A., Mauldin, R. L., and Smith, J. N.: Overview of the Manitou Experimental Forest Observatory: site description and selected science results from 2008 to 2013, Atmos. Chem. Phys., 14, 6345–6367, doi:10.5194/acp-14-6345-2014, 2014.

O'Keefe, A. and Deacon, D. A. G.: Cavity ring-down optical spectrometer for absorption measurements using pulsed laser sources, Rev. Sci. Instrum., 59, 2544–2551, doi:10.1063/1.1139895, 1988.

Parker, A. E., Jain, C., Schoemaecker, C., Szriftgiser, P., Votava, O., and Fittschen, C.: Simultaneous, time-resolved measurements of OH and HO_2 radicals by coupling of high repetition rate LIF and cw-CRDS techniques to a laser photolysis reactor and its application to the photolysis of H_2O_2, Appl. Phys. B., 103, 725–733, doi:10.1007/s00340-010-4225-1, 2011.

Peeters, J. and Nguyen, T. L.: Unusually Fast 1,6-H Shifts of Enolic Hydrogens in Peroxy Radicals: Formation of the First-Generation C2 and C3 Carbonyls in the Oxidation of Isoprene, J. Phys. Chem. A, 116, 6134–6141, doi:10.1021/jp211447q, 2012.

Peeters, J., Nguyen, T. L., and Vereecken, L.: HO_x radical regeneration in the oxidation of isoprene, Phys. Chem. Chem. Phys., 11, 5935–5939, doi:10.1039/B908511D, 2009.

Peeters, J., Müller, J.-F., Stavrakou, T., and Nguyen, V. S.: Hydroxyl Radical Recycling in Isoprene Oxidation Driven by Hydrogen Bonding and Hydrogen Tunneling: The Upgraded LIM1 Mechanism, J. Phys. Chem. A, 118, 8625–8643, doi:10.1021/jp5033146, 2014.

Platt, U. and Stutz, J.: Differential absorption spectroscopy, pp. 135–174, Physics of Earth and Space Environments, Springer, doi:10.1007/978-3-540-75776-4, 2008.

Poppe, D., Brauers, T., Dorn, H. P., Karl, M., Mentel, T., Schlosser, E., Tillmann, R., Wegener, R., and Wahner, A.: OH-initiated degradation of several hydrocarbons in the atmosphere simulation chamber SAPHIR, J. Atmos. Chem., 57, 203–214, doi:10.1007/s10874-007-9065-y, 2007.

Praske, E., Otkjær, R. V., Crounse, J. D., Hethcox, J. C., Stoltz, B. M., Kjaergaard, H. G., and Wennberg, P. O.: Atmospheric autoxidation is increasingly important in urban and suburban North America, Proc. Natl. Acad. Sci. U.S.A., 115, 64–69, doi:10.1073/pnas.1715540115, 2018.

Rindelaub, J. D., McAvey, K. M., and Shepson, P. B.: The photochemical production of organic nitrates from α-pinene and loss via acid-dependent particle phase hydrolysis, Atmos. Environ., 100, 193–201, doi:10.1016/j.atmosenv.2014.11.010, 2015.

Roehl, C. M., Bauer, D., and Moortgat, G. K.: Absorption spectrum and kinetics of the acetylperoxy radical, J. Phys. Chem., 100, 4038–4047, doi:10.1021/jp9526298, 1996.

Rohrer, F., Bohn, B., Brauers, T., Brüning, D., Johnen, F. J., Wahner, A., and Kleffmann, J.: Characterisation of the photolytic HONO-source in the atmosphere simulation chamber SAPHIR, Atmos. Chem. Phys., 5, 2189–2201, doi:10.5194/acp-5-2189-2005, 2005.

Rohrer, F., Lu, K., Hofzumahaus, A., Bohn, B., Brauers, T., Chang, C.-C., Fuchs, H., Häseler, R., Holland, F., Hu, M., Kita, K., Kondo, Y., Li, X., Lou, S., Oebel, A., Shao, M., Zeng, L., Zhu, T., Zhang, Y., and Wahner, A.: Maximum efficiency in the hydroxyl-radical-based self-cleansing of the troposphere, Nat. Geosci., 7, 559, doi:10.1038/ngeo2199, 2014.

Rolletter, M., Kaminski, M., Acir, I. H., Bohn, B., Dorn, H. P., Li, X., Lutz, A., Nehr, S., Rohrer, F., Tillmann, R., Wegener, R., Hofzumahaus, A., Kiendler-Scharr, A., Wahner, A., and Fuchs, H.: Investigation of the α-pinene photooxidation by OH in the atmospheric simulation chamber SAPHIR, Atmos. Chem. Phys., 19, 11 635–11 649, doi:10.5194/acp-19-11635-2019, 2019.

Rolletter, M., Assaf, E., Assali, M., Fuchs, H., and Fittschen, C.: The absorption spectrum and absolute absorption cross sections of acetylperoxy radicals, $CH_3C(O)O_2$ in the near IR, J. Quant. Spectrosc. Radiat. Transf., 245, 106 877, doi:10.1016/j.jqsrt.2020.106877, 2020a.

Rolletter, M., Blocquet, M., Kaminski, M., Bohn, B., Dorn, H. P., Hofzumahaus, A., Holland, F., Li, X., Rohrer, F., Tillmann, R., Wegener, R., Kiendler-Scharr, A., Wahner, A., and Fuchs, H.: Photooxidation of pinonaldehyde at ambient conditions investigated in the atmospheric simulation chamber SAPHIR, Atmos. Chem. Phys., 20, 13 701–13 719, doi:10.5194/acp-20-13701-2020, 2020b.

Romer Present, P. S., Zare, A., and Cohen, R. C.: The changing role of organic nitrates in the removal and transport of NOx, Atmos. Chem. Phys., 20, 267–279, doi:10.5194/acp-20-267-2020, 2020.

Rosenfeld, D., Sherwood, S., Wood, R., and Donner, L.: Climate Effects of Aerosol-Cloud Interactions, Science, 343, 379–380, doi:10.1126/science.1247490, 2014.

Saunders, S. M., Jenkin, M. E., Derwent, R. G., and Pilling, M. J.: Protocol for the development of the Master Chemical Mechanism, MCM v3 (Part A): tropospheric degradation of non-aromatic volatile organic compounds, Atmos. Chem. Phys., 3, 161–180, doi:10.5194/acp-3-161-2003, 2003.

Schlosser, E., Bohn, B., Brauers, T., Dorn, H.-P., Fuchs, H., Häseler, R., Hofzumahaus, A., Holland, F., Rohrer, F., Rupp, L. O., Siese, M., Tillmann, R., and Wahner, A.: Intercomparison of Two Hydroxyl Radical Measurement Techniques at the Atmosphere Simulation Chamber SAPHIR, J. Atmos. Chem., 56, 187–205, doi:10.1007/s10874-006-9049-3, 2007.

Schlosser, E., Brauers, T., Dorn, H. P., Fuchs, H., Häseler, R., Hofzumahaus, A., Holland, F., Wahner, A., Kanaya, Y., Kajii, Y., Miyamoto, K., Nishida, S., Watanabe, K., Yoshino, A., Kubistin, D., Martinez, M., Rudolf, M., Harder, H., Berresheim, H., Elste, T., Plass-Dülmer, C., Stange, G., and Schurath, U.: Technical Note: Formal blind intercomparison of OH measurements: results from the international campaign HOxComp, Atmos. Chem. Phys., 9, 7923–7948, doi:10.5194/acp-9-7923-2009, 2009.

Seinfeld, J. H. and Pandis, S. N.: Atmospheric Chemistry and Physics: From Air Pollution to Climate Change, John Wiley and Sons, Inc., Hoboken, New Jersey, 3rd edn., 2016.

Smit, L. A. M. and Heederik, D.: Impacts of Intensive Livestock Production on Human Health in Densely Populated Regions, GeoHealth, 1, 272–277, doi:10.1002/2017GH000103, 2017.

Steiner, A. H. and Goldstein, A. L.: Biogenic VOCs, pp. 82–128, Blackwell Publishing, doi:10.1002/9780470988657.ch3, 2007.

Stutz, J., Kim, E. S., Platt, U., Bruno, P., Perrino, C., and Febo, A.: UV-visible absorption cross sections of nitrous acid, J. Geophys. Res. Atmos., 105, 14 585–14 592, doi:10.1029/2000jd900003, 2000.

Taatjes, C. A., Shallcross, D. E., and Percival, C. J.: Research frontiers in the chemistry of Criegee intermediates and tropospheric ozonolysis, Phys. Chem. Chem. Phys., 16, 1704–1718, doi:10.1039/C3CP52842A, 2014.

Taraborrelli, D., Lawrence, M. G., Crowley, J. N., Dillon, T. J., Gromov, S., Groß, C. B. M., Vereecken, L., and Lelieveld, J.: Hydroxyl radical buffered by isoprene oxidation over tropical forests, Nat. Geosci., 5, 190–193, doi:10.1038/ngeo1405, 2012.

Thiebaud, J. and Fittschen, C.: Near infrared cw-CRDS coupled to laser photolysis: Spectroscopy and kinetics of the HO_2 radical, Appl. Phys. B., 85, 383–389, doi:10.1007/s00340-006-2304-0, 2006.

Tomas, A., Villenave, E., and Lesclaux, R.: Reactions of the HO_2 Radical with CH_3CHO and $CH_3C(O)O_2$ in the Gas Phase, J. Phys. Chem. A, 105, 3505–3514, doi:10.1021/jp003762p, 2001.

Troe, J.: Are Primary Quantum Yields of NO_2 Photolysis at $\lambda \leq 398$ nm Smaller than Unity?, Z. Phys. Chem, 214, 573–581, doi:10.1524/zpch.2000.214.5.573, 2000.

Vereecken, L. and Nozière, B.: H migration in peroxy radicals under atmospheric conditions, Atmos. Chem. Phys., 20, 7429–7458, doi:10.5194/acp-20-7429-2020, 2020.

Vereecken, L. and Peeters, J.: Decomposition of substituted alkoxy radicals—part I: a generalized structure–activity relationship for reaction barrier heights, Phys. Chem. Chem. Phys., 11, 9062–9074, doi:10.1039/B909712K, 2009.

Vereecken, L., Mueller, J. F., and Peeters, J.: Low-volatility poly-oxygenates in the OH-initiated atmospheric oxidation of α-pinene: impact of non-traditional peroxyl radical chemistry, Phys. Chem. Chem. Phys., 9, 5241–5248, doi:10.1039/b708023a, 2007.

Vereecken, L., Harder, H., and Novelli, A.: The reactions of Criegee intermediates with alkenes, ozone, and carbonyl oxides, Phys. Chem. Chem. Phys., 16, 4039–4049, doi:10.1039/C3CP54514H, 2014.

Votava, O., Mašát, M., Parker, A. E., Jain, C., and Fittschen, C.: Microcontroller based resonance tracking unit for time resolved continuous wave cavity-ringdown spectroscopy measurements, Rev. Sci. Instrum., 83, 043 110, doi:10.1063/1.3698061, 2012.

Wegener, R., Brauers, T., Koppmann, R., Rodríguez Bares, S., Rohrer, F., Tillmann, R., Wahner, A., Hansel, A., and Wisthaler, A.: Simulation chamber investigation of the reactions of ozone with short-chained alkenes, J. Geophys. Res. Atmos., 112, doi:10.1029/2006jd007531, 2007.

Whalley, L. K., Edwards, P. M., Furneaux, K. L., Goddard, A., Ingham, T., Evans, M. J., Stone, D., Hopkins, J. R., Jones, C. E., Karunaharan, A., Lee, J. D., Lewis, A. C., Monks, P. S., Moller, S. J., and Heard, D. E.: Quantifying the magnitude of a missing hydroxyl radical source in a tropical rainforest, Atmos. Chem. Phys., 11, 7223–7233, doi:10.5194/acp-11-7223-2011, 2011.

Winiberg, F. A. F., Dillon, T. J., Orr, S. C., Groß, C. B. M., Bejan, I., Brumby, C. A., Evans, M. J., Smith, S. C., Heard, D. E., and Seakins, P. W.: Direct measurements of OH and other product yields from the HO_2 + $CH_3C(O)O_2$ reaction, Atmos. Chem. Phys., 16, 4023–4042, doi:10.5194/acp-16-4023-2016, 2016.

Wisthaler, A., Jensen, N. R., Winterhalter, R., Lindinger, W., and Hjorth, J.: Measurements of acetone and other gas phase product yields from the OH-initiated oxidation of terpenes by proton-transfer-reaction mass spectrometry (PTR-MS), Atmos. Environ., 35, 6181–6191, doi:10.1016/s1352-2310(01)00385-5, 2001.

Wolfe, G. M., Cantrell, C., Kim, S., Mauldin Iii, R. L., Karl, T., Harley, P., Turnipseed, A., Zheng, W., Flocke, F., Apel, E. C., Hornbrook, R. S., Hall, S. R., Ullmann, K., Henry, S. B., DiGangi, J. P., Boyle, E. S., Kaser, L., Schnitzhofer, R., Hansel, A., Graus, M., Nakashima, Y., Kajii, Y., Guenther, A., and Keutsch, F. N.: Missing peroxy radical sources within a summertime ponderosa pine forest, Atmos. Chem. Phys., 14, 4715–4732, doi:10.5194/acp-14-4715-2014, 2014.

Xu, L., Møller, K. H., Crounse, J. D., Otkjær, R. V., Kjaergaard, H. G., and Wennberg, P. O.: Unimolecular Reactions of Peroxy Radicals Formed in the Oxidation of α-Pinene and β-Pinene by Hydroxyl Radicals, J. Phys. Chem. A, 123, 1661–1674, doi:10.1021/acs.jpca.8b11726, 2019.

Zhang, H., Yee, L. D., Lee, B. H., Curtis, M. P., Worton, D. R., Isaacman-VanWertz, G., Offenberg, J. H., Lewandowski, M., Kleindienst, T. E., Beaver, M. R., Holder, A. L., Lonneman, W. A., Docherty, K. S., Jaoui, M., Pye, H. O. T., Hu, W., Day, D. A., Campuzano-Jost, P., Jimenez, J. L., Guo, H., Weber, R. J., de Gouw, J., Koss, A. R., Edgerton, E. S., Brune, W., Mohr, C., Lopez-Hilfiker, F. D., Lutz, A., Kreisberg, N. M., Spielman, S. R., Hering, S. V., Wilson, K. R., Thornton, J. A., and Goldstein, A. H.: Monoterpenes are the largest source of summertime organic aerosol in the southeastern United States, Proc. Natl. Acad. Sci. U.S.A, 115, 2038–2043, doi:10.1073/pnas.1717513115, 2018.

Acronyms

AOM	Acousto-Optic Modulator
APD	Avalanche PhotoDiode
BEACHON-ROCS	Bio-hydro-atmosphere interactions of Energy, Aerosols, Carbon, H_2O, Organics and Nitrogen – RockyMountain Organic Carbon Study
BEARPEX09	Biosphere Effects on Aerosols and Photochemisty Experiment II
BVOC	Biogenic Volatile Organic Compound
CI	Criegee Intermediate
CIMS	Chemical Ionization Mass Spectrometer
CRDS	Cavity Ring-Down Spectroscopy
cw	Continuous-Wave
DFB	Distributed FeedBack
DOAS	Differential Optical Absorption Spectroscopy
FAGE	Fluorescence Assay by Gas Expansion
FEP	Fluoro-Ethylene-Propylen
FID	Flame Ionisation Detector
GC	Gas Chromatograph
GEOS	Goddard Earth Observing System
HO_x	Sum of OH and HO_2
HOM	Highly Oxygenated Organic Molecules
HUMPPA-COPEC	Hyytiälä United Photochemistry and Particles in Air – Comprehensive Organic Precursor Emission and Concentration study
IR	InfraRed
IUPAC	International Union of Pure and Applied Chemistry
k_{OH}	OH reactivity

LIF	Laser-Induced Fluorescence
LIM	Leuven Isoprene Mechanisms
LOPAP	Long-Path-Absorption-Photometer
LP–LIF	Laser Photolysis — Laser-Induced Fluorescence
MBO	2-methyl-3-butene-2-ol
MCM	Master Chemical Mechanism
MIM	Mainz Isoprene Mechanisms
MVK	Methyl-Vinyl-Ketone
NIR	Near-InfraRed
NMVOC	Non-Methane Volatile Organic Compound
NO_x	Sum of NO and NO_2
OVOC	Oxygenated Volatile Organic Compound
PAN	PeroxyAcetyl Nitrate
PINAL	Pinonaldehyde
PM	Particulate Matter
PMT	PhotoMultiplier Tube
ppbv	Parts Per Billion by Volume
pptv	Parts Per Trillion by Volume
PTR–MS	Proton Transfer Reaction Mass Spectrometer
PTR–TOF–MS	Proton Transfer Reaction – Time-Of-Flight Mass Spectrometer
SAPHIR	Simulation of Atmospheric PHotochemistry In a large Reaction chamber
SAR	Structure Activity Relationship
SOA	Secondary Organic Aerosol
SZA	Solar Zenith Angle
UV	UltraViolet
UWCM	University of Washington Chemical Model
VOC	Volatile Organic Compound

Acknowledgements

This work would not have been possible without the support of numberous people throughout my time in Jülich.

Firstly, I would like to thank Prof. Dr. Astrid Kiendler-Scharr and Prof. Dr. Andreas Wahner for giving me the opportunity to write my PhD thesis at the Institute of Energy and Climate Research: Troposphere (IEK-8) at the Forschungszentrum Jülich.

I would like to thank my Doktorvater PD Dr. Andreas Hofzumahaus for his guidance and support. He initially introduced me to the field of atmospheric science which is an enrichment for my life that I would not want to miss today.

I thank Prof. Dr. Axel Klein for acting as co-examiner of my thesis.

I wish to express my deepest gratitude to PD Dr. Hendrik Fuchs for his enduring support, patience, and motivation. He initially gave me the opportunity to start my PhD with the development of a new HO_2 CRDS instrument. He always had an idea when I got stuck and kept me on track.

I would like to thank Dr. Christa Fittschen and her group at the Université Lille 1 for sharing her knowledge of the cavity ring-down technique and for the numerous times they hosted me at their laboratory. I would especially like to thank Dr. Marion Blocquet for making me feel welcome in Lille and Dr. Emmanuel Assaf for the introduction to the CRDS instrument and the evaluation of CRDS data.

I would like to thank the whole LIF group. A special thank you to Dr. Anna Novelli for fruitful discussions and encouraging words. Mathias Bachner for his patience and the effort he put in the CRDS system. Dominik Raak and Kamil Kubik, who supported the setup and maintenance of the new CRDS instrument.

I would like to acknowledge the contribution of the whole SAPHIR team. Especially, I would like to thank Dr. Birger Bohn for his useful comments on the journal manuscripts. In addition, I would like to thank Dr. Luc Veerecken for his valuable input of theoretical chemistry that substantially improved my understanding of RO_2 chemistry.

I would like to pay my special regards to my office mates Dr. Tammarat Piansawan, David Reimer, and Avtandil Turdziladze who made the basement a nice place to work in. Furthermore, I would like to thank all my colleagues for our common time at the institute.

I deeply thank Caro, Gideon, Jannis, Malte, Natalie, and Sven for numerous entertaining train rides, discussions, and enlightening evenings.

I would like to thank Sandra Bollenbacher for proof-reading my thesis.

Finally, I wish to show my deepest gratitude to my parents, friends, and my girlfriend Franziska for their support and motivation, which made this work possible.

A Appendix

A.1 Supplementary materials to Chapter 3

Supplement of Atmos. Chem. Phys., 18, 11409–11422, 2018
https://doi.org/10.5194/acp-18-11409-2018-supplement

Atmospheric Chemistry and Physics Open Access EGU

Supplement of

Evaluation of OH and HO_2 concentrations and their budgets during photooxidation of 2-methyl-3-butene-2-ol (MBO) in the atmospheric simulation chamber SAPHIR

Anna Novelli et al.

Correspondence to: Anna Novelli (a.novelli@fz-juelich.de) and Hendrik Fuchs (h.fuchs@fz-juelich.de)

Zero-air phase model results

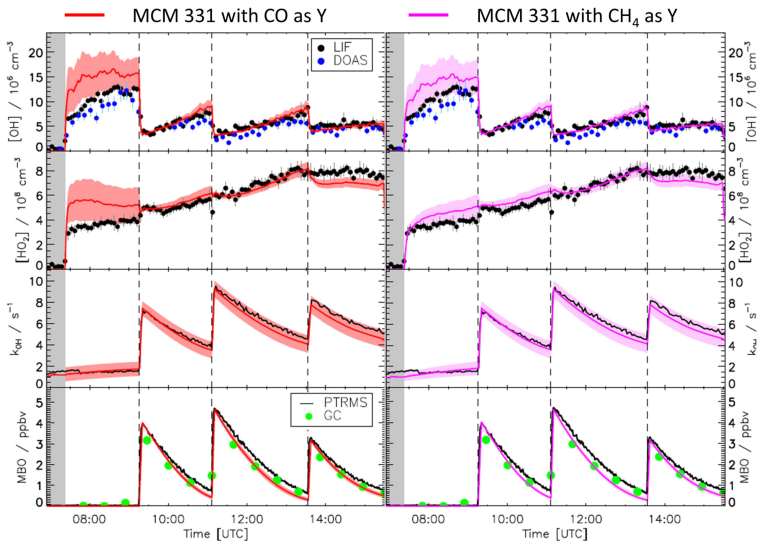

Figure S1: Measured time series of OH and HO_2 radical concentrations, OH reactivity and MBO concentrations compared to results obtained from modelling using the MCM version 3.3.1. On the left hand panels a hypothetical species Y that behaves like CO was introduced in the model to explain the background reactivity before addition of MBO. In the right hand panels Y is assumed to behave like CH_4 instead with a delayed secondary formation of HO_2 radicals. The red and pink shaded areas represent the uncertainty of the model caused by the uncertainties of the OH reactivity measurements (see text for details). Grey shaded areas indicate the times before opening the chamber roof and vertical dashed lines indicate the times when MBO was injected. Note that the model results after the injection of MBO do not differ significantly, i.e. the nature of the background reactivity in the chamber is secondary for the main part of the experiment. In Fig. 1 of the main manuscript the modelling results for the period before MBO injection were therefore omitted for clarity.

A.2 Supplementary materials to Chapter 4

Supplement of Atmos. Chem. Phys., 19, 11635–11649, 2019
https://doi.org/10.5194/acp-19-11635-2019-supplement

Atmospheric Chemistry and Physics Open Access EGU

Supplement of

Investigation of the α-pinene photooxidation by OH in the atmospheric simulation chamber SAPHIR

Michael Rolletter et al.

Correspondence to: Hendrik Fuchs (h.fuchs@fz-juelich.de)

S1 Calculation of product yields

To calculate the yield as described in Galloway et al. (2011) and Kaminski et al. (2017) it is necessary to correct measured concentrations for losses and additional sources. The correction term for the example of pinonaldehyde is shown in Eq. S1:

$$c_{\text{pinal corr}}[i] = c_{\text{pinal}}[i-1] + \Delta c_{\text{pinal}} + \Delta c_{\text{dil}} + \Delta c_{\text{rl}} + \Delta c_{\text{pl}} - \Delta c_{\text{O3}} \quad \text{(S1)}$$

To obtain the corrected pinonaldehyde concentration $c_{\text{pinal corr}}$ the measured concentration c_{pinal} has to be corrected for losses by photolysis Δc_{pl}, dilution Δc_{dil} and the reaction with OH radicals Δc_{rl}, as well as a source from the ozonolysis of α-pinene Δc_{O3}. The different terms are further explained in the equations S2 to S5:

$$\Delta c_{\text{dil}} = c_{\text{pinal}}[i-1] * \Delta t * k_{\text{dil}}[i-1] \quad \text{(S2)}$$

$$\Delta c_{\text{rl}} = c_{\text{pinal}}[i-1] * \Delta t * c_{\text{OH}}[i-1] * k_{\text{pinal + OH}} \quad \text{(S3)}$$

$$\Delta c_{\text{pl}} = c_{\text{pinal}}[i-1] * \Delta t * J_{\text{pinal}}[i-1] \quad \text{(S4)}$$

$$\Delta c_{\text{O3}} = c_{\text{pinal}}[i-1] * \Delta t * c_{\text{O3}}[i-1] * k_{\text{apinene + O3}} \quad \text{(S5)}$$

$c_{\text{pinal corr}}[i]$: corrected pinonaldehyde concentration at time *i*

$c_{\text{pinal}}[i-1]$: measured pinonaldehyde concentration at time *i*-1

Δc_{dil} : dilution

Δc_{rl} : loss due to the reaction with OH

Δc_{pl} : photolytic loss

Δc_{O3} : production from ozonolysis

$c_{\text{OH}}[i-1]$: measured OH concentration by DOAS at time *i*-1

$k_{\text{pinal + OH}}$: reaction rate of pinonaldehyde + OH (Atkinson et al., 2006)

$J_{\text{pinal}}[i-1]$: measured photolysis frequency at time *i*-1

$c_{\text{O3}}[i-1]$: O_3 concentration at time *i*-1

$k_{\text{apinene + O3}}$: reaction rate of α-pinene + O_3 (MCM, 2019)

An overview of all corrections made for the different species is shown in Table S1.

Fig. S1 shows the measured (blue) and corrected concentrations (red). For α-pinene the amount of reacted substance is accumulated over the whole duration of the experiment and corrected for losses by ozonolysis and dilution. The corrected HCHO, acetone and pinonaldehyde are then plotted versus the corrected amount of reacted α-pinene. The yield of the reaction α-pinene + OH is derived from the resulting slopes.

species	corrected for losses by	corrected for sources from
α-pinene	α-pinene + O_3 dilution	/
pinonaldehyde	pinonaldehyde + hν pinonaldehyde + OH dilution	α-pinene + O_3
acetone	acetone + OH dilution	chamber wall
HCHO	HCHO + OH HCHO + hν dilution	CH_3CHO + OH chamber wall

Table S1. Overview of correction terms for the analysed species applied in the yield calculation.

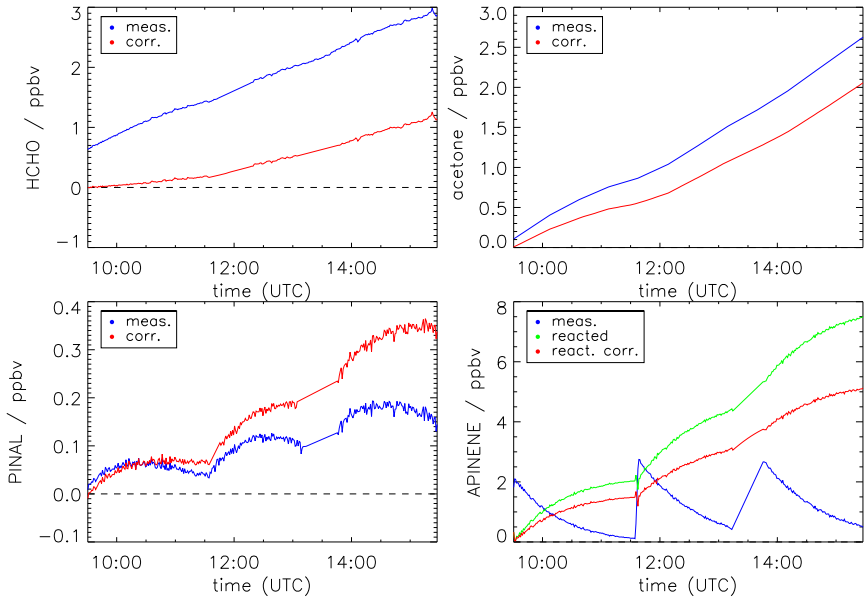

Figure S1. The blue curves show the measured concentrations. For α-pinene the green curve represents the amount of reacted substance. The individual concentrations after the applied correction are shown in red.

S2 Model modifications for M1 sensitivity study

All additions made in the sensitivity run M1 based on the suggestions by Vereecken et al. (2007) are shown in Tables S2 and S3. The naming schema of reactants starting with an "R" is according to Vereecken et al. (2007). Table S2 shows the initial oxidation step of the OH attack, and the subsequent chemistry of the RO_2 after the OH addition.

For simplification only one out of three hydrogen-abstraction pathways is included here forming compound ROOA. The subsequent chemistry of ROOA is shown in Table S3.

APINCO2 was replaced by synR1 and antiR1 as the mechanism by Vereecken et al. (2007) distinguishes the syn and anti stereoisomers of this compound following different pathways. Both synR1 and antiR1 can react with NO but this pathway is outrun by the unimolecular reactions 1,6-H shift, which is only happening for anti isomer, and the ring-closure forming R4. The late degradation products after the 1,6-H-shift are 8-OOH-menthen-6-one (R7P1) and 2-OH-OOH-menthen-6-one (R9P1). The ring-closure leads to the formation of a dicarbonyl cycloperoxide (R5P1).

The model introduced new RO_2, which are not been part of the MCM, and a substantial fraction of the total reaction procedes through these pathways. This underestimates the HO_2 loss by the reaction of RO_2 + OH, especially in the sensitivity run M2. Therefore the RO_2 + HO_2reactions in the lower half of Table S3 are added.

Table S2. Additional and modified reactions applied to the MCM based on the proposed mechanism by Vereecken et al. (2007). For additional OH abstraction chemistry see Table S3. All nitrate species are lumped as one species RNO3.

reaction	reaction rate constant
APINENE + OH→ROOA	$0.12 \times 1.2 \times 10^{-11} \exp(440\mathrm{K/T})\,\mathrm{cm^3 s^{-1}}$
APINENE + OH→APINAO2	$0.22 \times 1.2 \times 10^{-11} \exp(440\mathrm{K/T})\,\mathrm{cm^3 s^{-1}}$
APINENE + OH→APINBO2	$0.44 \times 1.2 \times 10^{-11} \exp(440\mathrm{K/T})\,\mathrm{cm^3 s^{-1}}$
APINENE + OH→synR1	$0.4 \times 0.22 \times 1.2 \times 10^{-11} \exp(440\mathrm{K/T})\,\mathrm{cm^3 s^{-1}}$
APINENE + OH→antiR1	$0.6 \times 0.22 \times 1.2 \times 10^{-11} \exp(440\mathrm{K/T})\,\mathrm{cm^3 s^{-1}}$
APINAO2 + NO→APINANO3	$0.03\times$ KRO2NO[a]
APINAO2 + NO→APINAO + NO2	$0.97\times$ KRO2NO[a]
APINAO →PINAL + HO2	$0.875\times$ KDEC[b]
APINAO →HCHO + HO2	$0.125\times$ KDEC[b]
APINBO2 + NO→APINBNO3	$0.07\times$ KRO2NO[a]
APINBO2 + NO→APINBO + NO2	$0.93\times$ KRO2NO[a]
antiR1 + NO →R2 + NO2	KRO2NO[a]
antiR1 →R4	$0.6\,\mathrm{s^{-1}}$
antiR1 →R7	$11.5\,\mathrm{s^{-1}}$
synR1 + NO→R2 + NO2	KRO2NO[a]
synR1 →R4	$2.6\,\mathrm{s^{-1}}$
R2 →R2P1 + CH3COCH3 + HO2	KDEC[b]
R4 + NO→RNO3	$0.1\times$ KRO2NO[a]
R4 + NO→R5 + NO2	$0.9\times$ KRO2NO[a]
R5 →R5P1 + HO2	KDEC[b]
R7 →R8	$0.5\times$ KDEC[b]
R7 →R7P1 + HO2	$0.5\times$KDEC[b]
R8 + NO→RNO3	$0.29\times$ KRO2NO[a]
R8 + NO→R9 + NO2	$0.71\times$ KRO2NO[a]
R9 →R9P1 + HO2	KDEC[b]

[a] value from MCM: KRO2NO= $2.7 \times 10^{-12} \exp(360\mathrm{K/T})\,\mathrm{cm^3 s^{-1}}$ (MCM, 2019)
[b] value from MCM: KDEC= 1.0×10^{6} (MCM, 2019)

Table S3. Additional OH abstraction reactions and subsequent product reactions applied to the MCM based on the proposed mechanism by Vereecken et al. (2007). All nitrate species are lumped as one species RNO3. All reaction products of RO_2 + HO_2 are lumped as one species RRO2.

reaction	reaction rate constant
ROOA + NO→RNO3	0.11× KRO2NO[a]
ROOA + NO→ROA + NO2	0.89× KRO2NO[a]
ROA →ROOB	0.6× KDEC[b]
ROA →ROOC	0.4× KDEC[b]
ROOB + NO→RNO3	0.11× KRO2NO[a]
ROOB + NO→ROB + NO2	0.89× KRO2NO[a]
ROB →CH3COCH3+HCHO + HO2	KDEC[b]
ROOC + NO→RNO3	0.11× KRO2NO[a]
ROOC + NO→ROC + NO2	0.89× KRO2NO[a]
ROC →HCHO+HO2	KDEC[b]
synR1 + HO2→ APINCOOH	KRO2HO2[c]
antiR1 + HO2→ APINCOOH	KRO2HO2[c]
R4 + HO2→ RRO2	KRO2HO2[c]
R8 + HO2→ RRO2	KRO2HO2[c]
R10 + HO2→ RRO2	KRO2HO2[c]
R12 + HO2→ RRO2	KRO2HO2[c]
ROOA + HO2→ RRO2	KRO2HO2[c]
ROOB + HO2→ RRO2	KRO2HO2[c]
ROOC + HO2→ RRO2	KRO2HO2[c]

[a] value from MCM: KRO2NO= $2.7 \times 10^{-12} \exp(360\mathrm{K}/\mathrm{T})\ \mathrm{cm}^3\mathrm{s}^{-1}$ (MCM, 2019)
[b] value from MCM: KDEC= 1.0×10^{6} (MCM, 2019)
[c] value from MCM: KRO2HO2= $2.91 \times 10^{-13} \exp(1300\mathrm{K}/\mathrm{T})\ \mathrm{cm}^3\mathrm{s}^{-1}$ (MCM, 2019)

S3 Sensitivity study for Xu et al.

Xu et al. (2019) studied the reaction α-pinene + OH and proposed a mechanism constrained by experimentally determined hydroxynitrates yields. An overall shift in the initial RO_2 distribution towards APINCO2 was proposed. We performed an additional sensitivity run based on M1 with the proposed initial RO_2 distribution for APINAO2/APINBO2/APINCO2 of 0.02/0.28/0.60 and 0.10 for H-abstraction reactions. The results are shown in Fig. S2. The pinonaldehyde production is lowered by 50 % compared to M1, but is still overestimating the measured pinonaldehyde concentration by a factor of 3. The additional pinonaldehyde is derived from the higher APINBO2 fraction of 28 % compared to 5 % in M2. The formation of formaldehyde is well reproduced. In contrast, the model underpredicts the acetone production, similar to M2, but with a smaller model-measurement discrepancy of 15 %. The agreement of modeled OH and HO_2 concentrations is around 10 % lower compared to M2, but both agree with the measurements within the stated uncertainty

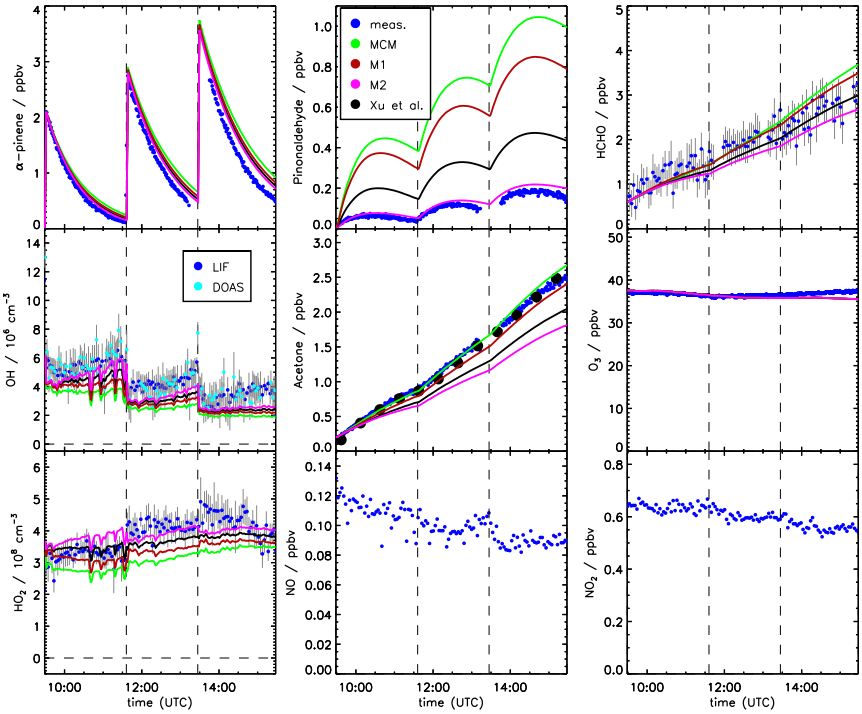

Figure S2. Time series of measured and modelled concentrations of radicals, inorganic and organic compounds during the α-pinene photooxidation at low NO (experiment on 02 July 2014).

References

Atkinson, R., Baulch, D. L., Cox, R. A., Crowley, J. N., Hampson, R. F., Hynes, R. G., Jenkin, M. E., Rossi, M. J., Troe, J., and Subcommittee, I.: Evaluated kinetic and photochemical data for atmospheric chemistry: Volume II - gas phase reactions of organic species, Atmos. Chem. Phys., 6, 3625–4055, https://doi.org/10.5194/acp-6-3625-2006, 2006.

Galloway, M. M., Huisman, A. J., Yee, L. D., Chan, A. W. H., Loza, C. L., Seinfeld, J. H., and Keutsch, F. N.: Yields of oxidized volatile organic compounds during the OH radical initiated oxidation of isoprene, methyl vinyl ketone, and methacrolein under high-NO_X conditions, Atmos. Chem. Phys., 11, 10 779–10 790, https://doi.org/10.5194/acp-11-10779-2011, 2011.

Kaminski, M., Fuchs, H., Acir, I. H., Bohn, B., Brauers, T., Dorn, H. P., Häseler, R., Hofzumahaus, A., Li, X., Lutz, A., Nehr, S., Rohrer, F., Tillmann, R., Vereecken, L., Wegener, R., and Wahner, A.: Investigation of the β-pinene photooxidation by OH in the atmosphere simulation chamber SAPHIR, Atmos. Chem. Phys., 17, 6631–6650, https://doi.org/10.5194/acp-17-6631-2017, 2017.

MCM: The Master Chemical Mechanism, v3.3.1, http://mcm.leeds.ac.uk/MCM, last access: 28 April, 2019.

Vereecken, L., Müller, J. F., and Peeters, J.: Low-volatility poly-oxygenates in the OH-initiated atmospheric oxidation of α-pinene: impact of non-traditional peroxyl radical chemistry, Phys. Chem. Chem. Phys., 9, 5241–5248, https://doi.org/10.1039/B708023A, 2007.

Xu, L., Møller, K. H., Crounse, J. D., Otkjær, R. V., Kjaergaard, H. G., and Wennberg, P. O.: Unimolecular Reactions of Peroxy Radicals Formed in the Oxidation of α-Pinene and β-Pinene by Hydroxyl Radicals, J. Phys. Chem. A,, 123, 1661–1674, https://doi.org/10.1021/acs.jpca.8b11726, 2019.

A.3 Supplementary materials to Chapter 5

Supplement of Atmos. Chem. Phys., 20, 13701–13719, 2020
https://doi.org/10.5194/acp-20-13701-2020-supplement

Atmospheric Chemistry and Physics Open Access EGU

Supplement of

Photooxidation of pinonaldehyde at ambient conditions investigated in the atmospheric simulation chamber SAPHIR

Michael Rolletter et al.

Correspondence to: Hendrik Fuchs (h.fuchs@fz-juelich.de)

Supplement

Model modifications based on Fantechi et al. (2002)

All additions and modifications made in the sensitivity runs Fantechi_a and Fantechi_b based on the suggestions by Fantechi et al. (2002) are shown in Table S1. The naming schema of reactants starting with an "R" is according to Fantechi et al. (2002).

In our calculations the exclusive fate of FAN_C3 is the formation of 4-hydroxynorpinonaldehyde and HO_2. Fantechi et al. (2002) state that at high NO conditions used in laboratory experiments, formic acid (HCOOH) could be formed instead.

To account for possible $RO_2 + HO_2$ reactions, a reaction scheme based on the reaction C97O2 + HO_2 is added for all newly introduced RO_2 species not included in the MCM. RO_2 form a corresponding hydroxyperoxide (ROOH) that can either react with OH to regenerate the RO_2 or photolyse to form the corresponding alkoxy radical (RO) that would be also formed by the reaction of RO_2 + NO. The general scheme is shown here for one RO_2 as an example:

$$\mathrm{FAN\_C1} + \mathrm{HO_2} \rightarrow \mathrm{FAN\_C1\_HO2} \quad (\mathrm{KRO2HO2}) \tag{R-S1}$$

$$\mathrm{FAN\_C1\_HO2} + \mathrm{OH} \rightarrow \mathrm{FAN\_C1} \quad (1 \times 10^{-11}\mathrm{cm^3 s^{-1}}) \tag{R-S2}$$

$$\mathrm{FAN\_C1\_HO2} + \mathrm{h}\nu \rightarrow \mathrm{R\_O3} \quad (\mathrm{J_{22}}) \tag{R-S3}$$

$$\mathrm{FAN\_C1\_HO2} + \mathrm{h}\nu \rightarrow \mathrm{R\_O3} \quad (\mathrm{J_{41}}) \tag{R-S4}$$

Reaction rate constants were used as stated in the MCM.

Table S1. Additional and modified reactions applied to the MCM based on the proposed mechanism by Fantechi et al. (2002). Names are taken from the MCM where existing. Newly introduced species are named either with the prefix "FAN" or "R". All nitrate species are lumped as one species $\mathrm{RNO3}$.

reaction	reaction rate constant
PINAL + OH → C96CO3	$0.61 \times 5.2 \times 10^{-12} \exp(600\mathrm{K/T})\ \mathrm{cm^3 s^{-1}}$
PINAL + OH → FAN_D1	$0.24 \times 5.2 \times 10^{-12} \exp(600\mathrm{K/T})\ \mathrm{cm^3 s^{-1}}$
PINAL + OH → PINALO2	$0.09 \times 5.2 \times 10^{-12} \exp(600\mathrm{K/T})\ \mathrm{cm^3 s^{-1}}$
PINAL + OH → FAN_G1	$0.06 \times 5.2 \times 10^{-12} \exp(600\mathrm{K/T})\ \mathrm{cm^3 s^{-1}}$
C96O → NORPINAL + $\mathrm{HO_2}$	$5.0 \times 10^4\ \mathrm{s^{-1}}$
C96O → FAN_C1	$6.5 \times 10^5\ \mathrm{s^{-1}}$
FAN_C1 + NO → R_O3 + $\mathrm{NO_2}$	$0.86\times$ KRO2NO[a]
FAN_C1 + NO → RNO3	$0.14\times$ KRO2NO[a]
R_O3 → FAN_C2 + HCHO	$1.2 \times 10^7\ \mathrm{s^{-1}}$
R_O3 → FAN_C3	$3.2 \times 10^8\ \mathrm{s^{-1}}$
FAN_C2 + NO → R_O5 +$\mathrm{NO_2}$	$0.91\times$ KRO2NO[a]
FAN_C2 + NO → RNO3	$0.09\times$ KRO2NO[a]
FAN_C3 → NORPINALOH + $\mathrm{HO_2}$	$2.0 \times 10^3\ \mathrm{s^{-1}}$
R_O5 → FAN_C5	$0.5\times$ KDEC[b]
R_O5 → FAN_C6	$0.5\times$ KDEC[b]
FAN_C5 + NO → FAN_C7 + $\mathrm{NO_2}$	$0.75\times$ KRO2NO[a]
FAN_C5 + NO → RNO3	$0.25\times$ KRO2NO[a]
FAN_C6 + NO → HCHO + $\mathrm{HO_2}$ + $\mathrm{NO_2}$	$0.93\times$ KRO2NO[a]
FAN_C6 + NO → RNO3	$0.07\times$ KRO2NO[a]
FAN_D1 + NO → R_O8 + $\mathrm{NO_2}$	$0.72\times$ KRO2NO[a]
FAN_D1 + NO → RNO3	$0.28\times$ KRO2NO[a]
R_O8 → NORPINAL + $\mathrm{HO_2}$	KDEC[b]
FAN_G1 + NO → FAN_G2 + $\mathrm{NO_2}$	KRO2NO[a]
FAN_G2 + NO → R_O13 + $\mathrm{NO_2}$	$0.89\times$ KRO2NO[a]
FAN_G2 + NO → RNO3	$0.11\times$ KRO2NO[a]
R_O13→ FAN_G3	$5.0 \times 10^{11}\ \mathrm{s^{-1}}$
FAN_G3 + NO → R_O14 + $\mathrm{NO_2}$	KRO2NO[a]
R_O14→ FAN_G4 + $\mathrm{CO_2}$	KDEC[b]
FAN_G4 + NO → R_O15 + $\mathrm{NO_2}$	$0.86\times$ KRO2NO[a]
FAN_G4 + NO → RNO3	$0.14\times$ KRO2NO[a]
R_O15→ FAN_G5	$0.5 \times 1.0 \times 10^5\ \mathrm{s^{-1}}$
R_O15→ FAN_G7	$0.5 \times 1.0 \times 10^5\ \mathrm{s^{-1}}$
FAN_G5 + NO → R_O16 + $\mathrm{NO_2}$	$0.97\times$ KRO2NO[a]
FAN_G5 + NO → RNO3	$0.03\times$ KRO2NO[a]
R_O16→ C818CO + HCHO + $\mathrm{HO_2}$	KDEC[b]
FAN_G7 + NO → R_O17 + $\mathrm{NO_2}$	$0.97\times$ KRO2NO[a]
FAN_G7 + NO → RNO3	$0.03\times$ KRO2NO[a]
R_O17→ CO23C4CHO + CH3COCH3 + $\mathrm{HO_2}$	KDEC[b]

[a] value from MCM: KRO2NO= $2.7 \times 10^{-12} \exp(360\mathrm{K/T})\ \mathrm{cm^3 s^{-1}}$ (MCM, 2017)
[b] value from MCM: KDEC= $1.0 \times 10^6\ \mathrm{s^{-1}}$ (MCM, 2017)

Sensitivity study S1 and additional sensitivity tests

In S1 the impact of hypothetical isomerization reactions of all 4 initially formed RO_2 radicals on model results was tested. Reactions shown in Tab. S2 were added to the model based on Fantechi et al. (2002). Possible isomerziation reactions in later stages of the mechanism were not tested.

Table S2. Overview of added reactions for sensitivity run S1.

reaction	reaction rate constant
C96CO3 $\rightarrow$ HO_2	0.1 s^{-1}
PINALO2 $\rightarrow$ HO_2	0.1 s^{-1}
FAN_D1 $\rightarrow$ HO_2	0.1 s^{-1}
FAN_G1 $\rightarrow$ HO_2	0.1 s^{-1}

However, only PINALO2, FAN_D1, and FAN_G1 have an aldehyde group with a hydrogen that can be easily abstracted. An additional sensitivity study (S1_mod) was performed that includes only isomerization reactions of these 3 RO_2 applying the same reaction rates used for S1. Figure S1 shows the calculated HO_2 and OH time series together with results from S1, model base case (MCM_a), and modified mechanism by Fantechi et al. (2002) (FAN_a).

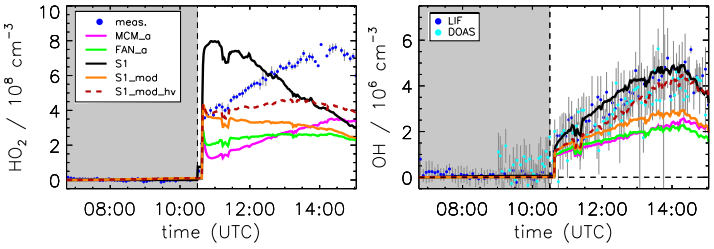

Figure S1. Model sensitivity studies of the impact of potential additional HO_2 formation by unimolecular RO_2 reactions of all 4 initial RO_2 (S1) and for RO_2 radicals with a –HCO group (S1_mod). The sensitivity test S1_mod_hv extends S1_mod by an additional photolysis of isomerization products. In addition, the model base case (MCM_a) and the case using the mechanism by Fantechi et al. (2002) (FAN_a) are shown. Grey shaded areas indicate times when the chamber roof was closed.

These RO_2 radicals are formed with a yield of 39 %. Therefore, HO_2 concentrations in the beginning of the experiment are reduced by a factor of 2 compared to S1 where the isomerization of all initial RO_2 leads to the formation of HO_2. The reduced HO_2 concentrations agree with observations at the start of the photooxidation, but show the same temporal trend as in model run S1 over the course of the experiment. This leads to an increasing model-measurement discrepancy of HO_2 concentrations of a factor of up to 3. Consistently, OH concentrations are reduced by a factor of 2 compared to S1.

Products of the rapid isomerization reaction could be peroxy acids with additional carbonyl functions. As seen for pinonaldehyde, photolysis frequencies of bi-carbonyl compounds could be generally underestimated in current models. An additional sensitivity test (S1_mod_hv) with isomerization of initially formed RO_2 with –HCO group followed by photolysis of the iso-

merization products with the photolysis frequency of glyoxal was performed. Because the photolysis frequency of glyoxal is slow compared to the reaction rate of the isomerization reaction, the HO_2 concentration time series in this sensitivity model run is similar to the sensitivity run with only isomerization (S1_mod). The formation of HO_2 is linked to the RO_2 concentration in this case and underestimated by the model.

Sensitivity test of RO_2 + NO reaction rate constants

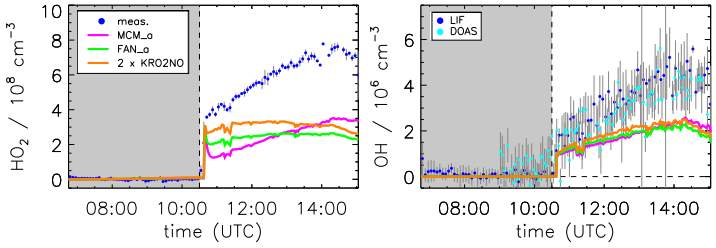

Figure S2. Model sensitivity run with modified reaction rate of 2xKRO2NO. The modified reaction rate constant was applied to all RO_2 that were introduced by the model modifications based on Fantechi et al. (2002). Grey shaded areas indicate times when the chamber roof was closed.

Sensitivity study S3

In the used mechanism based on Fantechi et al. (2002) 4-hydroxynorpinonaldehyde was formed as main product with an overall yield of approximately 25 % but no subsequent chemistry was considered in the MCM model and the modified Fantechi mechanism. To investigate if the subsequent chemistry of this product has the potential to partly explain the missing HO_2 source a mechanism was deduced from structure–activity relationship (SAR; Kwok and Atkinson, 1995; Vereecken and Peeters, 2009; Vereecken and Nozière, 2020). No theoretical calculations were performed.

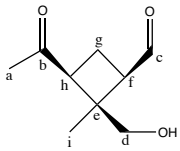

Figure S3. Structure of 4-hydroxynorpinonaldehyde and C-atom labeling.

The 4-hydroxynorpinonaldehyde structure is shown in Fig. S3. Reaction rate constants for the H-abstraction by OH were estimated based on Kwok and Atkinson (1995) and are shown in Table S3.

Table S3. Reaction rate constants for H-abstraction by OH for different carbon atoms based on Kwok and Atkinson (1995).

C-atom	reaction rate constant	fraction
c	1.69×10^{-11} cm^3 s^{-1}	79 %
d	3.27×10^{-12} cm^3 s^{-1}	15 %
f	5.43×10^{-13} cm^3 s^{-1}	3 %
g	2.62×10^{-13} cm^3 s^{-1}	1 %
h	5.43×10^{-13} cm^3 s^{-1}	3 %

A simplified mechanism of the subsequent degradation of 4-hydroxynorpinonaldehyde is shown in S4. An overview of added reactions is shown in Tab. S4. Reaction rates are base on Vereecken and Peeters (2009); Vereecken and Nozière (2020). Only the main reaction branches ($\geq 5\%$) were investigated. The mechanism was constructed according to Jenkin et al. (1997). For all RO_2 + NO reactions the standard reaction rate from MCM (KRO2NO) and an organic nitrate yield of 23 % was used. RO_2 + HO_2 reactions were included as described for the modified mechanism based on Fantechi et al. (2002). The photolysis frequency of pinononaldehyde was used for the photolysis of formed hydroperoxides (ROOH).

H-abstraction by OH mainly occurs at the aldehyde group forming the peroxy radical C1. After a rapid CO_2 elimination, C1 forms C2 and C3 in equal amounts. C2 can undergo an 1,5 H-shift to form a stable hydroperoxy compound (C5) and HO_2. Alternatively, C2 can form the alkoxy radical C4 after reaction with NO. Similarly, C3 forms the alkoxy radical C12. Ring-opening of the 4-membered ring in both C4 and C12 leads to the formation of a peroxy radical C6. Subsequently, the main fraction (approximately 90 %) rearranges after an 1,6 H-shift to C9. C9 either undergoes an 1,6 H-shift forming C10 or forms an alkoxy radical that further decomposes to a stable product and HO_2.

A sensitivity run (S3) using the degradation scheme of 4-hydroxynorpinonaldehyde was performed and results can be seen in Fig. S5. The modifications have only a small effect on HO_2 and OH concentrations. In the second half of the experiment the degradation of pinonaldehyde oxidation products becomes more relevant and additional HO_2 is formed by the 4-hydroxynorpinonaldehyde degradation scheme. However, the effect on the HO_2 concentration is small and HO_2 concentrations are increased by up to 10 % compared to FAN_a.

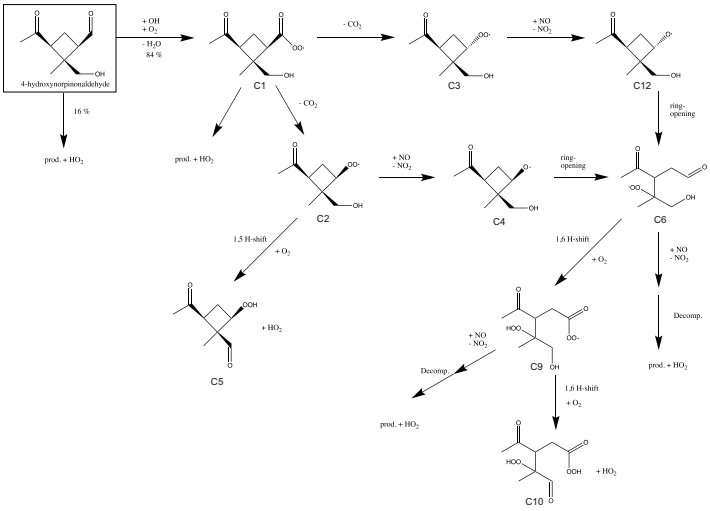

Figure S4. Simplified mechanism of the subsequent degradation of 4-hydroxynorpinonaldehyde. The mechanism is deduced from SAR. For details see text. $RO_2 + HO_2$ reactions and $RO_2 + NO$ reactions that form nitrates are not shown.

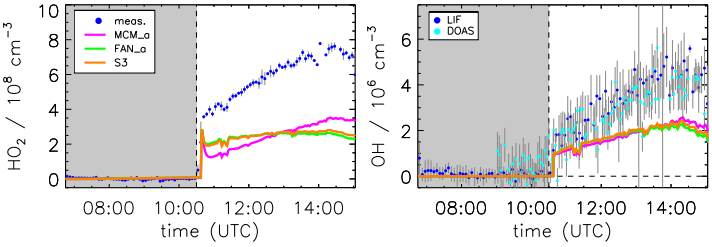

Figure S5. Model sensitivity study of the impact of a 4-hydroxynorpinonaldehyde degradation mechanism (S3) compared to the model base case (MCM_a) and the case using the mechanism by Fantechi et al. (2002) (FAN_a). Grey shaded areas indicate times when the chamber roof was closed.

Table S4. Extended mechanism for the further degradation of 4-hydroxynorpinonaldehyde used for sensitivity test S3. For details see text. All nitrate species are lumped as one species RNO3.

reaction	reaction rate constant
NORPINALOH + OH → C1	$1.69 \times 10^{-11}\,\mathrm{cm^3\,s^{-1}}$ [a]
NORPINALOH + OH → D1 + HO_2	$3.27 \times 10^{-12}\,\mathrm{cm^3\,s^{-1}}$ [a]
NORPINALOH + OH → F1 + HO_2	$5.43 \times 10^{-13}\,\mathrm{cm^3\,s^{-1}}$ [a]
NORPINALOH + OH → G1 + HO_2	$2.62 \times 10^{-13}\,\mathrm{cm^3\,s^{-1}}$ [a]
NORPINALOH + OH → H1 + HO_2	$5.43 \times 10^{-13}\,\mathrm{cm^3\,s^{-1}}$ [a]
NORPINALOH + hν → C2 + HO_2	j_{PINAL}
C1 → C2 + CO_2	KDEC[b]
C1 → C3 + CO_2	KDEC[b]
C1 → prod. + HO_2	$9.16 \times 10^{-2}\,\mathrm{s^{-1}}$
C1 + NO → C1O + NO_2	0.77*KRO2NO[c]
C1 + NO → RNO3	0.23*KRO2NO[c]
C1 + HO_2 → C1OOH	KRO2HO2[d]
C1OOH + OH → C1	$1.3 \times 10^{-11}\,\mathrm{cm^3\,s^{-1}}$
C1OOH + hν → C1O + OH	j_{PINAL}
C1O→ prod. + HO_2	KDEC[b]
C2 + NO → C4 + NO_2	0.77*KRO2NO[c]
C2 + NO → RNO3	0.23*KRO2NO[c]
C2 → C5 + HO_2	$1.3 \times 10^{-2}\,\mathrm{s^{-1}}$
C2 + HO_2 → C2OOH	KRO2HO2[d]
C2OOH + OH → C2	$1.3 \times 10^{-11}\,\mathrm{cm^3\,s^{-1}}$
C2OOH + hν → C4 + OH	j_{PINAL}
C4 → C6	KDEC[b]
C6 → C9	$2.8 \times 10^{-1}\,\mathrm{s^{-1}}$
C6 + NO → C7 + NO_2	0.77*KRO2NO[c]
C6 + NO → RNO3	0.23*KRO2NO[c]
C6 + HO_2 → C6OOH	KRO2HO2[d]
C6OOH + OH → C6	$1.3 \times 10^{-11}\,\mathrm{cm^3\,s^{-1}}$
C6OOH + hν → C7 + OH	j_{PINAL}
C7 → C8 + ACETOL	KDEC[b]
C8 → prod. + HO_2	KDEC[b]
C9 → C10 + HO_2	$6.6 \times 10^{-4}\,\mathrm{s^{-1}}$
C9 + NO → C11 + NO_2	0.77*KRO2NO[c]
C9 + NO → RNO3	0.23*KRO2NO[c]
C9 + HO_2 → C9OOH	KRO2HO2[d]
C9OOH + OH → C9	$1.3 \times 10^{-11}\,\mathrm{cm^3\,s^{-1}}$
C9OOH + hν → C11 + OH	j_{PINAL}
C11 → C13 + HO_2	KDEC[b]
C3 + NO → C12 + NO_2	0.77*KRO2NO[c]
C3 + NO → RNO3	0.23*KRO2NO[c]
C3 + HO_2 → C3OOH	KRO2HO2[d]
C3OOH + OH → C3	$1.3 \times 10^{-11}\,\mathrm{cm^3\,s^{-1}}$
C3OOH + hν → C12 + OH	j_{PINAL}
C12 → C6 + HO_2	KDEC[b]

[a] value from Kwok and Atkinson (1995)
[b] value from MCM: KDEC= $1.0 \times 10^6\,\mathrm{s^{-1}}$ (MCM, 2017)
[c] value from MCM: KRO2NO= $2.7 \times 10^{-12} \exp(360\mathrm{K/T})\,\mathrm{cm^3 s^{-1}}$ (MCM, 2017)
[d] value from MCM: KRO2HO2= $2.91 \times 10^{-13} \exp(1300\mathrm{K/T})\,\mathrm{cm^3 s^{-1}}$ (MCM, 2017)

Sensitivity test of additional acetone and HCHO formation by pathways II, III, and IV

In a sensitivity study it was tested if the pathways II, III, and IV that do not form 4-hydroxynorpinonaldehyde have the potential to explain the missing acetone and formaldehyde formation in the OH oxidation experiment. In a sensitivity test the first reaction step of the pathways II, III, and IV form one molecule of acetone and HCHO each. Results are shown in Fig. S6. The additional acetone and HCHO sources can reproduce observations in the first half of the experiment within the measurement uncertainty when contributions from OH reactions of product species are small. In later stages of the experiment, acetone and formaldehyde concentrations are underestimated by the sensitivity model run. Additional acetone and HCHO formation from further degradation of oxidation products not included in the MCM could explain the model-measurement discrepancy. See the response to comment 4 for more information of potential products of the degradation of 4-hydroxinorpinonaldehyde.

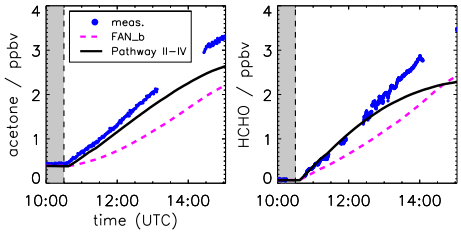

Figure S6. Measured and modeled formaldehyde and acetone mixing ratios for the experiment without OH scavenger. All model runs were done with measured photolysis frequencies for pinonaldehyde and with HO_2 constrained to measurements. Model runs were done using modifications described in Fantechi et al. (2002). For the model run shown in black an additional HCHO and acetone formation in pathways II, III, and IV is assumed.

References

Fantechi, G., Vereecken, L., and Peeters, J.: The OH-initiated atmospheric oxidation of pinonaldehyde: Detailed theoretical study and mechanism construction, Phys. Chem. Chem. Phys., 4, 5795–5805, https://doi.org/10.1039/B205901K, 2002.

Jenkin, M. E., Saunders, S. M., and Pilling, M. J.: The tropospheric degradation of volatile organic compounds: A protocol for mechanism development, Atmos. Environ., 31, 81–104, https://doi.org/10.1016/S1352-2310(96)00105-7, 1997.

Kwok, E. S. C. and Atkinson, R.: Estimation of hydroxyl radical reaction rate constants for gas-phase organic compounds using a structure-reactivity relationship: An update, Atmos. Environ., 29, 1685–1695, https://doi.org/10.1016/1352-2310(95)00069-B, 1995.

MCM: Master Chemical Mechanism, http://mcm.leeds.ac.uk/MCM/, last access: 04 March 2020, 2017.

Vereecken, L. and Nozière, B.: H migration in peroxy radicals under atmospheric conditions, Atmos. Chem. Phys., 20, 7429–7458, https://doi.org/10.5194/acp-20-7429-2020, 2020.

Vereecken, L. and Peeters, J.: Decomposition of substituted alkoxy radicals-part I: a generalized structure-activity relationship for reaction barrier heights, Phys. Chem. Chem. Phys., 11, 9062–9074, https://doi.org/10.1039/B909712K, 2009.

A.4 Supplementary materials to Chapter 9

WAVENUMBER	Sigma	WAVENUMBER	Sigma
6180.47	4.96168E-16	6600.66	8.24713E-16
6180.37	4.89272E-16	6600.44	9.19540E-17
6180.28	5.35824E-16	6600.22	9.31035E-16
6180.18	5.81420E-17	6600.01	7.90230E-17
6180.09	6.32184E-16	6599.79	7.01150E-17
6179.99	6.37931E-16	6599.57	7.72989E-16
6179.90	6.13029E-16	6599.35	7.55747E-16
6179.80	5.67625E-16	6599.14	7.72989E-16
6179.71	5.79121E-16	6598.92	7.21264E-16
6179.61	5.46743E-16	6598.70	7.01150E-17
6179.52	5.63410E-17	6598.48	8.64943E-16
6179.42	5.92144E-16	6598.26	8.96552E-16
6179.32	5.73755E-16	6598.05	9.28161E-16
6179.23	6.06322E-16	6597.83	9.02299E-16
6179.13	5.44828E-16	6597.61	9.10920E-17
6179.04	5.61878E-16	6597.39	1.02299E-15
6178.94	5.46552E-16	6597.18	1.18391E-15
6178.85	5.49809E-16	6596.96	1.29023E-15
6178.75	5.89270E-17	6596.74	1.25862E-15
6178.66	5.98851E-16	6596.52	1.26437E-15
6178.56	5.75673E-16	6596.31	1.35345E-15
6178.46	5.71839E-16	6596.09	1.38218E-15
6178.37	5.66092E-16	6595.87	1.31609E-15
6178.27	6.30270E-17	6595.65	1.31035E-15
6178.18	6.08431E-16	6595.44	1.21264E-15
6178.08	5.58429E-16	6595.22	1.12644E-15
6177.99	4.94828E-16	6595.00	1.14943E-15
6177.89	5.09579E-16	6594.78	1.15517E-15
6177.80	5.42337E-16	6594.57	1.10058E-15
6177.70	6.04023E-16	6594.35	1.11782E-15
6177.61	5.84868E-16	6594.13	1.16379E-15
6177.51	5.90615E-16	6593.91	1.19253E-15
6177.42	5.32184E-16	6593.70	1.15517E-15
6177.32	5.75673E-16	6593.48	1.02012E-15
6177.22	5.75673E-16	6593.26	1.09195E-15
6177.13	5.63793E-16	6593.04	1.17816E-15
6177.03	5.46552E-16	6592.83	1.07184E-15
6176.94	5.42720E-17	6592.61	1.05172E-15
6176.84	5.81035E-16	6592.39	1.05747E-15
6176.75	6.30845E-16	6592.18	9.65517E-16
6176.65	6.28925E-16	6591.96	9.94253E-16
6176.56	6.28925E-16	6591.74	1.06609E-15
6176.46	5.75287E-16	6591.52	1.02874E-15
6176.37	5.42529E-16	6591.31	9.97127E-16
6176.27	5.80270E-17	6591.09	9.33908E-16
6176.18	5.59962E-16	6590.87	9.33908E-16
6176.08	5.43295E-16	6590.65	9.74138E-16
6175.98	5.24138E-16	6590.44	9.54023E-16
6175.89	5.80845E-16	6590.22	9.62644E-16

6175.79	6.53259E-16	6590.00	9.13793E-16
6175.70	6.26437E-16	6589.79	8.56322E-16
6175.60	6.14943E-16	6589.57	8.59196E-16
6175.51	5.95787E-16	6589.35	8.90805E-16
6175.41	5.99810E-17	6589.13	9.39655E-16
6175.32	6.09385E-16	6588.92	8.73563E-16
6175.22	5.93104E-16	6588.70	7.90230E-17
6175.13	6.08236E-16	6588.48	7.90230E-17
6175.03	5.73755E-16	6588.27	8.90805E-16
6174.94	6.16856E-16	6588.05	9.48276E-16
6174.84	6.34098E-16	6587.83	8.62069E-16
6174.75	6.37931E-16	6587.62	9.36782E-16
6174.65	6.13029E-16	6587.40	9.62644E-16
6174.55	6.36017E-16	6587.18	9.16667E-16
6174.46	6.59006E-16	6586.96	9.51150E-17
6174.36	6.43104E-16	6586.75	9.05172E-16
6174.27	6.08621E-16	6586.53	9.39655E-16
6174.17	6.02874E-16	6586.31	1.00000E-20
6174.08	6.47512E-16	6586.10	9.13793E-16
6173.98	6.36971E-16	6585.88	8.56322E-16
6173.89	6.19730E-17	6585.66	9.54023E-16
6173.79	6.12069E-16	6585.45	9.88506E-16
6173.70	6.22604E-16	6585.23	9.39655E-16
6173.60	6.22604E-16	6585.01	9.48276E-16
6173.51	6.20690E-17	6584.80	9.74138E-16
6173.41	6.02684E-16	6584.58	1.01149E-15
6173.32	6.21839E-16	6584.36	1.00575E-15
6173.22	6.39081E-16	6584.15	8.67816E-16
6173.13	6.28161E-16	6583.93	8.18966E-16
6173.03	6.41569E-16	6583.71	8.76437E-16
6172.93	6.68391E-16	6583.50	9.13793E-16
6172.84	6.67816E-16	6583.28	9.28161E-16
6172.74	6.35247E-16	6583.06	9.13793E-16
6172.65	5.73947E-16	6582.85	8.73563E-16
6172.55	6.83908E-16	6582.63	9.10920E-17
6172.46	6.78351E-16	6582.41	1.00862E-15
6172.36	6.64943E-16	6582.20	1.01149E-15
6172.27	5.63410E-17	6581.98	1.00287E-15
6172.17	5.82374E-16	6581.76	1.00287E-15
6172.08	5.53448E-16	6581.55	9.36782E-16
6171.98	6.30075E-16	6581.33	8.85058E-16
6171.89	6.09385E-16	6581.11	9.13793E-16
6171.79	6.42144E-16	6580.90	8.96552E-16
6171.70	5.96167E-16	6580.68	8.33333E-16
6171.60	5.83523E-16	6580.46	8.16092E-16
6171.51	5.79695E-16	6580.25	8.64943E-16
6171.41	5.91190E-17	6580.03	8.96552E-16
6171.32	6.14943E-16	6579.81	8.79310E-17
6171.22	6.37931E-16	6579.60	8.56322E-16
6171.13	6.55172E-16	6579.38	8.76437E-16
6171.03	7.06897E-16	6579.16	8.90805E-16
6170.94	7.12644E-16	6578.95	8.39081E-16
6170.84	7.03063E-16	6578.73	8.30460E-17

6170.74	6.57086E-16	6578.51	9.25287E-16
6170.65	6.57086E-16	6578.30	9.94253E-16
6170.55	6.28351E-16	6578.08	9.65517E-16
6170.46	6.53259E-16	6577.87	8.50575E-16
6170.36	6.59006E-16	6577.65	7.75862E-16
6170.27	6.72414E-16	6577.43	8.18966E-16
6170.17	6.64753E-16	6577.22	9.02299E-16
6170.08	6.20115E-16	6577.00	9.39655E-16
6169.98	6.14368E-16	6576.78	9.22414E-16
6169.89	5.49042E-16	6576.57	9.28161E-16
6169.79	6.05172E-16	6576.35	8.85058E-16
6169.70	5.91764E-16	6576.14	8.04598E-16
6169.60	6.76247E-16	6575.92	8.90805E-16
6169.51	6.66667E-16	6575.70	1.00862E-15
6169.41	6.74328E-16	6575.49	1.00575E-15
6169.32	6.51339E-16	6575.27	9.22414E-16
6169.22	6.34098E-16	6575.05	8.67816E-16
6169.13	6.72414E-16	6574.84	8.93678E-16
6169.03	6.33523E-16	6574.62	8.99425E-16
6168.94	6.09385E-16	6574.41	9.25287E-16
6168.84	5.65326E-16	6574.19	9.68391E-16
6168.75	6.44443E-16	6573.97	9.94253E-16
6168.65	6.64753E-16	6573.76	1.02586E-15
6168.56	7.10730E-17	6573.54	1.02586E-15
6168.46	6.66667E-16	6573.33	1.00287E-15
6168.37	6.76247E-16	6573.11	8.90805E-16
6168.27	6.49425E-16	6572.89	8.64943E-16
6168.18	6.62833E-16	6572.68	8.79310E-17
6168.08	6.89655E-16	6572.46	8.76437E-16
6167.98	6.53638E-16	6572.25	9.19540E-17
6167.89	6.30649E-16	6572.03	9.42529E-16
6167.79	6.00000E-21	6571.81	9.74138E-16
6167.70	6.18776E-16	6571.60	1.03161E-15
6167.60	6.01914E-16	6571.38	1.05747E-15
6167.51	5.69349E-16	6571.17	1.00575E-15
6167.41	5.29885E-16	6570.95	9.94253E-16
6167.32	5.39081E-16	6570.73	1.00287E-15
6167.22	5.71648E-16	6570.52	9.77012E-16
6167.13	6.97316E-16	6570.30	9.54023E-16
6167.03	7.10730E-17	6570.09	1.01149E-15
6166.94	7.60535E-16	6569.87	1.02586E-15
6166.84	7.27971E-16	6569.65	1.12356E-15
6166.75	7.16477E-16	6569.44	1.14368E-15
6166.65	6.93489E-16	6569.22	1.08621E-15
6166.56	6.64753E-16	6569.01	1.07184E-15
6166.46	7.12644E-16	6568.79	9.59770E-17
6166.37	6.95402E-16	6568.58	9.51150E-17
6166.27	7.14558E-16	6568.36	9.85632E-16
6166.18	7.62454E-16	6568.14	1.05747E-15
6166.08	8.19925E-16	6567.93	1.10632E-15
6165.99	8.62069E-16	6567.71	1.08046E-15
6165.89	8.27586E-16	6567.50	1.05172E-15
6165.80	8.39081E-16	6567.28	1.00575E-15

6165.70	9.40615E-16	6567.07	1.01724E-15
6165.61	1.10345E-15	6566.85	1.11207E-15
6165.51	1.29310E-16	6566.63	1.10345E-15
6165.42	1.39464E-15	6566.42	1.08046E-15
6165.32	1.45594E-15	6566.20	1.12644E-15
6165.23	1.46935E-15	6565.99	1.07184E-15
6165.13	1.49809E-15	6565.77	1.08621E-15
6165.04	1.53257E-15	6565.56	1.08046E-15
6164.94	1.57088E-15	6565.34	1.07184E-15
6164.85	1.56131E-15	6565.13	1.02012E-15
6164.75	1.51149E-15	6564.91	9.82759E-16
6164.66	1.47126E-15	6564.70	1.01437E-15
6164.56	1.41379E-15	6564.48	1.00862E-15
6164.47	1.39464E-15	6564.26	1.00862E-15
6164.37	1.36016E-15	6564.05	1.12644E-15
6164.28	1.32567E-15	6563.83	1.16092E-15
6164.18	1.25671E-15	6563.62	1.06897E-15
6164.09	1.15709E-15	6563.40	1.03161E-15
6163.99	1.11686E-15	6563.19	1.04310E-16
6163.90	1.07855E-15	6562.97	1.02586E-15
6163.80	9.96167E-16	6562.76	1.02586E-15
6163.71	9.04213E-16	6562.54	1.03448E-15
6163.61	9.23374E-16	6562.33	1.01149E-15
6163.52	9.63604E-16	6562.11	1.07471E-15
6163.42	1.00575E-15	6561.90	1.07471E-15
6163.33	9.57856E-16	6561.68	9.74138E-16
6163.23	9.57856E-16	6561.46	9.94253E-16
6163.14	9.31035E-16	6561.25	1.14943E-15
6163.04	8.92718E-16	6561.03	1.10058E-15
6162.95	8.27586E-16	6560.82	1.14655E-15
6162.85	8.21839E-16	6560.60	1.18391E-15
6162.76	8.14178E-16	6560.39	1.07184E-15
6162.66	8.40994E-16	6560.17	1.15805E-15
6162.57	8.02684E-16	6559.96	1.20115E-15
6162.47	7.95017E-16	6559.74	1.16379E-15
6162.38	7.41379E-16	6559.53	1.13506E-15
6162.28	7.10730E-17	6559.31	1.20402E-15
6162.19	7.01150E-17	6559.10	1.27012E-15
6162.09	7.24138E-16	6558.88	1.18966E-15
6162.00	8.16092E-16	6558.67	1.15517E-15
6161.90	8.18006E-16	6558.45	1.11494E-15
6161.81	8.83144E-16	6558.24	1.07759E-15
6161.71	8.27586E-16	6558.02	1.12931E-15
6161.62	8.33333E-16	6557.81	1.25862E-15
6161.52	7.66282E-16	6557.59	1.18966E-15
6161.43	7.50960E-17	6557.38	1.19828E-15
6161.33	7.22224E-16	6557.16	1.27874E-15
6161.24	7.52874E-16	6556.95	1.19540E-16
6161.14	7.49040E-17	6556.73	1.25862E-15
6161.05	7.31799E-16	6556.52	1.31035E-15
6160.96	6.91569E-16	6556.30	1.28448E-15
6160.86	7.12644E-16	6556.09	1.18678E-15
6160.77	7.24138E-16	6555.87	1.22414E-15

6160.67	7.33718E-16	6555.66	1.29023E-15
6160.58	6.72414E-16	6555.44	1.22126E-15
6160.48	6.72414E-16	6555.23	1.24138E-15
6160.39	5.98276E-16	6555.01	1.22414E-15
6160.29	6.11684E-16	6554.80	1.23563E-15
6160.20	6.53833E-16	6554.58	1.24138E-15
6160.10	7.10730E-17	6554.37	1.27012E-15
6160.01	7.49040E-17	6554.15	1.34770E-16
6159.91	6.69351E-16	6553.94	1.46264E-15
6159.82	7.15328E-16	6553.72	1.69253E-15
6159.72	6.73178E-16	6553.51	2.01149E-15
6159.63	7.26052E-16	6553.29	2.23851E-15
6159.53	6.60920E-17	6553.08	2.25000E-20
6159.44	6.81994E-16	6552.87	2.45402E-15
6159.34	6.83908E-16	6552.65	2.58333E-15
6159.25	7.22224E-16	6552.44	2.46839E-15
6159.15	7.41379E-16	6552.22	2.41379E-15
6159.06	7.27971E-16	6552.01	2.43391E-15
6158.96	6.89655E-16	6551.79	2.39081E-15
6158.87	6.83908E-16	6551.58	2.19540E-16
6158.77	6.44638E-16	6551.36	2.11207E-15
6158.68	5.93868E-16	6551.15	2.08621E-15
6158.58	5.68966E-16	6550.93	1.90517E-15
6158.49	6.27397E-16	6550.72	1.70402E-15
6158.39	7.14558E-16	6550.50	1.69828E-15
6158.30	7.58621E-16	6550.29	1.81035E-15
6158.20	7.83523E-16	6550.08	1.84770E-16
6158.11	8.06512E-16	6549.86	1.74425E-15
6158.01	8.14178E-16	6549.65	1.62356E-15
6157.92	8.21839E-16	6549.43	1.55460E-16
6157.83	7.96937E-16	6549.22	1.54310E-16
6157.73	7.89270E-17	6549.00	1.50575E-15
6157.64	7.81609E-16	6548.79	1.50000E-20
6157.54	7.73948E-16	6548.57	1.53448E-15
6157.45	7.75862E-16	6548.36	1.44253E-15
6157.35	8.08431E-16	6548.15	1.40805E-15
6157.26	7.89270E-17	6547.93	1.43391E-15
6157.16	7.85443E-16	6547.72	1.35632E-15
6157.07	7.54787E-16	6547.50	1.25287E-15
6156.97	8.06512E-16	6547.29	1.29310E-16
6156.88	8.52489E-16	6547.07	1.29885E-15
6156.78	8.69730E-17	6546.86	1.31322E-15
6156.69	8.40994E-16	6546.65	1.38218E-15
6156.59	8.37167E-16	6546.43	1.34195E-15
6156.50	8.16092E-16	6546.22	1.29310E-16
6156.40	8.96552E-16	6546.00	1.25575E-15
6156.31	9.04213E-16	6545.79	1.22701E-15
6156.21	9.57856E-16	6545.57	1.23563E-15
6156.12	9.98086E-16	6545.36	1.35632E-15
6156.02	1.08812E-15	6545.15	1.35345E-15
6155.93	1.14559E-15	6544.93	1.29885E-15
6155.83	1.14751E-15	6544.72	1.32471E-15
6155.74	1.15517E-15	6544.50	1.33333E-15

6155.65	1.17816E-15	6544.29	1.39655E-15
6155.55	1.19924E-15	6544.07	1.45977E-15
6155.46	1.15901E-15	6543.86	1.47701E-15
6155.36	1.12644E-15	6543.65	1.56609E-15
6155.27	1.08046E-15	6543.43	1.69828E-15
6155.17	1.03832E-15	6543.22	1.73276E-15
6155.08	1.02299E-15	6543.00	1.81035E-15
6154.98	1.02299E-15	6542.79	1.90230E-16
6154.89	1.02299E-15	6542.58	1.98851E-15
6154.79	9.61684E-16	6542.36	2.02874E-15
6154.70	9.77012E-16	6542.15	2.02012E-15
6154.60	9.54023E-16	6541.93	2.00575E-15
6154.51	9.98086E-16	6541.72	2.00000E-20
6154.41	9.27201E-16	6541.51	1.97126E-15
6154.32	8.46741E-16	6541.29	1.85345E-15
6154.23	8.19925E-16	6541.08	1.83333E-15
6154.13	8.50575E-16	6540.86	1.79598E-15
6154.04	9.17626E-16	6540.65	1.72414E-15
6153.94	8.81224E-16	6540.44	1.70402E-15
6153.85	8.60155E-16	6540.22	1.57471E-15
6153.75	8.27586E-16	6540.01	1.54310E-16
6153.66	8.12259E-16	6539.79	1.64655E-15
6153.56	8.04598E-16	6539.58	1.52012E-15
6153.47	7.68201E-16	6539.37	1.40230E-16
6153.37	7.70115E-16	6539.15	1.50287E-15
6153.28	7.27971E-16	6538.94	1.51724E-15
6153.18	7.56707E-16	6538.73	1.52586E-15
6153.09	7.54787E-16	6538.51	1.52299E-15
6152.99	7.79695E-16	6538.30	1.41667E-15
6152.90	7.64368E-16	6538.08	1.34483E-15
6152.80	8.21839E-16	6537.87	1.39943E-15
6152.71	8.25673E-16	6537.66	1.39655E-15
6152.62	8.46741E-16	6537.44	1.30460E-16
6152.52	8.08431E-16	6537.23	1.30460E-16
6152.43	7.58621E-16	6537.02	1.40517E-15
6152.33	7.20305E-16	6536.80	1.45977E-15
6152.24	6.89655E-16	6536.59	1.47414E-15
6152.14	7.73948E-16	6536.38	1.45977E-15
6152.05	8.23753E-16	6536.16	1.45402E-15
6151.95	8.67816E-16	6535.95	1.41092E-15
6151.86	8.14178E-16	6535.73	1.35632E-15
6151.76	7.50960E-17	6535.52	1.53161E-15
6151.67	7.18391E-16	6535.31	1.52012E-15
6151.57	7.22224E-16	6535.09	1.34770E-16
6151.48	7.79695E-16	6534.88	1.37644E-15
6151.39	8.02684E-16	6534.67	1.45115E-15
6151.29	7.81609E-16	6534.45	1.41954E-15
6151.20	7.49040E-17	6534.24	1.40517E-15
6151.10	7.18391E-16	6534.03	1.48563E-15
6151.01	7.77776E-16	6533.81	1.52874E-15
6150.91	8.10345E-16	6533.60	1.51149E-15
6150.82	8.27586E-16	6533.39	1.41092E-15
6150.72	7.60535E-16	6533.17	1.31322E-15

6150.63	7.08810E-17	6532.96	1.34483E-15
6150.53	6.74328E-16	6532.75	1.37069E-15
6150.44	6.78161E-16	6532.53	1.48276E-15
6150.35	7.47127E-16	6532.32	1.59195E-15
6150.25	7.66282E-16	6532.11	1.46552E-15
6150.16	7.77776E-16	6531.89	1.40230E-16
6150.06	7.41379E-16	6531.68	1.43104E-15
6149.97	8.00764E-16	6531.47	1.43678E-15
6149.87	8.23753E-16	6531.25	1.54885E-15
6149.78	8.39081E-16	6531.04	1.62356E-15
6149.68	8.02684E-16	6530.83	1.63218E-15
6149.59	8.12259E-16	6530.61	1.66379E-15
6149.49	7.96937E-16	6530.40	1.76437E-15
6149.40	7.87356E-16	6530.19	1.82184E-15
6149.31	8.14178E-16	6529.97	1.81322E-15
6149.21	8.14178E-16	6529.76	1.80747E-15
6149.12	7.79695E-16	6529.55	1.74138E-15
6149.02	7.47127E-16	6529.33	1.72989E-15
6148.93	7.60535E-16	6529.12	1.77012E-15
6148.83	8.06512E-16	6528.91	1.83908E-15
6148.74	7.70115E-16	6528.69	1.89655E-15
6148.64	7.58621E-16	6528.48	1.81897E-15
6148.55	7.20305E-16	6528.27	1.68104E-15
6148.45	7.29885E-16	6528.05	1.63506E-15
6148.36	7.75862E-16	6527.84	1.64081E-15
6148.27	7.87356E-16	6527.63	1.71839E-15
6148.17	8.27586E-16	6527.42	1.76724E-15
6148.08	7.98851E-16	6527.20	1.74713E-15
6147.98	8.37167E-16	6526.99	1.70402E-15
6147.89	7.83523E-16	6526.78	1.64943E-15
6147.79	7.79695E-16	6526.56	1.63506E-15
6147.70	7.66282E-16	6526.35	1.67241E-15
6147.60	8.19925E-16	6526.14	1.76724E-15
6147.51	8.37167E-16	6525.92	1.78736E-15
6147.42	8.46741E-16	6525.71	1.66092E-15
6147.32	8.23753E-16	6525.50	1.65517E-15
6147.23	7.98851E-16	6525.29	1.70977E-15
6147.13	7.98851E-16	6525.07	1.64943E-15
6147.04	7.98851E-16	6524.86	1.62356E-15
6146.94	8.12259E-16	6524.65	1.60058E-15
6146.85	8.02684E-16	6524.43	1.64943E-15
6146.75	8.40994E-16	6524.22	1.76724E-15
6146.66	8.71650E-17	6524.01	1.75287E-15
6146.56	8.08431E-16	6523.80	1.68966E-15
6146.47	7.72029E-16	6523.58	1.73851E-15
6146.38	7.73948E-16	6523.37	1.69540E-16
6146.28	8.60155E-16	6523.16	1.62356E-15
6146.19	8.98466E-16	6522.94	1.69253E-15
6146.09	9.09960E-17	6522.73	1.71552E-15
6146.00	8.90805E-16	6522.52	1.77299E-15
6145.90	8.50575E-16	6522.31	1.74425E-15
6145.81	8.16092E-16	6522.09	1.68966E-15
6145.71	8.33333E-16	6521.88	1.70402E-15

6145.62	8.96552E-16	6521.67	1.67816E-15
6145.53	9.19540E-17	6521.46	1.77586E-15
6145.43	8.79310E-17	6521.24	1.76724E-15
6145.34	8.23753E-16	6521.03	1.55172E-15
6145.24	8.14178E-16	6520.82	1.51724E-15
6145.15	8.54408E-16	6520.60	1.63793E-15
6145.05	8.75477E-16	6520.39	1.68966E-15
6144.96	8.58236E-16	6520.18	1.68678E-15
6144.87	8.46741E-16	6519.97	1.67816E-15
6144.77	8.29500E-18	6519.75	1.65805E-15
6144.68	8.29500E-18	6519.54	1.64655E-15
6144.58	8.81224E-16	6519.33	1.64943E-15
6144.49	8.65902E-16	6519.12	1.59770E-16
6144.39	8.73563E-16	6518.90	1.58046E-15
6144.30	8.75477E-16	6518.69	1.64081E-15
6144.20	9.38695E-16	6518.48	1.70977E-15
6144.11	9.17626E-16	6518.27	1.72701E-15
6144.02	8.56322E-16	6518.06	1.75575E-15
6143.92	8.00764E-16	6517.84	1.72701E-15
6143.83	8.19925E-16	6517.63	1.69253E-15
6143.73	8.75477E-16	6517.42	1.85345E-15
6143.64	8.98466E-16	6517.21	1.93391E-15
6143.54	8.92718E-16	6516.99	1.88506E-15
6143.45	8.37167E-16	6516.78	1.92816E-15
6143.35	8.63983E-16	6516.57	2.01149E-15
6143.26	8.40994E-16	6516.36	2.04598E-15
6143.17	9.13793E-16	6516.14	2.01437E-15
6143.07	8.58236E-16	6515.93	1.97126E-15
6142.98	9.52109E-16	6515.72	1.91667E-15
6142.88	8.48661E-16	6515.51	1.92816E-15
6142.79	8.35247E-16	6515.29	1.95977E-15
6142.69	7.79695E-16	6515.08	1.86782E-15
6142.60	8.67816E-16	6514.87	1.84195E-15
6142.51	9.31035E-16	6514.66	1.93678E-15
6142.41	9.75098E-16	6514.45	1.86782E-15
6142.32	9.27201E-16	6514.23	1.75287E-15
6142.22	8.92718E-16	6514.02	1.70690E-16
6142.13	8.37167E-16	6513.81	1.70977E-15
6142.03	8.25673E-16	6513.60	1.72126E-15
6141.94	8.62069E-16	6513.38	1.68104E-15
6141.85	9.09960E-17	6513.17	1.71264E-15
6141.75	9.40615E-16	6512.96	1.78448E-15
6141.66	9.31035E-16	6512.75	1.72701E-15
6141.56	9.13793E-16	6512.54	1.79598E-15
6141.47	9.11879E-16	6512.32	1.96839E-15
6141.37	8.81224E-16	6512.11	2.08046E-15
6141.28	8.83144E-16	6511.90	2.35920E-16
6141.19	8.42914E-16	6511.69	2.79598E-15
6141.09	8.58236E-16	6511.48	3.48851E-15
6141.00	9.06132E-16	6511.26	4.32759E-15
6140.90	9.63604E-16	6511.05	4.79023E-15
6140.81	1.00000E-20	6510.84	4.85632E-15
6140.71	9.82759E-16	6510.63	4.87931E-15

6140.62	9.55937E-16	6510.42	4.73276E-15
6140.53	9.17626E-16	6510.20	4.52586E-15
6140.43	9.48276E-16	6509.99	4.32759E-15
6140.34	9.94253E-16	6509.78	4.05747E-15
6140.24	1.03257E-15	6509.57	3.85345E-15
6140.15	9.50190E-17	6509.36	3.67241E-15
6140.05	9.54023E-16	6509.15	3.38506E-15
6139.96	9.09960E-17	6508.93	3.12069E-15
6139.87	8.92718E-16	6508.72	2.98851E-15
6139.77	8.39081E-16	6508.51	2.85920E-16
6139.68	8.60155E-16	6508.30	2.80172E-15
6139.58	8.65902E-16	6508.09	2.77012E-15
6139.49	8.75477E-16	6507.87	2.63218E-15
6139.40	8.77397E-16	6507.66	2.47414E-15
6139.30	8.69730E-17	6507.45	2.39081E-15
6139.21	8.27586E-16	6507.24	2.24713E-15
6139.11	8.02684E-16	6507.03	2.20977E-15
6139.02	8.21839E-16	6506.82	2.16092E-15
6138.92	8.62069E-16	6506.60	2.06609E-15
6138.83	8.67816E-16	6506.39	2.07759E-15
6138.74	8.37167E-16	6506.18	1.95690E-16
6138.64	8.23753E-16	6505.97	1.82184E-15
6138.55	8.10345E-16	6505.76	1.80460E-16
6138.45	8.12259E-16	6505.55	1.81322E-15
6138.36	8.06512E-16	6505.33	1.77299E-15
6138.26	8.29500E-18	6505.12	1.83908E-15
6138.17	8.54408E-16	6504.91	1.84195E-15
6138.08	8.62069E-16	6504.70	1.66954E-15
6137.98	9.17626E-16	6504.49	1.77299E-15
6137.89	9.63604E-16	6504.28	1.84770E-16
6137.79	1.02682E-15	6504.06	1.77299E-15
6137.70	9.50190E-17	6503.85	1.81322E-15
6137.60	9.06132E-16	6503.64	1.76724E-15
6137.51	8.69730E-17	6503.43	1.64081E-15
6137.42	9.29121E-16	6503.22	1.72989E-15
6137.32	9.44443E-16	6503.01	1.78736E-15
6137.23	9.00385E-16	6502.80	1.77299E-15
6137.13	9.15707E-16	6502.58	1.77012E-15
6137.04	9.19540E-17	6502.37	1.80172E-15
6136.95	9.25287E-16	6502.16	1.83908E-15
6136.85	8.52489E-16	6501.95	1.83046E-15
6136.76	8.29500E-18	6501.74	1.91667E-15
6136.66	8.62069E-16	6501.53	1.82471E-15
6136.57	8.33333E-16	6501.32	1.86207E-15
6136.48	8.39081E-16	6501.10	1.89655E-15
6136.38	8.40994E-16	6500.89	1.79310E-16
6136.29	8.79310E-17	6500.68	1.85345E-15
6136.19	8.50575E-16	6500.47	1.88218E-15
6136.10	7.98851E-16	6500.26	1.84770E-16
6136.00	8.39081E-16	6500.05	1.86207E-15
6135.91	8.10345E-16	6499.84	1.96264E-15
6135.82	8.69730E-17	6499.63	1.96839E-15
6135.72	8.31420E-17	6499.42	1.91954E-15

6135.63	8.58236E-16	6499.20	2.10632E-15
6135.53	7.93104E-16	6498.99	2.31322E-15
6135.44	7.83523E-16	6498.78	2.56897E-15
6135.35	7.98851E-16	6498.57	2.84770E-16
6135.25	8.27586E-16	6498.36	2.99713E-15
6135.16	8.35247E-16	6498.15	3.18678E-15
6135.06	8.60155E-16	6497.94	3.25287E-15
6134.97	8.65902E-16	6497.73	3.08908E-15
6134.88	8.54408E-16	6497.51	3.01437E-15
6134.78	8.27586E-16	6497.30	2.89943E-15
6134.69	8.08431E-16	6497.09	2.75287E-15
6134.59	8.62069E-16	6496.88	2.68104E-15
6134.50	8.85058E-16	6496.67	2.54023E-15
6134.40	9.34868E-16	6496.46	2.39655E-15
6134.31	8.98466E-16	6496.25	2.32759E-15
6134.22	8.92718E-16	6496.04	2.24425E-15
6134.12	8.75477E-16	6495.83	2.12356E-15
6134.03	8.81224E-16	6495.62	2.06609E-15
6133.93	9.11879E-16	6495.40	2.00287E-15
6133.84	9.32948E-16	6495.19	1.99425E-15
6133.75	9.65517E-16	6494.98	1.93966E-15
6133.65	8.77397E-16	6494.77	1.84770E-16
6133.56	8.52489E-16	6494.56	1.67816E-15
6133.46	8.37167E-16	6494.35	1.62644E-15
6133.37	9.15707E-16	6494.14	1.72126E-15
6133.28	9.52109E-16	6493.93	1.64368E-15
6133.18	9.25287E-16	6493.72	1.62069E-15
6133.09	8.85058E-16	6493.51	1.63793E-15
6132.99	8.52489E-16	6493.30	1.62069E-15
6132.90	8.85058E-16	6493.08	1.65230E-16
6132.81	9.25287E-16	6492.87	1.57759E-15
6132.71	9.17626E-16	6492.66	1.55172E-15
6132.62	8.85058E-16	6492.45	1.56609E-15
6132.52	8.96552E-16	6492.24	1.59483E-15
6132.43	8.65902E-16	6492.03	1.58908E-15
6132.34	8.86971E-16	6491.82	1.55172E-15
6132.24	8.48661E-16	6491.61	1.53736E-15
6132.15	8.50575E-16	6491.40	1.54598E-15
6132.05	8.35247E-16	6491.19	1.58621E-15
6131.96	8.37167E-16	6490.98	1.60345E-15
6131.87	9.11879E-16	6490.77	1.56609E-15
6131.77	9.11879E-16	6490.56	1.51149E-15
6131.68	9.27201E-16	6490.35	1.51724E-15
6131.58	8.37167E-16	6490.13	1.44828E-15
6131.49	8.44828E-16	6489.92	1.46839E-15
6131.40	8.21839E-16	6489.71	1.58908E-15
6131.30	8.96552E-16	6489.50	1.51149E-15
6131.21	8.50575E-16	6489.29	1.40805E-15
6131.11	8.71650E-17	6489.08	1.41954E-15
6131.02	8.96552E-16	6488.87	1.41379E-15
6130.93	8.96552E-16	6488.66	1.41667E-15
6130.83	8.85058E-16	6488.45	1.39655E-15
6130.74	8.19925E-16	6488.24	1.41667E-15

6130.64	8.14178E-16	6488.03	1.41667E-15
6130.55	8.58236E-16	6487.82	1.42816E-15
6130.46	8.35247E-16	6487.61	1.51724E-15
6130.36	9.06132E-16	6487.40	1.60632E-15
6130.27	8.14178E-16	6487.19	1.66954E-15
6130.17	8.18006E-16	6486.98	1.67241E-15
6130.08	7.77776E-16	6486.77	1.77874E-15
6129.99	8.67816E-16	6486.56	1.77299E-15
6129.89	8.65902E-16	6486.35	1.72989E-15
6129.80	8.58236E-16	6486.14	1.72414E-15
6129.70	8.21839E-16	6485.93	1.64943E-15
6129.61	8.65902E-16	6485.72	1.66954E-15
6129.52	9.17626E-16	6485.50	1.64081E-15
6129.42	9.78925E-16	6485.29	1.67241E-15
6129.33	9.94253E-16	6485.08	1.70115E-15
6129.23	9.44443E-16	6484.87	1.73563E-15
6129.14	9.48276E-16	6484.66	1.84195E-15
6129.05	9.27201E-16	6484.45	1.84770E-16
6128.95	9.11879E-16	6484.24	1.83908E-15
6128.86	9.11879E-16	6484.03	1.74713E-15
6128.77	9.50190E-17	6483.82	1.72414E-15
6128.67	1.01916E-15	6483.61	1.72126E-15
6128.58	9.98086E-16	6483.40	1.64655E-15
6128.48	1.01341E-15	6483.19	1.60920E-16
6128.39	1.08237E-15	6482.98	1.47126E-15
6128.30	1.05172E-15	6482.77	1.37931E-15
6128.20	1.07280E-16	6482.56	1.39943E-15
6128.11	1.01916E-15	6482.35	1.42816E-15
6128.01	1.02682E-15	6482.14	1.35058E-15
6127.92	9.48276E-16	6481.93	1.36207E-15
6127.83	9.09960E-17	6481.72	1.35345E-15
6127.73	9.40615E-16	6481.51	1.29310E-16
6127.64	9.88506E-16	6481.30	1.33621E-15
6127.54	1.04214E-15	6481.09	1.37644E-15
6127.45	1.05364E-15	6480.88	1.37356E-15
6127.36	1.09770E-16	6480.67	1.32471E-15
6127.26	1.11303E-15	6480.46	1.25575E-15
6127.17	1.08429E-15	6480.25	1.14655E-15
6127.08	1.06322E-15	6480.04	1.12356E-15
6126.98	1.01724E-15	6479.83	1.13793E-15
6126.89	9.98086E-16	6479.62	1.21264E-15
6126.79	1.00000E-20	6479.41	1.22989E-15
6126.70	1.07280E-16	6479.20	1.25287E-15
6126.61	1.08237E-15	6478.99	1.31035E-15
6126.51	9.69351E-16	6478.78	1.20977E-15
6126.42	8.23753E-16	6478.57	1.14368E-15
6126.32	7.96937E-16	6478.36	1.20402E-15
6126.23	8.67816E-16	6478.15	1.19540E-16
6126.14	9.65517E-16	6477.94	1.12931E-15
6126.04	9.78925E-16	6477.73	1.13793E-15
6125.95	9.50190E-17	6477.52	1.12356E-15
6125.86	9.17626E-16	6477.31	1.11782E-15
6125.76	9.02299E-16	6477.10	1.17529E-15

6125.67	9.67431E-16	6476.89	1.22701E-15
6125.57	9.44443E-16	6476.68	1.20402E-15
6125.48	9.67431E-16	6476.47	1.20402E-15
6125.39	9.11879E-16	6476.26	1.13793E-15
6125.29	9.48276E-16	6476.05	1.07471E-15
6125.20	9.17626E-16	6475.85	1.20690E-16
6125.11	9.29121E-16	6475.64	1.19540E-16
6125.01	9.13793E-16	6475.43	1.10632E-15
6124.92	8.75477E-16	6475.22	1.13506E-15
6124.82	8.60155E-16	6475.01	1.15230E-16
6124.73	8.14178E-16	6474.80	1.08046E-15
6124.64	9.08046E-16	6474.59	1.03448E-15
6124.54	8.86971E-16	6474.38	1.09483E-15
6124.45	9.04213E-16	6474.17	1.08333E-15
6124.35	8.54408E-16	6473.96	1.01437E-15
6124.26	8.44828E-16	6473.75	9.97127E-16
6124.17	9.69351E-16	6473.54	1.07184E-15
6124.07	1.03257E-15	6473.33	1.04310E-16
6123.98	1.03640E-16	6473.12	9.28161E-16
6123.89	9.42529E-16	6472.91	9.59770E-17
6123.79	8.98466E-16	6472.70	9.25287E-16
6123.70	8.65902E-16	6472.49	8.67816E-16
6123.60	8.75477E-16	6472.28	9.88506E-16
6123.51	8.23753E-16	6472.07	1.01724E-15
6123.42	8.79310E-17	6471.86	9.59770E-17
6123.32	8.44828E-16	6471.65	1.00000E-20
6123.23	9.50190E-17	6471.44	9.36782E-16
6123.14	8.98466E-16	6471.24	8.33333E-16
6123.04	9.15707E-16	6471.03	8.18966E-16
6122.95	8.69730E-17	6470.82	8.44828E-16
6122.85	9.25287E-16	6470.61	8.21839E-16
6122.76	8.75477E-16	6470.40	8.76437E-16
6122.67	8.62069E-16	6470.19	8.76437E-16
6122.57	8.88891E-16	6469.98	7.78736E-16
6122.48	1.00766E-15	6469.77	8.30460E-17
6122.39	1.12835E-15	6469.56	8.59196E-16
6122.29	1.20115E-15	6469.35	9.05172E-16
6122.20	1.19157E-15	6469.14	9.05172E-16
6122.11	1.19732E-15	6468.93	9.33908E-16
6122.01	1.18966E-15	6468.72	8.96552E-16
6121.92	1.31993E-15	6468.51	8.44828E-16
6121.82	1.28927E-15	6468.31	7.90230E-17
6121.73	1.40805E-15	6468.10	8.10345E-16
6121.64	1.63602E-15	6467.89	9.54023E-16
6121.54	2.05939E-15	6467.68	9.08046E-16
6121.45	2.52108E-15	6467.47	9.25287E-16
6121.36	2.84674E-15	6467.26	1.03736E-15
6121.26	3.18200E-17	6467.05	1.08908E-15
6121.17	3.21839E-15	6466.84	1.01149E-15
6121.07	3.21839E-15	6466.63	9.82759E-16
6120.98	3.04214E-15	6466.42	1.07759E-15
6120.89	3.01149E-15	6466.21	1.10920E-16
6120.79	2.93295E-15	6466.00	1.07471E-15

6120.70	2.80843E-15	6465.80	1.07184E-15
6120.61	2.68966E-15	6465.59	1.02874E-15
6120.51	2.48276E-15	6465.38	1.02874E-15
6120.42	2.32950E-16	6465.17	1.03448E-15
6120.33	2.17433E-15	6464.96	9.85632E-16
6120.23	2.03065E-15	6464.75	9.16667E-16
6120.14	2.01916E-15	6464.54	8.27586E-16
6120.04	1.92337E-15	6464.33	8.33333E-16
6119.95	1.82950E-16	6464.12	8.01724E-16
6119.86	1.69540E-16	6463.92	7.18391E-16
6119.76	1.59579E-15	6463.71	7.18391E-16
6119.67	1.66092E-15	6463.50	7.35632E-16
6119.58	1.61878E-15	6463.29	7.35632E-16
6119.48	1.57663E-15	6463.08	7.72989E-16
6119.39	1.51341E-15	6462.87	7.55747E-16
6119.30	1.41379E-15	6462.66	7.18391E-16
6119.20	1.36016E-15	6462.45	7.24138E-16
6119.11	1.22031E-15	6462.24	6.89655E-16
6119.01	1.22222E-15	6462.04	7.32759E-16
6118.92	1.14751E-15	6461.83	6.89943E-16
6118.83	1.15517E-15	6461.62	6.00862E-16
6118.73	1.11303E-15	6461.41	6.32184E-16
6118.64	1.11878E-15	6461.20	6.81035E-16
6118.55	1.11494E-15	6460.99	7.12644E-16
6118.45	1.10536E-15	6460.78	6.37931E-16
6118.36	1.08046E-15	6460.57	6.03448E-16
6118.27	1.05939E-15	6460.37	7.01150E-17
6118.17	1.09195E-15	6460.16	7.52874E-16
6118.08	1.18966E-15	6459.95	7.38506E-16
6117.99	1.14176E-15	6459.74	7.01150E-17
6117.89	1.05172E-15	6459.53	6.98276E-16
6117.80	9.00385E-16	6459.32	7.12644E-16
6117.70	9.42529E-16	6459.11	6.86782E-16
6117.61	9.77012E-16	6458.91	6.72414E-16
6117.52	9.84672E-16	6458.70	7.47127E-16
6117.42	9.40615E-16	6458.49	7.35632E-16
6117.33	9.00385E-16	6458.28	6.63793E-16
6117.24	8.96552E-16	6458.07	7.15517E-16
6117.14	8.65902E-16	6457.86	6.34770E-17
6117.05	8.96552E-16	6457.65	6.00287E-16
6116.96	9.31035E-16	6457.45	6.86782E-16
6116.86	9.77012E-16	6457.24	6.78161E-16
6116.77	9.94253E-16	6457.03	6.81035E-16
6116.68	1.09579E-15	6456.82	6.55172E-16
6116.58	1.07663E-15	6456.61	5.97701E-16
6116.49	1.08237E-15	6456.40	5.72414E-16
6116.40	1.00383E-15	6456.19	5.36782E-16
6116.30	1.03448E-15	6455.99	5.62069E-16
6116.21	9.73178E-16	6455.78	6.09195E-16
6116.11	1.00766E-15	6455.57	6.23563E-16
6116.02	9.36782E-16	6455.36	5.77299E-16
6115.93	9.42529E-16	6455.15	5.68678E-16
6115.83	8.96552E-16	6454.94	6.06322E-16

6115.74	9.31035E-16	6454.74	6.58046E-16
6115.65	9.23374E-16	6454.53	6.21264E-16
6115.55	9.36782E-16	6454.32	6.06897E-16
6115.46	9.63604E-16	6454.11	6.26437E-16
6115.37	9.55937E-16	6453.90	6.17816E-16
6115.27	9.21454E-16	6453.69	6.98276E-16
6115.18	8.83144E-16	6453.49	6.27586E-16
6115.09	9.46362E-16	6453.28	5.78736E-16
6114.99	9.73178E-16	6453.07	7.09770E-17
6114.90	9.88506E-16	6452.86	7.04023E-16
6114.81	9.61684E-16	6452.65	6.81035E-16
6114.71	9.61684E-16	6452.45	7.18391E-16
6114.62	9.04213E-16	6452.24	6.66667E-16
6114.52	9.42529E-16	6452.03	6.32184E-16
6114.43	8.35247E-16	6451.82	6.35058E-16
6114.34	9.02299E-16	6451.61	5.97701E-16
6114.24	8.56322E-16	6451.40	5.74713E-16
6114.15	8.88891E-16	6451.20	5.20690E-17
6114.06	8.77397E-16	6450.99	5.60920E-17
6113.96	8.96552E-16	6450.78	5.83908E-16
6113.87	9.61684E-16	6450.57	5.72414E-16
6113.78	9.46362E-16	6450.36	6.20690E-17
6113.68	9.75098E-16	6450.16	5.65517E-16
6113.59	9.38695E-16	6449.95	5.79885E-16
6113.50	9.71264E-16	6449.74	6.03448E-16
6113.40	9.46362E-16	6449.53	5.63506E-16
6113.31	9.75098E-16	6449.32	6.66954E-16
6113.22	9.88506E-16	6449.12	6.17816E-16
6113.12	1.02299E-15	6448.91	4.76150E-17
6113.03	1.06322E-15	6448.70	5.27012E-16
6112.94	1.03257E-15	6448.49	5.88218E-16
6112.84	9.63604E-16	6448.28	5.63506E-16
6112.75	9.32948E-16	6448.08	5.14655E-16
6112.66	9.29121E-16	6447.87	6.17816E-16
6112.56	9.46362E-16	6447.66	6.46552E-16
6112.47	9.38695E-16	6447.45	5.06035E-16
6112.38	9.17626E-16	6447.25	4.96264E-16
6112.28	9.82759E-16	6447.04	6.02299E-16
6112.19	9.59770E-17	6446.83	5.60058E-16
6112.10	9.31035E-16	6446.62	5.62931E-16
6112.00	8.81224E-16	6446.41	5.66954E-16
6111.91	9.02299E-16	6446.21	5.07471E-16
6111.82	9.54023E-16	6446.00	5.07759E-16
6111.72	9.54023E-16	6445.79	5.52874E-16
6111.63	9.04213E-16	6445.58	6.60920E-17
6111.54	9.63604E-16	6445.38	6.46552E-16
6111.44	9.31035E-16	6445.17	5.91954E-16
6111.35	1.02108E-15	6444.96	5.41092E-16
6111.26	9.84672E-16	6444.75	4.99713E-16
6111.16	1.05172E-15	6444.54	5.09483E-16
6111.07	1.03832E-15	6444.34	5.31035E-16
6110.98	1.05556E-15	6444.13	5.08046E-16
6110.88	1.09962E-15	6443.92	5.30747E-16

6110.79	1.08046E-15	6443.71	5.85058E-16
6110.70	1.05939E-15	6443.51	5.28448E-16
6110.60	1.07088E-15	6443.30	4.99138E-16
6110.51	1.05364E-15	6443.09	5.25287E-16
6110.42	1.20498E-15	6442.88	5.58621E-16
6110.32	1.18774E-15	6442.68	6.09195E-16
6110.23	1.36398E-15	6442.47	5.45977E-16
6110.14	1.29119E-15	6442.26	4.24425E-16
6110.04	1.24713E-15	6442.05	3.94540E-17
6109.95	1.15709E-15	6441.85	4.39655E-16
6109.85	1.15709E-15	6441.64	5.20977E-16
6109.76	1.18199E-15	6441.43	5.56897E-16
6109.67	1.22605E-15	6441.22	5.36782E-16
6109.58	1.39272E-15	6441.02	5.65805E-16
6109.48	1.50766E-15	6440.81	6.23563E-16
6109.39	1.71073E-15	6440.60	5.31322E-16
6109.30	1.71264E-15	6440.39	4.56897E-16
6109.20	1.87165E-15	6440.19	4.66379E-16
6109.11	1.92337E-15	6439.98	4.96264E-16
6109.02	2.05556E-15	6439.77	4.75862E-16
6108.92	2.16283E-15	6439.56	5.34770E-17
6108.83	2.24713E-15	6439.36	5.31322E-16
6108.74	2.23755E-15	6439.15	3.65230E-17
6108.64	2.13985E-15	6438.94	4.38506E-16
6108.55	1.96743E-15	6438.74	5.72989E-16
6108.46	1.85249E-15	6438.53	5.71839E-16
6108.36	1.70306E-15	6438.32	5.36494E-16
6108.27	1.65326E-15	6438.11	5.29023E-16
6108.18	1.50958E-15	6437.91	4.88506E-16
6108.08	1.43487E-15	6437.70	4.77874E-16
6107.99	1.31418E-15	6437.49	5.07471E-16
6107.90	1.28927E-15	6437.28	5.37644E-16
6107.80	1.24713E-15	6437.08	5.31322E-16
6107.71	1.23755E-15	6436.87	4.99138E-16
6107.62	1.25479E-15	6436.66	5.63218E-16
6107.52	1.20881E-15	6436.46	5.36207E-16
6107.43	1.18199E-15	6436.25	4.73851E-16
6107.34	1.16667E-15	6436.04	4.52586E-16
6107.24	1.26245E-15	6435.83	3.76724E-16
6107.15	1.31418E-15	6435.63	4.68104E-16
6107.06	1.24713E-15	6435.42	5.35058E-16
6106.96	1.10920E-16	6435.21	5.07759E-16
6106.87	1.04598E-15	6435.01	5.19253E-16
6106.78	1.12069E-15	6434.80	4.48276E-16
6106.68	1.16667E-15	6434.59	3.91092E-16
6106.59	1.19732E-15	6434.39	4.50000E-21
6106.50	1.08429E-15	6434.18	6.01437E-16
6106.40	1.10345E-15	6433.97	6.22414E-16
6106.31	1.00766E-15	6433.76	5.55172E-16
6106.22	1.04789E-15	6433.56	5.17241E-16
6106.12	1.04981E-15	6433.35	5.38506E-16
6106.03	1.05172E-15	6433.14	4.85345E-16
6105.94	1.06513E-15	6432.94	4.26437E-16

6105.84	1.05172E-15	6432.73	4.77586E-16
6105.75	1.18008E-15	6432.52	4.66092E-16
6105.66	1.21839E-15	6432.32	5.27299E-16
6105.57	1.10920E-16	6432.11	5.89081E-16
6105.47	1.02490E-16	6431.90	4.96264E-16
6105.38	1.01341E-15	6431.70	4.84195E-16
6105.29	1.11303E-15	6431.49	5.65230E-17
6105.19	1.14559E-15	6431.28	5.88793E-16
6105.10	1.04981E-15	6431.08	5.43103E-16
6105.01	1.02874E-15	6430.87	4.87931E-16
6104.91	9.82759E-16	6430.66	5.09483E-16
6104.82	1.02299E-15	6430.45	5.22701E-16
6104.73	1.08237E-15	6430.25	5.43391E-16
6104.63	1.04598E-15	6430.04	5.10058E-16
6104.54	9.86592E-16	6429.83	4.91379E-16
6104.45	9.40615E-16	6429.63	5.10920E-17
6104.35	9.42529E-16	6429.42	4.97414E-16
6104.26	9.32948E-16	6429.21	4.73851E-16
6104.17	8.25673E-16	6429.01	3.75862E-16
6104.07	9.02299E-16	6428.80	3.75575E-16
6103.98	8.90805E-16	6428.59	5.20977E-16
6103.89	1.06897E-15	6428.39	5.89081E-16
6103.79	9.86592E-16	6428.18	4.56035E-16
6103.70	1.03065E-15	6427.97	4.12069E-16
6103.61	8.58236E-16	6427.77	4.20402E-16
6103.52	8.33333E-16	6427.56	4.14943E-16
6103.42	8.54408E-16	6427.35	4.49138E-16
6103.33	9.02299E-16	6427.15	3.78736E-16
6103.24	9.19540E-17	6426.94	4.52874E-16
6103.14	9.31035E-16	6426.74	4.87931E-16
6103.05	9.67431E-16	6426.53	4.41667E-16
6102.96	9.23374E-16	6426.32	3.89943E-16
6102.86	8.50575E-16	6426.12	3.73276E-16
6102.77	9.23374E-16	6425.91	4.39368E-16
6102.68	9.75098E-16	6425.70	3.82759E-16
6102.58	1.02299E-15	6425.50	3.64655E-16
6102.49	9.04213E-16	6425.29	3.37356E-16
6102.40	8.75477E-16	6425.08	3.18391E-16
6102.31	9.02299E-16	6424.88	3.92529E-16
6102.21	9.21454E-16	6424.67	4.47414E-16
6102.12	9.34868E-16	6424.46	5.36494E-16
6102.03	8.75477E-16	6424.26	4.76724E-16
6101.93	9.40615E-16	6424.05	4.49713E-16
6101.84	9.15707E-16	6423.85	4.31897E-16
6101.75	1.02108E-15	6423.64	4.32471E-16
6101.65	9.25287E-16	6423.43	5.18966E-16
6101.56	1.07088E-15	6423.23	5.29598E-16
6101.47	1.03257E-15	6423.02	5.06035E-16
6101.37	1.04789E-15	6422.81	4.67241E-16
6101.28	9.17626E-16	6422.61	5.06322E-16
6101.19	9.27201E-16	6422.40	5.38793E-16
6101.10	9.77012E-16	6422.20	5.28736E-16
6101.00	1.01724E-15	6421.99	5.85345E-16

6100.91	1.02682E-15	6421.78	5.19540E-17
6100.82	1.13985E-15	6421.58	3.54598E-16
6100.72	1.11111E-15	6421.37	3.60632E-16
6100.63	1.17050E-16	6421.16	4.67529E-16
6100.54	1.07088E-15	6420.96	4.92241E-16
6100.44	1.16667E-15	6420.75	4.43678E-16
6100.35	1.13793E-15	6420.55	4.46839E-16
6100.26	1.21264E-15	6420.34	3.96552E-16
6100.16	1.22797E-15	6420.13	4.08333E-16
6100.07	1.25479E-15	6419.93	4.05173E-16
6099.98	1.19924E-15	6419.72	3.46552E-16
6099.89	1.19732E-15		
6099.79	1.22989E-15		
6099.70	1.22797E-15		
6099.61	1.20881E-15		
6099.51	1.16858E-15		
6099.42	1.11111E-15		
6099.33	1.10154E-15		
6099.23	1.07280E-16		
6099.14	1.16475E-15		
6099.05	1.18008E-15		
6098.96	1.11303E-15		
6098.86	1.03448E-15		
6098.77	1.00766E-15		
6098.68	9.78925E-16		
6098.58	1.02682E-15		
6098.49	1.02874E-15		
6098.40	1.10345E-15		
6098.30	1.05172E-15		
6098.21	1.01916E-15		
6098.12	9.52109E-16		
6098.03	9.31035E-16		
6097.93	9.34868E-16		
6097.84	9.34868E-16		
6097.75	1.01341E-15		
6097.65	1.06513E-15		
6097.56	1.20115E-15		
6097.47	1.32375E-15		
6097.38	1.37548E-15		
6097.28	1.39655E-15		
6097.19	1.39847E-15		
6097.10	1.37740E-16		
6097.00	1.32950E-16		
6096.91	1.23947E-15		
6096.82	1.33717E-15		
6096.72	1.37356E-15		
6096.63	1.39847E-15		
6096.54	1.33142E-15		
6096.45	1.25287E-15		
6096.35	1.17816E-15		
6096.26	1.18008E-15		
6096.17	1.15326E-15		
6096.07	1.12069E-15		

6095.98	1.06131E-15
6095.89	1.03832E-15
6095.80	1.03448E-15
6095.70	9.92339E-16
6095.61	1.03640E-16
6095.52	1.00958E-15
6095.42	1.07471E-15
6095.33	1.05939E-15
6095.24	1.08621E-15
6095.15	9.34868E-16
6095.05	9.23374E-16
6094.96	8.54408E-16
6094.87	8.96552E-16
6094.77	7.73948E-16
6094.68	8.04598E-16
6094.59	7.06897E-16
6094.50	8.31420E-17
6094.40	8.18006E-16
6094.31	9.82759E-16
6094.22	9.21454E-16
6094.12	9.78925E-16
6094.03	9.10920E-17
6093.94	1.00000E-20

B Anhänge gemäß Prüfungsordnung

B.1 Own contribution

All four publications that formed the basis of this thesis include an author contribution section. For a simpler accessibility, they are copied to the list below.

1) Novelli, A., Kaminski, M., **Rolletter, M.**, Acir, I. H., Bohn, B., Dorn, H. P., Li, X., Lutz, A., Nehr, S., Rohrer, F., Tillmann, R., Wegener, R., Holland, F., Hofzumahaus, A., Kiendler-Scharr, A., Wahner, A., and Fuchs, H.: Evaluation of OH and HO_2 concentrations and their budgets during photooxidation of 2-methyl-3-butene-2-ol (MBO) in the atmospheric simulation chamber SAPHIR, Atmos. Chem. Phys., 18, 11409-11422, 10.5194/acp-18-11409-2018, 2018.

   HF and AH designed the experiments. HF conducted the HO_x radical measurements and SN was responsible for the OH reactivity measurements. BB conducted the radiation measurements. MK and RW were responsible for the GC measurements. RT, AL, and IHA were responsible for the PTR-MS measurements. XL was responsible for the HONO measurements and HPD for the DOAS OH data. FR was responsible for the NO_x and O_3 data. MR helped with the model. AN analysed the data and wrote the paper with the help of HF, FH, BB, AH, AKS, and AW.

2) **Rolletter, M.**, Kaminski, M., Acir, I. H., Bohn, B., Dorn, H. P., Li, X., Lutz, A., Nehr, S., Rohrer, F., Tillmann, R., Wegener, R., Hofzumahaus, A., Kiendler-Scharr, A., Wahner, A., and Fuchs, H.: Investigation of the α-pinene photooxidation by OH in the atmospheric simulation chamber SAPHIR, Atmos. Chem. Phys., 19, 11635-11649, 10.5194/acp-19-11635-2019, 2019.

   MR analyzed the data and wrote the paper. HF and MK designed the experiments. HF conducted the HO_x radical measurements and SN was responsible for the OH reactivity measurements. BB conducted the radiation measurements. MK and RW were responsible for the GC measurements. RT, AL, and IHA were responsible for the PTR-TOF-MS measurements. XL was responsible for the HONO measurements and HPD for the DOAS OH data. FR was responsible for the NO_x and O_3 data. All co-authors commented on the paper.

3) **Rolletter, M.**, Blocquet, M., Kaminski, M., Bohn, B., Dorn, H. P., Hofzumahaus, A., Holland, F., Li, X., Rohrer, F., Tillmann, R., Wegener, R., Kiendler-Scharr, A., Wahner, A., and Fuchs, H.: Photooxidation of pinonaldehyde at ambient conditions investigated in the atmospheric simulation chamber SAPHIR, Atmos. Chem. Phys., 20, 13701-13719, 10.5194/acp-20-13701-2020, 2020.

   MR analysed the data and wrote the paper. HF and MK designed the experiments. HF conducted the HO_x radical measurements. BB conducted the radiation measurements. MK and RW were responsible for the GC measurements. RT was responsible forthe PTR-TOF-MS measurements. XL was responsible for the HONO measurements and HPD for the DOAS OH data. FR was responsible for the NO_x and O_3 data. All co-authors commented on the manuscript.

4) **Rolletter, M.**, Assaf, E., Fuchs, H., and Fittschen, C.: The Absorption Spectrum and absolute Absorption Cross Sections of Acetylperoxy Radicals, $CH_3C(O)O_2$ in the near IR, J. Quant. Spectrosc. Radiat. Transf., 245, 106877, 10.1016/j.jqsrt.2020.106877, 2020.

   Michael Rolletter: Data curation, Writing - original draft. Emmanuel Assaf: Investigation, Data curation, Resources. Mohamed Assali: Investigation, Data curation. Hendrik Fuchs: Conceptualization, Writing - review & editing, Supervision, Funding acquisition. Christa Fittschen: Conceptualization, Writing - original draft, Supervision, Project administration, Funding acquisition.

B.2 Erklärung zur Dissertation

Ich versichere, dass ich die von mir vorgelegte Dissertation selbständig angefertigt, die benutzten Quellen und Hilfsmittel vollständig angegeben und die Stellen der Arbeit – einschließlich Tabellen, Karten und Abbildungen –, die anderen Werken im Wortlaut oder dem Sinn nach entnommen sind, in jedem Einzelfall als Entlehnung kenntlich gemacht habe; dass diese Dissertation noch keiner anderen Fakultät oder Universität zur Prüfung vorgelegen hat; dass sie – abgesehen von unten angegebenen Teilpublikationen – noch nicht veröffentlicht worden ist, sowie, dass ich eine solche Veröffentlichung vor Abschluss des Promotionsverfahrens nicht vornehmen werde.
Die Bestimmungen der Promotionsordnung sind mir bekannt. Die von mir vorgelegte Dissertation ist von PD Dr. Andreas Hofzumahaus betreut worden.

Köln, den 19.05.2021

Michael Rolletter

Teilpublikationen:

1) Novelli, A., Kaminski, M., **Rolletter, M.**, Acir, I. H., Bohn, B., Dorn, H. P., Li, X., Lutz, A., Nehr, S., Rohrer, F., Tillmann, R., Wegener, R., Holland, F., Hofzumahaus, A., Kiendler-Scharr, A., Wahner, A., and Fuchs, H.: Evaluation of OH and HO_2 concentrations and their budgets during photooxidation of 2-methyl-3-butene-2-ol (MBO) in the atmospheric simulation chamber SAPHIR, Atmos. Chem. Phys., 18, 11409-11422, DOI: 10.5194/acp-18-11409-2018, 2018.

2) **Rolletter, M.**, Kaminski, M., Acir, I. H., Bohn, B., Dorn, H. P., Li, X., Lutz, A., Nehr, S., Rohrer, F., Tillmann, R., Wegener, R., Hofzumahaus, A., Kiendler-Scharr, A., Wahner, A., and Fuchs, H.: Investigation of the α-pinene photooxidation by OH in the atmospheric simulation chamber SAPHIR, Atmos. Chem. Phys., 19, 11635-11649, DOI: 10.5194/acp-19-11635-2019, 2019.

3) **Rolletter, M.**, Blocquet, M., Kaminski, M., Bohn, B., Dorn, H. P., Hofzumahaus, A., Holland, F., Li, X., Rohrer, F., Tillmann, R., Wegener, R., Kiendler-Scharr, A., Wahner, A., and Fuchs, H.: Photooxidation of pinonaldehyde at ambient conditions investigated in the atmospheric simulation chamber SAPHIR, Atmos. Chem. Phys., 20, 13701-13719, DOI: 10.5194/acp-20-13701-2020, 2020.

4) **Rolletter, M.**, Assaf, E., Fuchs, H., and Fittschen, C.: The Absorption Spectrum and absolute Absorption Cross Sections of Acetylperoxy Radicals, $CH_3C(O)O_2$ in the near IR, J. Quant. Spectrosc. Radiat. Transf., 245, 106877, DOI: 10.1016/j.jqsrt.2020.106877, 2020.

Band / Volume 537
Kompressionseigenschaften der Gasdiffusionslage einer Hochtemperatur-Polymerelektrolyt-Brennstoffzelle
E. Hoppe (2021), viii, 153 pp
ISBN: 978-3-95806-549-9

Band / Volume 538
Transparent Passivating Contact for Crystalline Silicon Solar Cells
M. Köhler (2021), 186 pp
ISBN: 978-3-95806-550-5

Band / Volume 539
Distribution of trace gases with adverse effects on fuel cells
D. Klemp, R. Wegener, R. Dubus, L. Karadurmus, N. Kille, Z. Tan (2021), 160 pp
ISBN: 978-3-95806-551-2

Band / Volume 540
Cyclotron Irradiation on Tungsten & Co-relation of Thermo-Mechanical Properties to Displacement and Transmutation Damage
R. Rayaprolu (2021), xiv, 211 pp
ISBN: 978-3-95806-552-9

Band / Volume 541
Smart Energy in Haushalten:
Technologien, Geschäftsmodelle, Akzeptanz und Wirtschaftlichkeit
H. Shamon, T. Rehm, B. Helgeson, F. Große-Kreul, M. Gleue, U. Paukstadt, G. Aniello, T. Schneiders, C. Frings, A. Reichmann, A. Löschel, T. Gollhardt, W. Kuckshinrichs, K. Gruber, P. Overath, C. Baedeker, F. Chasin, K. Witte, J. Becker
(2021), VI, 142 pp
ISBN: 978-3-95806-554-3

Band / Volume 542
Deployment Status of Fuel Cells in Road Transport: 2021 Update
R. C. Samsun, L. Antoni, M. Rex, D. Stolten (2021), 37 pp
ISBN: 978-3-95806-556-7

Band / Volume 543
Processing and creep resistance of short SiC fiber containing Ti_3SiC_2 MAX phase composites
A. Dash (2021), vii, 125 pp
ISBN: 978-3-95806-558-1

Band / Volume 544
Synthese und Charakterisierung von Geopolymeren für die Entsorgung der Spaltprodukte ^{137}Cs und ^{90}Sr
S. K. Weigelt (2021), VI, 186 pp
ISBN: 978-3-95806-559-8

Band / Volume 545
Potential depletion of ozone in the mid-latitude lowermost stratosphere in summer under geoengineering conditions
S. Robrecht (2021), 185 pp
ISBN: 978-3-95806-563-5

Band / Volume 546
Two-phase Flow in Porous Transport Layers of Polymer Electrolyte Membrane Electrolysers
D. Borah (2021), xi, 196 pp
ISBN: 978-3-95806-564-2

Band / Volume 547
Effects of root temperature on food quality of horticultural crops
F. He (2021), V, 143 pp
ISBN: 978-3-95806-565-9

Band / Volume 548
Verhalten und Kontrolle von Schlacken des bioliq®-Vergasers
K. Mielke (2021), 162, XXXV pp
ISBN: 978-3-95806-566-6

Band / Volume 549
Gravity waves resolved in Numerical Weather Prediction products
C. Strube (2021), iii, 139 pp
ISBN: 978-3-95806-567-3

Band / Volume 550
Experimental study of the chemical degradation of biogenic volatile organic compounds by atmospheric OH radicals
M. Rolletter (2021), XIII, 199 pp
ISBN: 978-3-95806-568-0

Energie & Umwelt / Energy & Environment
Band / Volume 550
ISBN 978-3-95806-568-0

Mitglied der Helmholtz-Gemeinschaft

JÜLICH
Forschungszentrum